EF3 COL 2.0-27-A

2.5.2 Vibratory Ground Motion

This subsection provides a detailed description of vibratory ground motion assessments that were carried out for the Fermi 3 site. The subsection begins with a review of the approach outlined in U.S. Nuclear Regulatory Commission (NRC) Regulatory Guide (RG) 1.208 for conducting the vibratory ground motion studies. Following this review of the regulatory framework used for the project, results of the seismic hazard evaluation are documented and the site-specific ground motion response spectra (GMRS) for horizontal and vertical motions are developed.

RG 1.208 provides guidance on methods acceptable to the NRC to satisfy the requirements of the seismic and geologic regulation, 10 CFR 100.23, “Reactor Site Criteria,” for assessing the appropriate safe shutdown earthquake (SSE) ground motion levels for new nuclear power plants. RG 1.208 indicates that an acceptable starting point for this assessment at sites in the central and eastern United States (CEUS) is the probabilistic seismic hazard analysis (PSHA) conducted by the Electric Power Research Institute and Seismicity Owners Group (EPRI-SOG) in the 1980s (Reference 2.5.2-201). However, it states that if more up-to-date information is available, it should be incorporated.

On January 27, 2012, the Electric Power Research Institute/U.S. Department of Energy/U.S. Nuclear Regulatory Commission (EPRI/USDOE/USNRC) published as NUREG-2115 the Central and Eastern United States Seismic Source Characterization (CEUS SSC) model (Reference 2.5.2-202) for use in assessing seismic hazard at nuclear facilities. This study was conducted as a Senior Seismic Hazard Analysis Committee (SSHAC) Level 3 study (Reference 2.5.2-203). The CEUS SSC study was also conducted following guidance developed by the NRC for conducting SSHAC Level 3 and 4 studies that was published as NUREG-2117 (Reference 2.5.2-204). The CEUS SSC model is intended to be a replacement for the EPRISOG (Reference 2.5.2-201) and Lawrence Livermore National Laboratory (LLNL) (Reference 2.5.2-212) seismic source models. The acceptance of this model by the NRC as the up-to-date basis for characterizing seismic sources in the CEUS is evident by the requirement that the CEUS SSC model be used in responses to Recommendation 2.1 of the Fukushima Near-Term Task Force recommendations contained in SECY-12-0025 (Reference 2.5.2-205) as it pertains to the seismic hazard evaluation.

The other major component to assessing seismic hazards is the selection of appropriate ground motion models for evaluating the levels of strong ground motions produced by earthquakes. In 2004, EPRI conducted a SSHAC Level 3 study (Reference 2.5.2-206) to develop characterization of CEUS earthquake ground motions for assessing seismic hazards at nuclear power plant sites. The aleatory variability component of the 2004 EPRI (Reference 2.5.2-206) ground motion model was refined by the 2006 EPRI SSHAC Level 2 study (Reference 2.5.2-207). Again, acceptance of the EPRI 2004/2006 (Reference 2.5.2-206 and Reference 2.5.2-207) ground motion models as up-to-date information is evidenced by the requirement that they be used in responses to Recommendation 2.1 of the Fukushima Near- Term Task Force recommendations contained in SECY-12-0025 (Reference 2.5.2-205).

RG 1.208 further specifies that the adequacy of the PSHA input must be evaluated in light of new data and interpretations and evolving knowledge pertaining to seismic hazard evaluation. NUREG-2117 provides specific guidance on evaluation of the need to update existing acceptable (viable) characterizations of seismic sources and earthquake ground motions. This guidance was followed in the evaluation of the adequacy of the CEUS SSC model and the EPRI 2004/2006 ground motion models for performing the PSHA for the Fermi 3 site.

RG 1.208 provides guidance on performance goal-based methods acceptable to the NRC to satisfy the requirements of 10 CFR 100.23 for assessing the appropriate site-specific performance goal-based ground motions for new nuclear power plants. Specifically, the performance-based approach described in American Society of Civil Engineers/Structural Engineering Institute Standard 43-05, “Seismic Design Criteria for Structures, Systems, and Components in Nuclear Facilities,” may be used to define site-specific performance goal–based GMRS at the ground surface based on mean hazard results (Reference 2.5.2-208). The development of mean seismic hazard results is to be based on a site-specific PSHA combined with site-specific site amplification analyses. The procedures to be used to perform the PSHA and site amplification studies are described in RG 1.208.

This subsection discusses the following aspects of vibratory ground motion:

- Seismicity (Subsection 2.5.2.1)

- Geologic structures and seismic source models (Subsection 2.5.2.2)
- Correlation of earthquake activity with seismic sources (Subsection 2.5.2.3)
- Probabilistic seismic hazard analysis and controlling earthquakes (Subsection 2.5.2.4)
- Seismic wave transmission characteristics of the site (Subsection 2.5.2.5)
- Ground motion response spectra (Subsection 2.5.2.6)

2.5.2.1 Seismicity

An important component in developing a seismic hazard model for the Fermi 3 site is the seismic history of the region. The selected starting point for developing the site-specific PSHA for the Fermi 3 site is the CEUS SSC model for seismic sources presented in NUREG-2115. The first step in the process for evaluating the adequacy of this model for the assessment of seismic hazards at the Fermi 3 site involved the inclusion of recent information on the seismicity in the CEUS. The development of an updated earthquake catalog for the site region (320 km [200 mi] radius) and surrounding areas is described in Subsection 2.5.2.1.1. Information on significant earthquakes in the site region is provided in Subsection 2.5.2.1.2. Discussion of large-magnitude historical and prehistoric central and eastern North America (CENA) earthquakes located beyond the site region that have some significance to the seismic hazard at the Fermi 3 site that have occurred beyond the site region is provided in Subsection 2.5.2.2. An evaluation of the impact of the post-CEUS seismicity data, for the time period 2009 through 2012, on the CEUS SSC seismic source model is presented in Subsection 2.5.2.4.1.

The Fermi 3 Seismic Category I structures are founded on bedrock or on fill concrete above bedrock and are not subject to liquefaction potential as discussed in Subsection 2.5.4.8. No reports or studies exist on liquefaction and paleoliquefaction in the site vicinity (40 km [25 mi] radius) as presented in Subsection 2.5.1.2.6.6. Subsection 2.5.1.2.5 evaluates the site geologic hazard. The site is also relatively flat and the slopes are considered stable as discussed in Subsection 2.5.5.

2.5.2.1.1 Earthquake Catalog

Earthquake occurrence rates for the distributed seismicity sources (source zones) in the CEUS SSC seismic source model were based on

the CEUS SSC earthquake catalog that was developed for the time period of 1568 through the end of 2008. NUREG-2115 produced an earthquake catalog that is complete (in terms of known earthquakes) and uniformly processed for this time period. The NUREG-2115 catalog is the starting point for creating an updated earthquake catalog for the Fermi 3 site region.

The CEUS SSC earthquake catalog (described in Section 3 of NUREG-2115) was compiled by merging all available earthquake records from continental-scale earthquake catalogs such as the US Geological Survey (USGS) and Geological Survey of Canada (GSC) catalogs; from regional and state catalogs (e.g., the Southeastern US Seismic Network catalog, the Ohio Seismic Network catalog), and from a variety of studies addressing individual earthquakes or groups of earthquakes. In the process of merging records from multiple sources, duplicate entries and non-tectonic events were initially included. These duplicate entries and non-tectonic events were then removed as part of the CEUS SSC catalog processing. An important component of the NUREG-2115 CEUS catalog was the assignment of a uniform moment magnitude estimate, the expected moment magnitude (E[**M**]), to each earthquake. The E[**M**] is the expected value of the true moment magnitude (**M**) and is calculated for each earthquake from one or more alternative measurements of earthquake size, such as other magnitude scales or shaking intensity measures. In NUREG-2115, a set of empirical scaling relationships was developed to convert various instrumental magnitudes and macroseismic intensity measures (i.e., maximum epicentral intensity or felt area) to E[**M**]. As described by EPRI-SOG (Reference 2.5.2-201) and by Tinti and Mulargia (Reference 2.5.2-209), uncertainty in the estimated magnitudes for each earthquake can lead to biased estimates of earthquake recurrence parameters. To address this issue, EPRI-SOG introduced an adjusted magnitude M* for use in developing unbiased recurrence parameters (Reference 2.5.2-201). The EPRISOG approach is referred to as the M* approach in NUREG-2115. In the CEUS SSC project, an alternative approach was used to obtain unbiased recurrence parameters in which the earthquake counts in each magnitude interval are adjusted individually by a multiplicative factor using an adaptation of the method proposed by Tinti and Mulargia (Reference 2.5.2-209). This approach is referred to as the equivalent count or N* approach in NUREG-2115. Simulations documented in NUREG-2115 show that the N* approach

performs better than the M* approach when the earthquake catalog has varying levels of completeness as a function of magnitude.

Following the process used in NUREG-2115 for earthquake catalog development, the updated earthquake catalog within 320 km (200 mi) of the Fermi 3 site is obtained by merging a portion of the CEUS SSC catalog (between 39 and 45°N and 79 and 87.5°W) containing the independent[1] earthquakes (main shocks), with all available records of earthquakes that occurred in the same region in the time period from January 1, 2009, through December 31, 2012. Earthquake records in the post-CEUS SSC catalog period were obtained from the following sources:

- USGS National Earthquake Information Center (NEIC) website
- Advanced National Seismic System (ANSS) website
- Ohio Seismic Network website operated by the Ohio Geological Survey
- National Earthquake Database (NEDB) operated by the Geological Survey of Canada.

Duplicate entries and aftershocks were removed from the data set. The E[**M**] was used as the uniform magnitude scale in the CEUS SSC project because moment magnitude is the earthquake size measurement used in modern ground motion prediction equations (GMPEs) for the CEUS, as evidenced in the EPRI 2004/2006 ground motion models (Reference 2.5.2-206). The magnitude conversion equations developed in NUREG-2115 were used to obtain E[**M**] for all the post-CEUS SSC catalog earthquakes. For these post-CEUS SSC earthquakes, the equivalent counts (N* values) were obtained by applying the procedure described in NUREG-2115.

Figure 2.5.2-201 shows the spatial distribution of all earthquakes in the NUREG-2115 CEUS SSC catalog. The CEUS SSC earthquake catalog in NUREG-2115 incorporates the 320 km (200 mi) radius site region and all seismic sources contributing significantly to the Fermi 3 site earthquake hazard. Figure 2.5.2-202 shows the locations of earthquakes within 320 km (200 mi) of the Fermi 3 site. The earthquakes are color-coded on

1. The PSHA formulation used in this study assumes that the temporal occurrence of earthquakes conforms to a Poisson process, implying independence between the times of occurrence of earthquakes. Thus it is necessary to remove dependent events (such as foreshocks and aftershocks) from the earthquake catalog before estimating earthquake recurrence rates.

Figure 2.5.2-202 to indicate those events included in the CEUS SSC earthquake catalog for the time period 1568 to 2008, and those events that occurred after development of the CEUS SSC earthquake catalog for the time period 2009 through 2012. The earthquakes occurring after completion of the CEUS SSC earthquake catalog have similar spatial distributions and do not indicate new concentrations of seismicity.

Figure 2.5.2-203 shows the locations of earthquakes within 80 km (50 mi) of the Fermi 3 site. The earthquakes are again color-coded on Figure 2.5.2-203 to indicate those events included in the CEUS SSC earthquake catalog for the time period 1568 to 2008, and those events that occurred after development of the CEUS SSC earthquake catalog for the time period 2009 to 2012. As can be seen on Figure 2.5.2-203, the seismicity within 80 km (50 mi) of the Fermi 3 site is diffuse.

Appendix 2.5AA lists the earthquakes in the updated catalog that have occurred within 320 km (200 mi) of the Fermi 3 site. The list consists of 185 events of E[**M**] greater than 1.8 that occurred between 1776 and 2012.

Focal depths are either not determined (indicated by “n.a”) or fixed (set to 5, 10, 15, or 18 km) for most earthquakes. The deepest event recorded within 320 km (200 mi) of the Fermi 3 site has an estimated depth of 28.5 km (18 mi), but most of the seismicity is concentrated in the upper 10 km (6 mi). Focal depths of the post-CEUS SSC earthquakes with non fixed depths are generally within the upper 5 km (3 mi). These data are consistent with the observed focal depth distributions for the CEUS described in Section 5.4.4 of NUREG-2115.

2.5.2.1.2 Significant Earthquakes in the Site Region (320 km [200 mi] radius)

As shown on Figure 2.5.2-202 and Figure 2.5.2-203, seismicity in Michigan is sparse. Many of the historical events reported in Michigan were determined to be atmospheric shock waves, explosions, cryoseisms, or erroneous reports (Reference 2.5.2-210). The largest known earthquake within 320 km (200 mi) of the Fermi 3 site is the March 9, 1937, E[**M**] 5.11 earthquake that occurred near Anna, Ohio, approximately 190 km (120 mi) from the Fermi 3 site. The earthquake caused extensive damage with reported shaking intensities ranging between VII and VIII Modified Mercalli Intensity (MMI) near the epicenter, and was felt over a large area including Ohio and parts of Indiana, Illinois,

Kentucky and Michigan (Reference 2.5.2-211). This earthquake is included in the NUREG-2115 earthquake catalog.

As shown on Figure 2.5.2-202 and Figure 2.5.2-203, no significant (i.e., E[**M**] ≥ 4) earthquakes have occurred within 320 km (200 mi) of the Fermi 3 site in the time period following completion of the NUREG-2115 catalog. Several moderate size earthquakes have occurred in the time period following completion of the NUREG-2115 catalog, such as the March 23, 2011, E[**M**] 5.73 earthquake near Mineral, VA and the November 6, 2011, E[**M**] 5.66 earthquake in central Oklahoma. However, these events are more than 320 km (200 mi) from the Fermi 3 site. The impact of these moderate magnitude earthquakes on the CEUS SSC model is evaluated in Subsection 2.5.2.4.1.2.

2.5.2.2 Geologic Structures and Seismic Source Models

RG 1.208 specifies that the PSHA conducted for a site is to be based on an up-to-date characterization of seismic sources. The recently completed CEUS SSC model published as NUREG-2115 presents an up-to-date regional model of seismic sources for the CEUS developed specifically for nuclear facilities. The CEUS SSC model replaces previous regional seismic source models developed for this purpose, the EPRI-SOG model (Reference 2.5.2-201) and the LLNL model (Reference 2.5.2-212). The CEUS SSC model was developed using SSHAC Level 3 methodology (Reference 2.5.2-203) to provide a high level of confidence that the data, models, and methods of the larger technical community have been considered, and that the seismic source model represents the center, body, and range (CBR) of technically defensible interpretations (TDI) of these data, models, and methods.

This subsection presents a description of the CEUS SSC model focused on those components that are used for conducting the PSHA for the Fermi 3 site. Subsection 2.5.2.2.1 describes the overall framework of the seismic source model. The remaining subsections then present summaries of the geological, geophysical, and seismologic data used to define the three types of seismic sources in the CEUS SSC model: the Mmax zones, described in Subsection 2.5.2.2.2; the seismotectonic zones, described in Subsection 2.5.2.2.3; and the repeated large magnitude earthquake (RLME) sources, described in Subsection 2.5.2.2.4.

2.5.2.2.1 Framework of the CEUS SSC Model

The study region of the CEUS SSC model includes the CEUS east of longitude 105°W, approximately along the eastern foothills of the Rocky Mountains, and extends approximately 320 km (200 mi) to the north, south, and east beyond the US national borders. The master logic tree for the CEUS SSC model, shown on Figure 2.5.2-204, portrays the framework that establishes the context for the entire seismic source model. The master logic tree depicts the alternative interpretations and conceptual models that represent the range of TDI and the relative weights assessed for the alternatives. The CEUS SSC model consists of two types of seismic sources. The first type is seismic source zones used to model future distributed seismicity throughout the CEUS. As shown on Figure 2.5.2-204, two approaches are used to define the distributed seismicity sources, as indicated by the first node of the logic tree labeled "Conceptual Approach." The Mmax zones approach subdivides the CEUS into regions solely on the basis that they are expected to have different distributions for the maximum magnitude earthquake that can occur. The seismotectonic zones approach subdivides the CEUS into different source zones based on expected differences in maximum magnitude as well as additional seismotectonics data that would suggest spatial differences in the characteristics of future earthquakes. These distributed seismicity source zones allow for the occurrence of earthquakes at all locations in the CEUS.

The second type of seismic source is used to model the recurrence of repeated large magnitude earthquakes (RLMEs) that have been identified from the historical and paleoseismic record. The RLME sources are additional sources of large magnitude earthquakes that are added to the seismic hazard computed from the distributed seismicity sources – either the Mmax zones or the seismotectonic zones. This is represented in the logic tree shown on Figure 2.5.2-204 by the vertical line without a node.

The logic tree for the Mmax source zones is shown on Figure 2.5.2-205. The first node of the logic tree shows that there are two interpretations of the geometry of Mmax zones. The first is that the entire CEUS region is a single source zone and the second is that the CEUS is divided into two Mmax source zones, a region in which the earth's crust has undergone Mesozoic and younger extension, denoted as the MESE crustal region; and a region where no crustal extension has occurred or extension is

older than Mesozoic in age, denoted as the NMESE crustal region. The basis for this distinction arises from the analysis of a global database of large stable continental region[2] (SCR) earthquakes presented in NUREG-2115. Earlier work by Johnston et al. (Reference 2.5.2-213) found that the most useful factor for distinguishing SCRs with different maximum magnitudes was the presence or absence of crustal extension. The CEUS SSC study repeated the analysis of Johnston et al. (Reference 2.5.2-213) using an updated SCR earthquake database and found that the most useful distinguishing feature was the presence or absence of extension of Mesozoic age or younger. As shown on Figure 2.5.2-205, there are two interpretations for the location of the boundary between the MESE and NMESE Mmax zones in the CEUS. These two interpretations are referred to as the “narrow” and “wide” interpretations, and are shown on Figure 2.5.2-206 and Figure 2.5.2-207, respectively. The Fermi 3 site is located in the NMESE Mmax source zone in both interpretations. A description of the Mmax zones is provided in Subsection 2.5.2.2.2.

The logic tree for the seismotectonic source zones is shown on Figure 2.5.2-208. There are four interpretations of the geometries of the seismotectonic source zones, as indicated by the first two nodes of the logic tree. These alternative interpretations produce four alternative geometries for the Midcontinent-Craton (MIDC) seismotectonic source zone. The two interpretations for the location of the boundary between MESE and NMESE crust are used to define alternative boundaries for the Paleozoic Extended Zone (PEZ). In addition, two interpretations are made for the connection of the Reelfoot Rift (RR) with the Rough Creek Graben (RR-RCG). The resulting four source zone geometries are shown on Figure 2.5.2-209, Figure 2.5.2-210, Figure 2.5.2-211, and Figure 2.5.2-212. The Fermi 3 site is located within the MIDC seismotectonic zone in each case. As discussed in Subsection 2.5.2.4.3, the PSHA conducted for the Fermi 3 site includes the contributions from all or parts of each distributed seismicity source that lies within 1000 km (620 mi) of the site. As a result, the seismotectonic zones included in the PSHA are:

- Atlantic Highly Extended Crust (AHEX);
- Extended Continental Crust – Atlantic Margin (ECC-AM);
- Great Meteor Hotspot (GMH);

2. The CEUS is one example of a SCR region

- Illinois Basin Extended Basement (IBEB);
- Midcontinent-Craton (MIDC-A, MIDC-B, MIDC-C, and MIDC-D)
- Northern Appalachian (NAP)
- Paleozoic Extended Crust (PEZ-N and PEC-W)
- Reelfoot Rift (RR) and Reelfoot Rift-Rough Creek Graben (RR-RCG);
- St. Lawrence Rift (SLR).

These seismotectonic zones are all shown on Figure 2.5.2-209, Figure 2.5.2-210, Figure 2.5.2-211, and Figure 2.5.2-212. Each of these seismoteconic zones is described in Subsection 2.5.2.2.3.

In addition to the alternative geometries discussed above, the characterization of the distributed seismicity source zones includes the use of three alternative magnitude ranges for computing seismicity parameters (Case A, Case B, and Case E), alternative values for seismogenic crustal thickness, rupture geometry, maximum magnitude distributions for each source, and seismicity parameter distributions for each source. These are represented by the labeled nodes on the logic trees shown on Figure 2.5.2-205 and Figure 2.5.2-208. Seismicity parameters for each source are specified as a set of recurrence rates and b-values for individual 0.25 degree longitude by 0.25 degree latitude or 0.5 degree longitude by 0.5 degree latitude cells or partial cells that make up the source zone area. Uncertainty in the earthquake recurrence parameters is represented in the model by eight alternative sets of these rates and b-values – in essence eight alternative maps of predicted future seismicity rates. There are eight alternative sets for each of the three magnitude interval weights (Case A, Case B, and Case E), resulting in a total of 24 alternative sets of earthquake recurrence parameters. The maximum magnitudes for each source zone are represented by a five-point discrete probability distribution that spans a wide range of moment magnitudes. The maximum magnitude distributions for the seismic source zones included in the Fermi 3 PSHA are further described in Subsection 2.5.2.4.3.

The locations of the 10 RLME sources included in the CEUS SSC model are shown on Figure 2.5.2-213. By definition, RLME sources are the locations of repeated (more than one) large magnitude (**M** ≥ 6.5) earthquakes in the historical or paleoearthquake record, including interpretations of paleoliquefaction features and fault displacement (paleoseismic) studies. As indicated in NUREG-2115, the relationship of

the RLME sources to observed historical seismicity is not clear. Because of the rarity of RLMEs relative to the period of historical observation, evidence for these earthquakes comes largely from the paleoearthquake record. Some of the RLME sources are associated with elevated historical and instrumental seismicity (Figure 2.5.2-213 and Figure 2.5.2-214), such as the central New Madrid (Figure 2.5.2-214) and Charlevoix faults, but others occur within areas of moderate levels of seismicity (e.g., Charleston and Wabash Valley).

A subset of the RLME sources shown to contribute approximately 1 percent or more to the total hazard at the Fermi 3 site are included in the updated PSHA (Subsection 2.5.2.4.3.1). The RLME source with the greatest contribution to the Fermi 3 site hazard is the New Madrid fault system, which models the large earthquakes in the central New Madrid region. Other RLME sources that contribute 1 percent or more to the total hazard at the Fermi 3 site are the Charleston, Charlevoix, and Wabash Valley RLME sources. Each of these RLME sources is described in Subsection 2.5.2.2.4.

The characterization of each of the RLME sources is also in the form of a logic tree. Figure 2.5.2-215 shows the logic tree for the New Madrid fault system. The first node of each logic tree for all the RLME sources addresses the issue of temporal clustering of large-magnitude earthquakes. Clustering produces relatively short intervals between several earthquakes in a cluster. The cluster of earthquakes are followed or preceded by much longer time intervals without clustering. The assessment that a RLME source is currently in or out of a period of clustering thus affects the recurrence rate for RLMEs in the near future. Subsequent nodes in the logic tree address alternative geometries of the source and of future earthquake ruptures, uncertainty in the average magnitude of future RLMEs, and uncertainty in the recurrence frequency of future RLMEs.

2.5.2.2.2 Mmax Zones—Criteria for Defining the MESE/NMESE Boundary

The breakup of the supercontinent of Pangaea into Laurasia to the north and Gondwana to the south resulted in Mesozoic extension of the crust and consequent development of the Atlantic Ocean (Triassic), the passive Atlantic margin (Jurassic), and the Gulf of Mexico (from Triassic to Jurassic). As a result of this extension, both the Atlantic margin and Gulf Coast margins generally consist of three crustal domains: rifted

continental crust (also referred to as thick transitional crust), oceanic crust underlying the continental rise, and an intervening zone of thin transitional, or rift-stage, crust (Reference 2.5.2-214 and Reference 2.5.2-215).

The western limit of significant Mesozoic-and-younger extension in the CEUS is inferred from a variety of geologic, geophysical, and seismologic data. Criteria used to define this boundary are listed below, ordered from most diagnostic to least definitive for identifying Mesozoic-and-younger extension.

1. Grabens and sedimentary rift basins of Mesozoic age.
2. Mesozoic-and-younger plutons.
3. Extensive distributed brittle normal faults and basaltic (thoeliitic) dikes of Mesozoic-and-younger age.
4. Evidence for Mesozoic-and-younger regional uplift and unroofing with associated normal faulting or fault reactivation.
5. Localized extensional reactivation of pre-Mesozoic structures.
6. Favorably oriented older extensional faults (e.g., Iapetan rift faults proximal to regions of Mesozoic rifting).

Regions that generally meet the first three to four criteria are included in the MESE-narrow (MESE-N) zone. The MESE-N zone includes the AHEX, ECC-AM, GMH, NAP, PEZ-N, RR, and SLR seismotectonic zones (see Figure 2.5.2-209 and Figure 2.5.2-210).

The MESE-wide (MESE-W) boundary encompasses regions that have less definitive evidence for significant Mesozoic-and-younger extension. These regions include areas that have known or possible Iapetan-rift faults that may have been reactivated during the Mesozoic (e.g., the Rough Creek graben [RCG]) and older Precambrian compressional structures, such as the Clarendon-Linden fault and Central Metasedimentary Belt boundary structure in western New York and Ontario, Canada, that have evidence of extensional reactivation during late Precambrian/early Paleozoic Iapetan rifting, but have less definitive evidence for Mesozoic reactivation. The MESE-W zone includes AHEX, ECC-AM, GMH, NAP, PEZ-W, RR-RCG, and SLR seismotectonic zones (see Figure 2.5.2-211 and Figure 2.5.2-212).

As described in Chapter 5 of NUREG-2115, the assessment of Mmax distributions for the distributed seismicity sources is based in part on the largest earthquakes that have been observed within the source zone. The four largest earthquakes that have occurred in the MESE-N zone are the September 16, 1732, E[**M**] 6.25; March 1, 1925, E[**M**] 6.18; November 18, 1755, E[**M**] 6.10; and October 17, 1860, E[**M**] 6.08 earthquakes. The August 23, 2011, E[**M**] 5.73 Mineral, VA, earthquake also occurred in this zone.

The MESE-W zone encompasses the IBEB seismotectonic zone in which four paleoearthquakes have been identified that are not associated with the Wabash Valley RLME. These are the 3,950 years ago E[**M**] 6.3 Vallonia, Indiana; 5,670 years ago E[**M**] 6.2 Shoal Creek, Illinois; between 5,960 and 7,390 years ago E[**M**] 6.2 Springfield, Illinois; and between 3,500 and 8,500 years ago E[**M**] 6.2 Waverly, Indiana, earthquakes. Further discussion of the magnitude assessments for these earthquakes is presented in Subsection 2.5.1.1.4.4.2. These earthquakes are larger than nearly all of the historical earthquakes in the MESE-W zone and were used in NUREG-2115 to develop the Mmax distribution for MESE-W.

The NMESE-N zone also encompasses the IBEB seismotectonic zone and the four paleoearthquakes listed above were used in NUREG-2115 to develop the Mmax distribution. The four largest earthquakes that have occurred in the NMESE-W zone are the May 16, 1909, E[**M**] 5.72; November 6, 2011, E[**M**] 5.66; October 22, 1882, E[**M**] 5.58; and November 15, 1877, E[**M**] 5.50 earthquakes. The 1882 earthquake may have occurred in the MESE zone instead (Reference 2.5.2-202).

2.5.2.2.3 Seismotectonic Zones

Nine seismotectonic source zones are included in the seismic hazard model for the Fermi 3 site. The region within 320 km (200 mi) of the site is nearly entirely contained within the MIDC seismotectonic zone (see Figure 2.5.2-209 through Figure 2.5.2-212), and the characteristics of this zone are described below. Following the MIDC, the eight additional source zones included in the model are described in alphabetical order, as follows: AHEX, ECC-AM, GMH, IBEB, NAP, PEZ, RR/RR-RCG, and SLR.

Midcontinent-Craton Zone (MIDC)

The MIDC seismotectonic zone is a large intracratonic region underlain by several Precambrian terranes. It is composed of continental crust that has not experienced Mesozoic and younger crustal extension. Defining the extent of the MIDC seismotectonic zone centers primarily on the concept that continental crust that has experienced Mesozoic and younger crustal extension will have a different maximum magnitude probability than crust that has not experienced Mesozoic and younger extension (Reference 2.5.2-202). The MIDC zone is also defined as a seismic source in part to differentiate it from adjoining regions of the crust that are interpreted as producing different future rupture characteristics. For example, the trend of future ruptures in the adjoining IBEB and RR seismotectonic zones reflects preferred orientations of structures in those zones, which differ from the trend of ruptures modeled for the MIDC. Four alternative geometries for the MIDC zone are considered based on alternative geometries of the adjacent PEZ and RR/RR-RCG seismotectonic zones. These are shown on Figure 2.5.2-209, Figure 2.5.2-210, Figure 2.5.2-211, and Figure 2.5.2-212.

The continental interior (Midcontinent-Craton), which consists of those regions that have not been incorporated into Phaerozoic orogens of the continental margin, comprises two geologic provinces: the Canadian Shield, where Precambrian metamorphic and igneous basement rocks crop out at the ground, and the platform, where Precambrian basement rocks lie beneath a veneer of sedimentary strata (Reference 2.5.2-216).

Major Precambrian basement features have been interpreted by various parties based on interpretation of geologic data from drilling, deep crustal seismic profiles, and interpretation of geopotential field data (e.g., Reference 2.5.2-216, Reference 2.5.2-217, Reference 2.5.2-218, and Reference 2.5.2-219). These interpretations are shown on Figure 2.5.2-216 and Figure 2.5.2-217. Sims et al. (Reference 2.5.2-220) present a preliminary structure map of Precambrian basement rocks that indicate two orthogonal sets of shear zones and faults are predominant in the continent: (1) northeast-striking partitioned ductile shear zones and (2) northwest-trending strike-slip ductile-brittle faults. Marshak and Paulsen (Reference 2.5.2-216) identified similar north-northeast and west-northwest trends that break up the continental interior of the United States into roughly rectangular blocks. They refer to these as the Midcontinent fault and fold zones and suggest that the current intraplate

stress field of North America is sufficient to cause slight movements of crustal blocks in the interior, thereby triggering seismicity.

The four largest historical earthquakes recorded within the MIDC zone are the May 16, 1909, E[**M**] 5.72; November 6, 2011, E[**M**] 5.66; November 15, 1877, E[**M**] 5.50; and August 23, 2011, E[**M**] 5.31 earthquakes. The impact of the two post-CEUS SSC model earthquakes from the time period 2009 through 2012 on the assessment of Mmax is evaluated in Subsection 2.5.2.4.1.2. The locations of these earthquakes are shown on Figure 2.5.2-218. Seismicity within the MIDC zone is spatially variable, with moderate concentrations of earthquake activity separated by areas of very low seismicity. Previously recognized zones of seismicity include the Anna seismic zone in Ohio (Subsection 2.5.1.1.4.3.3.2), the Northeast Ohio seismic zone (Subsection 2.5.1.1.4.3.3.1), and a zone of moderate seismicity in the vicinity of the Nemaha Ridge-Humboldt fault seismic zone in Kansas (Figure 2.5.2-218). Reconnaissance paleoliquefaction surveys have not identified evidence for large-magnitude (**M** > 7) earthquakes in these zones.

Atlantic Highly Extended Crust Zone (AHEX)

As described in Subsection 2.5.2.2.2 for the Mmax zone branch (Subsection 2.5.2.2.2), the present-day passive Atlantic margin can be divided into three general zones based on characteristics that include crustal structure, composition, and thickness. The narrow zone of highly extended transitional crust is included in the AHEX seismotectonic zone, while the ECCAM seismotectonic zone to the west includes only the rifted and extended portion of the continental crust.

The highly extended crust that forms the AHEX zone is entirely offshore and approximately follows the continental shelf edge from Georgia to Nova Scotia (Figure 2.5.2-209). The eastward-thinning wedge of highly extended transitional crust that characterizes the AHEX zone is significantly thinner than the approximately 35 to 40 km (22 to 25 mi) thick extended continental crust of the adjacent ECC-AM seismotectonic zone. Crustal-scale seismic-reflection profiles derived from seismic studies offshore of South Carolina (Reference 2.5.2-221), Virginia (Reference 2.5.2-215), and Nova Scotia (Reference 2.5.2-222) indicate that the AHEX zone ranges in thickness from about 15 to 30 km (9.5 to 19 mi). The decreasing crustal thickness away from the continent

strongly argues that the seismogenic thickness (typically thinner than the crust or depth to the Moho) should also be thinner in the AHEX than in the adjoining ECCAM. These same studies also reveal that the zone of transitional crust of the AHEX zone corresponds to the strong positive East Coast magnetic anomaly (ECMA), a major geophysical feature of the North American Atlantic margin that extends from Georgia to Nova Scotia (Figure 2.5.2-219). The eastern limit of rifted continental crust is interpreted to correspond to the western margin of the ECMA, and the western limit of oceanic crust to correspond to the eastern margin of the ECMA (Reference 2.5.2-215 and Reference 2.5.2-221).

The ECMA is spatially correlated with a zone of transitional igneous crust, marking the seaward transition from rifted continental crust to mafic oceanic crust that extends along the entire Atlantic margin (Reference 2.5.2-215, Reference 2.5.2-221, Reference 2.5.2-223, Reference 2.5.2-224, and Reference 2.5.2-225). This implies that the basalts and underlying mafic intrusives produce the high magnetic values of the anomaly (Reference 2.5.2-226). The ECMA therefore marks a profound geological boundary beyond which little continental crust occurs (Reference 2.5.2-215). The AHEX zone was largely defined based on the location of the ECMA as this magnetic anomaly corresponds to the highly extended transitional crust comprising the AHEX (Figure 2.5.2-219). Although the boundary of the AHEX is generally well defined by high total magnetic values, the boundary is gradational, and thus local uncertainty about the location of the boundary between AHEX and ECC-AM seismotectonic zones could be on the order of tens of kilometers. The largest observed earthquake within the AHEX is the September 24, 1996, E[**M**] 2.89 earthquake (Figure 2.5.2-221).

Extended Continental Crust–Atlantic Margin Zone (ECC-AM)

The ECC-AM seismotectonic zone was defined to include the region characterized by the presence of extended continental crust developed during Mesozoic rifting along the Atlantic margin. The zone includes onshore portions as well as most of the offshore continental shelf region extending from Georgia to Nova Scotia (Figure 2.5.2-209). The basis for defining the ECC-AM seismotectonic zone centers primarily on the assessment that Mesozoic and younger extended crust has produced all **M** ≥ 7 stable craton earthquakes worldwide, and that extended or rifted crust may provide a basis for differentiating Mmax (Reference 2.5.2-202 and Reference 2.5.2-213). The western boundary of the ECC-AM

generally follows the western edge of the Triassic-Jurassic onshore basins or the boundaries of the structural blocks in which they occur. The eastern boundary of the ECC-AM follows the western margin of the ECMA.

A distinguishing structural feature of the Mesozoic extended crust within the ECC-AM is that it includes an older, east-dipping Paleozoic master basal detachment surface separating overthrusted Paleozoic Appalachian terranes from the underlying rocks of the North American craton. In general, Paleozoic thrust sheets above the master detachment surface change across the Appalachian orogenic belt in the ECC-AM from dominantly “thin-skinned” in the west over the North American craton, to dominantly “thick-skinned” in the accreted terranes to the east over the cratonic margin (Reference 2.5.2-214). An abundance of major shear zones and faults, most of which are related to the Paleozoic accretion of terranes during the Appalachian orogenies, occur within the ECC-AM. Mesozoic normal faults bound the rift basins throughout the ECC-AM. The locations of these basins are shown on Figure 2.5.2-220. The location and geometry of these rift basins are interpreted to have been controlled mainly by existing Paleozoic structures, which were reactivated as brittle normal faults when the Mesozoic extension direction was at a high angle to the preexisting fault (Reference 2.5.2-227 and Reference 2.5.2-228). The occurrence of late Cenozoic movement along the faults mapped in the ECC-AM is difficult to assess because of poor exposure, lack of suitable stratigraphy, relatively small displacements, and low slip rates on these faults.

Seismicity within the ECC-AM is spatially variable, with moderate concentrations of earthquake activity separated by areas of very low seismicity. The most prominent of these zones of seismicity are located in the Central Virginia seismic zone and the greater New York City–Philadelphia area. To a lesser degree, these prominent zones include clusters of seismicity in the Charleston, South Carolina, area, the Piedmont region of South Carolina and Georgia, and New England (Figure 2.5.2-221). As characterized by Bollinger et al. (Reference 2.5.2-229), hypocenters in the Atlantic Coastal Plain are distributed throughout the upper 13 km (8 mi) of the crust where focal mechanisms indicate a north-northeast maximum horizontal compressive stress. The largest earthquake within the ECC-AM is the 1886 Charleston earthquake. Due to the strong paleoliquefaction evidence for RLMEs in

the Charleston area, a separate RLME seismic source zone is defined for Charleston (described in Subsection 2.5.2.2.4). The four largest non-RLME earthquakes that have occurred in the ECC-AM zone are the November 18, 1755, E[**M**] 6.10 Cape Ann (which may have occurred within the NAP seismotectonic zone); August 23, 2011, E[**M**] 5.73 Mineral, VA; June 11, 1638, E[**M**] 5.32; and March 23, 1758, E[**M**] 4.95 earthquakes (Figure 2.5.2-221).

Great Meteor Hotspot Zone (GMH)

The GMH seismotectonic zone lies within the Western Quebec seismic zone, containing two distinct bands of seismicity as defined by Adams and Basham (Reference 2.5.2-230). One band that trends west-northwest along the Ottawa River between Ottawa and Lake Timiskaming is associated with rift faults of the Ottawa-Bonnechere graben, and the other band is interpreted to be part of the SLR seismotectonic zone (described below). The second band trends north-northwest to the north of the Ottawa River, and Adams and Basham (Reference 2.5.2-230) have suggested that this second band of seismicity is due to crustal fractures that formed as the North American Plate rode over a Cretaceous hotspot (Reference 2.5.2-231). The geometry of the GMH zone is consistent with a region of thinner crust northeast of the Ottawa-Bonnechere graben observed by Eaton et al. (Reference 2.5.2-232) and with the progressive change from kimberlitic melts in the interior of the craton to more voluminous crustal magmatism as the hotspot interacted with a progressively thinner lithosphere (Reference 2.5.2-233). Morgan (Reference 2.5.2-234) attributed the age distribution of these rocks to two hotspot tracks passing through New England at different times: the Verde hotspot track at 160 million years ago (Ma) and the Meteor hotspot at about 120 Ma. Elevated seismicity rates are present within Grenville-age crust that lacks Iapetan rifting but exhibits Cretaceous volcanism and reactivation, and these form the basis of the GMH seismotectonic zone.

The GMH has been associated with clusters of midcrustal seismicity by Ma and Eaton (Reference 2.5.2-233). Ma and Atkinson (Reference 2.5.2-235) attribute the wide hypocentral depth distribution (2 to 25 km [1.2 to 15.5 mi]) for relocated earthquakes in the Western Quebec seismic zone to faults of through-going crustal extent or faults of varying depths in the crust. Ma and Eaton (Reference 2.5.2-233) recognize that seismicity cannot be easily correlated with Grenville or Iapetan structures

within this zone and conclude that the GMH provides the only compelling explanation for seismicity within the Western Quebec seismic zone. Seismicity may result from either weakened crust caused by reheating or from stress concentrations caused by strength contrasts between mafic and felsic crust (Reference 2.5.2-233). Adams and Basham (Reference 2.5.2-230) postulate that elevated rates of seismicity in western Quebec are due to thermally stressed and fractured crust, whereas plutonism in New England may have healed deep crustal fractures. Therefore, the geometry for the GMH seismotectonic zone encompasses the volume of crust likely to produce frequent moderate earthquakes associated with thermally stressed crust.

The three largest earthquakes that have been recorded in the GMH zone are the June 23, 2010, E[**M**] 5.11; February 10, 1914, E[**M**] 5.10; and October 19, 1990, E[**M**] 4.53 earthquakes (Figure 2.5.2-222).

Illinois Basin Extended Basement Zone (IBEB)

The IBEB source zone is defined to characterize sources of moderate- to large-magnitude earthquakes (excluding those attributed to the Wabash Valley RLME source) that may occur on deep structures in the Precambrian basement and on Paleozoic faults that extend into the overlying Paleozoic sedimentary rocks. Southern Indiana and southern Illinois are characterized by higher rates of seismicity than adjacent craton regions. Braile et al. (Reference 2.5.2-236) proposed that two branches or arms of the Reelfoot rift, the Wabash Valley and St. Louis arms, extend into southern Indiana and southeast Missouri, respectively. Although subsequent studies (e.g., Reference 2.5.2-237) have demonstrated that highly extended rifted crust does not extend into these regions as far as Braile et al. (Reference 2.5.2-236) proposed, the interpretation of seismic profiles and the mapping and dating of paleoliquefaction features in the southern Illinois basin provide evidence for multiple paleoearthquakes having magnitudes larger than historical earthquakes that have occurred in this region. The two largest paleoearthquakes that appear to be localized within the Wabash Valley are included in the Wabash Valley RLME source zone (Subsection 2.5.2.2.4). Four additional paleoearthquakes are recorded by more widely distributed liquefaction features and inferred energy centers for moderate-sized earthquakes beyond the limits of the Wabash Valley RLME source. These are the approximate **M** 6.3 Vallonia, approximate **M**

6.2 Shoal Creek, approximate **M** 6.2 Springfield, and **M** 6.2 Waverly earthquakes (Figure 2.5.2-223) (Reference 2.5.2-202).

The southern part of the Illinois basin is one of the most structurally complex areas of the Midcontinent with crust that is distinct from that of the neighboring craton. Upper-mantle heterogeneity, sequences of Precambrian layered volcanic rocks, and a circular to oval pattern of these sequences are all suggestive of a large collapsed caldera complex (Reference 2.5.2-238). McBride, Hildenbrand, et al. (Reference 2.5.2-239) and McBride et al. (Reference 2.5.2-238) have completed integrated analyses of geophysical, industry seismic reflection profile, and well data to evaluate possible fault sources for historical earthquakes in the southern Illinois basin. These studies suggest that both Precambrian basement and Paleozoic structures within the southern Illinois basin have been reactivated by recent moderate-sized earthquakes, and that to a large degree, Paleozoic structures may be decoupled from deeper seismogenic Precambrian basement structures. A clear association of seismicity with mapped structural trends, however, is not well documented throughout the southern Illinois basin (Reference 2.5.2-238).

The four largest historical earthquakes recorded within the zone are the September 27, 1891, E[**M**] 5.52; November 9, 1968, E[**M**] 5.32; April 18, 2008, E[**M**] 5.30; and October 8, 1857, E[**M**] 5.13 earthquakes (Figure 2.5.2-224). These earthquakes are smaller than the paleoearthquakes identified in the IBEB zone and the paleoearthquake data was used in NUREG-2115 to develop the Mmax distribution.

Northern Appalachian Zone (NAP)

The NAP seismotectonic zone (Figure 2.5.2-209) contains crust initially formed during the Paleozoic that subsequently experienced multiple phases of extension into the Mesozoic. This area of crust was characterized by Wheeler (Reference 2.5.2-240) as the Iapetan rifted margin (IRM) following work by Johnston et al. (Reference 2.5.2-213), which determined that zones of rifted crust in SCRs correlate directly with increased earthquake activity (number and maximum magnitude) when compared to zones of nonrifted SCRs. The IRM concept is incorporated in source characterization for the national seismic hazard maps for the United States (Reference 2.5.2-241) and Canada (Reference 2.5.2-242). For the CEUS SSC project, crust of the IRM source zone of Wheeler

(Reference 2.5.2-240) and Adams et al. (Reference 2.5.2-242) has been divided into the NAP, PEZ, and SLR seismotectonic zones according to geologic criteria established for separating crust on the basis of Mmax and future earthquake characteristics (for more information see NUREG-2115).

The geometry for the NAP seismotectonic zone is modified from the Northern Appalachians source zone of the Geological Survey of Canada (Reference 2.5.2-243 and Reference 2.5.2-244). Terranes of the NAP zone formed outboard of the Laurentian margin after Iapetan rifting and were subsequently accreted to the passive margin. The zone is characterized as extending from the landward limit of Mesozoic extensional faulting to the seaward limit of thinned Grenville crust of the Iapetan passive margin. Seismicity occurs above the continental margin within crust of Appalachian terranes (Reference 2.5.2-245). Crust of the NAP seismotectonic zone is separated from the ECC-AM seismotectonic zone on the basis of lack of late Paleozoic (Alleghanian) structure and fault-bounded Mesozoic rift basins. The crust postdates Iapetan rifting and therefore is excluded from the adjacent SLR and PEZ seismotectonic zones.

The four largest observed earthquakes in the NAP seismotectonic zone include the March 21, 1904, E[**M**] 5.73 Passamaquoddy Bay; October 22, 1869, E[**M**] 5.47; January 8, 1982, E[**M**] 5.47 Miramichi; and the December 20, 1940, E[**M**] 5.08 earthquakes. The locations of these earthquakes are shown on Figure 2.5.2-225. There is also some possibility that the largest observed earthquake in the ECC-AM seismotectonic zone (1755, E[**M**] 6.10 Cape Ann earthquake) occurred in the NAP seismotectonic zone.

Paleozoic Extended Crust (PEZ)

The PEZ seismotectonic zone consists of continental crust that includes known and inferred normal faults that formed parallel to the passive margin of Laurentia during the late Proterozoic–early Paleozoic opening of the Iapetus Ocean. This area of crust was characterized by Wheeler (Reference 2.5.2-240) as the IRM, which includes the NAP and SLR in addition to the PEZ seismotectonic zones.

Compressional reactivation of favorably oriented Iapetan faults has been suggested as the causal mechanism for several seismically active regions within the PEZ seismotectonic zone, including Giles County,

Virginia, and eastern Tennessee (Reference 2.5.2-240, Reference 2.5.2-246, and Reference 2.5.2-247) (Figure 2.5.2-226).

The PEZ seismotectonic zone is differentiated from the adjacent SLR, EEC-AM, and MIDC seismotectonic zones to accommodate alternative potential differences in Mmax. In contrast to the SLR and ECC-AM zones in which there is clear evidence for Mesozoic reactivation of faults, Mesozoic extension within the PEZ zone is equivocal, but cannot be precluded, as it can be in the MIDC seismotectonic zone. Work by Faure et al. (Reference 2.5.2-248) suggests that Atlantic rifting was a widespread extensional event that extended as far as 400 km (250 mi) into the North American plate. Pliocene and younger deformation in Giles County (Reference 2.5.2-249 and Reference 2.5.2-250) and the Rome trough (Reference 2.5.2-251) can be considered a proxy for Mesozoic activity in the PEZ. Therefore, unlike adjacent zones, the PEZ is considered to contain either MESE or NMESE crust.

Two alternative geometries are considered for PEZ, namely the PEZ Narrow (PEZ-N) and PEZ Wide (PEZ-W) zones reflecting the alternative locations for the MESE/NMESE boundary (Figure 2.5.2-209 and Figure 2.5.2-211). PEZ-N is defined based on structural and seismologic evidence that provides the most convincing evidence for the presence of Iapetan faults or rift sediments below the detachment (Reference 2.5.2-240). PEZ-W geometry extends to the west to capture additional crust that was extended to a lesser degree during opening of the Iapetan Ocean. This alternative includes the Rome trough in Kentucky and West Virginia and the Central Metamorphic Belt Boundary zone (CMBBZ) in Ontario, Canada (Reference 2.5.2-252, Reference 2.5.2-253, and Reference 2.5.2-254).

Paleoseismic investigations from the Rome trough, eastern Tennessee, and the vicinity of the Clarendon-Lindon fault system do not provide evidence for RLMEs in these areas of historically higher seismicity. Preliminary observations from an NRC-sponsored research effort suggest that the Eastern Tennessee seismic zone (ETSZ) has produced surface faulting and generated one or more strong earthquakes during late Quaternary time (Reference 2.5.2-255). However, these preliminary results could not qualify that RLMEs had occurred in the ETSZ, and were therefore insufficient to determine whether the ETSZ could be considered an RLME zone. Therefore, the ETSZ was considered to be a part of PEZ in the CEUS SSC model.

A paleoliquefaction study of the Clarendon-Linden fault system was conducted by Tuttle et al. (Reference 2.5.2-256). These investigations observed a lack of earthquake-induced liquefaction features in geologic units susceptible to liquefaction, suggesting that the fault system did not generate large (**M** > 6) earthquakes during the past 12,000 years. Tuttle et al. (Reference 2.5.2-256) conclude that the fault system could have produced small and moderate earthquakes, but probably not large earthquakes during the late Wisconsinan and Holocene.

Paleoseismic investigations in other areas of the PEZ seismotectonic zone have not been carried out. Therefore, the maximum magnitude for PEZ-N and PEZ-W is assessed using historical earthquakes. The four largest observed earthquakes in the PEZ seismotectonic zone are the May 31, 1897, E[**M**] 5.91 Giles County; August 31, 1861, E[**M**] 5.63; April 29, 1852, E[**M**] 5.21; and May 2, 1853, E[**M**] 5.16 earthquakes (Figure 2.5.2-226).

Reelfoot Rift (RR) and Reelfoot Rift-Rough Creek Graben (RR-RCG) Zones

The Reelfoot Rift (RR) seismotectonic zone beneath the northern Mississippi embayment is interpreted as a Cambrian aulacogen (or tectonic trough, bounded by normal faults) (Reference 2.5.2-257 and Reference 2.5.2-258). The RR zone includes the Reelfoot graben as defined by gravity, magnetic, and seismic data, as well as the regions marginal to the rift graben where crustal extension also is indicated by secondary structures and Mesozoic mafic and ultramafic plutons (Reference 2.5.2-259).

The Reelfoot graben structures are part of the Reelfoot rift–Rough Creek graben–Rome trough intracratonic rift zone that formed during the disassembly of Rodinia and opening of the Iapetus Ocean in late Proterozoic time (Reference 2.5.2-260 and Reference 2.5.2-261). An anomalously dense layer is present at the base of the crust and thickens beneath a broad northeast-trending graben that formed during the initial stages of Iapetan rifting. The thickest part of the anomalous crust underlies the region of greatest seismic activity within the geographic limits of the Reelfoot rift (Reference 2.5.2-262). The principal seismic activity within the upper Mississippi embayment currently is interior to the Reelfoot rift along the New Madrid Fault System (NMFS, a separate and

independent RLME source within the RR/RR-RCG zones, described in Subsection 2.5.2.2.4).

Major basement structures and tectonic features associated with the Reelfoot rift graben are shown on Figure 2.5.2-227. Using a structure-contour map and a three-dimensional computer model of the top of the Precambrian crystalline basement, Csontos et al. (Reference 2.5.2-263) show the Reelfoot rift to consist of two major basins, separated by an intra-rift uplift, that are further subdivided into eight subbasins bounded by northeast- and southeast-striking rift faults, some of which have been reactivated as reverse or oblique-slip faults. Tectonic landforms within the central Mississippi River valley are directly linked to the underlying Reelfoot rift faults (Figure 2.5.2-227) (Reference 2.5.2-263, Reference 2.5.2-264, and Reference 2.5.2-265). Recent seismologic, geologic, and geophysical studies have associated some of these basement faults with the large-magnitude historical earthquakes that occurred in 1811 and 1812; these faults are referred to as the NMFS. Quaternary displacement also has been documented along the Eastern Rift margin (Reference 2.5.2-266, Reference 2.5.2-267, and Reference 2.5.2-268), Western Rift Margin (Reference 2.5.2-269 and Reference 2.5.2-270), Axial fault (Reference 2.5.2-271 and Reference 2.5.2-272), Reelfoot fault (Reference 2.5.2-273, Reference 2.5.2-274, Reference 2.5.2-275, Reference 2.5.2-276, and Reference 2.5.2-277), and Fluorspar Area fault complex (Reference 2.5.2-278, Reference 2.5.2-279, Reference 2.5.2-280, Reference 2.5.2-281, and Reference 2.5.2-282). With the exception of the Fluorspar Area fault complex, these are all modeled as RLME sources in the CEUS-SSC model.

The Reelfoot graben structures were reactivated during Mesozoic rifting and experienced Mesozoic and younger plutonic activity. The extended crust within and adjacent to the central rift basin contrasts with the surrounding, more stable non-extended crust. The higher rate of seismicity within the RR and the occurrence of multiple Quaternary active faults and tectonic landforms within the RR, in addition to the identified RLME sources, suggest that tectonic strain has been localized within and adjacent to the rift. The RR is expected to have distinct differences in future earthquake characteristics compared to surrounding regions.

Two alternative geometries are considered for the RR seismotectonic source. One alternative limits the RR to the more seismically active part of the rift that also experienced greater Mesozoic extension. An

alternative RR geometry includes the Rough Creek graben (RR-RCG), which has less evidence of Mesozoic reactivation of deep-penetrating faults (Reference 2.5.2-283) (Figure 2.5.2-210 and Figure 2.5.2-212).

The four largest historical, non RLME earthquakes recorded within the RR and RR-RCG zones are the January 5, 1843, E[**M**] 6.00; October 31, 1895, E[**M**] 6.00; August 17, 1865, E[**M**] 5.21; and July 2, 1869, E[**M**] 5.08 earthquakes. The locations of these earthquakes are shown on Figure 2.5.2-227. (The 1811-1812 sequence of earthquakes and other large-magnitude prehistoric earthquakes recognized in the RR are included in the characterization of the Reelfoot Rift-New Madrid Seismic Zone RLME source described in Subsection 2.5.2.2.4)

St. Lawrence Rift Zone (SLR)

The SLR seismotectonic zone consists of crust initially rifted during the late Proterozoic–early Paleozoic opening of the Iapetus Ocean; faults within the rifted crust were subsequently reactivated during the Paleozoic and Mesozoic. In southeastern Canada, Iapetan rifting is expressed along the St. Lawrence River valley and associated with the Ottawa and Saguenay failed arms, or aulacogens, that formed transverse to the faulted edge of the ancient continental margin (Reference 2.5.2-242). The SLR seismotectonic zone is characterized by elevated rates of seismicity and contains significant historical earthquakes, including the 1935 Timiskaming E[**M**] 6.02 earthquake, the 1988 Saguenay E[**M**] 5.84 earthquake, and historical earthquakes in the Charlevoix region (Figure 2.5.2-228). Large magnitude earthquakes located within the Charlevoix area are characterized as part of the Charlevoix RLME seismic source zone (Subsection 2.5.2.2.4), whereas the moderate-magnitude seismicity at Charlevoix is characterized as part of the SLR seismotectonic zone. Historical earthquakes and paleoseismic evidence suggest that the entire rift system is capable of generating moderate- to large magnitude earthquakes. Compressional reactivation of favorably oriented Iapetan faults has been postulated as the causal mechanism for several seismically active regions within the SLR seismotectonic zone, including the St. Lawrence Rift, Charlevoix and the lower St. Lawrence Valley in Quebec, Canada (Reference 2.5.2-284).

Crust of the SLR seismotectonic zone is distinguished from the NAP and PEZ seismotectonic zones on the basis of age, history of reactivation, and earthquake characteristics.

A paleoseismic study conducted by Aylsworth et al. (Reference 2.5.2-285) in the eastern part of the Ottawa-Bonnechere graben provides evidence for two moderate- to large-magnitude Holocene earthquakes occurring at about 7,060 and 4,550 years ago that could be as large as the 1663 Charlevoix E[**M**] 7 earthquake. Subsequent studies by Aylsworth and Lawrence (Reference 2.5.2-286) suggested the magnitude of the 7,060 years ago earthquake was at least **M** ≥ 6.2 and likely **M** ≥ 6.5.

Given that the magnitude of the largest observed earthquake within the SLR seismotectonic zone lies within the range of uncertainty of the magnitudes estimated by Aylsworth and Lawrence (Reference 2.5.2-286), Mmax for the SLR seismotectonic zone was assessed using historical seismicity. The four largest observed non-RLME earthquakes in SLR are the September 16, 1732, E[**M**] 6.25; March 1, 1925, E[**M**] 6.18; October 17, 1860, E[**M**] 6.08; and November 1, 1935, E[**M**] 6.06 earthquakes (Figure 2.5.2-228).

2.5.2.2.4 RLME Sources

Four RLME sources are included in the seismic hazard model for the Fermi 3 site: Charlevoix, Charleston, the New Madrid fault system, and Wabash Valley. The characteristics of each of these sources are described below in order of the importance of the source to the Fermi 3 site hazard. Additional details on the RLME sources of the CEUS SSC model are provided in Chapter 6 of NUREG-2115.

Reelfoot Rift–New Madrid Fault System

The New Madrid region is the source of the 1811-1812 New Madrid earthquake sequence, which includes the three largest earthquakes to have occurred in historical time in the CEUS (Figure 2.5.2-229). Extensive geologic, geophysical, and seismologic studies have been conducted to characterize the location and extent of the likely causative faults of each of these earthquakes and to assess the maximum magnitude and recurrence of earthquakes in this region (see discussion in Subsection 2.5.1.1.4.4.1). Based on the results of these studies, a system of faults within the New Madrid seismic zone (NMSZ) in the northern Reelfoot rift has been identified as an RLME source (herein referred to as the New Madrid fault system [NMFS] RLME source).

Numerous models have been proposed to explain the origin of stresses driving active deformation in the CEUS and specifically in the NMSZ. These models include local stress concentrations, high local heat flow, loading and unloading from ice sheets and sediments, as well as other mechanisms that provide explanations for localization of seismicity and recurrence of large-magnitude earthquakes in the NMSZ (e.g., Reference 2.5.2-287, Reference 2.5.2-288, Reference 2.5.2-289, Reference 2.5.2-290, Reference 2.5.2-291, and Reference 2.5.2-292).

The principal seismic activity within the upper Mississippi embayment is interior to the Reelfoot rift along the NMSZ. The NMSZ consists of three principal trends of seismicity: two northeast-trending arms and a connecting northwest-trending arm (Figure 2.5.2-229). This seismicity pattern has been interpreted as a northeast-trending right-lateral strike-slip fault system with a compressional left-stepover zone, referred to as the NMSZ (Reference 2.5.2-273, Reference 2.5.2-293, and Reference 2.5.2-294). Johnston and Schweig (Reference 2.5.2-295) identify a number of fault segments within the central fault system of the NMSZ. They outline three rupture scenarios associating each of the three 1811-1812 earthquakes with fault segments (individually or in various combinations) using historical accounts and geologic evidence. Their interpretation is consistent with the spatial distribution and source characteristics of contemporary NMSZ seismicity (Reference 2.5.2-296). Alternative scenarios for these earthquake sources that have been proposed by other researchers (e.g. Reference 2.5.2-277, Reference 2.5.2-297, Reference 2.5.2-298, Reference 2.5.2-299, Reference 2.5.2-300, and Reference 2.5.2-301) were considered in defining fault sources for the CEUS SSC model.

Maximum magnitudes in the New Madrid region are based largely on the analysis of intensity data from the 1811-1812 earthquake sequence (Reference 2.5.2-295, Reference 2.5.2-297, Reference 2.5.2-298, Reference 2.5.2-302, Reference 2.5.2-303, and Reference 2.5.2-304) and, to a lesser degree, on magnitude assessments inferred from paleoliquefaction features (Reference 2.5.2-305). Uncertainty distributions for the expected magnitude for the RLME for the NMFS faults (New Madrid North [NMN], New Madrid South [NMS], and Reelfoot thrust faults [RFT]) were developed, ranging from **M** 6.7 to 7.9 (Figure 2.5.2-215).

Constraints on the recurrence of large-magnitude earthquakes in the NMSZ come from paleoliquefaction studies (e.g., Reference 2.5.2-305, Reference 2.5.2-306, and Reference 2.5.2-307) and from evaluation of fault-related deformation along the Reelfoot scarp (Reference 2.5.2-308 and Reference 2.5.2-274). Tuttle, Schweig, et al. (Reference 2.5.2-305) note that, given uncertainties in dating liquefaction events, the recurrence time between the three most recent New Madrid earthquakes (AD 900, AD 1450, and 1811-1812) may have been as short as 200 years or as long as 800, with an average of 500 years.

Geodetic and geologic observations suggest that both temporal clustering and spatial migration of seismicity occurs within the Reelfoot rift, and various researchers have argued that the NMFS faults are not presently accumulating strain at a rate consistent with that recorded by the Holocene paleoliquefaction record and that they may be entering a less active period (e.g., Reference 2.5.2-292 and Reference 2.5.2-310). Therefore, three options are considered in the CEUS SSC model, as shown on Figure 2.5.2-215:

- The recent behavior of all three of the faults in the NMFS as inferred from paleoliquefaction studies (in a period of clustered earthquakes) is interpreted to be representative of the rate of future earthquakes (i.e., the recent period of activity for the three faults will continue into the future at the same rate; weight of 0.9).
- The NMSZ is shutting down as suggested by geodetic observations that show little or none of the interseismic motion expected before a future large earthquake (i.e., out of a period of clustered earthquakes; Reference 2.5.2-311 and Reference 2.5.2-312). In this case, the hazard is modeled by the underlying seismotectonic zone (Reelfoot rift zone) on the seismotectonic branch of the master logic tree or by global spatial smoothing of seismicity on the Mmax branch of the logic tree (weight of 0.05).
- Only the Reelfoot thrust (RFT) fault, which shows geomorphic evidence of an earlier phase of activity inferred from fluvial geomorphology (Reference 2.5.2-313), is considered to be in an active phase. In this case, the RFT is currently producing RLMEs at a lower rate (weight of 0.05).

The model for the NMFS RLME source addresses uncertainties in temporal clustering of earthquakes in the present tectonic stress regime,

in the location and extent of the causative faults that ruptured during the 1811-1812 earthquake sequence (represented by alternative geometries for the NMS, NMN, and RFT faults), and in the earthquake recurrence data and recurrence models used to assess the annual frequency of RLMEs.

Wabash Valley

Mapping and dating of liquefaction features throughout most of the southern Illinois basin and in parts of Indiana, Illinois, and Missouri have identified energy centers for at least eight Holocene and latest Pleistocene earthquakes having estimated moment magnitudes of **M** 6 to approximately 7.8 (Reference 2.5.2-314, Reference 2.5.2-315, Reference 2.5.2-316, Reference 2.5.2-317, Reference 2.5.2-318, and Reference 2.5.2-319) (see discussion in Subsection 2.5.1.1.4.4.2). The proximity of the energy centers for the two largest earthquakes inferred from the paleoliquefaction data (referred to as the Vincennes and Skelton paleoearthquakes), both of which are located within 25 to 40 km (16 to 25 mi) of Vincennes, Indiana, suggests that there is a source of RLMEs (approximate **M** = 6.7 to 7.8) in the Wabash Valley region. These two paleoearthquakes are located in the general vicinity of the most numerous and strongest historical earthquakes (E[**M**] 4 to 5.5) in the lower Wabash Valley of Indiana and Illinois (Reference 2.5.2-317). The Wabash Valley RLME source zone encompasses the structural features, postulated neotectonic deformation, and locations of the inferred energy centers for the Vincennes and Skelton earthquakes (Figure 2.5.2-230).

The causative structures for the paleoearthquakes are unknown. Given the uncertainty in the location of the causative faults, the boundaries of the Wabash Valley RLME source zone are modeled as “leaky,” such that ruptures that nucleate within the zone may also propagate outside the source zone. The magnitude assessments for the Wabash Valley RLME source are based on recent analysis of paleoliquefaction features associated with the Vincennes and Skelton energy centers using recently developed magnitude-bound curves for the CEUS and worldwide databases, as well as on estimates based on a suite of geotechnical analyses (i.e., cyclic stress and energy stress methods) in the vicinity of the lower Wabash Valley (e.g., Reference 2.5.2-317, Reference 2.5.2-321, Reference 2.5.2-322, and Reference 2.5.2-323). The difference in the estimated sizes of the Vincennes and Skelton paleoearthquakes is on the order of 0.5 to 1 magnitude units. Therefore,

a broad probability distribution is used to capture the range in uncertainty in the magnitude of earthquakes in the Wabash Valley RLME (**M** 6.75 to 7.5).

The model for the Wabash Valley RLME also incorporates uncertainty in the thickness of the seismogenic crust and in the assessment of RLME recurrence rates. Both an earthquake recurrence interval approach and a Poisson recurrence model are used to estimate the annual frequency of RLMEs.

Charlevoix

Repeated historical earthquakes have occurred within the Charlevoix region of the lower SLR (Figure 2.5.2-231), including the February 5, 1663, E[**M**] 7.00; December 6, 1791, E[**M**] 5.50; October 17, 1860, E[**M**] 6.08; October 20, 1870, E[**M**] 6.55; and March 1, 1925, E[**M**] 6.18 earthquakes (Reference 2.5.2-324). Only two of these earthquakes, the 1663 and 1870 earthquakes, are considered RLME earthquakes. The others are considered to be part of seismicity occurring in the distributed seismicity sources. In addition, paleoseismic investigations have identified evidence of paleoearthquakes throughout the Holocene (Reference 2.5.2-325, Reference 2.5.2-326, and Reference 2.5.2-327) that are spatially restricted to the Charlevoix area (Reference 2.5.2-325).

Several explanations have been offered for why RLMEs occur within the Charlevoix seismic zone. Adams and Basham (Reference 2.5.2-284) attribute seismicity of the SLR system to earthquakes occurring on rift structures in the regional stress field of southeast-to-east compression, recognizing that a Devonian impact structure also exists in the general area and may be related to the spatial concentration of seismicity in the Charlevoix area. The observation that seismicity continues beyond the impact structure with orientations indicative of reactivation of rift faults led Adams and Basham (Reference 2.5.2-284) to de-emphasize the role of impact structures. Lamontagne and Ranalli (Reference 2.5.2-328) correlate large-magnitude Charlevoix earthquakes to reactivation of rift faults in response to regional and local stress and/or strength conditions. In another paper, Lamontagne and Ranalli (Reference 2.5.2-329) attribute earthquakes in the Charlevoix seismic zone to factors that include high pore-fluid pressure at mid- to lower-crustal depths and low coefficients of friction related to highly fractured zones at depth. Mazzotti and Adams (Reference 2.5.2-330) have also observed that the

discrepancy between modeled seismic moment and strain rates derived from earthquake statistics may represent a short-term process such as postglacial rebound.

The geometry of the Charlevoix RLME source, shown on Figure 2.5.2-231, is defined to encompass the locations of earthquakes with **M** greater than 6, mapped rift faults, and the Charlevoix impact structure (crater). Lamontagne (Reference 2.5.2-331) observed that small to moderate earthquakes of the Charlevoix seismic zone occur between, not along, rift faults and extend northeast of the impact structure as a result of the asymmetric placement of rift faults through the crater (Reference 2.5.2-332). Large-magnitude earthquakes are thought to occur along weakened rift faults that concentrate stress into the crater (Reference 2.5.2-332). The location of causative faults within the Charlevoix RLME source is uncertain; thus, the boundaries of the Charlevoix RLME source allow ruptures to extend beyond the source boundary.

Uncertainty in the thickness of seismogenic crust, in the expected RLME magnitude (distribution between **M** 6.75 and 7.5), and in the specification of the annual frequency of RLMEs were all incorporated in the model for the Charlevoix RLME source.

Charleston

The September 1 (August 31 local time), 1886, E[**M**] 6.90 earthquake that occurred in the Charleston, South Carolina, area is the largest historical earthquake ever recorded in the Eastern United States. This earthquake produced modified Mercalli intensity (MMI) X shaking in the epicentral area near Charleston, and was felt as far away as Chicago (Reference 2.5.2-333). Strong ground shaking during the 1886 Charleston earthquake resulted in extensive liquefaction, which was expressed primarily as sand-blow craters at the ground surface (Reference 2.5.2-334). Because no primary tectonic surface rupture has been identified as the causative structure for the 1886 earthquake, a combination of geologic, geophysical, geomorphic, and instrumental seismicity data have been used by multiple investigators to suggest several different faults as the potential source for Charleston-area seismicity (e.g. Reference 2.5.2-335, Reference 2.5.2-336, Reference 2.5.2-337, Reference 2.5.2-338, Reference 2.5.2-339, Reference

2.5.2-340, Reference 2.5.2-341, Reference 2.5.2-342, Reference 2.5.2-343, Reference 2.5.2-344, and Reference 2.5.2-345).

The existence of pre-1886 sand-blow craters and other paleoliquefaction features that occur throughout coastal South Carolina also provide evidence for prior strong ground motions during prehistoric large earthquakes in the region (e.g., Reference 2.5.2-346, Reference 2.5.2-347, Reference 2.5.2-348, Reference 2.5.2-349, Reference 2.5.2-350, and Reference 2.5.2-351). Paleoliquefaction studies conducted in coastal South Carolina since the 1980s provide evidence that the Charleston seismic source exhibits RLMEs and appears to be confined to the Charleston area. Based on the strong field evidence for RLMEs derived from the study of liquefaction and paleoliquefaction features, the Charleston seismic zone is characterized as an RLME source (Figure 2.5.2-232). Neither the 1886 nor the prehistoric (i.e., pre-1886) earthquakes in the Charleston area have been definitively attributed to any specific fault or fault zone.

The model for the Charleston RLME incorporates uncertainty in the issue of temporal clustering of earthquakes in the present tectonic stress regime; in parameters that characterize source geometry, seismogenic crustal thickness, and rupture orientation; in the magnitude of future large earthquakes in the Charleston RLME source (distribution of **M** 6.7 to 7.5); and in the earthquake recurrence data and recurrence models used to assess the annual frequency of RLMEs within this RLME source.

2.5.2.3 Correlation of Earthquake Activity with Seismic Sources

RG 1.208 indicates that earthquake activity should be correlated with seismic sources. The principal database for assessing earthquake recurrence is the historical and instrumental earthquake record. To satisfy this requirement, an updated catalog of independent historical and instrumental earthquakes covering the Fermi 3 site region was developed (see discussion in Subsection 2.5.2.1.1).

The distribution of earthquake epicenters from the CEUS SSC catalog with respect to the CEUS SSC model sources is shown on Figure 2.5.2-206, Figure 2.5.2-207, Figure 2.5.2-209, Figure 2.5.2-210, Figure 2.5.2-211, Figure 2.5.2-212, and Figure 2.5.2-213. Comparison of the more recent instrumental earthquakes catalog, for the time period 2009 through 2012, to the CEUS SSC earthquake catalog and seismic sources yields the following conclusions:

- As shown on Figure 2.5.2-202 and Figure 2.5.2-203, the updated earthquake catalog does not show a pattern of seismicity within the site region different from that exhibited by earthquakes in the CEUS SSC catalog that would suggest a new seismic source, i.e., one in addition to those included in the CEUS SSC model characterizations. The similarity of the spatial distribution of the post- CEUS earthquakes to that shown by the CEUS SSC catalog also indicates that no significant revisions to the geometry of seismic sources defined in the CEUS SSC model are required in the Fermi 3 site region.
- The closest principal sources of seismic activity are the Anna seismic zone, in the vicinity of Anna, Ohio, and the Northeast Ohio seismic zone, in the vicinity of Cleveland, Ohio. Seismicity in the Anna seismic zone occurs near the Ft. Wayne rift (Figure 2.5.1-207). Seismicity in the Northeast Ohio seismic zone has been associated with the Akron Magnetic Boundary (Reference 2.5.2-352) (Figure 2.5.1-207). These areas lie at a distance of greater than 150 km (90 mi) from the Fermi 3 site. The concentrations of seismicity in these areas were recognized and considered in the CEUS SSC model, as discussed in Subsection 2.5.2.2.3.
- With the exception of the Anna and Northeast Ohio seismic zones discussed in the previous bulleted item, the updated CEUS SSC catalog does not show any earthquakes within the site region that can be associated with a known geologic structure.

2.5.2.4 Probabilistic Seismic Hazard Analysis and Controlling Earthquake

This subsection describes the PSHA conducted for the Fermi 3 site. Guidance provided in RG 1.208 states that the site-specific PSHA is to be performed with up-to-date interpretations of earthquake sources, earthquake recurrence, and earthquake ground motions. The most up-todate interpretation of earthquake sources and earthquake recurrence for use at nuclear facilities in the CEUS is the CEUS SSC model presented in NUREG-2115. The most up-to-date comprehensive model for characterizing ground motions at nuclear power plant sites is the EPRI 2004 and EPRI 2006 ground motion models (Reference 2.5.2-206 and Reference 2.5.2-207, respectively). Evidence of this is shown by the NRC's request that the CEUS SSC model in NUREG-2115 and the 2004/2006 EPRI ground motion model be used in responses to Recommendation 2.1 of the Fukushima Near-Term Task Force

recommendations contained in SECY-12-0025 (Reference 2.5.2-205). Both the 2004 EPRI ground motion model and the NUREG-2115 CEUS SSC model were conducted as SSHAC Level 3 studies in accordance with the guidance presented in Budnitz et al. (Reference 2.5.2-203) and, for NUREG-2115, the guidance provided in NUREG-2117 (Reference 2.5.2-204). The aleatory variability component of the 2004 EPRI (Reference 2.5.2-206) ground motion model was replaced by the 2006 EPRI SSHAC Level 2 study (Reference 2.5.2-207).

RG 1.208 discusses the need to evaluate if the impact of new information warrants updating the seismic source model. The CEUS SSC model presented in NUREG-2115 was completed at the end of 2011 and considered data and interpretations available at that time. One important component of the CEUS SSC model was the earthquake catalog used in the assessment of earthquake recurrence rates and maximum magnitude distributions for distributed seismicity sources. The earthquake catalog used in development of the CEUS SSC model presented in NUREG-2115 was complete through the end of 2008. Earthquakes that have occurred in the CEUS in the intervening 4 years from 2009 through 2012 represent a source of new information that should be considered in evaluating the use of the CEUS SSC model (see Subsection 2.5.2.1).

Section 6 of NUREG-2117 provides specific guidance on how a SSHAC Level 3 study like the CEUS SSC model in NUREG-2115 should be updated. Following NUREG-2117, the CEUS SSC model would be classified as a “viable” study, as the CEUS SSC model is given in NUREG-2117 as a specific example of a SSHAC Level 3 study that considered data, models, and methods in the larger technical community, and produced a model representative of the CBR of TDI. Given that the CEUS SSC model in NUREG-2115 is a viable study, incorporation of the additional 4 years of earthquake data should be evaluated as a refinement of an existing model for a site-specific application. As described in Section 6.4 of NUREG-2117, the first step of the refinement process is to evaluate if the new data warrant a refinement of the model. Two criteria are recommended in NUREG-2117 for this assessment: (1) an assessment should be made of whether or not the new information would lead to a change in the estimates of the CBR of TDI in the major components of the model, and (2) an analysis should evaluate the magnitude of the change in the calculated hazard results and the

significance to the subsequent use of the results. The assessment of the need for refinement of the CEUS SSC model considering the additional 4 years of earthquake catalog data is described in Subsection 2.5.2.4.1. This assessment uses the methods developed in NUREG-2115 to evaluate the impact of the additional data on maximum magnitudes for the distributed seismic sources and compares the observed number of earthquakes within the site region with predictions from the CEUS SSC model to evaluate the rate of earthquake recurrence in the Fermi 3 site region. In addition, hazard calculations described in Subsection 2.5.2.4.3 are used to evaluate the impact of potential changes to CEUS SSC model on the hazard at the Fermi 3 site. The results of these evaluations are used to assess the need for refinement of the CEUS SSC model in accordance with NUREG-2117.

Similarly, since the completion of the 2004/2006 EPRI (Reference 2.5.2-206 and Reference 2.5.2-207) ground motion model, a number of new GMPEs for CEUS earthquakes have been published. Comparisons of these GMPEs with the 2004/2006 EPRI (Reference 2.5.2-206 and Reference 2.5.2-207) ground motion model are presented in Subsection 2.5.2.4.2 to assess the need to update the EPRI ground motion model.

2.5.2.4.1 New Information Relative to Seismic Sources

This section describes the evaluation the CEUS SSC model in light of the additional 4 years of catalog data from the time period 2009 through 2012. Seismic source characterization data and information that could affect the predicted level of seismic hazard include the following:

- Identification of possible additional seismic sources in the site region.
- Changes in the characterization of the rate of earthquake occurrence for the CEUS SSC seismic sources in the Fermi 3 site region.
- Changes in the characterization of the maximum magnitude for the CEUS SSC seismic sources utilized in the Fermi 3 PSHA.

As discussed in Subsection 2.5.2.3, the additional 4 years of earthquake catalog data does not indicate the presence of additional seismic sources in the site region. The earthquakes that have occurred in the CEUS after completion of the CEUS SSC model catalog are all less than the minimum magnitude of **M** 6.5 considered for RLME sources, and therefore, do not affect the RLME source characterization. No new information relative to the characterization of RLME sources was identified after completion of the CEUS SSC model.

2.5.2.4.1.1 Earthquake Occurrence Rates within 320 km (200 mi) of the Fermi 3 Site

Subsection 2.5.2.1 describes the development of an updated earthquake catalog for the Fermi 3 site region. This updated catalog includes the addition of earthquakes that occurred after completion of the earthquake catalog for the CEUS SSC model in the time period 2009 through 2012. The new catalog information was assessed by evaluating the effect of the additional data on earthquake recurrence estimates within the 320 km (200 mi) site region. The updated earthquake catalog shows that from 2009 through 2012, two earthquakes of E[**M**] greater than or equal to 2.9 have occurred within 320 km (200 mi) of the Fermi 3 site. The first of these earthquakes had a magnitude of E[**M**] 3.79; the second had E[**M**] of 3.66. Figure 2.5.2-206 and Figure 2.5.2-207 show that the Fermi 3 site is located within the NMESE Mmax zone (both NMESE-N and NMESE-W). The site is also located in the Mmax zone that encompasses the entire CEUS study region. Figure 2.5.2-209 through Figure 2.5.2-212 show that the Fermi 3 site is located in the MIDC seismotectonic zone.

The earthquake recurrence parameters developed in NUREG-2115 for the portions of the entire CEUS study region Mmax zone, the NMESE Mmax zone, and the MIDC seismotectonic zone within 320 km (200 mi) of the Fermi 3 site were used to calculate the predicted annual frequency of earthquakes with **M** greater than or equal to 2.9 (the minimum magnitude used for recurrence calculations in the CEUS SSC model) and **M** greater than or equal to 3.6 (the lower limit of the magnitude interval containing the two observed earthquakes). The results are listed in Table 2.5.2-201.

NUREG-2115 modeled the recurrence of earthquakes associated with the distributed seismicity sources as a Poisson process. A one-side exact Poisson test was used to test the hypothesis that the observation of two earthquakes in the 4 year period from 2009 through 2012 is consistent with the earthquake recurrence rates derived from the CEUS SSC model (Reference 2.5.2-353). The test computes the probability of the occurrence of two or more earthquakes in four years using the range of recurrence rates listed in Table 2.5.2-201. The resulting probability, or p-value, is used as a measure of the significance of the test result. Commonly, p-values of 5 or 10 percent are used to indicate that the hypothesis may not be correct. As shown in Table 2.5.2-201, the p-values for the range in recurrence rates derived from the CEUS SSC model for

earthquakes with **M** greater than or equal to 2.9 are all well above 10 percent. The test was repeated using the recurrence rates for earthquakes with **M** greater than or equal to 3.6, as both earthquakes would be placed in the **M** 3.6 to 4.3 interval used in the NUREG-2115 recurrence calculations. Again for this case, the computed p-values are all above 10 percent. The results indicate that the two observed earthquakes within 320 km (200 mi) of the Fermi 3 site are consistent with the distribution of earthquake recurrence rates derived from the CEUS SSC model. Therefore, it is concluded that the observed seismicity does not warrant an update of the earthquake recurrence rates for the distributed seismicity source zones of the CEUS SSC model in the Fermi 3 site region.

The small slivers of Mmax zone MESE-W and seismotectonic zone PEZ-W that lie within the 320 km (200 mi) site region (e.g., see Figure 2.5.2-207 and Figure 2.5.2-211) were not included in the calculation of the earthquake recurrence rates. Neglecting the contribution from these small source zone pieces is conservative for estimating the earthquake recurrence rate since including additional earthquakes from these small slivers would slightly increase the predicted total rate from the CEUS SSC model and, thus, raise the p-values listed in Table 2.5.2-201 further above 10 percent.

2.5.2.4.1.2 Effect of Updated Catalog on Maximum Magnitude Distribution for CEUSSC Source Zones

NUREG-2115 used earthquakes of E[**M**] greater than or equal to 4.3 in the calculation of Mmax distributions for the seismotectonic and Mmax zones, with the exception of Mmax zones MESEW, NMESE-N, the entire CEUS study region, and the IBEB seismotectonic zone. For these latter zones, the magnitudes of paleoearthquakes were used instead of historical seismicity data to assess the Mmax distributions. Table 2.5.2-202 lists the twelve earthquakes that have occurred after completion of the CEUS SSC model catalog in the time period from 2009 through 2012 with E[**M**] greater than or equal to 4.3. The location of the twelve earthquakes is shown on Figure 2.5.2-233. As indicated in Table 2.5.2-202, these earthquakes potentially affect the Mmax distribution for seismotectonic zones ECC-AM, GMH, MIDC-A, MIDC-B, MIDC-C, and MIDC-D, and Mmax zones MESE-N and NMESE-W (Some earthquakes also occurred in the ECC-GC seismotectonic zone, but this source is not included in the PSHA for the Fermi 3 site because of its greater distance

from the site). The earthquakes do not affect the Mmax distributions for MESE-W, NMESE-N, and the entire study region (Study-R) because they are based on paleoearthquake magnitudes that are larger than those of the observed historical and instrumental magnitudes.

Following the procedure described in Section 5.2.1 of NUREG-2115, the Bayesian (Reference 2.5.2-213) and Kijko (Reference 2.5.2-354) approaches were used to compute Mmax distributions for the source zones listed in Table 2.5.2-203 including the post-CEUS SSC catalog earthquakes listed in Table 2.5.2-202. The analysis indicates that for zones ECC-AM, MIDC-A, MIDC-B, MIDC-C, MIDC-D, and NMESE-W, the magnitudes of the post-CEUS SSC earthquakes are similar to the largest previously observed. The impact of adding another earthquake or earthquakes of similar magnitude is a slight upward shift in the lower tail of the magnitude distribution. Figure 2.5.2-234 through Figure 2.5.2-237 compare the Mmax distributions from NUREG-2115 for the NMESE-W, ECC-AM, MIDC-A and MIDC-B, and MIDC-C and MIDC-D source zones, respectively, to the adjusted distributions based on the updated earthquake catalog data. For these source zones, incorporation of the updated earthquake catalog data results in a truncation of the lowest magnitude portion of the NUREG-2115 Mmax distributions. For Mmax zone NMESE-W and the MIDC seismotectonic zones, there is also an increase in the probability weight in the lower portion of the adjusted distributions. Table 2.5.2-203 presents the 5-point adjusted Mmax distributions for these zones that incorporate the post-CEUS SSC catalog earthquake data. For the MESE-N Mmax zone and the GMH seismotectonic zone, the additional earthquake data has an insignificant effect on the computed Mmax distribution.

Also listed in Table 2.5.2-203 are Mmax distributions for the NMESE-N, ECC-AM, and MIDC source zones used in sensitivity hazard calculations presented in Subsection 2.5.2.4.3. These Mmax sensitivity distributions were created by simply increasing the magnitude at the lower tail of the 5-point discrete distributions given in NUREG-2115 by 0.1 magnitude units to account for the post-CEUS SSC catalog earthquakes. The Mmax sensitivity distributions are similar or slightly conservative compared to the adjusted Mmax distributions that account for the post-CEUS SSC catalog earthquakes.

As shown in Table 2.5.2-203, the effect of the post-CEUS SSC catalog earthquakes on the adjusted Mmax distributions for the ECC-AM, MIDC,

and NMESE-W zones is minor and it is concluded that it does not constitute a change to the CBR of TBI, as discussed in Section 6.4 of NUREG-2117. Furthermore, as discussed in Subsection 2.5.2.4.3, the effect of including these adjusted Mmax distributions in the hazard calculation is to produce at most a 0.3 percent increase in total mean hazard at 1 Hz and 10 Hz spectral accelerations for the Fermi 3 site. The small change is well below the levels of precision in hazard calculations described in Chapter 9 of NUREG-2115 and indicates that the effect of the change in the Mmax distributions on the site hazard is not significant. Therefore, it is concluded that the moderate magnitude earthquakes that have occurred in the CEUS after December 31, 2008, do not warrant an update to the CEUS SSC model Mmax distributions for distributed seismicity sources since the adjustments do not significantly impact the subsequent seismic hazard results.

2.5.2.4.2 New Information Relative to Earthquake Ground Motions

2.5.2.4.2.1 Models for Median Ground Motions

EPRI completed a study in 2004 to update the methods used to estimate strong ground motion in the CEUS for application in PSHA for nuclear facilities (Reference 2.5.2-206). The EPRI study recommended four alternative sets of median ground motion models (termed model clusters) to represent alternative modeling approaches for defining the median ground motions as a function of earthquake magnitude and source-to-site distance. Three of these ground motion clusters are appropriate for use in assessing the hazard from moderate-sized local earthquakes occurring randomly in source zones (i.e., distributed seismicity sources in the CEUS SSC model), and all four are to be used for assessing the hazard from sources whose hazard contribution is from large magnitude earthquakes (i.e., RLME sources in the CEUS SSC model).

The left hand side of Figure 2.5.2-238 shows how the EPRI ground motion model logic tree is applied to the CEUS SSC model in the Fermi 3 PSHA (Reference 2.5.2-206). The first (leftmost) node of the logic tree shown in Figure 2.5.2-238 provides the weights assigned to the three median cluster models appropriate for distributed seismicity sources. These three cluster models are used to compute the hazard from the Mmax and seismotectonic zones. The second node addresses the appropriate ground motion cluster median model to use for the large

magnitude RLME sources in the CEUS SSC model. Two alternatives are provided. The first alternative is to use the cluster model used for the distributed seismicity sources. In this case, if the cluster 1 models are used for the distributed seismicity sources at the first node of the logic tree, then the cluster 1 models are also used for the RLME sources. The second alternative is to use the cluster 4 model for the RLME sources. In this case, the cluster 1 models are used for the distributed seismicity sources and are combined with the use of the cluster 4 models for the RLME sources. This same logic is repeated on the branches for the clusters 2 and 3 models leading from the first node of the logic tree.

EPRI (Reference 2.5.2-206) provided estimates of the epistemic uncertainty in the median ground motion model for each cluster. As shown by the third node of the logic tree (Figure 2.5.2-238), the uncertainty in each cluster median model is modeled by a three-point discrete distribution with ground motion relationships for the 5th, 50th, and 95th percentiles of the epistemic uncertainty in the median level of earthquake ground motion as a function of magnitude and distance for each ground motion cluster.

A number of GMPEs for CENA[3] earthquakes have been published since the completion of the EPRI ground motion median model. These newer GMPEs are compared to the EPRI (Reference 2.5.2-206) 5th, 50th, and 95th percentile 10 Hz and 1 Hz ground motion median models according to the cluster in which they could be assigned.

The EPRI (Reference 2.5.2-206) ground motion median models for cluster 1 (single corner stochastic models) were based in large part on the CENA ground motion models developed by Silva et al. (Reference 2.5.2-355). Silva et al. (Reference 2.5.2-356) published updated versions of their single corner variable stress (SCVS), single corner constant stress (SCCS), and single corner constant stress with saturation (SCCSS) GMPEs. Figure 2.5.2-239a compares the 10 Hz and 1 Hz spectral accelerations obtained using these newer GMPEs to those obtained using the EPRI cluster 1 models for **M** 5 and **M** 7.5 earthquakes as a function of horizontal surface distance from the rupture (Joyner-Boore distance). The ground motions obtained using the newer GMPEs are in the range of motions obtained using the EPRI ground motion median models for cluster 1.

3. Note that most GMPEs are designated for use in CENA, not just the CEUS portion of CENA

The EPRI (Reference 2.5.2-206) ground motion median models for cluster 2 (double corner stochastic models) were based on the CENA ground motion models developed by Atkinson and Boore (Reference 2.5.2-357) and Silva et al (Reference 2.5.2-355). Silva et al. (Reference 2.5.2-356) published updated versions of their double corner (DC) and double corner with saturation (DCS) GMPEs. Atkinson and Boore (Reference 2.5.2-358) published an updated GMPE for CENA earthquake motions in which they used finite fault stochastic simulations instead of double corner point source stochastic simulations. Atkinson and Boore (Reference 2.5.2-359) subsequently revised their 2006 model to account for recent information on the scaling of small to moderate magnitude earthquakes. This revised GMPE is labeled AB06' by Atkinson and Boore (Reference 2.5.2-359). The ground motions obtained using the Silva et al. (Reference 2.5.2-356) and AB06' GMPEs are shown on Figure 2.5.2-239b for **M** 5 and **M** 7.5 earthquakes as a function of horizontal surface distance from the rupture. The AB06' GMPE uses rupture distance as the distance measure and the convention for depth to top of rupture described in Atkinson and Boore (Reference 2.5.2-359) was used to compute the corresponding surface distance. The ground motions obtained using the newer GMPEs are generally within or below the range of motions obtained using the EPRI (Reference 2.5.2-206) ground motion median models for cluster 2.

The EPRI (Reference 2.5.2-206) ground motion median models for cluster 3 were based on hybrid empirical models (e.g., Campbell, Reference 2.5.2-360). More recently, Tavakoli and Pezeshk (Reference 2.5.2-361) presented a hybrid ground motion model for the CENA based on the approach developed by Campbell (Reference 2.5.2-360). The Tavakoli and Pezeshk (Reference 2.5.2-361) model has been subsequently updated by Pezeshk et al. (Reference 2.5.2-362) using the recently developed Next Generation Attenuation (NGA) GMPEs for Western North America (WNA) (Reference 2.5.2-363). Ground motions predicted by the Pezeshk et al. (Reference 2.5.2-362) hybrid empirical GMPE are compared to those obtained using the EPRI (Reference 2.5.2-206) ground motion median models for cluster 3 on Figure 2.5.2-239c for **M** 5 and **M** 7.5 earthquakes as a function of horizontal surface distance from the rupture. The convention for depth to top of rupture described in Atkinson and Boore (2011) was again used to compute the corresponding surface distance. Atkinson (Reference 2.5.2-364) published a GMPE for CENA based on a referenced empirical

approach which may be considered a form of hybrid model. Atkinson and Boore (Reference 2.5.2-359) subsequently revised the Atkinson (Reference 2.5.2-364) GMPE to account for recent information on the scaling of small to moderate magnitude earthquakes. This revised GMPE is labeled A08' by Atkinson and Boore (Reference 2.5.2-359). The ground motions obtained using the A08' model are also shown on Figure 2.5.2-239c. The ground motions obtained using the newer models are generally within or below the range of motions obtained using the EPRI (Reference 2.5.2-206) ground motion median models for cluster 3.

There are no newer GMPEs for CENA that are comparable to the finite source/Green's function model of Somerville et al. (Reference 2.5.2-365) used to define the EPRI (Reference 2.5.2-206) ground motion median models for cluster 4.

The comparisons on Figure 2.5.2-239a, Figure 2.5.2-239b, and Figure 2.5.2-239c indicate that the median ground motions obtained using the newer GMPEs for CENA generally fall within the range or are lower than ground motions obtained using the EPRI (Reference 2.5.2-206) ground motion median models. Therefore, it is concluded that there is no need to update the EPRI median ground motion models for the purpose of computing the hazard at the Fermi 3 site. Based on these comparisons, it is expected that the hazard computed using the newer models would be lower than that obtained using the EPRI ground motion median models.

2.5.2.4.2.2 Models for Ground Motion Aleatory Variability

EPRI (Reference 2.5.2-206) also provided a characterization of the aleatory variability in CEUS ground motions based on a composite of the aleatory variability models associated with the GMPEs that were used to develop the cluster median models. In 2006, EPRI conducted a study focused in part on evaluating the appropriate aleatory variability for CEUS ground motions (Reference 2.5.2-207). The thrust of the study was to identify reasons why the aleatory variability for CEUS motions may be different than that observed for the large empirical database of strong ground motion in the western United States (WUS) and other tectonically active regions, and then to evaluate the extent to which these reasons are supported by empirical data. The EPRI (Reference 2.5.2-207) study produced a recommended model for aleatory variability for CEUS ground motions.

The EPRI (Reference 2.5.2-207) model for aleatory variability in CEUS ground motions is represented by the fourth and fifth nodes of the ground motion logic tree shown on Figure 2.5.2-238. The fourth node of the logic tree addresses the overall aleatory model. Two alternative models were defined. Model 1A is based on WUS aleatory variability with small increase in inter-event variability for CEUS earthquakes. Model 1B includes the increase in inter-event variability of model 1A along with a small decrease in intra-event aleatory variability to account for greater uniformity in CEUS hard rock site conditions compared to WUS site conditions. Model 1A was favored based on the available data.

The earlier EPRI (Reference 2.5.2-206) aleatory model included an additional component of aleatory variability to account for variability in source depth at small source-to-site distances when the Joyner-Boore distance measure is used for ground motion models developed from point-source numerical simulations. EPRI (Reference 2.5.2-207) evaluated the empirical evidence for additional aleatory variability at small Joyner-Boore distances and concluded that the adjustments proposed by EPRI (Reference 2.5.2-206) were not supported by empirical data. Instead, three alternatives were recommended:

1. Model 2A — no adjustment.
2. Model 2B — an additional 0.12 standard error in the natural log of ground motion amplitude.
3. Model 2C — an additional 0.23 standard error in the natural log of ground motion amplitude.

The additional standard deviation is to be combined with aleatory model 1A or 1B in Figure 2.5.2-238 as the sum of variances to produce the final standard error for Joyner-Boore distances less than or equal to 10 km (6 mi). A log-linear decrease in the additional standard deviation is to be applied over the distance range of 10 to 20 km (6 to 12 mi), with no additional adjustment for distances greater than 20 km (12 mi). These alternative models define the fifth node of the logic tree shown on Figure 2.5.2-238. These additional standard deviation models are applied to the EPRI median models that use the Joyner-Boore distance measure (clusters 1, 2, and 4) (Reference 2.5.2-206).

The new GMPEs described in Subsection 2.5.2.4.2.1 have associated models for aleatory variability. The updated Silva et al, (Reference 2.5.2-356) GMPEs have aleatory variability models that are nearly the

same as the earlier Silva et al. (Reference 2.5.2-355) models that were used to develop the EPRI (Reference 2.5.2-206) aleatory model. EPRI (Reference 2.5.2-207) concluded that it was more appropriate to used aleatory variability models based on empirical data. Atkinson and Boore (Reference 2.5.2-358) give a value for aleatory variability based on their simulations and note that the value is similar to that for empirical data in WNA. Atkinson (Reference 2.5.2-364) did not discuss aleatory variability and Atkinson and Boore (Reference 2.5.2-359) did not update their aleatory variability estimates. However, more recently, Atkinson (Reference 2.5.2-366) concluded that aleatory variability in ground motions in WNA and CENA should be similar. Pezeshk et al. (Reference 2.5.2-362) use an average of the NGA aleatory variability values from WNA for their GMPE.

This information indicates the use of the EPRI (Reference 2.5.2-207) aleatory variability model based on empirical ground motion data from active tectonic regions such as WNA in the Fermi 3 PSHA is appropriate.

2.5.2.4.3 PSHA Sensitivity Analysis

Consistent with the guidance provided in RG 1.208, PSHA sensitivity studies were conducted to aid in the development of the appropriate inputs to the PSHA for the Fermi 3 site. These sensitivity studies were conducted for two purposes:

- Selection of an appropriate set of RLME sources from the CEUS SSC model to include in the PSHA.
- Sensitivity to the use of the adjusted Mmax distributions for the distributed seismicity source zones (Mmax zones and seismotectonic zones) in Subsection 2.5.2.4.1.2.

Sensitivity analyses were not conducted to address the effect of the newer GMPEs described in Subsection 2.5.2.4.2.1 since the new GMPEs produce similar or lower ground motion amplitudes compared to the EPRI (Reference 2.5.2-206) ground motion median models, and thus are likely to produce lower hazard levels.

2.5.2.4.3.1 Selection of RLME Seismic Sources

The PSHA inputs used for the Fermi 3 site consist of the distributed seismicity sources (Mmax zones and seismotectonic zones), or portions of these sources, that are within 1,000 km (620 mi) of the Fermi 3 site. Any significant hazard contribution from earthquakes at greater distances

would come from frequent, large magnitude earthquakes. The sources of such earthquakes would be the RLME sources characterized in the CEUS SSC model. Therefore, specific tests were performed to identify those RLME sources to include in the PSHA model for the Fermi 3 site.

The eight RLME sources closest to the Fermi 3 site were examined: the Commercial Fault Zone (CFZ), Charleston (CHS), Charlevoix (CHV), Eastern Rift Margin – North (ERM-N), Eastern Rift Margin – South (ERM-S), Marianna Zone (MAR), New Madrid faults (NMF), and the Wabash Valley (WV) sources. The source contributions were tested for 1 Hz and 10 Hz spectral accelerations. Figure 2.5.2-240 and Figure 2.5.2-241 show the results of these calculations for 1 Hz and 10 Hz spectral accelerations, respectively. Three RLME sources, CHS, NMF, and WV, contribute more than 1 percent to the total mean hazard at the Fermi 3 site, and the CHV RLME source contributes nearly 1 percent. The remaining four RLMEs tested (CFZ, ERM-N, ERM-S, and MAR) produce less than 1 percent hazard. The remaining two RLME sources (Cheraw Fault, Meers Fault) in the CEUS SSC model would produce even less hazard as they are at greater distances that the tested RLME sources.

Based on these results, the PSHA for the Fermi 3 site is conducted including the CHV, CHS, NMF, and WV RLME sources.

2.5.2.4.3.2 PSHA Sensitivity to Adjusted Mmax Distributions

Subsection 2.5.2.4.1.2 describes adjusted Mmax distributions for several of the RLME sources based on earthquakes that have occurred post-CEUS SSC catalog in the time period from 2009 through 2012. The adjusted Mmax distributions typically involved a minor increase in the lower tail of the 5-point discrete Mmax distributions. As shown in Table 2.5.2-203, Mmax sensitivity distributions were developed for the NMESE-W, ECC-AM, and MIDC source zones by increasing the lowest magnitude in the 5-point discrete Mmax distributions for these sources by 0.1 magnitude units. Use of these Mmax sensitivity distributions produced at most a 0.3 percent increase in the mean hazard at 1 Hz and 10 Hz spectral accelerations for the Fermi 3 site compared to use of the distributions published in NUREG-2115. Based on the minor change to the adjusted Mmax distributions and the insignificant change the Mmax sensitivity distributions produced in the site hazard, it was concluded in Subsection 2.5.2.4.2.1 that the CEUS SSC Mmax distributions in the

model did not need to be updated. However, for conservatism, the PSHA for the Fermi 3 site was conducted using the Mmax sensitivity distributions for the NMESE-W, ECC-AM, and MIDC source zones given in Table 2.5.2-203.

2.5.2.4.4 PSHA for the Fermi 3 Site

The PSHA for the Fermi 3 site was conducted using the modified CEUS SSC model described in Subsection 2.5.2.4.3. Earthquake ground motions were modeled using the median ground motion models and the ground motion aleatory variability models developed by 2004/2006 EPRI (Reference 2.5.2-206 and Reference 2.5.2-207).

Earthquakes occurring in the CEUS SSC distributed seismic sources were modeled as point sources, and the EPRI (Reference 2.5.2-206) models for distance adjustment and additional aleatory variability resulting from the use of point sources (epicenter) to model earthquakes were applied. The models based on the assumption of a random rupture location with respect to the epicenter were used. Earthquakes occurring in the RLME sources were modeled as extended ruptures, and the distance adjustment and additional aleatory variability models were not applied to these sources. The adjustment to use the value 4.35 instead of 4.366 in Equation H-1 of NUREG-2115 was applied in calculating the magnitude-dependent rupture area of earthquakes for the RLME sources (Reference 2.5.2-367).

EPRI (Reference 2.5.2-207) concluded that there was no basis for truncation of the lognormal distribution for ground motion amplitude other than the strength of the subsurface materials. Accordingly, untruncated lognormal distributions for earthquake ground motions were used in the PSHA.

The EPRI (Reference 2.5.2-206) ground motion models represent the ground motions for a generic hard rock condition in the CEUS. Thus, the site-specific PSHA results presented in this subsection represent the motions on outcropping rock with a shear wave velocity in excess of about 2800 m/s (9200 fps). The effect of the sediments overlying this generic rock condition on defining the hazard at other locations is addressed in Subsection 2.5.2.5 and Subsection 2.5.2.6.

The generic CEUS hard rock hazard was computed using a fixed lower bound magnitude of **M** 5.0. These results were used to develop the

appropriate response spectra and time histories for the site response analyses.

2.5.2.4.4.1 PSHA Results for Generic Hard Rock Conditions

PSHA calculations were performed for response spectral accelerations at the seven structural frequencies provided in the EPRI ground motion model: 0.5, 1.0, 2.5, 5, 10, 25 Hz, and peak ground acceleration (PGA). For development of response spectra, PGA is placed at a structural frequency of 100 Hz. Figure 2.5.2-242 through Figure 2.5.2-248 show the resulting mean hazard curves and the 5th, 16th, 50th (median), 84th, and 95th fractile hazard curves for each ground motion measure. These values are listed in Table 2.5.2-204 through Table 2.5.2-210. At low spectral frequencies (≤ 1 Hz), the mean hazard approaches the 84th percentile hazard due to the relatively larger epistemic uncertainty in the ground motion models at these frequencies as compared to that for higher-frequency ground motions.

Figure 2.5.2-249 through Figure 2.5.2-255 show the contribution of the distributed seismicity sources and the four RLME sources to the mean hazard at the seven structural frequencies provided in the EPRI ground motion model. The NMF RLME is the largest contributor to the hazard for 0.5 Hz and 1 Hz spectral accelerations at exceedance frequencies between 10^{-4} and 10^{-5}.

2.5.2.4.4.2 Uniform Hazard Spectra for Generic CEUS Rock and Identification of Controlling Earthquakes

The mean hazard results listed in Table 2.5.2-204 through Table 2.5.2-210 were interpolated to obtain uniform hazard response spectra (UHRS) for generic CEUS hard rock conditions. The spectra were computed for mean annual frequencies of exceedance of 10^{-3}, 10^{-4}, 10^{-5}, and 10^{-6}. These spectra are shown on Figure 2.5.2-256 and are listed in Table 2.5.2-211.

Figure 2.5.2-257 through Figure 2.5.2-260 show the deaggregation of the mean hazard for the four values of exceedance frequency. Following the procedure outlined in Appendix D of RG 1.208, the deaggregation is conducted for two frequency bands: (1) the average of the 5 Hz and 10 Hz hazard results representing the high-frequency (HF) range, and (2) the average of the 1 Hz and 2.5 Hz hazard results representing the low-frequency (LF) range. The results shown on the figures were obtained by first computing the percentage contribution of events in each

magnitude-distance bin individually for the four spectral frequencies (1, 2.5, 5, and 10 Hz). The HF deaggregation was then obtained by averaging these values for 5 and 10 Hz and the LF deaggregation was obtained by averaging the results for 1 and 2.5 Hz. The HF deaggregation shows a progression from domination of the hazard by large, distant earthquakes at a mean exceedance frequency of 10^{-3} to dominance by nearby small-magnitude earthquakes at a mean exceedance frequency of 10^{-6}. This effect can be seen in the change in shapes of the UHRS, which become more sharply peaked at 25 Hz as the contributions from nearby small magnitude earthquakes increase. The LF deaggregation indicates that the distant large magnitude earthquakes dominate the hazard at the 10^{-3} to 10^{-5} annual exceedance frequencies. At the 10^{-6} exceedance frequency, the LF hazard contributions are largely from closer, moderate magnitude earthquakes.

Appendix D of RG 1.208 specifies how the deaggregation results are used to define what are called controlling earthquakes for the HF and LF motions. These earthquakes represent the weighted mean magnitude and weighted geometric mean distance, where the weights are defined by the relative contributions to the total hazard for each magnitude and distance interval. Table 2.5.2-212 lists the mean magnitudes and geometric mean distances computed for the HF and LF spectral frequency ranges for the four mean annual exceedance frequencies. The values for the LF hazard are listed considering all earthquakes and considering only those earthquakes occurring at distances greater than 100 km (60 mi), consistent with the procedure outlined in Appendix D of RG 1.208.

The approach to be used to compute the effects of the Fermi 3 site sediments on the generic hard rock motions is Approach 2B for site response analyses described in McGuire et al. (Reference 2.5.2-368). This approach defines what are called reference earthquakes (RE). The REs are defined in the same manner as the controlling earthquakes defined in Appendix D of RG 1.208.

Comparison of the computed controlling or RE magnitudes and distances with the deaggregation results indicates that in many cases the mean magnitude and mean distance correspond to a magnitude-distance bin that has a relatively small contribution to the hazard, particularly for the HF hazard results. Site response Approach 2B addresses this issue by using a range of magnitude-distance pairs to reflect the distribution of

earthquakes contributing to the HF and LF hazard. Typically, three deaggregation earthquakes (DE) at high frequency and three at low frequency are adequate to represent the distribution of earthquakes contributing to the hazard. These are designated DEL, DEM, and DEH for the low-magnitude, middle-magnitude, and high-magnitude DEs, respectively. The site response uses ground motions representative of the DEL, DEM, and DEH as input ground motions.

For the Fermi 3 site, the DEL, DEM, and DEH magnitude-distance values were defined to represent the modes in the magnitude-distance deaggregation. As shown by the red-blue-green color coding on Figure 2.5.2-257 through Figure 2.5.2-260, three magnitude-distance domains were identified that represent peaks in the deaggregated hazard and that, in combination, account for greater than 99 percent of the hazard. The DE magnitude and distances are computed as the weighted mean values over the defined domains. The resulting DEs are listed in Table 2.5.2-212. The weight assigned to each DE is defined by the relative contribution of the earthquakes in the magnitude-distance domain to the total hazard. The resulting weights are listed in the right-hand column of Table 2.5.2-212. The weighted combination of the DEs also produces a magnitude-distance pair that is very close to the RE.

2.5.2.4.4.3 Response Spectra for Reference and Deaggregation Earthquakes

Smooth response spectra were developed to represent each of the REs and DEs listed in Table 2.5.2-212. These spectra were developed using the EPRI (Reference 2.5.2-206) median ground motions models, the EPRI (Reference 2.5.2-207) aleatory variability models, and the spectral shape functions for CEUS ground motions presented in McGuire et al. (Reference 2.5.2-368).

The DEs are intended to represent the motions from earthquakes that are contributing to the hazard in a specific frequency range, either 1 to 2.5 Hz (LF) or 5 to 10 Hz (HF), for the purpose of computing site amplification functions. The development of the appropriate spectral shapes for the DEs uses the concept of the conditional mean spectrum developed by Baker and Cornell (Reference 2.5.2-369). The conditional mean spectrum is defined as the expected earthquake spectrum given that the spectral acceleration matches a specific value at a specific frequency. This spectrum is constructed taking into account the correlation between response spectral amplitudes at two different frequencies observed in

strong ground motion. For example, the 10^{-4} UHRS amplitude at a frequency of 10 Hz may represent the 84th percentile ground motions at 10 Hz spectral acceleration based on the DEL magnitude and distance and one of the EPRI ground motion models. Given that the spectral acceleration at 10 Hz represents a 1-epsilon ground motion, the expected value of epsilon at other frequencies is equal to the epsilon at 10 Hz multiplied by the correlation coefficient between the motions at 10 Hz and other frequencies. The resulting conditional mean spectrum represents the expected frequency content of earthquake motions that produce ground motions equal to the UHRS at the target frequency of 10 Hz.

Baker and Cornell (Reference 2.5.2-370) developed a model for the correlation coefficient between spectral accelerations at any two frequencies. Their model covered the frequency range of 0.2 to 20 Hz. Baker and Jayaram (Reference 2.5.2-371) have extended the Baker and Cornell (Reference 2.5.2-370) model to cover the frequency range of 0.1 to 100 Hz. The Baker and Jayaram (Reference 2.5.2-371) correlation model is based on data from a wide range of site conditions. As indicated in Figure 3 of Baker and Jayaram (Reference 2.5.2-371), similar correlations were obtained from the examination of different datasets containing differing mixtures of site conditions, indicating that the correlation is not greatly sensitive to site conditions.

This extended model was used to compute conditional mean spectra for the DEs. As an example, the 10^{-4} DEH for LF is listed in Table 2.5.2-212 as an **M** 7.6 earthquake occurring at a distance of 585 km (364 mi) from the site. A combination of a median ground motion model and aleatory variability model defined in the ground motion model logic tree (Figure 2.5.2-238) is used to compute the number of standard deviations (typically denoted by ε) that the 1 Hz and 2.5 Hz 10^{-4} UHRS accelerations lie away from the median ground motion defined by the selected model. These two values of ε are averaged and assigned to a frequency equal to the geometric mean of 1 Hz and 2.5 Hz. The expected value of ε at other frequencies is then computed using the Baker and Jayaram model (Reference 2.5.2-371). The conditional mean spectral shape is then computed using the selected median and aleatory variability models. The spectral shape is smoothed between the seven frequencies defined in the EPRI ground motion model using the average of the single-corner and double-corner spectral shape models developed in McGuire et al. (Reference 2.5.2-368).

The McGuire et al. (Reference 2.5.2-368) spectral shape models are also used to extrapolate the EPRI median ground motion model predictions from a frequency of 0.5 Hz down to a frequency of 0.1 Hz (spectral period of 10 seconds) to extend the response spectra for the DEL and DEM events and the HF RE events from 0.5 to 0.1 Hz. The magnitudes and distances for these events fall within the ranges of values considered by McGuire et al. (Reference 2.5.2-368) in developing their spectral shapes. The DEH events and the LF RE events represent large earthquakes occurring at large distances from the Fermi 3 site. The ability of the McGuire et al. (Reference 2.5.2-368) spectral shape models to represent the low-frequency portion of the spectrum for these events was examined by comparing the predicted spectral shape with spectral shapes of recent CEUS ground motion models that provide ground motion values at frequencies below 0.5 Hz.

Figure 2.5.2-261 presents response spectral shapes for a **M** 7.5 earthquake at a distance of 650 km (404 mi). This magnitude and distance was selected based on deaggregation of the hazard for 0.5 Hz spectral acceleration. The spectral shapes are presented in terms of pseudo-spectral velocity as this provides a clearer picture of the low-frequency spectral shape. The spectral shapes are normalized by the predicted amplitude at a frequency of 0.5 Hz as it is the extrapolation below 0.5 Hz that is of interest. Normalized spectral shapes are presented for the two McGuire et al. (Reference 2.5.2-368) CEUS spectral shape models and for a number of recently developed models. Also shown are normalized spectral shapes obtained using recently developed CEUS ground motion models described in Subsection 2.5.2.4.2. The recently developed ground motion models suggest that the extrapolation of the response spectral shape between 0.2 and 0.5 Hz for this large, distant earthquake is close to constant spectral velocity (1/T spectral acceleration scaling). At frequencies below 0.2 Hz, the spectra shape begins to deviate from constant spectral velocity towards constant spectral displacement. Therefore, constant spectral velocity scaling was used to extend the DEH and LF RE spectra from 0.5 to 0.2 Hz and then a small decrease from constant spectral velocity for the frequency range of 0.2 to 0.1 Hz. The model used is shown on Figure 2.5.2-261.

The extrapolation from 0.5 to 0.1 Hz requires an assessment of the aleatory variability in spectral acceleration at frequencies less than 0.5 Hz. The EPRI (Reference 2.5.2-207) aleatory models are based on

empirical ground motion models developed as part of the Pacific Earthquake Engineering Research (PEER) Center's NGA Project. The five NGA ground motion models available from PEER (Reference 2.5.2-372 through Reference 2.5.2-376) include estimates of aleatory variability for spectral frequencies between 0.1 and 100 Hz. These models indicate that the standard deviation of the natural log of spectral acceleration is, on average, 15 percent higher at a frequency of 0.1 Hz than it is at a frequency of 0.5 Hz. A linear increase in aleatory variability with decreasing log frequency from 0 percent at 0.5 Hz to 15 percent at 0.1 Hz was used to extend the EPRI (Reference 2.5.2-207) aleatory variability models down to a frequency of 0.1 Hz.

The calculation of the conditional mean spectra is performed for each combination of median and aleatory variability models defined by the ground motion logic tree shown on Figure 2.5.2-238. A weighted average of these spectra is then and the resulting spectral shape is smoothed and rescaled to match, on average, the UHRS at 1 and 2.5 Hz for LF spectra and 5 and 10 Hz for the HF spectra. The resulting DE response spectra are shown on Figure 2.5.2-262 through Figure 2.5.2-265.

The RE or controlling earthquake spectra are used to define a smooth spectral shape representative of the rock UHRS. Their primary use in Approach 2B is to produce a smooth surface spectrum consistent with the rock UHRS when multiplied by the site amplification function. As such, they represent the composite effects of a range of earthquake magnitude and distances, and it is desirable that their spectra lie close to the UHRS over a broad frequency range. Accordingly, the spectral shapes for the REs were developed using the above process with the modification that the correlation in ε between spectral frequencies was set to 1.0. The resulting RE spectral shapes are also shown on Figure 2.5.2-262 through Figure 2.5.2-265.

As can be seen on Figure 2.5.2-262 through Figure 2.5.2-265, the rock UHRS at 0.5 Hz is typically above the LF RE spectra. Thus, scaling the LF RE spectrum by the LF amplification function will underestimate the appropriate surface motions that are hazard consistent with the rock UHRS. To address this issue, the rock UHRS was extended from 0.5 Hz down to 0.1 Hz by computing a second LF RE spectrum that matches the UHRS at 0.5 Hz. This additional spectrum is denoted by the "LF Extended" spectral shape shown on Figure 2.5.2-262 through Figure

2.5.2-265. This spectral shape was developed using the spectral scaling model for a large, distant earthquake shown on Figure 2.5.2-261.

2.5.2.5 Seismic Wave Transmission Characteristics of the Site

The UHRS shown on Figure 2.5.2-256 represent ground motions occurring on generic CEUS hard rock conditions. As described in Subsection 2.5.4.2.1, the materials underlying the Fermi 3 site consist of thin layers of fill, lacustrine deposits, and glacial till overlying dolomite of the Bass Islands and Salina groups. The velocities of the upper approximately 130 m (425 ft) of these rocks are generally lower than the generic CEUS hard rock velocity, thus necessitating an assessment of site amplification to develop the site surface motions.

Site response analyses were conducted to evaluate the effect of the sedimentary bedrock on the generic CEUS hard rock ground motions. The intent of these analyses is to develop ground motions at the surface that are hazard-consistent with the hazard levels defined for the generic rock conditions. This hazard consistency is achieved through the use of the site response Approach 2B outlined in NUREG/CR-6728 (Reference 2.5.2-368). The following steps are involved in this approach:

1. Characterize the dynamic properties of the subsurface materials.
2. Randomize these properties to represent their uncertainty and variability across the site.
3. Based on the deaggregation of the rock hazard, define the distribution of magnitudes contributing to the controlling earthquakes for HF and LF ground motions (these are termed DEs in McGuire et al. (Reference 2.5.2-368), and define the response) spectra appropriate for each of the DEs.
4. Obtain appropriate rock site time histories to match the response spectra for the DEs.
5. Compute the mean site amplification function for the HF and LF controlling earthquakes based on the weighted average of the amplification functions for the DEs.
6. Scale the response spectra for the controlling earthquakes by the mean amplification function to obtain surface motions.
7. Envelop these scaled spectra to obtain surface motions hazard consistent with the generic CEUS hard rock hazard levels.

Step 3 of this process is described in Subsection 2.5.2.4.4. Steps 6 and 7 are described in Subsection 2.5.2.6. Steps 1, 2, 4, and 5 are presented in this subsection.

2.5.2.5.1 Dynamic Properties of the Fermi 3 Site

The shear (V_S) and compression (V_P) wave velocity data obtained at the Fermi 3 site are described in Subsection 2.5.4.4.1.

The interval velocity data was used to construct travel time plots in terms of layered velocity models (Reference 2.5.2-377). These are shown by the lines labeled “PS Layered Model” on Figure 2.5.2-266 through Figure 2.5.2-269. These interpretations provide a useful basis for defining the appropriate velocity for depth intervals where the average velocity is relatively constant. The interval velocity data and the interpreted layered velocity models indicate three general velocity layers within the rock units. As presented in Subsection 2.5.4.4.1, the average interval shear wave velocities in Salina Group Unit B are generally greater than 2800 m/s (9200 fps), and, therefore, elevation 48 m (156 ft) NAVD 88 is taken to be the point at which CEUS generic hard rock is encountered at the site.

The interval velocity data shown on Figure 2.5.2-266 through Figure 2.5.2-269 indicate that the transition from the Bass Islands Group to the Salina Group Unit F occurs over a transition zone rather than as an abrupt step. The thickness of this zone is in the range of 2 to 6 m (6 to 20 ft). Similarly, there appears to be a transition in velocity at the boundary between Salina Group Units F and E. Velocities in this transition zone were assessed by computing the harmonic mean of the suspension interval velocities over specific depth ranges. These velocity values are indicated by curves labeled “Averaged PS” on Figure 2.5.2-266 through Figure 2.5.2-269. The “Averaged PS” velocities are close to the PS Layered Model values where the averaging is done over the same depth range, indicating that the two approaches for estimating an average layer velocity produce consistent estimates.

Using the PS Layered Model and Averaged PS interpretations, velocity profiles were developed for each boring as shown on Figure 2.5.2-266 through Figure 2.5.2-269. Figure 2.5.2-270 compares these four velocity profiles. The four profiles have similar characteristics, indicating that a single velocity profile is appropriate for the Fermi 3 site. This profile is

computed as the geometric mean of the velocity profiles developed for each boring and is shown on Figure 2.5.2-270.

RG 1.208 states that the site safe shutdown earthquake (SSE, defined as the [GMRS]) is to be defined at the ground surface or at the top of the first competent layer, nominally with a velocity of 305 m/s (1000 fps) or greater. The materials overlying the Bass Islands Group rock consist of approximately 4 m (13 ft) of fill, approximately 1.5 m (5 ft) of low-velocity lacustrine deposits, and 3.4 m (11 ft) of glacial till. The planned finished ground level grade for the Fermi 3 site is at elevation of 179.6 m (589.3 ft) NAVD 88. This elevation is to be achieved by excavating to the top of the Bass Island Group bedrock at an average elevation of 168.1 m (551.7 ft) NAVD 88, and placing engineered granular backfill with an average depth of 11.5 m (37.6 ft). Therefore, the GMRS location is taken to be at the top of the Bass Island Group bedrock with an average elevation of 168.2 m (551.7 ft) NAVD 88 because all in-situ materials above this elevation are to be removed in the vicinity of Seismic Category I structures.

The velocity profile extending from the top of the Bass Islands Group bedrock is used for the development of the GMRS elevation amplification functions. The velocities and average layer thickness of the GMRS analysis profile are listed in Table 2.5.2-213.

In addition to the GMRS, the following spectra are developed and presented in Subsection 3.7.1:

- Performance-based surface response spectra (PBSRS) at the finished ground level grade.
- Foundation input response spectra (FIRS) at the base of the Reactor Building/Fuel Building (RB/FB), Control Building (CB), and Fire Water Service Complex (FWSC).

2.5.2.5.1.1 Density

Table 2.5.2-213 lists the average unit weight of the subsurface materials. These are taken from Table 2.5.4-202.

2.5.2.5.1.2 Shear Modulus and Damping

The GMRS profile consists of dolomites and claystones with shear wave velocities in excess of 910 m/s (3000 fps). This material is expected to remain essentially linear at the levels of shaking defined by the rock hazard. The damping within these materials was established using the following procedure.

The site response analyses were conducted using an updated version of program SHAKE, originally developed by Schnabel et al. (Reference 2.5.2-378). The energy lost in shear wave propagation was measured by the shear wave quality factor, Q_S, which can be equated to two other representations of energy loss in wave-propagation analysis. For the linear viscoelastic wave-propagation modeling used in program SHAKE, the material damping, ξ, is obtained by the relationship:

$$\xi = \frac{1}{2Q_S} \quad \text{[Eq. 1]}$$

Parameter Q_S is also related to the high-frequency attenuation parameter κ developed by Anderson and Hough (Reference 2.5.2-379) by the relationship:

$$\kappa = \frac{H}{Q_S V_S} \quad \text{[Eq. 2]}$$

where H_i is the thickness of the crust over which the energy loss occurs, typically taken to be 1 to 2 km (0.6 to 1.2 mi) (Reference 2.5.2-380). Silva and Darragh (Reference 2.5.2-380) find that Q_S is proportional to shear wave velocity:

$$Q_S = \gamma V_S \quad \text{[Eq. 3]}$$

where γ is the constant of proportionality. Using this assumption, the amount of high-frequency attenuation in the i^{th} layer of a velocity profile, K_i, is given by the relationship:

$$\kappa_i = \frac{H_i}{\gamma V_{Si}^2} \quad \text{[Eq. 4]}$$

where H_i is the layer thickness and V_{Si} is the layer shear-wave velocity. Given the total value of K appropriate for the site, one can solve for the corresponding value of γ. Using the resulting value of γ and Equations 1, 2, and 4, the appropriate damping values for each layer are then obtained.

The attenuation models for CEUS hard rock are developed assuming a shallow crustal κ of approximately 0.006 second (Reference 2.5.2-379). This point is placed at elevation 48 m (156 ft). The material above this elevation will contribute additional damping and, thus, add to the total site κ EPRI (Reference 2.5.2-381) gives the following relationship between total site κ and site shear wave velocity:

$$\log(\kappa) = 2.2189 - 1.0930 \log(V_S) \qquad \text{[Eq. 5]}$$

where V_S is shear wave velocity in fps and κ is in seconds. The average shear wave velocity of the rocks above elevation 48 m (156 ft) is 1737 m/s (5700 fps). Using this value in Equation 5 yields a κ value of 0.013 seconds. Subtracting the hard rock value of 0.006 yields a remaining κ of 0.007 seconds. If this value is attributed to the top 121 m (396 ft) of dolomite, the damping values computed using the above equations will be in the range of 3 to 7 percent. These values appear to be large in comparison with the low strain damping values typically assigned to soft rock materials. Silva et al. (Reference 2.5.2-382), as modified by Silva (Reference 2.5.2-383), proposed modulus reduction and damping relationships for soft rock that have low-strain damping values on the order of 3 percent. These would be expected to apply to relatively low velocity rocks. The Salina Group Unit F layer at the Fermi 3 site is perhaps in the upper range of soft rock velocities. A set of modulus reduction and damping relationships used by EPRI (Reference 2.5.2-381) to model the behavior of soft rock that has low-strain damping values on the order of 1 percent or less. Based on these values, it was assumed that the low-stain damping in the softest rock layer, Salina Group Unit F is in the range of 1 percent to 3 percent. Using Equations 1, 2, and 4, damping values were computed for the remaining rock layers assuming that Q_S is proportional to V_S. The resulting values are listed in Table 2.5.2-214 along with the corresponding values of κ for each layer. The result is that the assigned values of damping add an additional κ of 0.001 to 0.003 seconds.

The value of κ assigned to a site profile is a measure of the total damping due to both material damping and scattering effects. To account for this in a one-dimensional (1-D) site response model, the conversion from κ to material damping should account for the scattering (reflection) of waves off layer boundaries, particularly velocity reversals. In addition

to those present in the initial velocity model, the process of profile randomization to account for site variability, discussed in Subsection 2.5.2.5.1.3, will introduce additional velocity reversals. The amount of κ that is attributed to scattering in the site velocity profiles was assessed by comparing the median response of the randomized velocity profiles to a simple model with uniform velocity layers. The process used is shown on Figure 2.5.2-271. The randomized velocity profiles are used to compute the response of the site with the value of κ set to zero in the rock layers under a very low level of input motion. The randomized velocity profiles are then replaced by a simple model of a single layer with a velocity equal to the average velocity of the rock profile (1730 m/s [5680 fps]). The response computed using this model and zero κ is higher at high frequencies. The response analysis for the single layer model is repeated, gradually increasing the value of κ until the high frequency response is similar to that for the randomized site profiles. As shown on Figure 2.5.2-271, the resulting value of κ is 0.001 seconds.

The range in total site κ obtained by combining the generic CEUS hard rock value, the site scattering value and the values based on the damping assigned to the rock layers is 0.008 to 0.010 seconds.

2.5.2.5.1.3 Randomization of Dynamic Properties

Site response analyses were conducted using randomized shear wave velocity profiles to account for variations in shear wave velocity. The randomized profiles were generated using the shear wave velocity correlation model developed in Silva et al. (Reference 2.5.2-382). In this model, the shear wave velocity in the sediment layers are modeled as correlated, lognormal distributed variables. The expression for the correlation coefficient between the velocities in two adjacent layers, ρ, is given by:

$$\rho(h,t) = (1 - \rho_d(h))\rho_t(t) + \rho_d(h) \qquad \text{[Eq. 6]}$$

where $\rho_d(h)$ represents the depth-dependent correlation (generally increasing with increasing depth), and $\rho_t(t)$ is the thickness-dependent correlation (generally decreasing with increasing layer thickness). The factors $\rho_d(h)$ and $\rho_t(t)$ are obtained from the expressions:

$$\rho_d(h) = \begin{cases} \rho_{200}\left[\dfrac{h+h_0}{200+h_0}\right]^b & for \quad h \le 200\ m \\ \rho_{200} & for \quad h > 200\ m \end{cases} \qquad \text{[Eq. 7]}$$

and

$$\rho_t(t) = \rho_0 \exp\left[-\left(\frac{t}{\Delta}\right)^{\alpha}\right] \qquad \text{[Eq. 8]}$$

where *h* is the average of the midpoint depths of layers i and i-1, and t is the difference between those midpoint depths. Parameters h_0, ρ_0, ρ_{200}, Δ, α, and *b* are parameters of the model. The correlation model parameters developed in Silva et al. for USGS Category C soil sites were used in the simulations (Reference 2.5.2-382). The principal geologic units that immediately underlie the Fermi 3 site are relatively flat-lying sedimentary rocks. Because the rocks have not been subjected to severe deformation during their history, it is expected that the current correlation structure reflects the correlation structure that was created when the sediments that form the bedrock were first deposited. On this basis, the correlation model described in (Reference 2.5.2-382) USGS Category C, a relatively deep soil site, was selected because this model exhibits higher correlation than other models published in Reference 2.5.2-382.

The data from the Fermi site display low to moderate variability in velocity at shallow depth with a $\sigma_{\ln(V_S)}$ of approximately 0.1, increasing to 0.2 in the Salina Group Unit F. These values are similar to those obtained from analyses of individual firm soil sites (Reference 2.5.2-382), and these values were used to develop randomized velocity profiles. The locations of velocity layer boundaries were randomized to vary uniformly within the range of layer thickness observed in the site borings.

Sixty randomized V_S profiles were generated for the GMRS profile. Figure 2.5.2-272 and Figure 2.5.2-273 show the randomized velocity profiles. The statistics of the randomized profiles are compared to the input target values for median velocity and standard deviation (sigma) of $\ln(V_S)$ on Figure 2.5.2-274.

The damping in the sedimentary rocks beneath the soil profile was also randomized in the analysis. The standard deviation of $\ln(k)$ was set equal to 0.3, consistent with the variability in K used in McGuire et al.

(Reference 2.5.2-368) and EPRI (Reference 2.5.2-381). The corresponding damping ratio in the sedimentary rock layers was then computed using the randomized sedimentary rock layer velocities and thicknesses and the randomly selected value of K.

2.5.2.5.2 Acceleration Time Histories for Input Rock Motions

Response spectra were developed for each DE, as described in Subsection 2.5.2.4.4.3. Thirty time histories were developed to represent each DE from the time history sets given in McGuire et al. (Reference 2.5.2-368). Table 2.5.2-214 lists the time history sets used. The selected time histories were scaled to approximately match the target DE spectrum using a limited number of iterations of the routine RSPM06 that implements the time domain spectral matching approach developed by Lilhanand and Tseng (Reference 2.5.2-384). Figure 2.5.2-275 shows the response spectra for the 30 time histories scaled to match the HF and LF DEL, DEM, and DEH spectra for mean 10^{-4} ground motions.

The purpose of randomization of the site properties is to account for natural variability in defining the site response. Part of the natural variability is variability in the ground motions of an individual earthquake. That is why only weak scaling of the time histories was performed. The weak scaling produces recordings that have, in general, the desired relative frequency content of the DE spectra while maintaining a degree of natural variability. However, even with a limited number of iterations of spectral matching, the response spectra for the scaled time histories are close to the target spectra, as shown on Figure 2.5.2-275. The use of three DEs for both HF and LF motions along with a large number of recordings provides adequate coverage of the frequency band of interest. The acceleration time histories represent free field outcropping motions for generic CEUS hard rock.

2.5.2.5.3 Site Amplification Functions

Site amplification functions were developed for each DE. The 60 randomized velocity profiles were paired with the 30 scaled time histories by using each time history to compute the response of two profiles. For each analysis, the response spectrum for the computed surface motion was divided by the response spectrum for the input motion to obtain a site amplification function. The arithmetic mean of the 60 individual response spectral ratios is then computed to define the amplification function.

For each DE, mean amplification functions were computed for the three sets of values of rock damping. The results from the three DEs are then combined to produce a weighted mean amplification function for the RE. Figure 2.5.2-276 shows the site response model logic tree used to compute the RE mean amplification function. The weights assigned to the DEs are given in Table 2.5.2-215.

The sensitivity of the mean amplification function to the value of rock damping for the 10^{-4} exceedance level is shown on Figure 2.5.2-277. The range in damping leads to less than 15 percent difference in mean amplification at 100 Hz, less than 25 percent difference near 40 Hz, and decreasing to less than 6 percent at 10 Hz. The effect of the assigned damping continues to decreases for frequencies below 10 Hz.

For LF and HF, Figure 2.5.2-278 shows the DEL, DEM, and DEH amplification functions for 10^{-4} ground motions for the GMRS profile. The site amplification functions are insensitive to the differences in the DEs. The DEL amplification functions show a tendency to increase above a value near unity at very low frequencies (less than about 0.3 Hz). The cause of this behavior is the fact that in frequency bands where the ground motion time histories have very little energy, response spectral amplitudes are affected by energy in other frequency ranges due to the band width of the damped single degree of freedom oscillator response. This artificial increase due to the frequency bandwidth is unimportant for the HF amplification functions as they are not used at these low frequencies. For the LF amplification functions, this artificial increase was removed by smoothing. The straight line behavior exhibited by the amplification functions above 60 Hz reflects the fact that response spectral ratios were computed only at 50 and 60 Hz and that the ratio of PGA was used to define the amplification at 100 Hz. The plotted amplification curves were constructed using straight line segments between these points. Response spectral ratios at these three frequency points are sufficient to define smooth surface spectra at high frequencies.

Figure 2.5.2-279 shows the LF and HF smoothed mean GMRS site amplification functions for the four levels of input motion. The site amplification is insensitive to the level of motion due to the presence of a relatively hard rock that is modeled as a linear material.

The statistics for the level of effective strain computed in the analyses for the 10^{-4} and 10^{-5} input ground motions are show on Figure 2.5.2-280 and Figure 2.5.2-281, respectively. The effective strains are generally

less than 0.01 percent in the is-situ rock layers. The shear modulus reduction and damping relationships for soft rock presented in EPRI (Reference 2.5.2-381) show little departure from linear behavior at strain levels less than 0.01 percent, indicating the assumption of linear behavior in the in situ bedrock under the GMRS loading levels is appropriate.

2.5.2.6 Ground Motion Response Spectra

2.5.2.6.1 Hazard-Consistent Surface Spectra

Surface hazard spectra for the GMRS profile are obtained by scaling the rock RE and UHRS by the site amplification functions. The process used is illustrated on Figure 2.5.2-282 for the 10^{-4} level ground motions.

- The reference (controlling) spectra for LF and HF motions developed were scaled by the appropriate smoothed amplification function to produce ground surface spectra.
- The generic hard rock UHRS was also scaled using the appropriate LF and HF amplification values.
- A smooth envelope of the scaled spectra is constructed to define the surface 10^{-4} UHRS.

The rock UHRS exhibit a sharp peak at 25 Hz as shown on Figure 2.5.2-256. This peak is an artifact of the fact that the PSHA is computed for frequencies of 10, 25, and 100 Hz (PGA) and that the RE spectra are defined for frequencies in the range of 5 to 10 Hz. The spectral shapes for CEUS earthquakes developed in McGuire et al. (Reference 2.5.2-368) show a broader peak in the spectrum in the frequency range of 10 to 100 Hz. Therefore, the approach described in Subsection 2.5.2.4.4.3 was used to smoothly interpolate the rock UHRS between 10 and 100 Hz. An additional HF RE spectral shape was constructed to match the rock UHRS at 25 Hz. This shape was then adjusted to match the UHRS at 10 and 100 Hz by applying adjustment factors that varied linearly with log frequency from 0 at 25 Hz to the appropriate value at 10 or 100 Hz. This smoothed rock UHRS was then multiplied by the HF amplification function.

The amplification functions and the corresponding surface spectrum show a dip in the frequency range of 4 to 20 Hz. This results from a peak in the GMRS site amplification function occurring near 4 Hz from the overall rock profile, and the peak near 25 Hz in the hard rock UHRS. The dip was conservatively removed in constructing the surface UHRS. As a

result, the final spectra will be conservative in the frequency range of 4 to 20 Hz.

Similar operations were performed to develop surface spectra for the 10^{-5} and 10^{-6} exceedance level motions. These smooth envelope spectra represent the surface UHRS for the site defined as free field outcropping motions at elevation 168 m (551.7 ft) NAVD88. The UHRS for the GMRS elevation are shown on Figure 2.5.2-283.

2.5.2.6.2 GMRS

2.5.2.6.2.1 Horizontal GMRS

RG 1.208 defines the GMRS as a risk-consistent design response spectrum computed from the site-specific UHRS at a mean annual frequency of exceedance of 10^{-4} by the relationship:

$$GMRS = DF \times UHRS(10^{-4}) \quad \text{[Eq. 9]}$$

Parameter *DF* is the design factor specified by the expression:

$$DF = Maximum(1.0, 0.6(A_R)^{0.8}) \quad \text{[Eq. 10]}$$

in which A_R is the ratio of the UHRS ground motions for annual exceedance frequencies of 10^{-4} and 10^{-5}, specifically:

$$A_R = \frac{UHRS(10^{-5})}{UHRS(10^{-4})} \quad \text{[Eq. 11]}$$

RG 1.208 also specifies that when the value of A_R exceeds 4.2, the value of the GMRS is to be no less than 0.45 × SA(0.1H_D), that is, 45 percent of the 10^{-5} UHRS. Figure 2.5.2-284 shows the horizontal GMRS calculated using the two approaches. The final GMRS is taken as the envelope of the two, which for the Fermi 3 site is given by the 10^{-4} UHRS multiplied by the DF. These values are listed in Table 2.5.2-216 along with the horizontal mean 10^{-4} and 10^{-5} UHRS.

2.5.2.6.2.2 Vertical GMRS

McGuire et al. (Reference 2.5.2-368) recommended vertical to horizontal (V/H) spectral ratios for generic CEUS hard rock. These are given as a function of frequency for three levels of horizontal peak acceleration, as shown on Figure 2.5.2-285. Because the shear wave velocity of the site is relatively high, as the assessed value of site κ is not much greater than the generic hard rock value, the vertical GMRS were developed from the horizontal GMRS using these V/H values for peak acceleration between 0.2 g and 0.5 g. A vertical GMRS was then computed by multiplying the horizontal GMRS by this V/H ratio. The resulting vertical GMRS is listed in Table 2.5.2-216 along with the values of V/H.

2.5.2.6.2.3 Comparison with CSDRS

Figure 2.5.2-286 shows the horizontal and vertical GMRS (5 percent damping) for the Fermi 3 site based on the CEUS SSC model. Also shown are the ESBWR Certified Seismic Design Response Spectra (CSDRS), which are applied at the foundation level for the RB/FB and CB (Reference 2.5.2-385). The GMRS are enveloped by the ESBWR CSDRS at all frequencies between 0.1 and 100 Hz. Comparisons of the ESBWR CSDRS with the FIRS for the Seismic Category 1 structures are presented in Subsection 3.7.1.

2.5.2.7 References

2.5.2-201 Electric Power Research Institute and Seismic Owners Group, “Seismic Hazard Methodology for the Central and Eastern United States,” Technical Report NP-4726-A, Volumes 1–10, 1988.

2.5.2-202 Electric Power Research Institute, U.S. Department of Energy, and U.S. Nuclear Regulatory Commission, “Technical Report: Central and Eastern United States Seismic Source Characterization for Nuclear Facilities,” NUREG-2115, U.S. Nuclear Regulatory Commission, Washington, D.C., 2012.

2.5.2-203 Budnitz, R.J., G. Apostolakis, D.M. Boore, L.S. Cluff, K.J. Coppersmith, C.A. Cornell, and P.A. Morris, “Recommendations for Probabilistic Seismic Hazard Analysis: Guidance on Uncertainty and Use of Experts,” NUREG/CR-6372, U.S. Nuclear Regulatory Commission, Washington, D.C., 1997.

2.5.2-204 Kammerer, A.M., and J.P. Ake, “Practical Implementation Guidelines for SSHAC Level 3 and 4 Hazard Studies,” NUREG-2117, Rev. 1, U.S. Nuclear Regulatory Commission, 2012.

2.5.2-205 U.S. Nuclear Regulatory Commission, “Proposed Orders and Requests for Information in Response to Lessons Learned from Japan’s March 11, 2011, Great Tohoku Earthquake and Tsunami,” SECY-12-0025, February 17, 2012.

2.5.2-206 Electric Power Research Institute, “CEUS Ground Motion Project Final Report,” EPRI Report 1009684, December 2004.

2.5.2-207 Electric Power Research Institute, “Program on Technology Innovation: Truncation of the Lognormal Distribution and Value of the Standard Deviation for Ground Motion Models in the Central and Eastern United States,” EPRI TR-1014381, August 2006.

2.5.2-208 American Society of Civil Engineers and Structural Engineering Institute, “Seismic Design Criteria for Structures, Systems, and Components in Nuclear Facilities,” ASCE Standard ASCE/SEI 43-05, 98 pp., 2005.

2.5.2-209 Tinti S., and Mulargia F., “Effects of Magnitude Uncertainties on Estimating the Parameters in the Gutenberg-Richter Frequency-Magnitude Law,” Bulletin of the Seismological Society of America, Vol. 75, pp. 1681-1697, 1985.

2.5.2-210 Fujita, K., and N.H. Sleep, “A Re-examination of the Seismicity of Michigan,” Tectonophysics, Vol. 186, pp. 75-106, 1991.

2.5.2-211 U.S. Geological Survey, Earthquake Hazards Program, “Earthquake History of Ohio,” http://earthquake.usgs.gov/earthquakes/states/ohio/history.php, accessed January 24, 2013.

2.5.2-212 Bernreuter, D.L., J.B. Savy, R.W. Mensing, J.C. Chen, and B.C. Davis, “Seismic Hazard Characterization of 69 Nuclear Plant Sites East of the Rocky Mountains,” U.S. Nuclear Regulatory Commission, NUREG/CR-5250, Volumes 1–8, Washington, D.C., January 1989.

2.5.2-213 Johnston, A.C., K.J. Coppersmith, L.R. Kanter, and C.A. Cornell, “The Earthquakes of Stable Continental Regions:

Final Report Submitted to Electric Power Research Institute (EPRI)," TR-102261, 5-volume proprietary report prepared for Electric Power Research Institute, Palo Alto, California, 1994.

2.5.2-214 Klitgord, K.D., D.R. Hutchinson, and H. Schouten, "U.S. Atlantic Continental Margin; Structural and Tectonic Framework," in Sheridan, R.E., and J.A. Grow (eds.), The Atlantic Continental Margin, U.S., Geological Society of America, The Geoloy of North America, Vol. I-2, Chap. 3, pp. 19-55, 1988.

2.5.2-215 Holbrook, W.S., E.C. Reiter, G.M. Purdy, D. Sawyer, P.L. Stoffa, J.A. Austin, J. Oh, and J. Makris, "Deep Structure of the U.S. Atlantic Continental Margin, Offshore South Carolina, from Coincident Ocean Bottom and Multichannel Seismic Data," Journal of Geophysical Research, Vol. 99, No. B5, pp. 9155-9178, 1994.

2.5.2-216 Marshak, S., and T. Paulsen, "Structural Style, Regional Distribution, and Seismic Implications of Midcontinent Fault-and-Fold Zones, United States," Seismological Research Letters, Vol. 68, No. 4. pp. 511-520, 1997.

2.5.2-217 Braile, L.W., W.J. Hinze, G.R. Keller, E.G. Lidiak, and J.L. Sexton, "Tectonic Development of the New Madrid Rift Complex, Mississippi Embayment, North America," *Tectonophysics*, Vol. 131, pp. 1-21, 1986.

2.5.2-218 Pratt, T., R. Culotta, E. Hauser, D. Nelson, L. Brown, S. Kaufman, J. Oliver, and W. Hinze, "Major Proterozoic Basement Features of the Eastern Midcontinent of North America Revealed by Recent COCORP Profiling," Geology, Vol. 17, No. 6, pp. 505-509, 1989.

2.5.2-219 Atekwana, E.A., "Precambrian Basement Beneath the Central Midcontinent United States as Interpreted from Potential Field Data," in B.A. van der Pluijm and P.A. Catacosinos (eds.), Basement and Basins of Eastern North America, Geological Society of America Special Paper 308, 1996.

2.5.2-220 Sims, P.K., R.W. Saltus, and E.D. Anderson, "Preliminary Precambrian Basement Structure Map of the Continental United States—An Interpretation of Geologic and Aeromagnetic Data," U.S. Geological Survey Open-File Report 2005-1029, 2005.

2.5.2-221 Holbrook, W.S., G.M. Purdy, R.E. Sheridan, L. Glover III, M. Talwani, J. Ewing, and D. Hutchinson, “Seismic Structure of the U.S. Mid-Atlantic Continental Margin,” Journal of Geophysical Research, Vol. 99, No. B9, pp. 17871-17891, 1994.

2.5.2-222 Funck, T., H.R. Jackson, K.E. Louden, S.A. Kehler, and Y. Wu, “Crustal Structure of the Northern Nova Scotia Rifted Continental Margin (Eastern Canada),” Journal of Geophysical Research, Vol. 109, B09102, doi:10.1029/2004JB003008, 2004.

2.5.2-223 Austin, J.A., P.L. Stoffa, J.D. Phillips, J. Oh, D.S. Sawyer, G.M. Purdy, E. Reiter, and J. Makris, “Crustal Structure of the Southeast Georgia Embayment-Carolina Trough: Preliminary Results of a Composite Seismic Image of a Continental Suture (?) and a Volcanic Passive Margin,” Geology, Vol. 18, pp. 1023-1027, 1990.

2.5.2-224 LASE Study Group, “Deep Structure of the U.S. East Coast Passive Margin from Large Aperture Seismic Experiments (LASE),” Marine and Petroleum Geology, Vol. 3, pp. 234-242, 1986.

2.5.2-225 Trehu, A.M., A. Ballard, L.M. Dorman, J.F. Gettrust, K.D. Klitgord, and A. Schreiner, “Structure of the Lower Crust Beneath the Carolina Trough, U.S. Atlantic Margin,” Journal of Geophysical Research, Vol. 94, pp. 10,585-10,600, 1989.

2.5.2-226 Talwani, M., J. Ewing, R.E. Sheridan, D.L. Musser, L. Glover III, S. Holbrook, and M. Purdy, EDGE Lines of the U.S. Mid-Atlantic Margin and the East Coast Magnetic Anomaly,” Eos, Transactions of the American Geophysical Union, Vol. 73, No. 14, Fall meeting supplement, pp. 490-491, 1992.

2.5.2-227 Cook, F.A., L.D. Brown, S. Kaufman, J.E. Oliver, and T.A. Petersen, “COCORP Seismic Profiling of the Appalachian Orogen Beneath the Coastal Plain of Georgia,” Geological Society of America Bulletin, Vol. 92, No. 10, 1981.

2.5.2-228 Schlische, R.W., “Anatomy and Evolution of the Triassic-Jurassic Continental Rift System, Eastern North America,” Tectonics, Vol. 12, No. 4, pp. 1,026-1,042, 1993.

2.5.2-229 Bollinger, G.A., A.C. Johnston, P. Talwani, L.T. Long, K.M. Shedlock, M.S. Sibol, and M.C. Chapman, “Seismicity of the

Southeastern United States; 1698 to 1986," in Slemmons, D.B., E.R. Engdahl, M.D. Zoback, and D. Blackwell (eds.), Neotectonics of North America: Geological Society of America, Decade Map Volume 1, 1991.

2.5.2-230 Adams, J., and P. Basham, "The Seismicity and Seismotectonics of Eastern Canada," in Slemmons, D.B., E.R. Engdahl, M.D. Zoback, and D.D. Blackwell (eds.), Neotectonics of North America, Geological Society of America, Decade Map, Volume 1, 1991.

2.5.2-231 Crough, S.T., "Mesozoic Hotspot Epeirogeny in Eastern North America," Geology, Vol. 9, pp. 2-6, 1981.

2.5.2-232 Eaton, D.W., S. Dineva, and R. Mereu, "Crustal Thickness and *Vp/Vs* Variations in the Grenville Orogen (Ontario, Canada) from Analysis of Teleseismic Receiver Functions," Tectonophysics, Vol. 420, pp. 223-238, 2006.

2.5.2-233 Ma, S., and D.W. Eaton, "Western Quebec Seismic Zone (Canada): Clustered, Midcrustal Seismicity Along a Mesozoic Hot Spot Track," Journal of Geophysical Research, Vol. 112, B06305, doi:10.1029/2006JB004827, 2007.

2.5.2-234 Morgan, W.J., "Hotspot Tracks and the Early Rifting of the Atlantic," Tectonophysics, Vol. 94, pp. 123-139, 1983.

2.5.2-235 Ma, S., and G.M. Atkinson, "Focal Depths for Small to Moderate Earthquakes ($m_N \geq 2.8$) in Western Quebec, Southern Ontario, and Northern New York," Bulletin of the Seismological Society of America, Vol. 96, pp. 609-623, 2006.

2.5.2-236 Braile, L., W. Hinze, J. Sexton, G.R. Keller, and E. Lidiak, "Tectonic Development of the New Madrid Seismic Zone," in Hays, W.W., and P.L. Gori (eds.), Proceedings of the Symposium on the New Madrid Seismic Zone, U.S. Geological Survey Open-File Report 84-770, 1984.

2.5.2-237 Wheeler, R.L., and C.H. Cramer, "Updated Seismic Hazard in the Southern Illinois Basin: Geological and Geophysical Foundations for Use in the 2002 USGS National Seismic-Hazard Maps," Seismological Research Letters, Vol. 73, No. 5, pp. 776-791, 2002.

2.5.2-238 McBride, J.H., H.E. Leetaru, R.A. Bauer, B.E. Tingey, and S.E.A. Schmidt, "Deep Faulting and Structural Reactivation

Beneath the Southern Illinois Basin," Precambrian Research, Vol. 157, pp. 289-313, doi:10.1016/j.precamres.2007.02.020, 2007.

2.5.2-239 McBride, J.H., T.G. Hildenbrand, W.J. Stephenson, and C.J. Potter, "Interpreting the Earthquake Source of the Wabash Valley Seismic Zone (Illinois, Indiana, and Kentucky) from Seismic Reflection, Gravity, and Magnetic Intensity," Seismological Research Letters, Vol. 73, No. 5, pp. 660-686, 2002.

2.5.2-240 Wheeler, R.L., "Earthquakes and the Cratonward Limit of Iapetan Faulting in Eastern North America," Geology, Vol. 23, No. 2, pp. 105-108, 1995.

2.5.2-241 Petersen, M.D., A.D. Frankel, S.C. Harmsen, C.S. Mueller, K.M. Haller, R.L. Wheeler, R.L. Wesson, Y.Z. Oliver, S. Boyd, D.M. Perkins, N. Luco, E.H. Field, C.J. Wills, and K.S. Rukstales, "Documentation for the 2008 Update of the United States National Seismic Hazard Maps," USGS Open-File Report 2008-1128, 128 pp., 2008.

2.5.2-242 Adams, J., P.W. Basham, and S. Halchuk, S., "Northeastern North American Earthquake Potential—New Challenges for Seismic Hazard Mapping," Current Research 1995-D, Geological Survey of Canada, 1995.

2.5.2-243 Adams, J., D.H. Weichert, S. Halchuk, and P.W. Basham, Trial Seismic Hazard Maps of Canada—1995: Final Values for Selected Canadian Cities: Geological Survey of Canada, Open File 3283, 1996.

2.5.2-244 Adams, J., and S. Halchuk, Fourth Generation Seismic Hazard Maps of Canada: Values for over 650 Canadian Localities Intended for the 2005 National Building Code of Canada: Geological Survey of Canada, Open File 4459, 2003.

2.5.2-245 Spencer, C., A. Green, P. Morel-a-l'Huissier, and B. Milkereit, "The Extension of Grenville Basement Beneath the Northern Appalachians: Results from the Quebec-Maine Seismic Reflection and Refraction Surveys," Tectonics, Vol. 8, No. 4, pp. 677-696, 1989.

2.5.2-246 Bollinger, G.A., and R.L. Wheeler, "The Giles County, Virginia, Seismogenic Zone—Seismological Results and

Geological Interpretations," U.S. Geological Survey Professional Paper 1355,1988.

2.5.2-247 Powell, C.A., G.A. Bollinger, M.C. Chapman, M.S. Sibol, A.C. Johnston, and R.L. Wheeler, "A Seismotectonic Model for the 300-Kilometer-Long Eastern Tennessee Seismic Zone," Science, Vol. 264, pp. 686-688, 1994.

2.5.2-248 Faure, S., A. Tremblay, M. Malo, and J. Angelier, "Paleostress Analysis of Atlantic Crustal Extension in the Quebec Appalachians," The Journal of Geology, Vol. 114, pp. 435-448, 2006.

2.5.2-249 Law, R.D., M.C. Pope, R.H. Wirgart, K.A. Eriksson, D. Carpenter, E.S. Robinson, and G.A. Bollinger, "Geologically Recent Near-Surface Folding and Faulting in the Valley and Ridge Province: New Exposures of Extensional Faults in Alluvial Sediments, Giles County, SW Virginia [abstract]," Eos, Transactions of the American Geophysical Union, Vol. 74, No. 16, p. 282, 1993.

2.5.2-250 Law, R.D., E.S. Robinson, S., Sayer, J.S. Cyrnak, R.T. Williams, J. Callis, and M. Pope, "Geologically-Recent Faulting and Folding of Alluvial Sediments near Pearisburg, Giles County, Virginia—Tectonic Faulting or Karst Subsidence in Origin?" in Dennison, J.M., and K.G. Stewart (eds.), Geologic Field Guide to Extensional Structures along the Allegheny Front in Virginia and West Virginia near the Giles County Seismic Zone: Southeastern Section, Geological Society of America, Charleston, West Virginia, March 28-29, 1998, Guidebook, pp. 95-101, 1998.

2.5.2-251 Van Arsdale, R.B., and R.E. Sergeant, "Post-Pliocene Displacement on Faults Within the Kentucky River Fault System of East-Central Kentucky," Kentucky Geological Survey, Series 11, Reprint 34, reprinted from U.S. Nuclear Regulatory Commission Report NUREG/CR-4685 (1987), 36 pp., 1992.

2.5.2-252 Milkereit, B., D.A. Forsyth, A.G. Green, A. Davidson, S. Hanmer, D.R. Hutchinson, W.J. Hinze, and R.F. Mereu, Seismic Images of a Grenvillian Terrane Boundary," Geology, Vol. 20, pp. 1027-1030, 1992.

2.5.2-253 Forsyth, D.A., B. Milkereit, A. Davidson, S. Hanmer, D.R. Hutchinson, W.J. Hinze, and R.F. Mereu, "Seismic Images of

a Tectonic Subdivision of the Grenville Orogen Beneath Lakes Ontario and Erie," Canadian Journal of Earth Sciences, Vol. 31, pp. 229-242, 1994.

2.5.2-254 O'Dowd, C.R., D. Eaton, D. Forsyth, and H.W. Asmis, "Structural Fabric of the Central Metasedimentary Belt of Southern Ontario, Canada, from Deep Seismic Profiling," Tectonophysics, Vol. 388, pp. 145-159, 2004.

2.5.2-255 Obermeier, S.F., J.D. Vaughn, and R.D. Hatcher, Jr., "Field Trip Guide—Paleoseismic Features in and near Douglas Reservoir, East Tennessee Seismic Zone, Northeastern Tennessee," East Tennessee Seismic Zone Pilot Study sponsored by the U.S. Nuclear Regulatory Commission, University of Tennessee, 2010.

2.5.2-256 Tuttle, M.P., K. Dyer-Williams, and N.L. Barstow, "Paleoliquefaction Study of the Clarendon-Linden Fault System, Western New York State," Tectonophysics, Vol. 353, pp. 263-286, 2002.

2.5.2-257 Ervin, G.P., and L.D. McGinnis, "Reelfoot Rift: Reactivated Precursor to the Mississippi Embayment," Geological Society of America Bulletin, Vol. 86, pp. 1287-1295, 1975.

2.5.2-258 Thomas, W.A., "The Appalachian-Ouachita Rifted Margin of Southeastern North America," Geological Society of America Bulletin, Vol. 103, pp. 415-431, 1991.

2.5.2-259 Hildenbrand, T.G., and J.D. Hendricks, "Geophysical Setting of the Reelfoot Rift and Relations Between Rift Structures and the New Madrid Seismic Zone," in Shedlock, K.M., and A.C. Johnston (eds.), *Investigations of the New Madrid Seismic Zone*, U.S. Geological Survey Professional Paper 1538-E, 30 pp., 1995.

2.5.2-260 Thomas, W.A., "Evolution of Ouachita-Appalachian continental margin," Journal of Geology, Vol. 84, pp. 323-342, 1976.

2.5.2-261 Thomas, W.A., "Tectonic Inheritance at a Continental Margin" [2005 GSA presidential address], GSA Today, Vol. 16, No. 2, pp. 4-11, 2006.

2.5.2-262 Hildenbrand, T.G., "Model of the Southeastern Margin of the Mississippi Valley Graben near Memphis, Tennessee, from

Interpretation of Truck-Magnetometer Data," Geology, Vol. 10, pp. 476-480, 1982.

2.5.2-263 Csontos, R., R. Van Arsdale, R. Cox, and B. Waldron, "Reelfoot Rift and Its Impact on Quaternary Deformation in the Central Mississippi River Valley," Geosphere, Vol. 4, No. 1, pp. 145-158, 2008.

2.5.2-264 Mihills, R.K., and R.B. Van Arsdale, "Late Wisconsin to Holocene Deformation in the New Madrid Seismic Zone," Bulletin of the Seismological Society of America, Vol. 89, pp. 1019-1024, 1999.

2.5.2-265 Csontos, R., and R. Van Arsdale, "New Madrid Seismic Zone Fault Geometry," Geosphere, Vol. 4, No. 5, pp. 802-813, 2008.

2.5.2-266 Cox, R.T., R.B. Van Arsdale, and J.B. Harris, "Identification of Possible Quaternary Deformation in the Northeastern Mississippi Embayment Using Quantitative Geomorphic Analysis of Drainage-Basin Asymmetry," Geological Society of America Bulletin, Vol. 113, pp. 615-624, 2001.

2.5.2-267 Cox, R.T., R.B. Van Arsdale, J.B. Harris, and D. Larsen, Neotectonics of the Southeastern Reelfoot Rift Zone Margin, Central United States, and Implications for Regional Strain Accommodation," Geology, Vol. 29, No. 5, pp. 419-422, 2001.

2.5.2-268 Cox, R.T., J. Cherryhomes, J.B. Harris, D. Larsen, R.B. Van Arsdale, and S.L. Forman, "Paleoseismology of the Southeastern Reelfoot Rift in Western Tennessee and Implications for Intraplate Fault Zone Evolution," Tectonics, Vol. 25, No. TC3019, 17 pp., doi:10.1029/2005TC001829, 2006.

2.5.2-269 Van Arsdale, R.B., R.A. Williams, E.S. Schweig, K.M. Shedlock, J.K. Odum, and K.W. King, "The Origin of Crowley's Ridge, Northeastern Arkansas: Erosional Remnant or Tectonic Uplift?" Bulletin of the Seismological Society of America, Vol. 85, No. 4, pp. 963-985, 1995.

2.5.2-270 Baldwin, J.N., J.B. Harris, R.B. Van Arsdale, R. Givler, K.I. Kelson, J.L. Sexton, and M. Lake, "Constraints on the Location of the Late Quaternary Reelfoot and New Madrid North Faults in the New Madrid Seismic Zone, Central United

States: Seismological Research Letters, Vol. 76, No. 6, pp. 772-789, 2005.

2.5.2-271 Van Arsdale, R.B., "Seismic Hazards of the Upper Mississippi Embayment," U.S. Army Corps of Engineers Waterways Experiment Station Contract Report GL-98-1, 126 pp., 1998.

2.5.2-272 Guccione, M.J., R.B. Van Arsdale, and L.H. Hehr, "Origin and Age of the Manila High and Associated Big Lake 'Sunklands,' New Madrid Seismic Zone, Northeastern Arkansas," Geological Society of America Bulletin, Vol. 112, pp. 579-590, 2000.

2.5.2-273 Russ, D.P., "Style and Significance of Surface Deformation in the Vicinity of New Madrid, Missouri: Investigations of the New Madrid, Missouri, Earthquake Region," U.S. Geological Survey Professional Paper 1236-H, 1982.

2.5.2-274 Kelson, K.I., G.D. Simpson, R.B. Van Arsdale, J.B. Harris, C.C. Haraden, and W.R. Lettis, "Multiple Late Holocene Earthquakes Along the Reelfoot Fault, Central New Madrid Seismic Zone," Journal of Geophysical Research, Vol. 101, No. B-3, pp. 6151-6170, 1996.

2.5.2-275 Mueller, K., J. Champion, M. Guccione, and K. Kelson, "Fault Slip Rates in the Modern New Madrid Seismic Zone," Science, Vol. 286, pp. 1135-1138, 1999.

2.5.2-276 Van Arsdale, R.B., R.T. Cox, A.C. Johnston, W.J. Stephenson, and J.K. Odum, Southeastern Extension of the Reelfoot Fault," Seismological Research Letters, Vol. 70, No. 3, pp. 348-359, 1999.

2.5.2-277 Champion, J., K. Mueller, A. Tate, and M. Guccione, "Geometry, Numerical Models and Revised Slip Rate for the Reelfoot Fault and Trishear Fault-Propagation Fold, New Madrid Seismic Zone," Engineering Geology, Vol. 62, pp. 31-49, 2001.

2.5.2-278 Nelson, W.J., F.B. Denny, J.A. Devera, L.R. Follmer, and J.M. Masters, "Tertiary and Quaternary Tectonic Faulting in Southernmost Illinois," Engineering Geology, Vol. 46, pp. 235-258, 1997.

2.5.2-279 Nelson, W.J., F.B. Denny, L.R. Follmer, and J.M. Masters, "Quaternary Grabens in Southernmost Illinois: Deformation

near an Active Intraplate Seismic Zone," Tectonophysics, Vol. 305, pp. 381-397, 1999.

2.5.2-280 McBride, J.H., W.J. Nelson, and W.J. Stephenson, "Integrated Geological and Geophysical Study of Neogene and Quaternary-Age Deformation in the Northern Mississippi Embayment," Seismological Research Letters, Vol. 73, No. 5, pp. 597-627, 2002.

2.5.2-281 Science Applications International Corporation(SAIC), "Seismic Investigation Report for Siting of a Potential On-Site CERCLA Waste Disposal Facility at the Paducah Gaseous Diffusion Plant, Paducah, Kentucky," Report prepared by SAIC Engineering, Inc., Oak Ridge, Tennessee, for Bechtel Jacobs Company and the U.S. Department of Energy, Office of Environmental Management, DOE/OR/07-2038&D1, August 2002.

2.5.2-282 Woolery, E.W., J. Baldwin, K. Kelson, S. Hampson, and R. Givler, "Site-Specific Fault Rupture Hazard Assessment—Fluorspar Area Fault Complex, Western Kentucky," presentation given at meeting of CEUS Earthquake Hazards Program, U.S. Geological Survey, October 28-29, Memphis, Tenn., 2009

2.5.2-283 Wheeler, R.L., "Boundary Separating the Seismically Active Reelfoot Rift from the Sparsely Seismic Rough Creek Graben, Kentucky, and Illinois," Seismological Research Letters, Vol. 68, No. 4, pp. 586-598, 1997.

2.5.2-284 Adams, J., and P. Basham, "The Seismicity and Seismotectonics of Eastern Canada," in D.B. Slemmons, E.R. Engdahl, M.D. Zoback, and D.D. Blackwell (eds.), Neotectonics of North America, Geological Society of America, Decade Map, Volume 1, 1991.

2.5.2-285 Aylsworth, J.M., D.E. Lawrence, and J. Guertin, "Did Two Massive Earthquakes in the Holocene Induce Widespread Landsliding and Near-Surface Deformation in Part of the Ottawa Valley, Canada?" Geology, Vol. 28, pp. 903-906, 2000.

2.5.2-286 Aylsworth, J.M., and D.E. Lawrence, "Earthquake-Induced Landsliding East of Ottawa: A Contribution to the Ottawa Valley Landslide Project," Geohazards 2003, Proceedings of the 3rd Canadian Conference on Geotechnique and Natural

Hazards, June 9 and 10, Edmonton, Alberta, Canada, pp. 57-64, 2003.

2.5.2-287 Grana, J.P., and R.M. Richardson, “Tectonic Stress Within the New Madrid Seismic Zone,” Journal of Geophysical Research, Vol. 101, pp. 5445-5458, 1996.

2.5.2-288 Liu, L., and M.D. Zoback, “Lithospheric Strength and Intraplate Seismicity in the New Madrid Seismic Zone,” Tectonics, Vol. 16, No. 4, pp. 585-595, 1997.

2.5.2-289 Grollimund, B.R., and M.D. Zoback, “Did Deglaciation Trigger Intraplate Seismicity in the New Madrid Seismic Zone?” Geology, Vol. 29, No. 2, pp. 175-178, 2001.

2.5.2-290 Van Arsdale, R., R. Bresnahan, N. McCallister, and B. Waldron, “Upland Complex of the Central Mississippi River Valley: Its Origin, Denudation, and Possible Role in Reactivation of the New Madrid Seismic Zone,” in Stein, S., and S. Mazzotti (eds.), Continental Intraplate Earthquakes: Science, Hazard, and Policy Issues, Geological Society of America Special Paper 425, pp. 177-192, doi:10.1130/2007.2425(13), 2007.

2.5.2-291 Li, Q., M. Liu, and S. Stein, “Spatiotemporal Complexity of Continental Intraplate Seismicity: Insights from Geodynamic Modeling and Implications for Seismic Hazard Estimation,” Bulletin of the Seismological Society of America, Vol. 99, No. 1, pp. 52-60, 2009.

2.5.2-292 Calais, E., and S. Stein, “Time-Variable Deformation in the New Madrid Seismic Zone,” Science, Vol. 323, p. 1442, doi:0.1126/science.1168122, 2009.

2.5.2-293 Chiu, J.M., A.C. Johnston, and Y.T. Yang, “Imaging the Active Faults of the Central New Madrid Seismic Zone Using PANDA Array Data,” Seismological Research Letters, Vol. 63, No. 3, pp. 375-393, 1992.

2.5.2-294 Schweig, E.S., and M.A. Ellis, “Reconciling Short Recurrence Intervals with Minor Deformation in the New Madrid Seismic Zone,” Science, Vol. 264, pp. 1308-1311, 1994.

2.5.2-295 Johnston, A.C., and E.S. Schweig, “The Enigma of the New Madrid Earthquakes of 1811-1812,” Annual Review of Earth and Planetary Sciences, Vol. 24, pp. 339-384, 1996.

2.5.2-296 Hough, S.E., and S. Martin, “Magnitude Estimates of Two Large Aftershocks of the 16 December 1811 New Madrid Earthquake,” Bulletin of the Seismological Society of America, Vol. 92, No. 8, pp. 3259-3268, 2002.

2.5.2-297 Mueller, K., S.E. Hough, and R. Bilham, “Analysing the 1811-1812 New Madrid Earthquakes with Recent Instrumentally Recorded Aftershocks,” Nature, Vol. 429, pp. 284-288, 2004.

2.5.2-298 Bakun, W.H., and M.G. Hopper, “Catalog of Significant Historical Earthquakes in the Central United States,” U.S. Geological Survey Open-File Report 2004-1086, 2004.

2.5.2-299 Guccione, M.J., R. Marple, and W.J. Autin, “Evidence for Holocene Displacements on the Bootheel Fault (Lineament) in Southeastern Missouri: Seismotectonic Implications for the New Madrid Region,” Geological Society of America Bulletin, Vol. 117, pp. 319-333, doi:10.1130/B25435.1, 2005.

2.5.2-300 Baldwin, J.N., A.D. Barron, and K.I. Kelson, J.B. Harris, and S.M. Cashman, “Preliminary Paleoseismic and Geophysical Investigation of the North Farrenburg Lineament, Farrenburg, Missouri: Deformation Associated with the New Madrid North Fault?” Seismological Research Letters, Vol. 73, No. 3, pp. 395-413, 2002.

2.5.2-301 Van Arsdale, R.B., “Displacement History and Slip Rate on the Reelfoot Fault of the New Madrid Seismic Zone,” Engineering Geology, Vol. 55, No. 4, pp. 219-226, 2000.

2.5.2-302 Johnston, A.C., “Seismic Moment Assessment of Earthquakes in Stable Continental Regions—II. Historical Seismicity,” Geophysical Journal International, Vol. 125, pp. 639-678, 1996.

2.5.2-303 Hough, S., J.G. Armbruster, L. Seeber, and J.F. Hough, “On the Modified Mercalli Intensities and Magnitudes of the 1811-1812 New Madrid Earthquakes,” Journal of Geophysical Research, Vol. 105, No. B10, pp. 23,839-23,864, 2000.

2.5.2-304 Hough, S.E., and M. Page, “Toward a Consistent Model for Strain Accrual and Release for the New Madrid, Central United States,” Journal of Geophysical Research, Vol. 116, B03311, doi:10.1029/2010JB007783, 2011.

2.5.2-305 Tuttle, M.P., E.S. Schweig, J.D. Sims, R.H. Lafferty, L.W. Wolf, and M.I. Haynes, “The Earthquake Potential of the New Madrid Seismic Zone,” Bulletin of the Seismological Society of America, Vol. 92, No. 6, pp. 2080-2089, 2002.

2.5.2-306 Tuttle, M.P., J.D. Sims, K. Dyer-Williams, R.H. Lafferty III, and E.S. Schweig III, “Dating of Liquefaction Features in the New Madrid Seismic Zone,” NUREG/GR-0018, U.S. Nuclear Regulatory Commission, Washington, D.C., 42 pp., 2000.

2.5.2-307 Tuttle, M.P., and L.W. Wolf, “Towards a Paleoearthquake Chronology of the New Madrid Seismic Zone,” U.S. Geological Survey, Earthquake Hazards Program, Progress Report (01-HQGR-0164), 38 pp., 2003.

2.5.2-308 Kelson, K.I., R.B. Van Arsdale, G.D. Simpson, and W.R. Lettis, “Assessment of the Style and Timing of Surficial Deformation Along the Central Reelfoot Scarp, Lake County, Tennessee,” Seismological Research Letters, Vol. 63, No. 3, pp. 349-356, 1992.

2.5.2-309 Not Used

2.5.2-310 McKenna, J., S. Stein, and C.A. Stein, “Is the New Madrid seismic zone hotter and weaker than its surroundings?” in Stein, S., and S. Mazzotti (eds.), *Continental Intraplate Earthquakes: Science, Hazard, and Policy Issues*, Geological Society of America Special Paper 425, pp. 167-175, doi:10.1130/2007.2425(12), 2007.

2.5.2-311 Newman, A., S. Stein, J. Weber, J. Engeln, A. Mao, and T. Dixon, 1999, “Slow Deformation and Lower Seismic Hazard at the New Madrid Seismic Zone,” Science, Vol. 284, No. 5414, pp. 619-621, 1999.

2.5.2-312 Calais, E., G. Mattioli, C. DeMets, J.M. Nocquet, S. Stein, A. Newman, and P. Rydelek, “Tectonic Strain in the Interior of the North American Plate?” Nature, Vol. 438, doi:10.1038/nature04428, 2005.

2.5.2-313 Holbrook, J., W.J. Autin, T.M. Rittenour, S. Marshak, and R.J. Goble, “Stratigraphic Evidence for Millennial-Scale Temporal Clustering of Earthquakes On A Continental-Interior Fault: Holocene Mississippi River Floodplain Deposits, New Madrid Seismic Zone, USA,” Tectonophysics, Vol. 420, pp. 431-454, 2006.

2.5.2-314 Obermeier, S.F., N.K. Bleurer, C.A. Munson, P.J. Munson, W.S. Marin, K.M. McWilliams, D.A. Tabaczynski, J.K. Odum, M. Rubin, and D.L. Eggert, Evidence of Strong Earthquake Shaking in the Lower Wabash Valley from Prehistoric Liquefaction Features," Science, Vol. 251, pp. 1061-1063, 1991.

2.5.2-315 Munson, P.J., S.M. Obermeier, C.A. Munson, and E.R. Hajic, "Liquefaction Evidence for Holocene and Latest Pleistocene in the Southern Halves of Indiana and Illinois—A Preliminary Overview," Seismological Research Letters, Vol. 68, No. 4, pp. 523-536, 1997.

2.5.2-316 Pond, E.C., and J.R. Martin, "Estimated Magnitudes and Accelerations Associated with Prehistoric Earthquakes in the Wabash Valley Region of the Central United States," in Kolata, D.R., and T.G. Hildenbrand (eds.), Investigations of the Illinois Basin Earthquake Region, Seismological Research Letters, Vol. 68, pp. 611-623, 1997.

2.5.2-317 Obermeier, S.F., "Liquefaction Evidence for Strong Earthquakes of Holocene and Latest Pleistocene Ages in the States of Indiana and Illinois, USA," *Engineering Geology,* Elsevier Science, Vol. 50, pp. 227-254, 1998.

2.5.2-318 McNulty, W.E., and S.F. Obermeier, "Liquefaction Evidence for at Least Two Strong Holocene Paleoearthquakes in Central and Southwestern Illinois, USA," Environmental and Engineering Geoscience, Vol. 5, No. 2, pp. 133-146, 1999.

2.5.2-319 Tuttle, M., J. Chester, R. Lafferty, K. Dyer-Williams, and B. Cande, "Paleoseismology Study Northwest of the New Madrid Seismic Zone," NUREG/CR-5730, U.S. Nuclear Regulatory Commission, Washington, D.C., 98 pp., 1999.

2.5.2-320 Not Used

2.5.2-321 Castilla, R.A., and F.A. Audemard, "Sand Blows as a Potential Tool for Magnitude Estimation of Pre-Instrumental Earthquakes," Journal of Seismology, Vol. 11, pp. 473-487, doi:10.1007/s10950-007-9065-z, 2007.

2.5.2-322 Obermeier, S.F., J.R. Martin, A.D. Frankel, T.L. Youd, P.J. Munson, C.A. Munson, and E.C. Pond, "Liquefaction Evidence for One or More Strong Holocene Earthquakes in the Wabash Valley of Southern Indiana and Illinois, with a

Preliminary Estimate of Magnitude," U.S. Geological Survey Professional Paper 1536, 27 pp., 1993.

2.5.2-323 Green, R.A., S.F. Obermeier, and S.M. Olson, "Engineering Geologic and Geotechnical Analysis of Paleoseismic Shaking Using Liquefaction Effects: Field Examples," Engineering Geology, Vol. 76, pp. 263-293, 2005.

2.5.2-324 Lamontagne, M., S. Halchuck, J.F. Cassidy, and G.C. Rogers, "Significant Canadian Earthquakes of the Period 1600-2006," Seismological Research Letters, Vol. 79, pp. 211-223, 2008.

2.5.2-325 Tuttle, M.P., and G.M. Atkinson, "Localization of Large Earthquakes in the Charlevoix Seismic Zone, Quebec, Canada, During the Past 10,000 Years," Seismological Research Letters, Vol. 81, pp. 140-147, 2010.

2.5.2-326 Doig, R., "Effects of Strong Seismic Shaking in Lake Sediments, and Earthquake Recurrence Interval, Témiscaming, Quebec," Canadian Journal of Earth Sciences, Vol. 28, pp. 1349-1352, 1991.

2.5.2-327 Filion, L., F. Quinty, and C. Bégin, "A Chronology of Landslide Activity in the Valley of Rivierre du Gouffre, Charlevoix, Quebec," Canadian Journal of Earth Sciences, Vol. 28, pp. 103-118, 1991.

2.5.2-328 Lamontagne, M., and G. Ranalli, "Faults and Spatial Clustering of Earthquakes near La Malbaie, Charlevoix Seismic Zone, Canada," Seismological Research Letters, Vol. 68, No. 2, pp. 337-352, 1997.

2.5.2-329 Lamontagne, M., and G. Ranalli, "Thermal and Rheological Constraints on the Earthquake Depth Distribution in the Charlevoix, Canada, Intraplate Seismic Zone," Tectonophysics, Vol. 257, pp. 55-69, 1996.

2.5.2-330 Mazzotti, S., and J. Adams, "Rates and Uncertainties on Seismic Moment and Deformation Rates in Eastern Canada," Journal of Geophysical Research, Vol. 110, B09301, doi:10.1029/2004JB003510, 2005.

2.5.2-331 Lamontagne, M., "Rheological and Geological Constraints on the Earthquake Distribution in the Charlevoix Seismic Zone," Ph.D. thesis, Carleton University, published as Geological Survey of Canada Open-File Report, D-3778, 353 pp., 1999.

2.5.2-332 Baird, A.F., S.D. McKinnon, and L. Godin, “Stress Channelling and Partitioning of Seismicity in the Charlevoix Seismic Zone, Québec, Canada,” Geophysical Journal International, Vol. 179, pp. 559-568, 2009.

2.5.2-333 Johnston, A.C., “Seismic Moment Assessment of Earthquakes in Stable Continental Regions—III. New Madrid 1811-1812, Charleston 1886, and Lisbon 1755,” Geophysical Journal International, Vol. 126, pp. 314-344, 1996.

2.5.2-334 Dutton, C.E., “The Charleston Earthquake of August 31, 1886,” U.S. Geological Survey Ninth Annual Report, 1887-88, pp. 203-528, 1889.

2.5.2-335 Behrendt, J.C., R.M. Hamilton, H.D. Ackermann, and V.J. Henry, “Cenozoic Faulting in the Vicinity of the Charleston, South Carolina, 1886 Earthquake,” Geology, Vol. 9, No. 3, pp. 117-122, 1981.

2.5.2-336 Talwani, P., “An Internally Consistent Pattern of Seismicity near Charleston, South Carolina,” Geology, Vol. 10, No. 12, pp. 655-658, 1982.

2.5.2-337 Hamilton, R.M., J.C. Behrendt, and H.D. Ackermann, “Land Multichannel Seismic-Reflection Evidence for Tectonic Features near Charleston, South Carolina,” in Gohn, G.S. (ed.), Studies Related to the Charleston, South Carolina Earthquake of 1886—Tectonics and Seismicity, U.S. Geologic Survey Professional Paper 1313-I, pp. I1-I18, 1983.

2.5.2-338 Behrendt, J.C., and A. Yuan, “The Helena Banks Strike-Slip (?) Fault Zone in the Charleston, South Carolina, Earthquake Area: Results from a Marine, High-Resolution, Multichannel, Seismic-Reflection Survey,” Geological Society of America Bulletin, Vol. 98, No. 5, pp. 591-601, 1987.

2.5.2-339 Marple, R., and P. Talwani, “Evidence for a Buried Fault System in the Coastal Plain of the Carolinas and Virgina—Implications for Neotectonics in the Southeastern United States,” Geological Society of America Bulletin, Vol. 112, pp. 200-220, 2000.

2.5.2-340 Weems, R.E., and W.C. Lewis, “Structural and Tectonic Setting of the Charleston, South Carolina, Region: Evidence from the Tertiary Stratigraphic Record,” Geological Society of America Bulletin, Vol. 114, No. 1, pp. 24-42, 2002.

2.5.2-341 Talwani, P., and M. Katuna, “Macroseismic Effects of the 1886 Charleston Earthquake,” Carolina Geological Society Field Trip Guidebook, 18 pp., 2004.

2.5.2-342 Dura-Gomez, I., and P. Talwani, “Finding Faults in the Charleston Area, South Carolina: 1. Seismological Data,” Seismological Research Letters, Vol. 80, No. 5, pp. 883-900, 2009.

2.5.2-343 Talwani, P., and I. Dura-Gomez, “Finding Faults in the Charleston Area, South Carolina: 2. Complementary Data,” Seismological Research Letters, Vol. 80, No. 5, pp. 901-919, 2009.

2.5.2-344 Chapman, M.C., and J.N. Beale, “Mesozoic and Cenozoic Faulting Imaged at the Epicenter of the 1886 Charleston, South Carolina Earthquake,” Bulletin of the Seismological Society of America, Vol. 98, pp. 2533-2542, 2008.

2.5.2-345 Chapman, M.C., and J.N. Beale, “On the Geologic Structure at the Epicenter of the 1886 Charleston, South Carolina, Earthquake,” Bulletin of the Seismological Society of America, Vol. 100, No. 3, pp. 1010-1030, 2010.

2.5.2-346 Obermeier, S.F., R.E. Weems, R.B. Jacobson, and G.S. Gohn, “Liquefaction Evidence for Repeated Holocene Earthquakes in the Coastal Region of South Carolina,” Annals of the New York Academy of Sciences, Vol. 558, pp. 183-195, 1989.

2.5.2-347 Weems, R.E., and S.F. Obermeier, “The 1886 Charleston Earthquake—An Overview of Geological Studies,” in *Proceedings of the U.S. Nuclear Regulatory Commission Seventeenth Water Reactor Safety Information Meeting,* NUREG/CP-0105, U.S. Nuclear Regulatory Commission, Washington, D.C., Vol. 2, pp. 289-313, 1990.

2.5.2-348 Amick, D., R. Gelinas, G. Maurath, R. Cannon, D. Moore, E. Billington, and H. Kemppinen, “Paleoliquefaction Features along the Atlantic Seaboard,” NUREG/CR-5613 RA, U.S. Nuclear Regulatory Commission, Washington, D.C., 1990.

2.5.2-349 Amick, D., G. Maurath, and R. Gelinas, “Characteristics of Seismically Induced Liquefaction Sites and Features Located in the Vicinity of the 1886 Charleston, South Carolina

Earthquake," Seismological Research Letters, Vol. 61, No. 2, pp. 117-130, 1990.

2.5.2-350 Talwani, P., and W. Schaeffer, "Recurrence Rates of Large Earthquakes in the South Carolina Coastal Plain Based on Paleoliquefaction Data," Journal of Geophysical Research, Vol. 106, pp. 6621-6642, 2001.

2.5.2-351 Talwani, P., I. Dura-Gomez, S. Gassman, M. Hasek, and A. Chapman, "Studies Related to the Discovery of a Prehistoric Sandblow in the Epicentral Area of the 1886 Charleston SC Earthquake: Trenching and Geotechnical Investigations," *Program and Abstracts, Eastern Section of the Seismological Society of America,* p. 50*,* 2008.

2.5.2-352 Seeber, L., and J.G. Armbruster, "Natural and Induced Seismicity in the Lake Erie – Lake Ontario Region: Reactivation of Ancient Faults with Little Neotectonic Displacement," Géographie Physique et Quaternaire, Vol. 47, No. 3, 1993.

2.5.2-353 Fay, M.P., "Two-sided Exact Tests and Matching Confidence Intervals for Discrete Data, " R Journal, Vol. 2, No. 1, pp. 53-58, 2010.

2.5.2-354 Kijko, A., "Estimation of the Maximum Earthquake magnitude, Mmax," Pure and Applied Geophysics, Vol. 161, pp. 1-27, 2004.

2.5.2-355 Silva, W., N. Gregor, and R. Darragh, "Development of Regional Hard Rock Attenuation Relations for Central and Eastern North America," unpublished report by Pacific Engineering and Analysis (1 November 2002), http://pacificengineering.org/rpts_page1.shtml, accessed 28 July 2008.

2.5.2-356 Silva, W., N. Gregor, and R. Darragh, "Development of Regional Hard Rock Attenuation Relations for Central and Eastern North America, Mid-Continent and Gulf Coast Areas," unpublished report by Pacific Engineering and Analysis (13 August 2003), http://pacificengineering.org/rpts_page1.shtml, accessed 28 July 2008.

2.5.2-357 Atkinson, G.M., and D.M. Boore, "Ground-Motion Relations for Eastern North America," Bulletin of the Seismological Society of America, Vol. 85, No. 1, pp. 17-30, 1995.

2.5.2-358 Atkinson, G.M., and D.M. Boore, “Earthquake ground-motion prediction equations for eastern North America,” Bulletin of the Seismological Society of America, Vol. 96, pp. 2181-2205, 2006.

2.5.2-359 Atkinson, G.M., and D.M. Boore, “Modifications to Existing Ground-Motion Prediction Equations in Light of New Data,” Bulletin of the Seismological Society of America, Vol. 101, No. 3, pp. 1121-1135, 2011.

2.5.2-360 Campbell, K.W., “Prediction of Strong Ground Motion Using the Hybrid Empirical Method and Its Use in the Development of Ground-Motion (Attenuation) Relations in Eastern North America,” Bulletin of the Seismological Society of America, Vol. 93, pp. 1012-1033, 2003.

2.5.2-361 Tavakoli, B., and S. Pezeshk, “Empirical-Stochastic Ground-Motion Prediction for Eastern North America,” Bulletin of the Seismological Society of America, Vol. 95, No. 6, pp. 2283–2296, 2005.

2.5.2-362 Pezeshk, S., A. Zandieh, and B. Tavakoli, “Hybrid Empirical Ground-Motion Prediction Equations for Eastern North America Using NGA Models and Updated Seismological Parameters,” Bulletin of the Seismological Society of America, Vol. 101, No. 4, pp. 1859-1870, 2011.

2.5.2-363 Abrahamson, N.A., G. Atkinson, D. Boore, Y. Bozorgnia, K. Campbell, B. Chiou, I.M. Idriss, W. Silva, and R. Youngs, “Comparisons of the NGA Ground-Motion Relations,” Earthquake Spectra, Vol. 24, No. 1, pp. 45-66, 2008.

2.5.2-364 Atkinson, G., “Ground-Motion Prediction Equations for Eastern North America from a Referenced Empirical Approach: Implications for Epistemic Uncertainty,” Bulletin of the Seismological Society of America, Vol. 98, No. 3, pp. 1304-1318, 2008.

2.5.2-365 Somerville, P., N. Collins, N. Abrahamson, R. Graves, and C. Saikia, “Ground Motion Attenuation Relations for the Central and Eastern United States, Final Report, June 30, 2001,” external research project funded by U.S. Geological Survey Award No. 99HQGR0098, 38 pp., 2001.

2.5.2-366 Atkinson, G. “Empirical Evaluation of Aleatory and Epistemic Uncertainty in Eastern Ground Motions,” Seismological Research Letters, Vol. 84, No. 1, pp. 130-138, 2013.

2.5.2-367 Progress Energy Florida, Inc., “Revised Supplement 4 to Response to NRC RAI Letter 108 – Implementation of Fukushima Near-Term Task Force recommendations,” Letter to U.S. Nuclear Regulatory Commission from Christopher M. Fallon, dated October 31, 2012, Serial: NPD-NRC-2012-036, ADAMS accession number ML12313A163, 2012

2.5.2-368 McGuire, R.K., W.J. Silva, and C.J. Costantino, “Technical Basis for Revision of Regulatory Guidance on Design Ground Motions: Hazard- and Risk-Consistent Ground Motion Spectra Guidelines,” NUREG/CR-6728, U.S. Nuclear Regulatory Commission, Washington D.C., 2001.

2.5.2-369 Baker, J.W., and C.A. Cornell, “Spectral Shape, Epsilon and Record Selection,” Earthquake Engineering & Structural Dynamics, Vol. 35, No. 9, pp. 1077-1095, 2006.

2.5.2-370 Baker, J.W., and C.A. Cornell, “Correlation of Response Spectral Values for Multicomponent Ground Motions,” Bulletin of the Seismological Society of America, Vol. 96, No. 1, pp. 215-227, 2006.

2.5.2-371 Baker, J.W., and N. Jayaram, “Correlation of Spectral Acceleration Values from NGA Ground Motion Models,” Earthquake Spectra, Vol. 24, No. 1, pp. 299-317, 2008.

2.5.2-372 Abrahamson, N.A., and W.J. Silva, “Summary of the Abrahamson & Silva NGA Ground Motion Relations,” Earthquake Spectra, Vol. 24, No. 1, pp. 67-97, 2008.

2.5.2-373 Boore, D.M., and G.M. Atkinson, “Ground Motion Prediction Equations for the Average Horizontal Component of PGA, PGV, and 5% Damped PSA at Spectral Periods between 0.01s and 10.0 s,” Earthquake Spectra, Vol. 24, No. 1, pp. 99-138, 2008.

2.5.2-374 Campbell, K.W., and Y. Bozorgnia, “NGA Ground Motion Relations for the Geometric Mean Horizontal Component of PGA, PGV, PGD, and 5% Damped Linear Elastic Response Spectra for Periods Ranging from 0.01 s to 10 s,” Earthquake Spectra, Vol. 24, No. 1, pp. 139-171, 2008.

2.5.2-375 Chiou, B.S.-J., and R.R. Youngs, “An NGA Model for the Average Horizontal Component of Peak Ground Motion and Response Spectra,” Earthquake Spectra, Vol. 24, No. 1, pp. 173-215, 2008.

2.5.2-376 Idriss, I.M., “An NGA Empirical Model for Estimating the Horizontal Spectral Values Generated by Shallow Crustal Earthquakes,” Earthquake Spectra, Vol. 24, No. 1, pp. 217-242, 2008.

2.5.2-377 GEOVision, Inc., *Final Report, Borehole And Surface Geophysics, Boreholes CB-C3, RB-C4, RB-C8, RB-C6, and TB-C5, Surface Arrays Near RW-C1, RB-C4, MW-393 and MW-381,* Report 7297-01, Rev 0, March 12, 2008.

2.5.2-378 Schnabel, P.B., J. Lysmer, and H.B. Seed, “SHAKE — A Computer Program for Earthquake Response Analysis of Horizontally Layered Sites,” Earthquake Research Center, EERC 72-12, 1972.

2.5.2-379 Anderson, J.G., and S.E. Hough, “A Model for the Shape of the Fourier Amplitude Spectrum of Acceleration at High Frequencies,” *Bulletin of the Seismological Society of America*, Vol. 74, pp. 1969-1993, 1984.

2.5.2-380 Silva, W.J., and R. Darragh, “Engineering Characterization of Earthquake Strong Ground Motion Recorded at Rock Sites,” Electric Power Research Institute, TR-102261, 1995.

2.5.2-381 Electric Power Research Institute, *“Assessment of a Performance-Based Approach for Determining the SSE Ground Motion for New Plant Sites,”* Vol. 2, Seismic Hazard Results at 28 Sites, Final Report 1012045, May 2005.

2.5.2-382 Silva, W.J., N. Abrahamson, G. Toro, and C. Costantino, *“Description and Validation of the Stochastic Ground Motion Model,”* report submitted to Brookhaven National Laboratory, 1996.

2.5.2-383 Silva, W.J., “Base Case and Recommended Limits of Modulus Reduction and Damping Relationships,” Data files EPRIRR1L.MAT, EPRIRR1U.MAT, EPRISR1.MAT, EPRISR1L.MAT, and EPRISR1U.MAT, transmitted March 18, 2007.

2.5.2-384 Lilhanand, K., and W.S. Tseng, “Development and Application of Realistic Earthquake Time Histories with Multiple-Damping Design Spectra,” Proceedings of Ninth World Conference on Earthquake Engineering, Tokyo, Japan, August 2–9, 1988, Vol. 2, pp. 819-824, 1988.

2.5.2-385 GE-Hitachi Nuclear Energy, ESBWR Design Control Document Tier 2, Chapter 2, 26A6642AB, Revision 9, December 2010.

2.5.2-386 Crone, A.J., and R.L. Wheeler, “Data for Quaternary Faults, Liquefaction Features, and Possible Tectonic Features in the Central and Eastern United States, East of the Rocky Mountain Front,” U.S. Geological Survey Open-File Report 00-0260, 342 pp., 2000.

2.5.2-387 Crone, A.J., M.N. Machette, L. Bradley, and S.A. Mahan, “Late Quaternary Surface Faulting on the Cheraw Fault, Southeastern Colorado,” U.S. Geological Survey Geologic Investigations Map I-2591, includes 7 pp. pamphlet, 1997.

2.5.2-388 Niemi, T.M., A.N. Ferris, and G.A. Abers, “Investigation of Microearthquakes, Macroseismic Data, and Liquefaction Associated with the 1867 Wamego Earthquake in Eastern Kansas,”Bulletin of the Seismological Society of America, Vol. 94, No. 6, pp. 2317-2329, 2004.

2.5.2-389 Steltenpohl, M.G., I. Zietz, J.W. Horton, Jr., and D.L. Daniels, “New York–Alabama Lineament: A Buried Right-Slip Fault Bordering the Appalachians and Mid-continent North America,” Geology, Vol. 38, No. 6, pp. 571-574, 2010.

2.5.2-390 Aleinikoff, J.N., R.E. Zartman, M. Walter, D.W. Rankin, P.T. Lyttle, and W.C. Burton, “U-Pb Ages of Metarhyolites of the Catoctin and Mount Rogers Formations, Central and Southern Appalachians: Evidence for Two Pulses of Iapetan Rifting,” American Journal of Science, Vol. 295, pp. 428-454, 1995.

2.5.2-391 Hodych, J.P., and R.A. Cox, “ Ediacaran U-Pb Zircon Dates for the Lac Matapédia and Mt. St.-Anselme Basalts of the Quebec Appalachians: Support for a Long-Lived Mantle Plume During the Rifting Phase of Iapetus Opening,” Canadian Journal of Earth Sciences, Vol. 44, pp. 565-581, 2007.

2.5.2-392 Valentino, D.W., and A.E. Gates, “Iapetan Rift-Related Turbidite-Fan Deposits from the Central Appalachian Piedmont,” American Journal of Science, Vol. 295, pp. 78-97, 1995.

2.5.2-393 Law, R.D., M.C. Pope, R.H. Wirgart, K.A. Eriksson, E.S. Robinson, S. Sayer, E.J. Phinney, and G.A. Bollinger, “Geologically Recent Near-Surface Faulting and Folding in Giles County, Southwest Virginia: New Exposures of Extensional and Apparent Reverse Faults in Alluvial Sediments Between Pembroke and Pearisburg,” Proceedings of the U.S. Nuclear Regulatory Commission for 1994, Twenty-First Water Reactor Safety Information Meeting, October 25-27, 1993, Bethesda, Maryland, NUREG/CP-0133, Vol. 3, pp. 415-432, 1994.

2.5.2-394 Ouassaa, K., and D.A. Forsyth, “Interpretation of Seismic and Potential Field Data from Western New York State and Lake Ontario,” Tectonophysics, Vol. 353, pp. 115-149, 2002.

2.5.2-395 Odum, J.K., W.J. Stephenson, and R.A. Williams, Multi-source, High-Resolution Seismic-Reflection Imaging of Meeman-Shelby Fault and a Possible Tectonic Model for a Joiner Ridge–Manila High Stepover Structure in the Upper Mississippi Embayment Region,” Seismological Research Letters, Vol. 81, No. 4, pp. 647-663, 2010.

2.5.2-396 Wheeler, R.L., S. Rhea, and R.L. Dart, Map Showing Structure of the Mississippi Valley Graben in the Vicinity of New Madrid, Missouri, U.S. Geological Survey Miscellaneous Field Studies Map MF-2264-D, 1994.

2.5.2-397 King, P.B., and H.M. Beikman (compilers), Geologic Map of the United States, U.S. Geological Survey, 3 sheets, scale 1:2,500,000, 1974.

2.5.2-398 Reed, J.C., J.O. Wheeler, and B.E. Tucholke, Decade of North American Geology, Geologic Map of North America, 1:5,000,000 continent-scale map 001, Geological Society of America, Inc., Boulder, Colo., 2005.

Table 2.5.2-201 Results of Significance Tests of Predicted Seismicity Rates Within 320 km (200 mi) of the Fermi 3 Site [EF3 COL 2.0-27-A]

Earthquake Recurrence Rates Derived from CEUS SSC Model			
Magnitude	Distribution Level	Rate of Occurence (earthquakes per year)	P-Value
E[**M**] ≥ 2.9	5^{TH}%	0.813	83.5%
	MEAN	1.27	96.2%
	95^{TH}%	2.14	99.8%
E[**M**] ≥ 3.6	5^{TH}%	0.182	16.6%
	MEAN	0.282	31.1%
	95^{TH}%	0.479	57.1%

Table 2.5.2-202 Post-CEUS Earthquakes Used In Assessing Mmax Distributions [EF3 COL 2.0-27-A]

Year	Month	Day	Hour	Minute	Second	Latitude (degrees)	Longitude (degrees)	Depth (km)	E[M]	Sigma E[M]	Source Zone Location
2010	6	23	17	41	41	45.880	-75.480	22	5.11	0.07	GMH, MESE-N
2010	10	13	14	6	30	35.192	-97.320	13	4.38	0.03	MIDC(A, B, C, D) NMESE-W
2011	2	28	5	0	50.2	35.265	-92.344	3	4.74	0.11	MIDC(A, B, C, D) NMESE-W
2011	8	22	23	30	19.87	37.032	-104.554	5	4.81	0.11	MIDC(A, B, C, D) NMESE-W
2011	8	23	5	46	18.25	37.063	-104.701	4	5.31	0.06	MIDC(A, B, C, D) NMESE-W
2011	8	23	17	51	4.59	37.936	-77.933	6	5.73	0.06	ECC-AM, MESE-N
2011	9	11	12	27	44.32	32.848	-100.769	5	4.42	0.08	MIDC(A, B, C, D) NMESE-W
2011	10	20	12	24	41.6	28.865	-98.079	5	4.72	0.10	ECC-GC, MESE-N
2011	11	5	7	12	45	35.550	-96.764	3	4.79	0.21	MIDC(A, B, C, D) NMESE-W
2011	11	6	3	53	10	35.532	-96.765	5	5.66	0.06	MIDC(A, B, C, D) NMESE-W
2011	11	8	2	46	57	35.531	-96.788	5	4.89	0.13	MIDC(A, B, C, D) NMESE-W
2012	5	17	8	12	0.99	31.926	-94.369	5	4.88	0.03	ECC-GC, MESE-N

Table 2.5.2-203 Maximum Magnitude Distributions for Select CEUS SSC Distributed Seismicity Source Zones [EF3 COL 2.0-27-A]

CEUS SSC Source Zone	NUREG-2115 Mmax Distribution (**M**, [weight])	Adjusted Mmax Distribution[a] (**M**, [weight])	Mmax Sensitivity Distribution (**M**, [weight])
MESE-N	6.4 [0.101]	6.4 [0.101]	Unchanged from NUREG-2115
	6.8 [0.244]	6.8 [0.244]	
	7.2 [0.310]	7.2 [0.310]	
	7.7 [0.244]	7.7 [0.244]	
	8.1 [0.101]	8.1 [0.101]	
NMESE-W	5.7 [0.101]	5.7 [0.101]	5.8 [0.101]
	6.1 [0.244]	6.1 [0.244]	6.1 [0.244]
	6.6 [0.310]	6.6 [0.310]	6.6 [0.310]
	7.2 [0.244]	7.2 [0.244]	7.2 [0.244]
	7.9 [0.101]	7.9 [0.101]	7.9 [0.101]
ECC-AM	6.0 [0.101]	6.1 [0.101]	6.1 [0.101]
	6.7 [0.244]	6.7 [0.244]	6.7 [0.244]
	7.2 [0.310]	7.2 [0.310]	7.2 [0.310]
	7.7 [0.244]	7.7 [0.310]	7.7 [0.244]
	8.1 [0.101]	8.1 [0.101]	8.1 [0.101]
GMH	6.0 [0.101]	6.0 [0.101]	Unchanged from NUREG-2115
	6.7 [0.244]	6.7 [0.244]	
	7.2 [0.310]	7.2 [0.310]	
	7.7 [0.244]	7.7 [0.244]	
	8.1 [0.101]	8.1 [0.101]	
MIDC	5.6 [0.101]	5.7 [0.101]	5.7 [0.101]
(A, B, C, & D)	6.1 [0.244]	6.0 [0.244]	6.1 [0.244]
	6.6 [0.310]	6.5 [0.310]	6.6 [0.310]
	7.2 [0.244]	7.2 [0.244]	7.2 [0.244]
	8.0 [0.101]	7.9 [0.101]	8.0 [0.101]

a.Adjusted to include post-CEUS earthquakes for the time period 2009 through 2012

Table 2.5.2-204 Generic CEUS Hard Rock Hazard Results for 0.5 Hz Spectral Acceleration for the Fermi 3 Site [EF3 COL 2.0-27-A]

0.5 Hz Spectral Acceleration (g)	Annual Exceedance Frequency					
	Mean	5th%	16th%	50th%	84th%	95th%
1.00E-05	1.79E-01	1.35E-01	1.55E-01	1.78E-01	1.95E-01	2.04E-01
1.00E-04	1.04E-01	4.47E-02	6.46E-02	8.91E-02	1.48E-01	1.66E-01
1.00E-03	1.70E-02	5.25E-03	7.76E-03	1.41E-02	2.82E-02	3.89E-02
2.00E-03	8.27E-03	1.91E-03	3.16E-03	6.76E-03	1.45E-02	2.14E-02
5.00E-03	2.93E-03	3.16E-04	6.46E-04	2.00E-03	5.50E-03	9.12E-03
1.00E-02	1.18E-03	5.75E-05	1.29E-04	5.50E-04	2.34E-03	4.68E-03
2.00E-02	4.08E-04	8.13E-06	1.95E-05	1.00E-04	6.46E-04	2.09E-03
3.00E-02	2.03E-04	2.51E-06	6.03E-06	3.47E-05	2.40E-04	1.02E-03
5.00E-02	7.96E-05	5.13E-07	1.32E-06	9.12E-06	6.03E-05	2.88E-04
1.00E-01	1.88E-05	4.68E-08	1.59E-07	1.48E-06	1.02E-05	3.31E-05
3.00E-01	7.86E-07	1.41E-09	3.89E-09	6.31E-08	6.17E-07	1.74E-06
1.00E+00	1.31E-08	0.00E+00	6.03E-10	1.74E-09	2.19E-08	7.76E-08

Table 2.5.2-205 Generic CEUS Hard Rock Hazard Results for 1 Hz Spectral Acceleration for the Fermi 3 Site [EF3 COL 2.0-27-A]

1 Hz Spectral Acceleration (g)	Annual Exceedance Frequency					
	Mean	5th%	16th%	50th%	84th%	95th%
1.00E-04	1.43E-01	7.76E-02	1.02E-01	1.38E-01	1.74E-01	1.91E-01
1.00E-03	3.40E-02	1.15E-02	1.74E-02	2.63E-02	5.75E-02	6.92E-02
3.00E-03	1.08E-02	3.02E-03	4.90E-03	8.71E-03	1.91E-02	2.69E-02
1.00E-02	2.40E-03	3.47E-04	6.61E-04	1.70E-03	4.47E-03	7.59E-03
2.00E-02	8.26E-04	7.41E-05	1.48E-04	4.37E-04	1.48E-03	3.31E-03
3.00E-02	4.01E-04	2.82E-05	5.62E-05	1.70E-04	6.31E-04	1.78E-03
5.00E-02	1.46E-04	7.59E-06	1.59E-05	5.01E-05	1.82E-04	6.31E-04
1.00E-01	3.07E-05	1.20E-06	2.63E-06	9.33E-06	3.16E-05	9.12E-05
2.00E-01	4.93E-06	1.41E-07	3.89E-07	1.74E-06	6.17E-06	1.29E-05
3.00E-01	1.59E-06	3.39E-08	1.18E-07	6.31E-07	2.40E-06	5.01E-06
5.00E-01	3.88E-07	5.37E-09	2.09E-08	1.59E-07	7.24E-07	1.55E-06
1.00E+00	5.70E-08	1.23E-09	2.24E-09	1.78E-08	1.12E-07	2.57E-07

Table 2.5.2-206 Generic CEUS Hard Rock Hazard Results for 2.5 Hz Spectral Acceleration for the Fermi 3 Site [EF3 COL 2.0-27-A]

2.5 Hz Spectral Acceleration (g)	Annual Exceedance Frequency					
	Mean	5th%	16th%	50th%	84th%	95th%
1.00E-04	1.75E-01	1.32E-01	1.48E-01	1.74E-01	1.91E-01	2.00E-01
1.00E-03	6.86E-02	2.95E-02	3.80E-02	5.75E-02	1.05E-01	1.23E-01
3.00E-03	2.51E-02	1.02E-02	1.38E-02	2.14E-02	4.17E-02	5.37E-02
1.00E-02	6.11E-03	1.82E-03	2.82E-03	5.37E-03	1.12E-02	1.66E-02
2.00E-02	2.25E-03	5.25E-04	8.32E-04	1.70E-03	4.17E-03	7.08E-03
5.00E-02	4.44E-04	8.51E-05	1.35E-04	2.75E-04	6.92E-04	1.51E-03
1.00E-01	1.10E-04	2.00E-05	3.24E-05	6.76E-05	1.51E-04	3.02E-04
2.00E-01	2.46E-05	4.68E-06	7.94E-06	1.70E-05	3.47E-05	6.03E-05
3.00E-01	1.01E-05	1.86E-06	3.31E-06	7.41E-06	1.55E-05	2.57E-05
5.00E-01	3.21E-06	5.01E-07	9.77E-07	2.40E-06	5.25E-06	8.71E-06
1.00E+00	6.09E-07	5.75E-08	1.38E-07	4.27E-07	1.07E-06	1.82E-06
3.00E+00	2.42E-08	1.51E-09	3.02E-09	1.23E-08	4.68E-08	9.33E-08

Table 2.5.2-207 Generic CEUS Hard Rock Hazard Results for 5 Hz Spectral Acceleration for the Fermi 3 Site [EF3 COL 2.0-27-A]

5 Hz Spectral Acceleration (g)	Annual Exceedance Frequency					
	Mean	5th%	16th%	50th%	84th%	95th%
1.00E-03	8.21E-02	4.17E-02	5.13E-02	7.08E-02	1.18E-01	1.41E-01
3.00E-03	3.27E-02	1.51E-02	1.91E-02	2.75E-02	5.01E-02	6.76E-02
1.00E-02	9.02E-03	3.39E-03	4.90E-03	8.71E-03	1.59E-02	2.34E-02
2.00E-02	3.67E-03	1.12E-03	1.62E-03	3.16E-03	6.92E-03	1.12E-02
3.00E-02	2.00E-03	5.50E-04	8.13E-04	1.59E-03	3.55E-03	6.17E-03
5.00E-02	8.60E-04	2.19E-04	3.31E-04	6.31E-04	1.38E-03	2.51E-03
1.00E-01	2.49E-04	6.31E-05	9.55E-05	1.78E-04	3.55E-04	6.31E-04
2.00E-01	6.79E-05	1.74E-05	2.82E-05	5.25E-05	9.55E-05	1.62E-04
3.00E-01	3.16E-05	8.13E-06	1.32E-05	2.57E-05	4.68E-05	7.41E-05
5.00E-01	1.20E-05	2.88E-06	4.90E-06	9.77E-06	1.86E-05	2.82E-05
1.00E+00	2.85E-06	5.50E-07	1.02E-06	2.29E-06	4.57E-06	7.08E-06
3.00E+00	1.64E-07	1.51E-08	3.55E-08	1.10E-07	2.82E-07	5.01E-07

Table 2.5.2-208 Generic CEUS Hard Rock Hazard Results for 10 Hz Spectral Acceleration for the Fermi 3 Site [EF3 COL 2.0-27-A]

10 Hz Spectral Acceleration (g)	Annual Exceedance Frequency					
	Mean	5th%	16th%	50th%	84th%	95th%
1.00E-03	7.53E-02	3.47E-02	4.57E-02	6.46E-02	1.07E-01	1.32E-01
3.00E-03	3.15E-02	1.48E-02	1.86E-02	2.63E-02	4.47E-02	6.31E-02
1.00E-02	9.85E-03	3.98E-03	5.50E-03	9.55E-03	1.62E-02	2.57E-02
2.00E-02	4.46E-03	1.51E-03	2.09E-03	3.72E-03	7.76E-03	1.41E-02
5.00E-02	1.25E-03	3.63E-04	5.25E-04	9.33E-04	1.86E-03	3.55E-03
1.00E-01	4.08E-04	1.15E-04	1.70E-04	3.02E-04	5.62E-04	1.07E-03
2.00E-01	1.23E-04	3.55E-05	5.37E-05	9.77E-05	1.74E-04	2.95E-04
3.00E-01	6.08E-05	1.74E-05	2.75E-05	5.01E-05	8.91E-05	1.41E-04
5.00E-01	2.53E-05	6.61E-06	1.12E-05	2.14E-05	3.89E-05	5.75E-05
1.00E+00	7.20E-06	1.55E-06	2.82E-06	5.89E-06	1.15E-05	1.74E-05
2.00E+00	1.63E-06	2.46E-07	5.01E-07	1.26E-06	2.69E-06	4.37E-06
5.00E+00	1.29E-07	9.55E-09	2.46E-08	8.13E-08	2.24E-07	4.27E-07

Table 2.5.2-209 Generic CEUS Hard Rock Hazard Results for 25 Hz Spectral Acceleration for the Fermi 3 Site [EF3 COL 2.0-27-A]

25 Hz Spectral Acceleration (g)	Annual Exceedance Frequency					
	Mean	5th%	16th%	50th%	84th%	95th%
1.00E-03	5.96E-02	1.86E-02	2.69E-02	5.50E-02	9.12E-02	1.18E-01
3.00E-03	2.67E-02	9.33E-03	1.35E-02	2.19E-02	3.80E-02	5.37E-02
1.00E-02	9.70E-03	3.09E-03	4.17E-03	7.24E-03	1.59E-02	2.69E-02
3.00E-02	3.13E-03	7.94E-04	1.12E-03	2.00E-03	4.79E-03	1.05E-02
1.00E-01	6.61E-04	1.32E-04	1.95E-04	3.72E-04	8.71E-04	1.95E-03
2.00E-01	2.26E-04	4.47E-05	6.92E-05	1.35E-04	2.88E-04	6.61E-04
3.00E-01	1.15E-04	2.29E-05	3.72E-05	7.41E-05	1.51E-04	3.31E-04
5.00E-01	4.86E-05	9.55E-06	1.62E-05	3.39E-05	6.92E-05	1.35E-04
1.00E+00	1.50E-05	2.46E-06	4.57E-06	1.10E-05	2.40E-05	4.17E-05
2.00E+00	4.25E-06	4.68E-07	9.55E-07	2.75E-06	7.41E-06	1.32E-05
5.00E+00	5.72E-07	2.40E-08	6.03E-08	2.51E-07	9.33E-07	2.34E-06
7.00E+00	2.37E-07	7.59E-09	1.74E-08	8.32E-08	3.55E-07	1.10E-06

Table 2.5.2-210 Generic CEUS Hard Rock Hazard Results for (100 Hz Spectral Acceleration) for the Fermi 3 Site [EF3 COL 2.0-27-A]

Peak Ground Acceleration (g)	Annual Exceedance Frequency					
	Mean	5th%	16th%	50th%	84th%	95th%
1.00E-03	4.47E-02	1.86E-02	2.34E-02	3.31E-02	8.13E-02	1.07E-01
3.00E-03	1.68E-02	6.76E-03	9.33E-03	1.45E-02	2.88E-02	4.37E-02
1.00E-02	4.50E-03	1.29E-03	1.82E-03	3.16E-03	8.91E-03	1.62E-02
2.00E-02	1.75E-03	4.37E-04	6.31E-04	1.12E-03	3.02E-03	6.31E-03
3.00E-02	9.45E-04	2.24E-04	3.24E-04	5.89E-04	1.48E-03	3.09E-03
5.00E-02	4.12E-04	9.77E-05	1.45E-04	2.63E-04	5.75E-04	1.23E-03
1.00E-01	1.26E-04	3.16E-05	5.01E-05	9.33E-05	1.78E-04	3.31E-04
2.00E-01	4.01E-05	9.77E-06	1.66E-05	3.24E-05	6.17E-05	9.55E-05
3.00E-01	2.08E-05	4.57E-06	8.13E-06	1.66E-05	3.31E-05	5.01E-05
5.00E-01	8.73E-06	1.51E-06	2.88E-06	6.76E-06	1.45E-05	2.29E-05
1.00E+00	2.22E-06	2.29E-07	4.79E-07	1.45E-06	3.89E-06	6.92E-06
3.00E+00	1.12E-07	3.63E-09	8.71E-09	4.47E-08	1.74E-07	5.13E-07

Table 2.5.2-211 Uniform Hazard Response Spectra for the Fermi 3 Site for Generic Hard Rock Conditions [EF3 COL 2.0-27-A]

Period (sec)	Frequency (Hz)	Spectral Acceleration (g) for Annual Exceedance Frequency of:			
		Mean 10^{-3}	Mean 10^{-4}	Mean 10^{-5}	Mean 10^{-6}
0.01	100	0.0289	0.1151	0.4616	1.3409
0.04	25	0.0725	0.3260	1.2492	3.8724
0.1	10	0.0577	0.2252	0.8410	2.4356
0.2	5	0.0458	0.1629	0.5478	1.5523
0.4	2.5	0.0323	0.1047	0.3008	0.8203
1	1	0.0178	0.0598	0.1544	0.3542
2	0.5	0.0111	0.0441	0.1244	0.2760

Table 2.5.2-212 Rock Hazard Reference and Deaggregation Earthquakes
[EF3 COL 2.0-27-A]

Hazard Level	Reference (Controlling) Earthquake CEUS SSC Model		Deaggregation Earthquakes CEUS SSC Mode		
	Magnitude (M)	Distance (km)	Magnitude (M)	Distance (km)	Weight
Mean 10^{-3} 5 and 10 Hz	6.1	143	5.5	84	0.588
			6.5	152	0.197
			7.4	580	0.215
Mean 10^{-3} 1 and 2.5Hz	6.8	290	5.5	72	0.231
			6.5	161	0.165
	7.1[a]	439*	7.4	588	0.604
Mean 10^{-4} 5 and 10 Hz	6.0	48	5.5	25.8	0.616
			6.5	76	0.291
			7.6	585	0.093
Mean 10^{-4} 1 and 2.5Hz	6.8	165	5.5	22.5	0.240
	7.4*	457*	6.6	84	0.250
			7.6	585	0.510
Mean 10^{-5} 5 and 10 Hz	5.9	15.1	5.5	10.8	0.657
			6.4	22.4	0.286
			7.4	73	0.057
Mean 10^{-5} 1 and 2.5Hz	6.7	63	5.5	11.5	0.295
	7.6*	468*	6.7	37	0.395
			7.7	594	0.310
Mean 10^{-6} 5 and 10 Hz	6.0	10.9	5.5	8.3	0.531
			6.4	12.5	0.385
			7.4	26	0.084
Mean 10^{-6} 1 and 2.5Hz	6.6	24.5	5.6	8.7	0.238
	7.7*	445*	6.7	20.1	0.649
			7.7	595	0.113

a.computed using earthquakes with distances > 100 km

Table 2.5.2-213 Site Response Analysis Profile [EF3 COL 2.0-27-A]

GMRS Profile, Top of Profile Elevation 551.7 ft (NAVD 88)

Layer Number	Thickness (ft.)	Geometric Mean Shear Wave Velocity (fps)	Unit Weight (kips/ft.^{3})	Material Curves	Soil/Rock Type
1	9.7	6650	0.150	Linear, κ layer 1	Bass Islands
2	10	6650	0.150	Linear, κ layer 1	Bass Islands
3	10	6650	0.150	Linear, κ layer 1	Bass Islands
4	10	6650	0.150	Linear, κ layer 1	Bass Islands
5	11	6650	0.150	Linear, κ layer 1	Bass Islands
6	12	6650	0.150	Linear, κ layer 1	Bass Islands
7	12	6650	0.150	Linear, κ layer 1	Bass Islands
8	15	4600	0.150	Linear, κ layer 2	Bass Islands
9	20	3350	0.150	Linear, κ layer 3	Salina F
10	20	3350	0.150	Linear, κ layer 3	Salina F
11	20	3350	0.150	Linear, κ layer 3	Salina F
12	21	3350	0.150	Linear, κ layer 3	Salina F
13	21	4050	0.150	Linear, κ layer 4	Salina F
14	21	4050	0.150	Linear, κ layer 4	Salina F
15	10	5600	0.150	Linear, κ layer 5	Salina E
16	20	9450	0.150	Linear, κ layer 6	Salina E
17	21	9450	0.150	Linear, κ layer 6	Salina E
18	21	9450	0.150	Linear, κ layer 6	Salina E
19	21	9450	0.150	Linear, κ layer 6	Salina E
20	45	9000	0.160	Linear, κ layer 7	Salina C
21	45	9000	0.160	Linear, κ layer 7	Salina C
Halfspace		9300	0.169	0.1% Damping	Salina B

Table 2.5.2-214 Rock Damping Values for Site Response Analyses

[EF3 COL 2.0-27-A]

Layer	Thickness (ft.)	V_s (fps)	1% Damping		2% Damping		3% Damping	
			Damping Ratio (%)	κ (sec)	Damping Ratio (%)	κ (sec)	Damping Ratio (%)	κ (sec)
Bass Islands 1	75	6650	0.52%	0.0001	1.03%	0.0002	1.55%	0.0003
Bass Islands 2	15	4600	0.75%	0.0000	1.49%	0.0001	2.24%	0.0001
Salina F 1	81	3350	1.03%	0.0005	2.05%	0.0010	3.08%	0.0015
Salina F 2	42	4050	0.85%	0.0002	1.70%	0.0004	2.55%	0.0005
Salina E 1	10	5600	0.61%	0.0000	1.23%	0.0000	1.84%	0.0001
Salina E 2	83	9450	0.36%	0.0001	0.73%	0.0001	1.09%	0.0002
Salina C	90	9000	0.38%	0.0001	0.76%	0.0002	1.15%	0.0002
				Total 0.001		Total 0.002		Total 0.003

Table 2.5.2-215 Time History Data Sets Used for Each Deaggregation Earthquake

[EF3 COL 2.0-27-A]

Hazard Level	Deaggregation Earthquakes (DE)				
	Designation	Magnitude (M)	Distance (km)	Weight	NRUEG/CR-6728 CEUS Data Set
Mean 10^{-3} 5 and 10 Hz	HF DEL	5.5	84	0.588	**M** 4.5–6, D 50–100 km
	HF DEM	6.5	152	0.197	**M** 6–7, D 100–200 km
	HF DEH	7.4	580	0.215	**M** >7, D 100–200 km
Mean 10^{-3} 1 and 2.5 Hz	LF DEL	5.5	72	0.231	**M** 4.5–6, D 0-50 km
	LF DEM	6.5	161	0.165	**M** 6–7, D 100–200 km
	LF DEH	7.4	588	0.604	**M** >7, D 100-200 km
Mean 10^{-4} 5 and 10 Hz	HF DEL	5.5	25.8	0.616	**M** 4.5–6, D 0–50 km
	HF DEM	6.5	76	0.291	**M** 6–7, D 50–100 km
	HF DEH	7.6	585	0.093	**M** >7, D 100–200 km
Mean 10^{-4} 1 and 2.5 Hz	LF DEL	5.5	22.5	0.240	**M** 4.5–6, D 0–50 km
	LF DEM	6.6	84	0.250	**M** 6–7, D 50-100 km
	LF DEH	7.6	585	0.510	**M** >7, D 100–200 km
Mean 10^{-5} 5 and 10 Hz	HF DEL	5.5	10.8	0.657	**M** 4.5–6, D 0–50 km
	HF DEM	6.4	22.4	0.286	**M** 6–7, D 10–50 km
	HF DEH	7.4	73	0.057	**M** >7, D 50–100 km
Mean 10^{-5} 1 and 2.5 Hz	LF DEL	5.5	11.5	0.295	**M** 4.5–6, D 0–50 km
	LF DEM	6.7	37	0.395	**M** 6–7, D 10–50 km
	LF DEH	7.7	594	0.310	**M** >7, D 100-200 km
Mean 10^{-6} 5 and 10 Hz	HF DEL	5.5	8.3	0.531	**M** 4.5–6, D 0–50 km
	HF DEM	6.4	12.5	0.385	**M** 6–7, D 10–50 km
	HF DEH	7.4	26	0.084	**M** >7, D 10–50 km
Mean 10^{-6} 1 and 2.5 Hz	LF DEL	5.6	8.7	0.238	**M** 4.5–6, D 0–50 km
	LF DEM	6.7	20	0.649	**M** 6–7, D 10–50 km
	LF DEH	7.7	595	0.113	**M** >7, D 100–200 km

Table 2.5.2-216 GMRS for the Fermi 3 Site (Sheet 1 of 3) [EF3 COL 2.0-27-A]

Spectral Frequency (Hz)	5% Damped Spectral Acceleration (g)				
	10^{-4} UHRS	10^{-5} UHRS	Horizontal GMRS	Vertical/Horizontal	Vertical GMRS
100.000	0.1250	0.4775	0.2191	1.0000	0.2191
60.241	0.2310	0.8757	0.4025	1.1374	0.4578
50.000	0.2737	1.0407	0.4780	1.1244	0.5375
40.000	0.3054	1.1649	0.5347	1.0426	0.5575
33.333	0.3188	1.2188	0.5592	0.9675	0.5411
30.303	0.3212	1.2238	0.5619	0.9400	0.5282
25.000	0.3259	1.2340	0.5673	0.8800	0.4992
23.810	0.3215	1.2168	0.5595	0.8681	0.4857
22.727	0.3173	1.2007	0.5521	0.8569	0.4731
21.739	0.3134	1.1855	0.5451	0.8461	0.4613
20.833	0.3097	1.1712	0.5386	0.8355	0.4500
20.000	0.3062	1.1575	0.5323	0.8255	0.4394
18.182	0.3056	1.1140	0.5161	0.8069	0.4164
16.667	0.3051	1.0757	0.5016	0.7984	0.4005
15.385	0.3047	1.0320	0.4851	0.7906	0.3835
14.286	0.3043	0.9931	0.4703	0.7834	0.3685
13.333	0.3039	0.9915	0.4696	0.7769	0.3648
12.500	0.3035	0.9900	0.4689	0.7708	0.3614
11.765	0.3031	0.9885	0.4683	0.7651	0.3582
11.111	0.3028	0.9872	0.4676	0.7597	0.3553
10.526	0.3025	0.9860	0.4671	0.7547	0.3525
10.000	0.3022	0.9848	0.4665	0.7500	0.3499
9.091	0.3017	0.9826	0.4655	0.7500	0.3491
8.333	0.3012	0.9805	0.4646	0.7500	0.3485
7.692	0.3007	0.9787	0.4638	0.7500	0.3478
7.143	0.3003	0.9770	0.4630	0.7500	0.3472
6.667	0.2999	0.9754	0.4623	0.7500	0.3467
6.250	0.2995	0.9739	0.4616	0.7500	0.3462
5.882	0.2992	0.9725	0.4610	0.7500	0.3457
5.556	0.2989	0.9712	0.4604	0.7500	0.3453
5.263	0.2986	0.9700	0.4598	0.7500	0.3448
5.000	0.2983	0.9688	0.4593	0.7500	0.3444
4.545	0.2978	0.9666	0.4583	0.7500	0.3437
4.167	0.2973	0.9494	0.4516	0.7500	0.3387
3.846	0.2862	0.9090	0.4328	0.7500	0.3246
3.571	0.2719	0.8488	0.4056	0.7500	0.3042
3.333	0.2517	0.7724	0.3704	0.7500	0.2778

Table 2.5.2-216 GMRS for the Fermi 3 Site (Sheet 2 of 3) [EF3 COL 2.0-27-A]

Spectral Frequency (Hz)	5% Damped Spectral Acceleration (g)				
	10^{-4} UHRS	10^{-5} UHRS	Horizontal GMRS	Vertical/Horizontal	Vertical GMRS
3.125	0.2339	0.7055	0.3394	0.7500	0.2546
2.941	0.2141	0.6366	0.3072	0.7500	0.2304
2.778	0.1968	0.5769	0.2792	0.7500	0.2094
2.632	0.1803	0.5302	0.2564	0.7500	0.1923
2.500	0.1682	0.4827	0.2346	0.7500	0.1759
2.381	0.1587	0.4474	0.2182	0.7500	0.1636
2.273	0.1505	0.4188	0.2048	0.7500	0.1536
2.174	0.1421	0.3923	0.1921	0.7500	0.1441
2.083	0.1351	0.3686	0.1809	0.7500	0.1357
2.000	0.1286	0.3484	0.1713	0.7500	0.1285
1.818	0.1165	0.3164	0.1554	0.7500	0.1166
1.667	0.1057	0.2903	0.1423	0.7500	0.1068
1.538	0.0979	0.2687	0.1317	0.7500	0.0988
1.429	0.0914	0.2511	0.1231	0.7500	0.0923
1.333	0.0852	0.2351	0.1151	0.7500	0.0864
1.250	0.0798	0.2213	0.1083	0.7500	0.0812
1.176	0.0754	0.2110	0.1031	0.7500	0.0773
1.111	0.0715	0.2013	0.0982	0.7500	0.0736
1.053	0.0681	0.1909	0.0932	0.7500	0.0699
1.000	0.0652	0.1828	0.0892	0.7500	0.0669
0.909	0.0621	0.1714	0.0839	0.7500	0.0630
0.833	0.0594	0.1610	0.0791	0.7500	0.0594
0.769	0.0571	0.1517	0.0749	0.7500	0.0561
0.714	0.0547	0.1467	0.0723	0.7500	0.0542
0.667	0.0528	0.1434	0.0705	0.7500	0.0529
0.625	0.0510	0.1401	0.0687	0.7500	0.0515
0.588	0.0495	0.1368	0.0670	0.7500	0.0502
0.556	0.0481	0.1342	0.0656	0.7500	0.0492
0.526	0.0469	0.1317	0.0643	0.7500	0.0482
0.500	0.0457	0.1292	0.0630	0.7500	0.0472
0.455	0.0424	0.1213	0.0590	0.7500	0.0442
0.417	0.0394	0.1140	0.0553	0.7500	0.0415
0.385	0.0371	0.1085	0.0525	0.7500	0.0394
0.357	0.0349	0.1034	0.0499	0.7500	0.0374
0.333	0.0333	0.0987	0.0476	0.7500	0.0357
0.313	0.0316	0.0944	0.0455	0.7500	0.0341
0.294	0.0301	0.0906	0.0436	0.7500	0.0327

Table 2.5.2-216 GMRS for the Fermi 3 Site (Sheet 3 of 3) [EF3 COL 2.0-27-A]

Spectral Frequency (Hz)	5% Damped Spectral Acceleration (g)				
	10^{-4} UHRS	10^{-5} UHRS	Horizontal GMRS	Vertical/Horizontal	Vertical GMRS
0.278	0.0288	0.0872	0.0419	0.7500	0.0314
0.263	0.0276	0.0840	0.0404	0.7500	0.0303
0.250	0.0265	0.0812	0.0390	0.7500	0.0292
0.238	0.0256	0.0785	0.0376	0.7500	0.0282
0.227	0.0247	0.0761	0.0364	0.7500	0.0273
0.217	0.0238	0.0738	0.0353	0.7500	0.0265
0.208	0.0231	0.0717	0.0343	0.7500	0.0257
0.200	0.0223	0.0698	0.0333	0.7500	0.0250
0.182	0.0202	0.0638	0.0304	0.7500	0.0228
0.167	0.0185	0.0588	0.0280	0.7500	0.0210
0.154	0.0170	0.0546	0.0259	0.7500	0.0195
0.143	0.0158	0.0509	0.0242	0.7500	0.0181
0.133	0.0147	0.0477	0.0226	0.7500	0.0170
0.125	0.0136	0.0445	0.0211	0.7500	0.0158
0.118	0.0127	0.0416	0.0197	0.7500	0.0148
0.111	0.0118	0.0391	0.0185	0.7500	0.0139
0.100	0.0104	0.0349	0.0165	0.7500	0.0123

Figure 2.5.2-201 Earthquake Catalog for the CEUS SSC Model [EF3 COL 2.0-27-A]

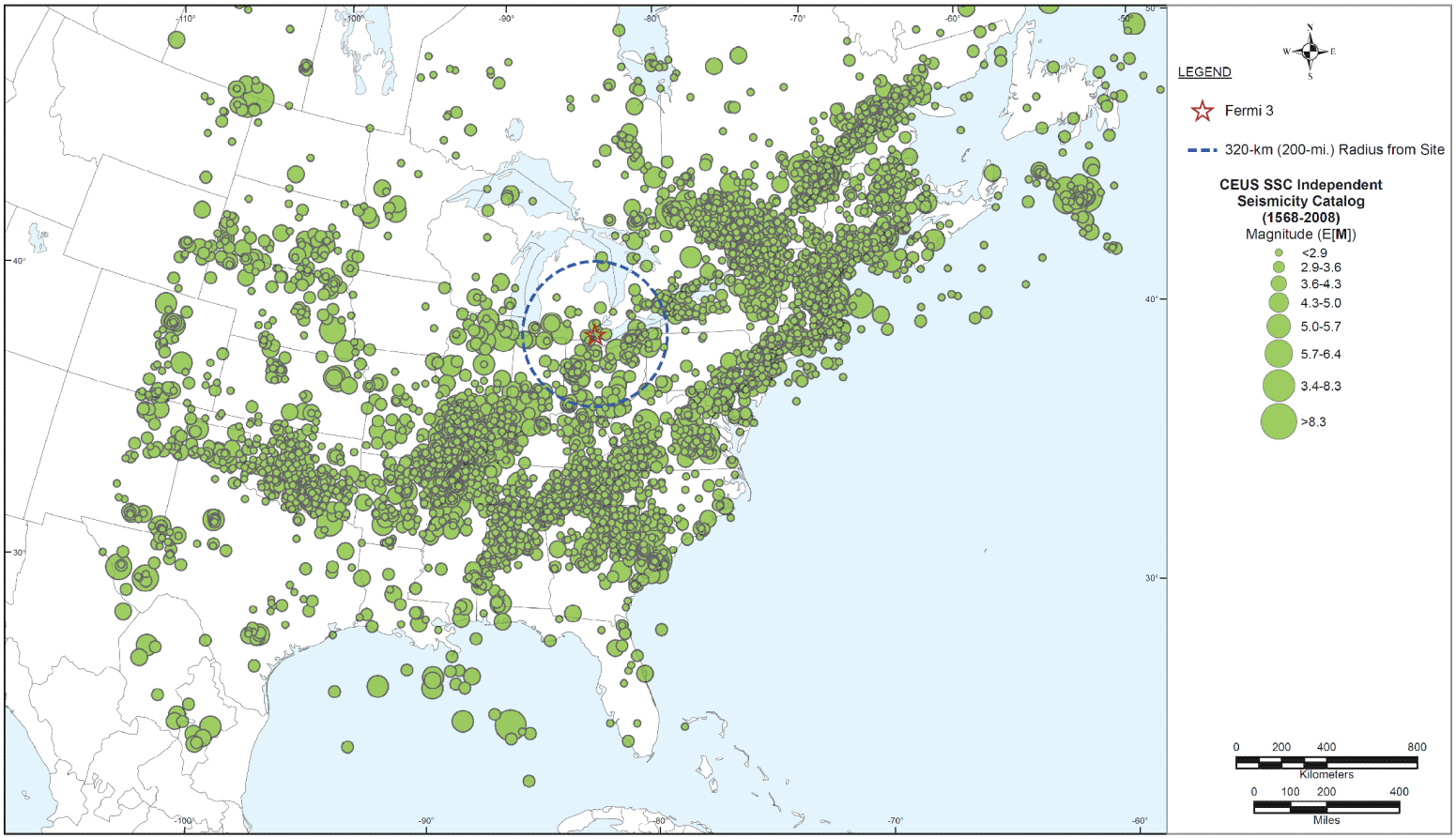

Figure 2.5.2-202 Location of Earthquakes within 320 km (200 mi) of the Fermi 3 Site [EF3 COL 2.0-27-A]

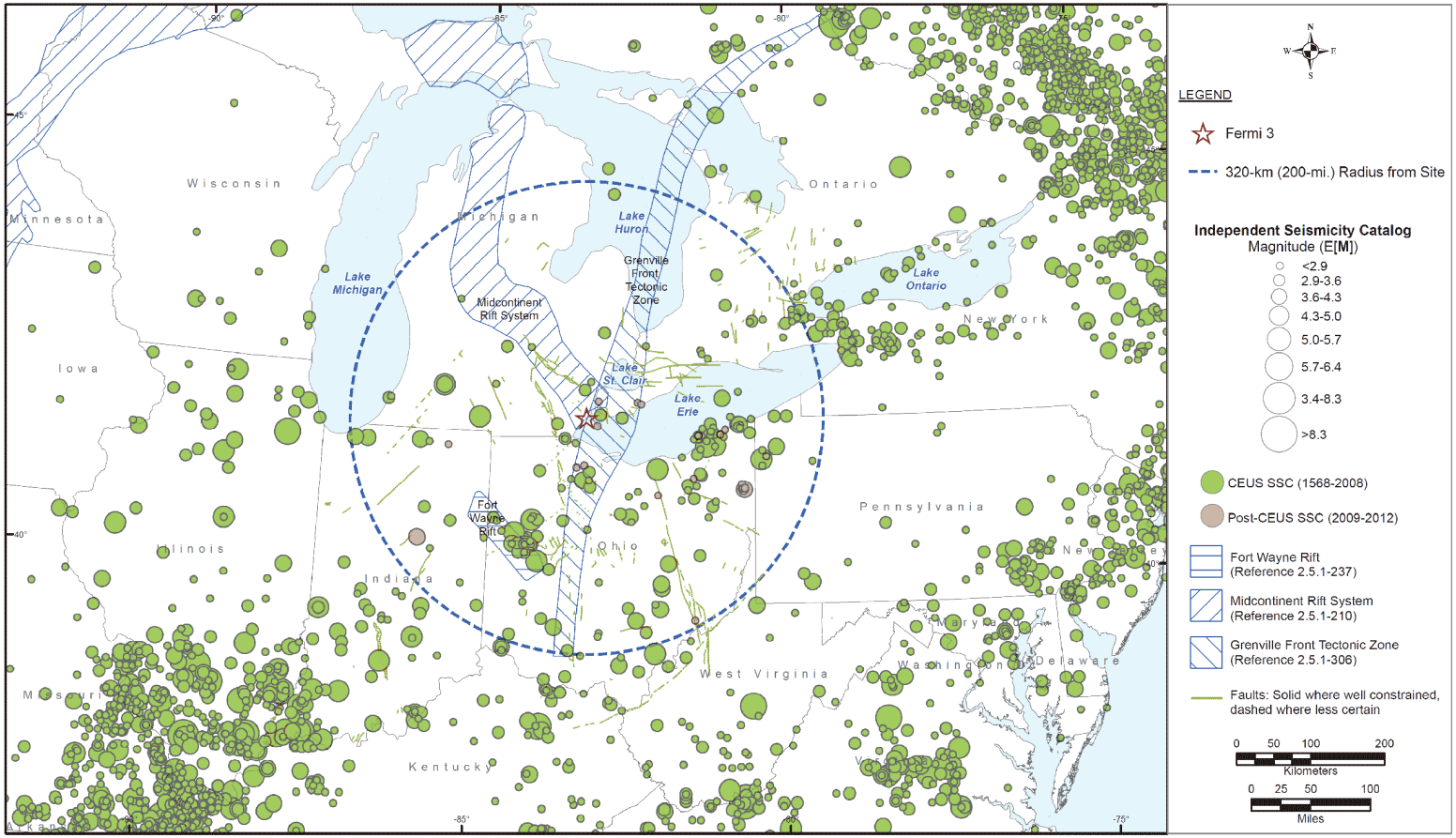

Figure 2.5.2-203 Location of Earthquakes within 80 km (50 mi) of the Fermi 3 Site [EF3 COL 2.0-27-A]

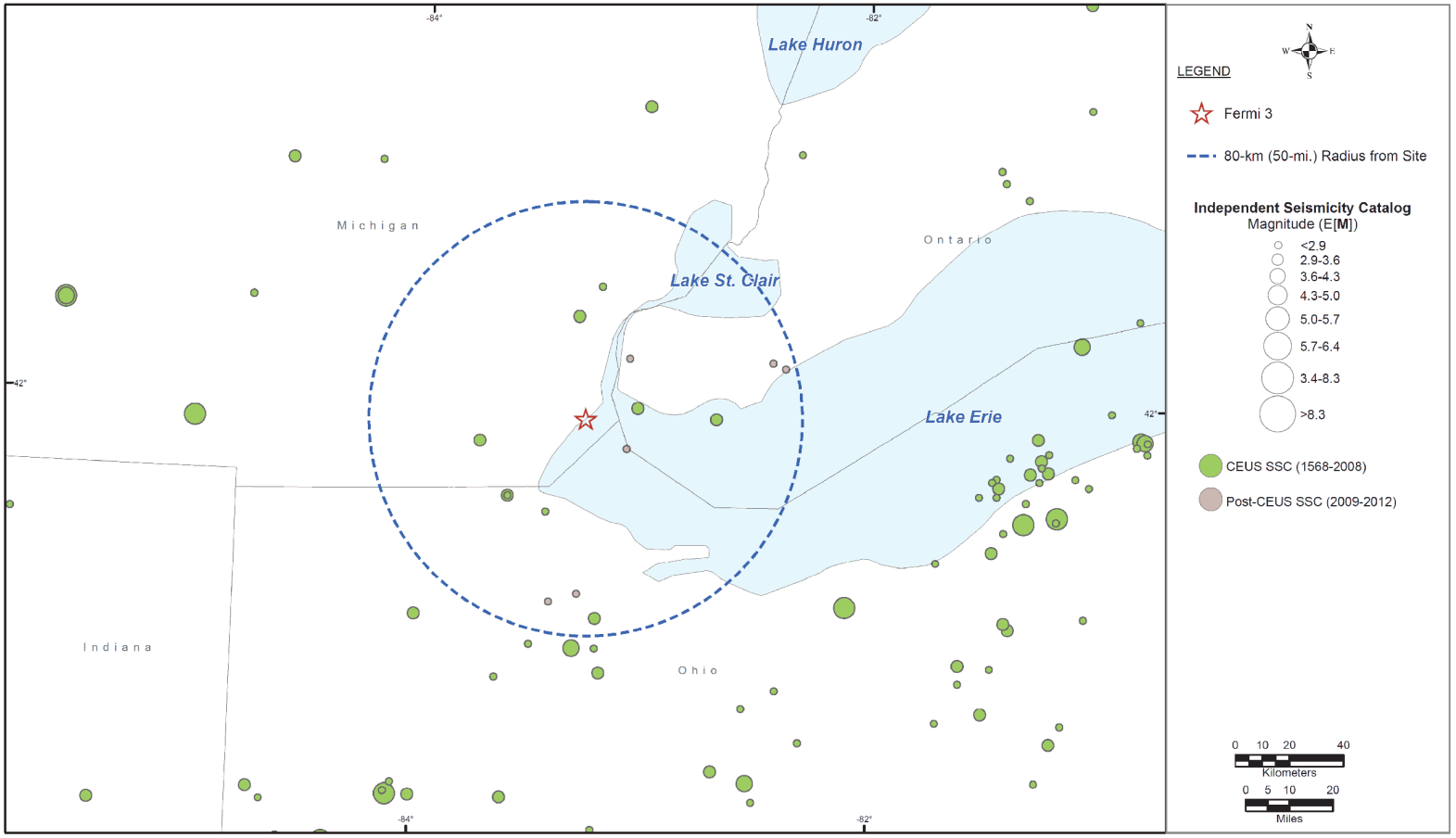

Figure 2.5.2-204 Master Logic Tree for the CEUS SSC Model [EF3 COL 2.0-27-A]

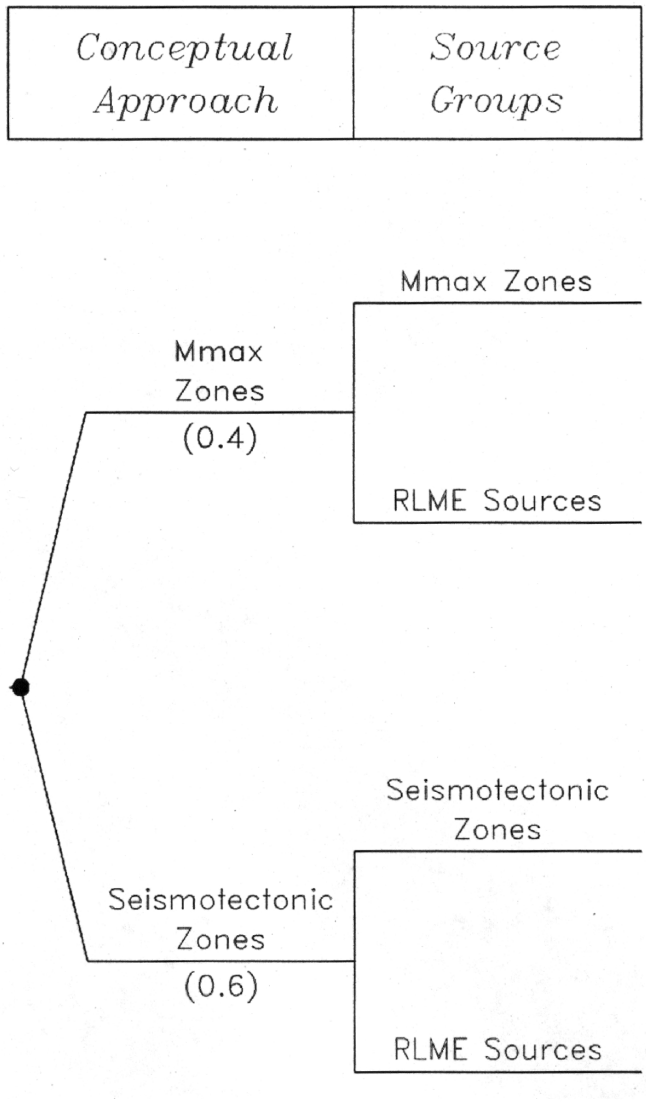

Source: Reference 2.5.2-202, Fig. 4.2.1-1

Figure 2.5.2-205 Logic Tree for the Mmax Zones Branch of the Master Logic Tree for the CEUS SSC Model

[EF3 COL 2.0-27-A]

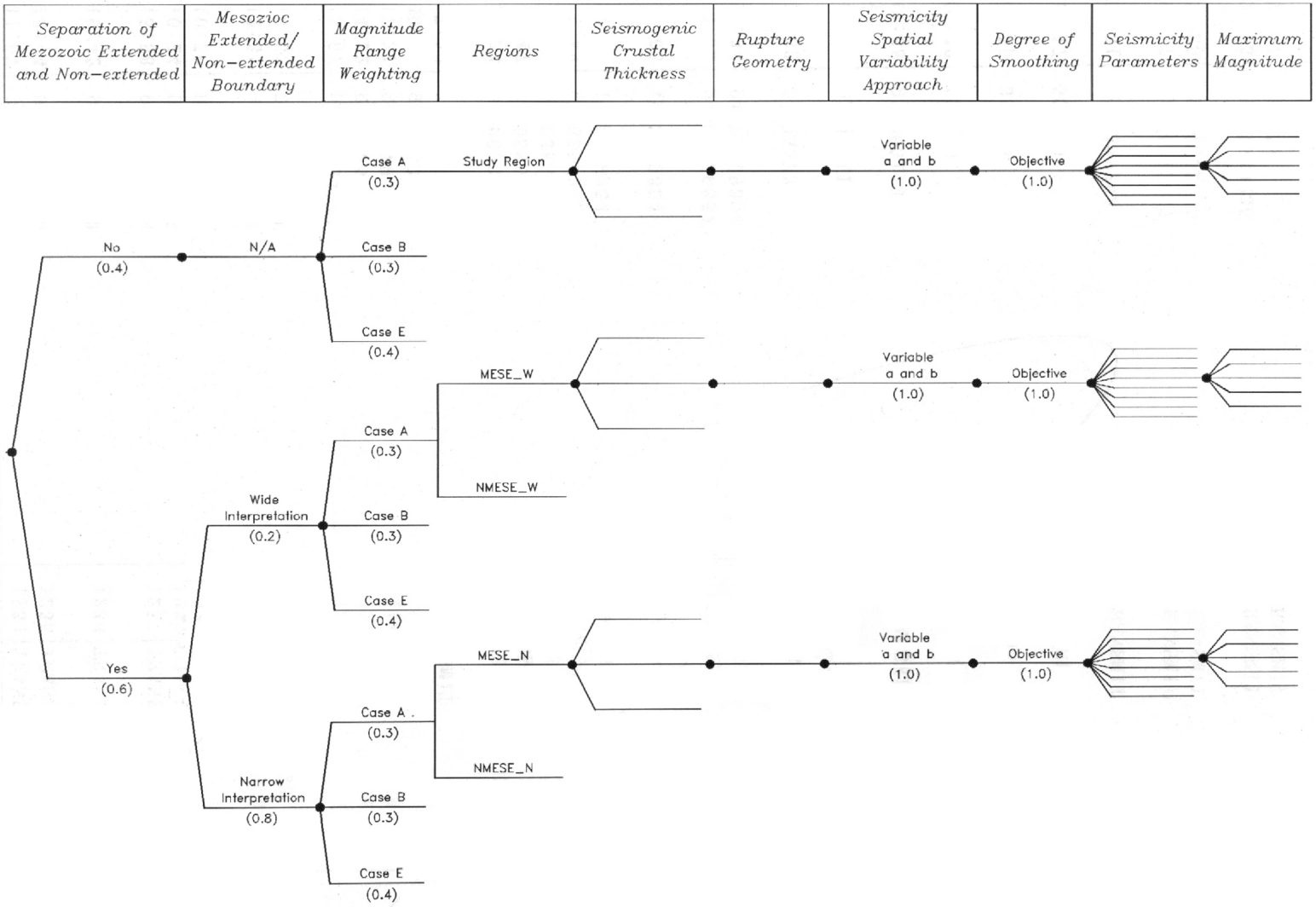

Source: Reference 2.5.2-202, Fig. 4.2.3-1

Figure 2.5.2-206 Location of the MESE and NMESE Mmax Zones for the "Narrow" Interpretation for the CEUS SSC Model [EF3 COL 2.0-27-A]

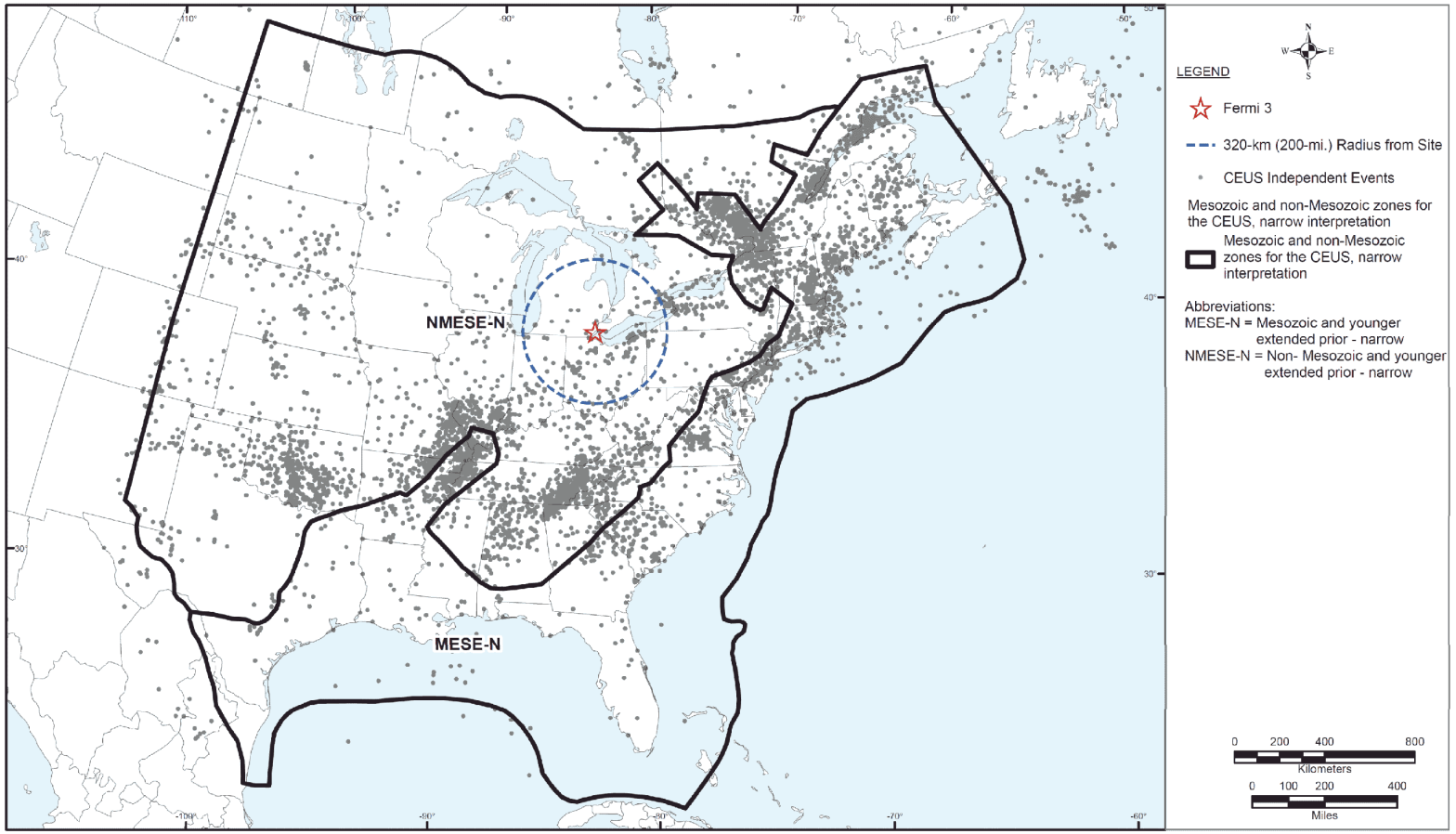

Source: Reference 2.5.2-202

Figure 2.5.2-207 Location of the MESE and NMESE Mmax Zones for the "Wide" Interpretation for the CEUS SSC Model [EF3 COL 2.0-27-A]

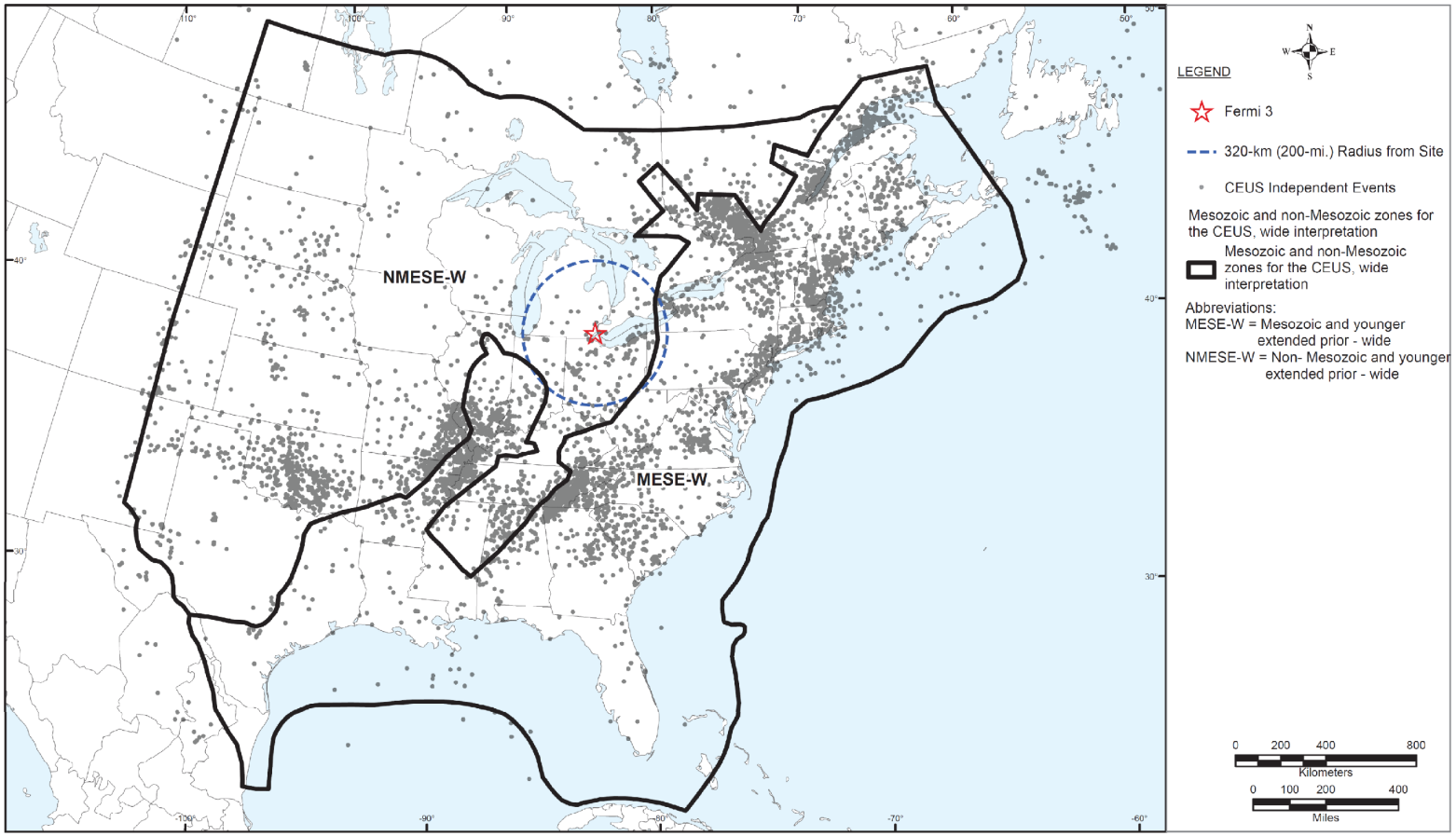

Source: Reference 2.5.2-202

Figure 2.5.2-208 Logic Tree for the Seismotectonic Zones Branch of the Master Logic Tree for the CEUS SSC Model [EF3 COL 2.0-27-A]

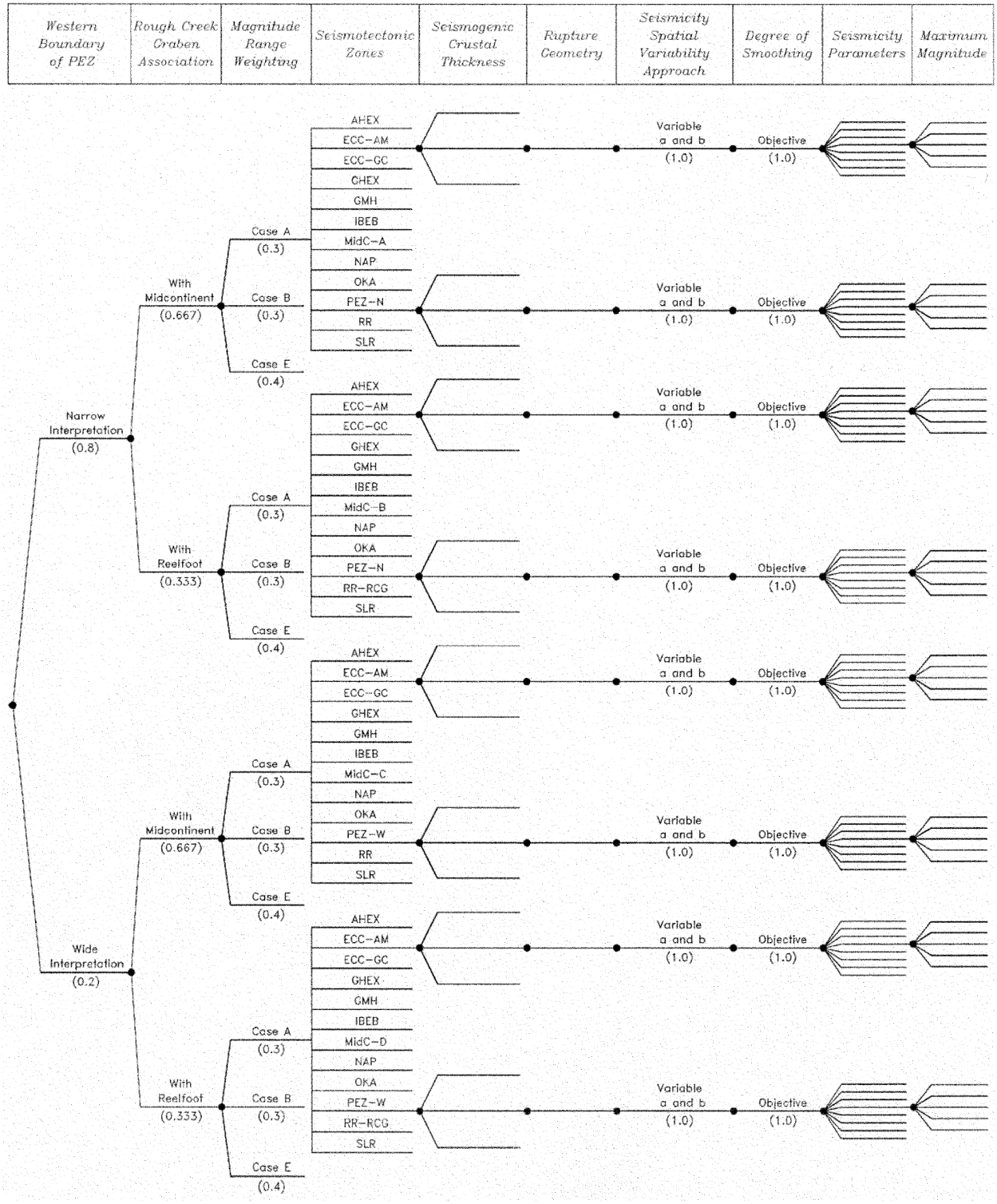

Source: Reference 2.5.2-202, Fig. 4.2.4-1a, 4.2.4-1b

Figure 2.5.2-209 Seismotectonic Zones Where the Rough Creek Graben Is Not Part of the Reelfoot Rift (RR) and the Narrow Paleozoic Extended Zone (PEZ-N) [EF3 COL 2.0-27-A]

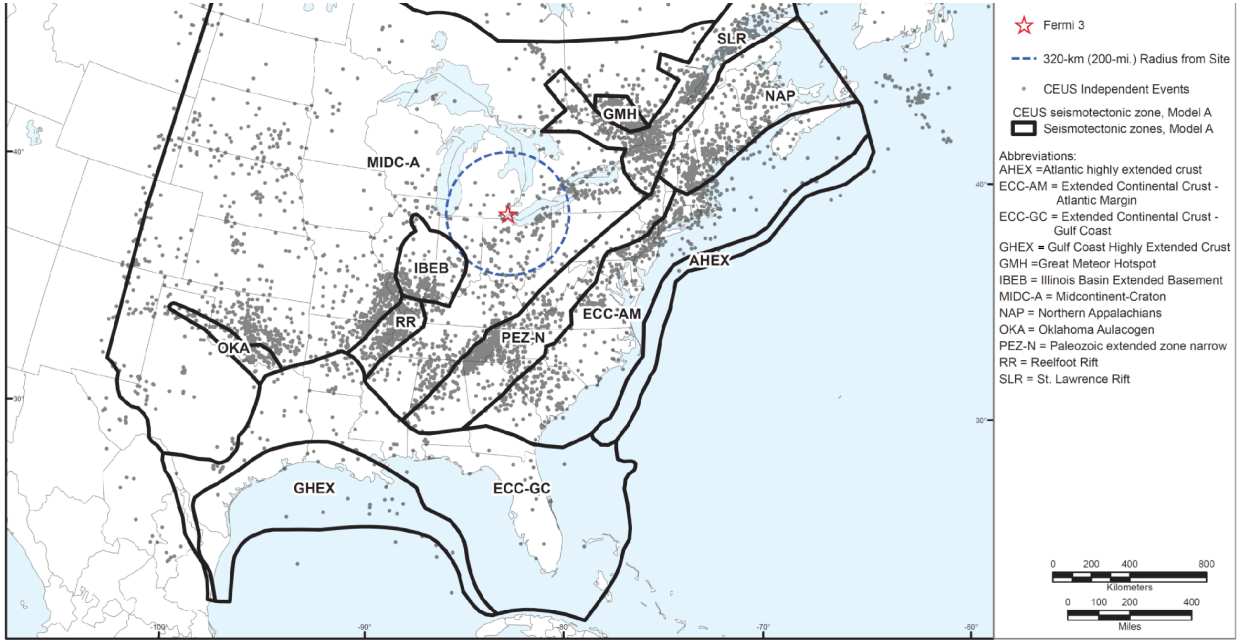

Source: Reference 2.5.2-202

Figure 2.5.2-210 Seismotectonic Zones Where the Rough Creek Graben Is Part of the Reelfoot Rift (RR-RCG) and the Narrow Paleozoic Extended Zone (PEZ-N) [EF3 COL 2.0-27-A]

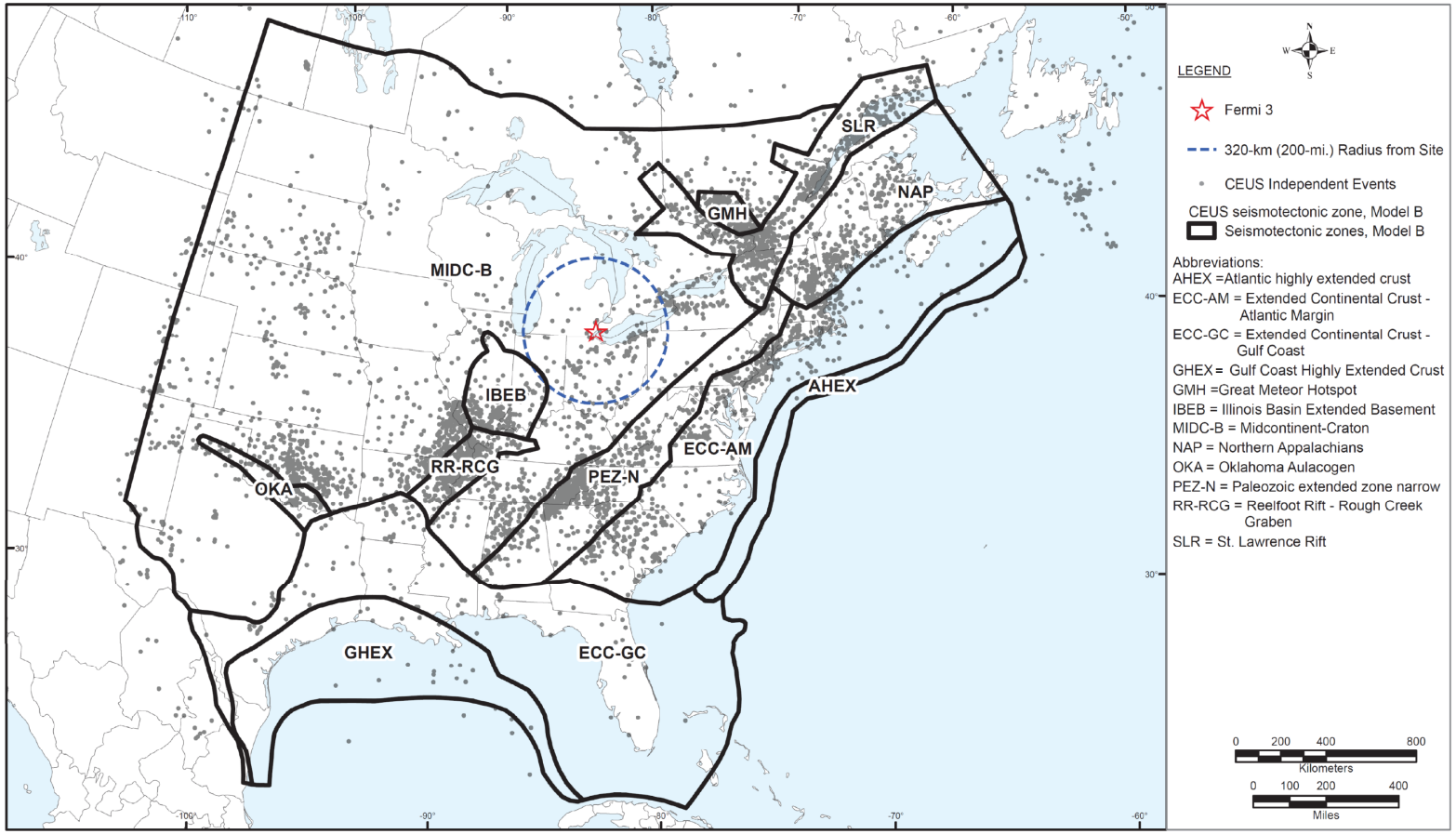

Source: Reference 2.5.2-202

Figure 2.5.2-211 Seismotectonic Zones Where the Rough Creek Graben Is Not Part of the Reelfoot Rift (RR) and the Wide Paleozoic Extended Crust (PEZ-W) [EF3 COL 2.0-27-A]

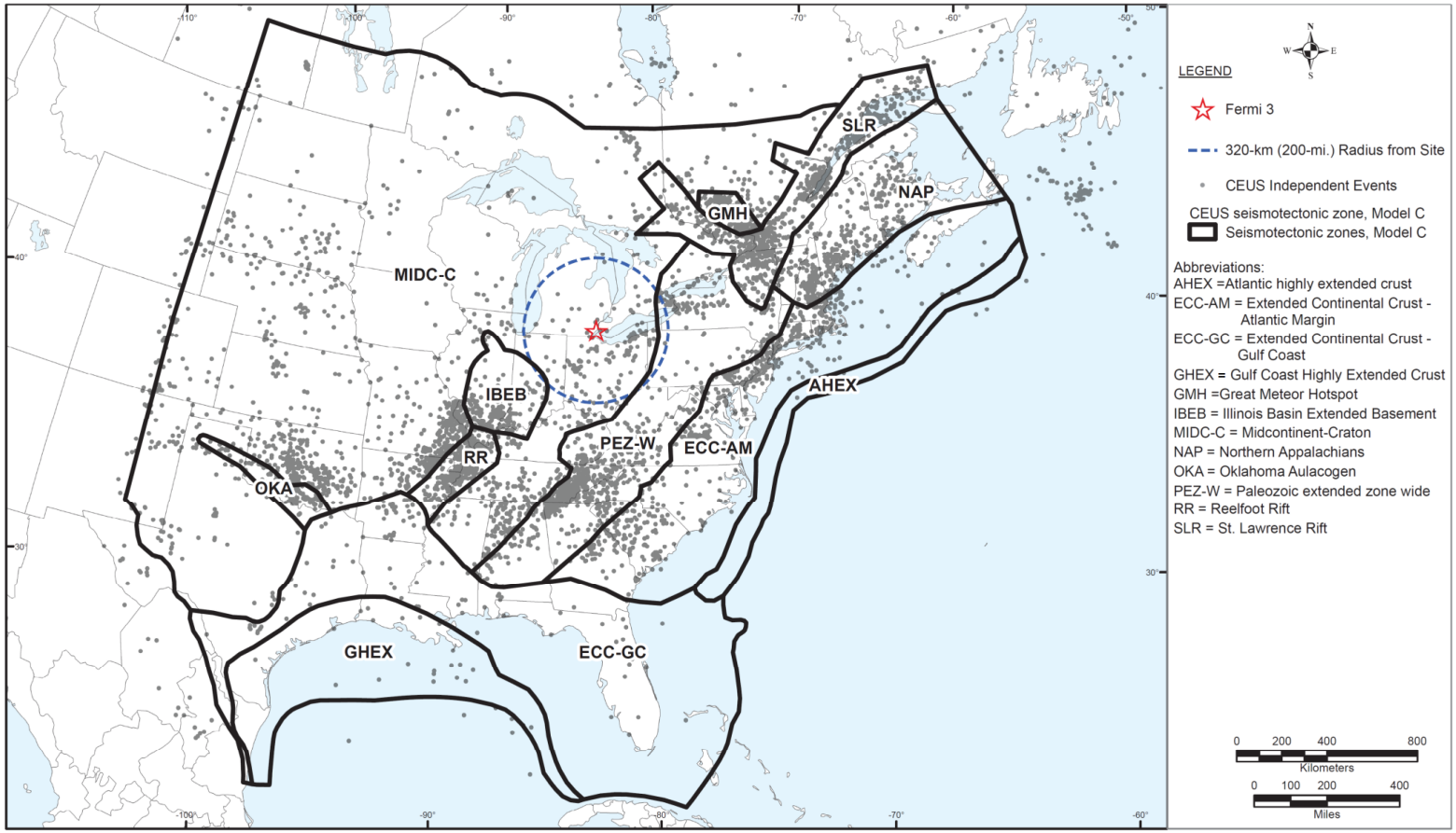

Source: Reference 2.5.2-202

Figure 2.5.2-212 Seismotectonic Zones Where the Rough Creek Graben Is Part of the Reelfoot Rift (RR-RCG) and the Wide Paleozoic Extended Crust (PEZ-W) [EF3 COL 2.0-27-A]

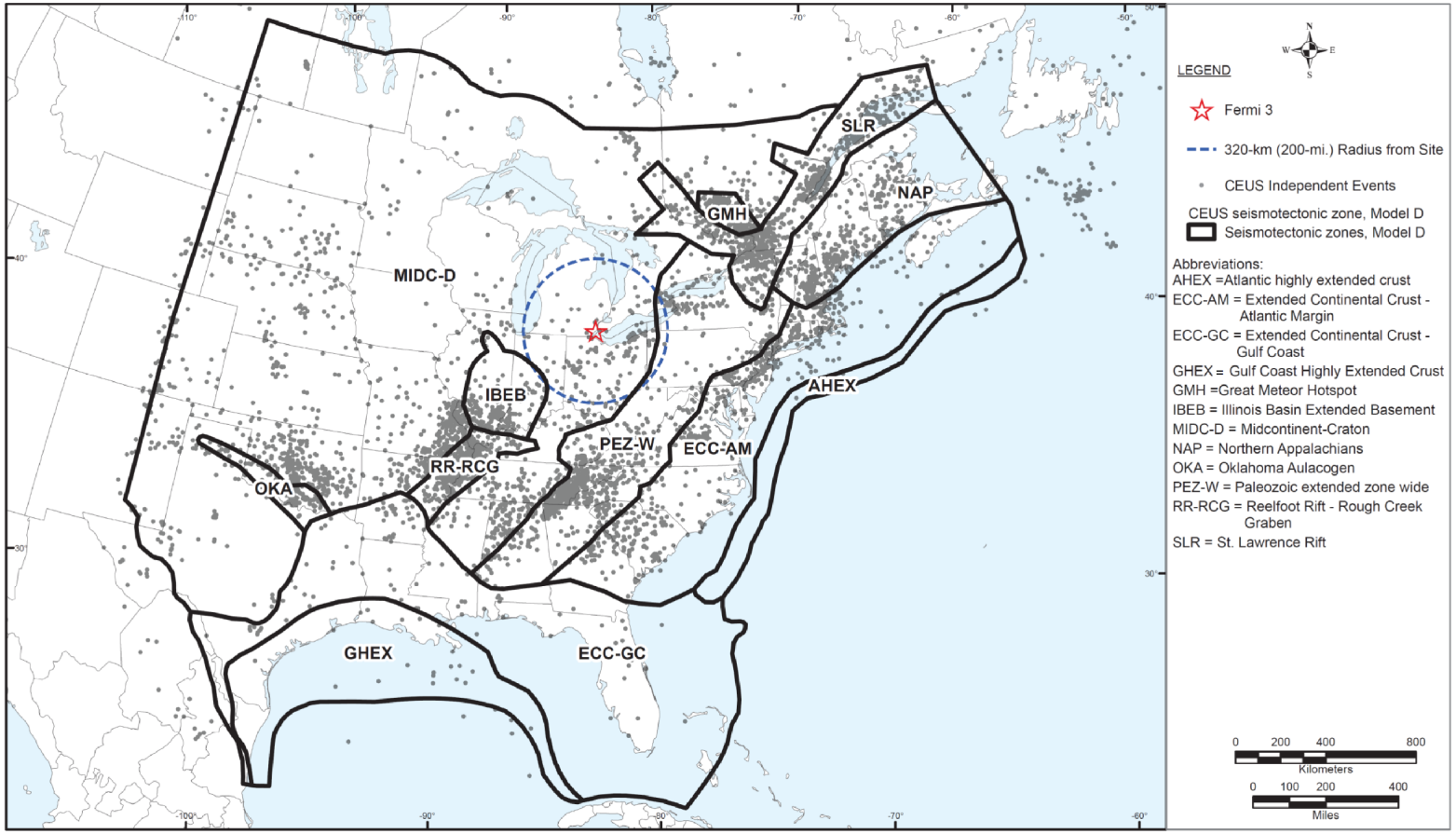

Source: Reference 2.5.2-202

Figure 2.5.2-213 Location of RLME Sources Characterized in the CEUS SSC Model [EF3 COL 2.0-27-A]

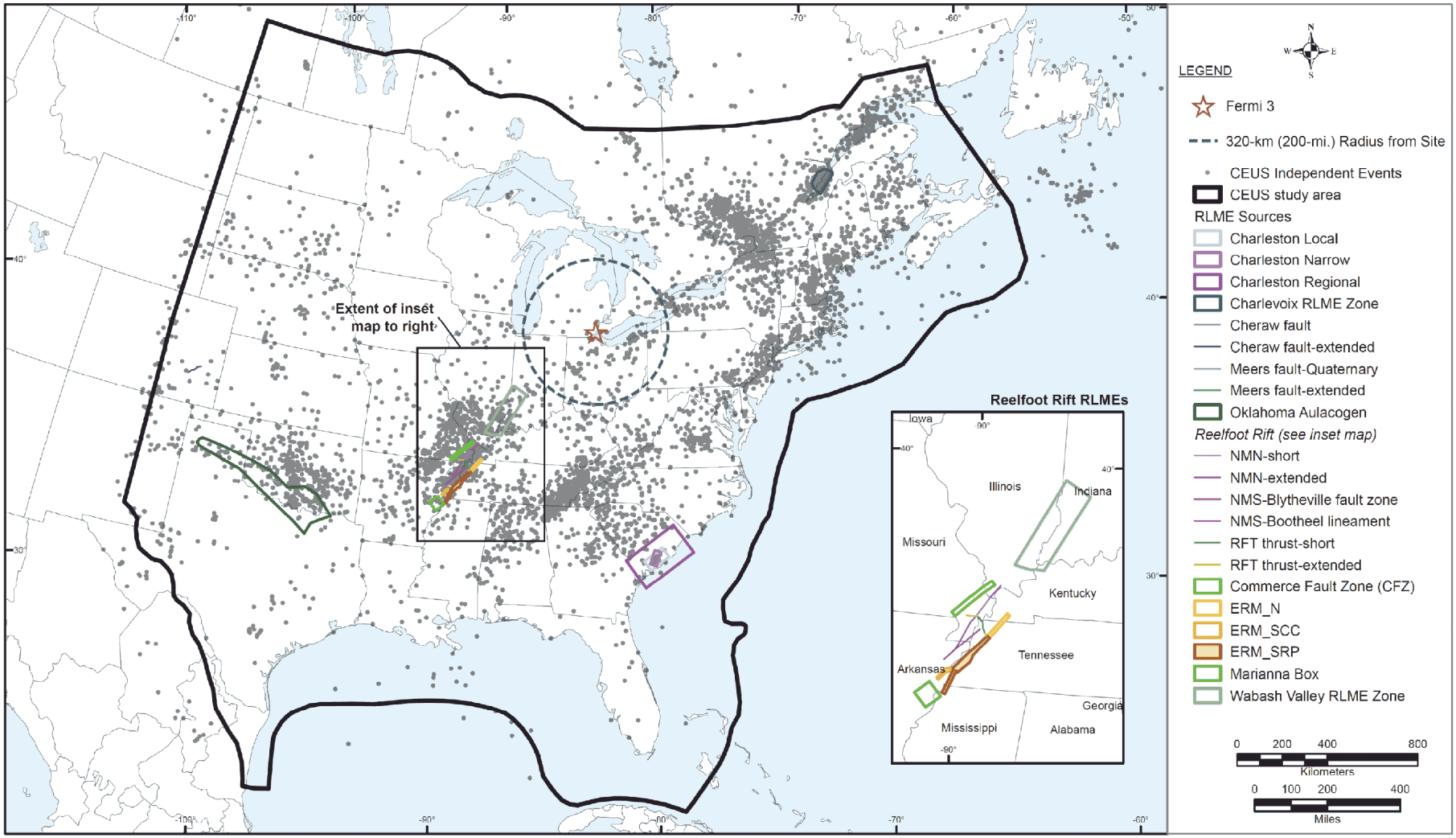

Source: Reference 2.5.2-202

Figure 2.5.2-214 Map Showing the RLME Sources and Seismicity from the CEUS SSC Earthquake Catalog

[EF3 COL 2.0-27-A]

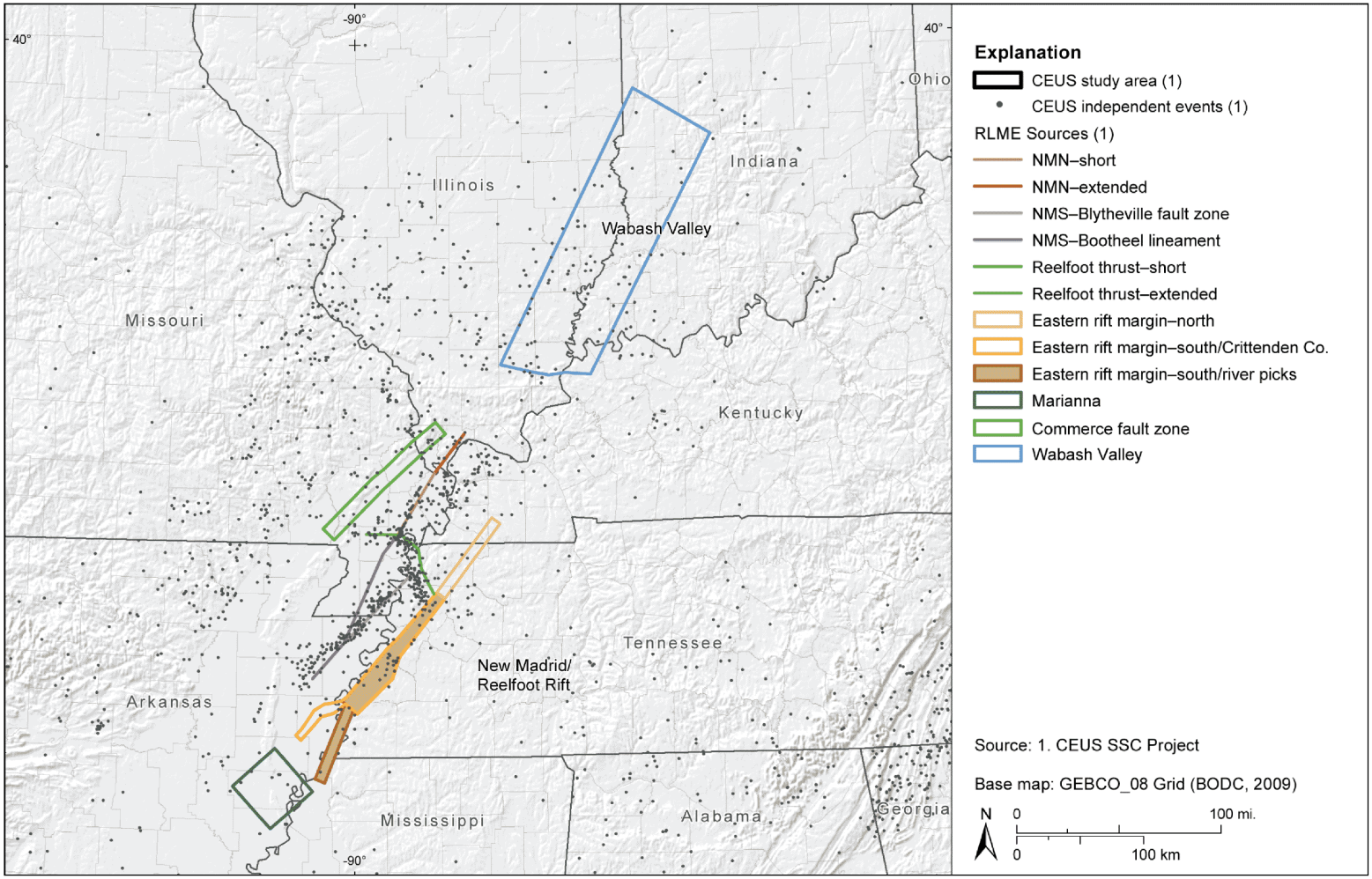

Source: Reference 2.5.2-202, Fig. 6.1-2b

Figure 2.5.2-215 Logic Tree for the New Madrid Faults RLME [EF3 COL 2.0-27-A]

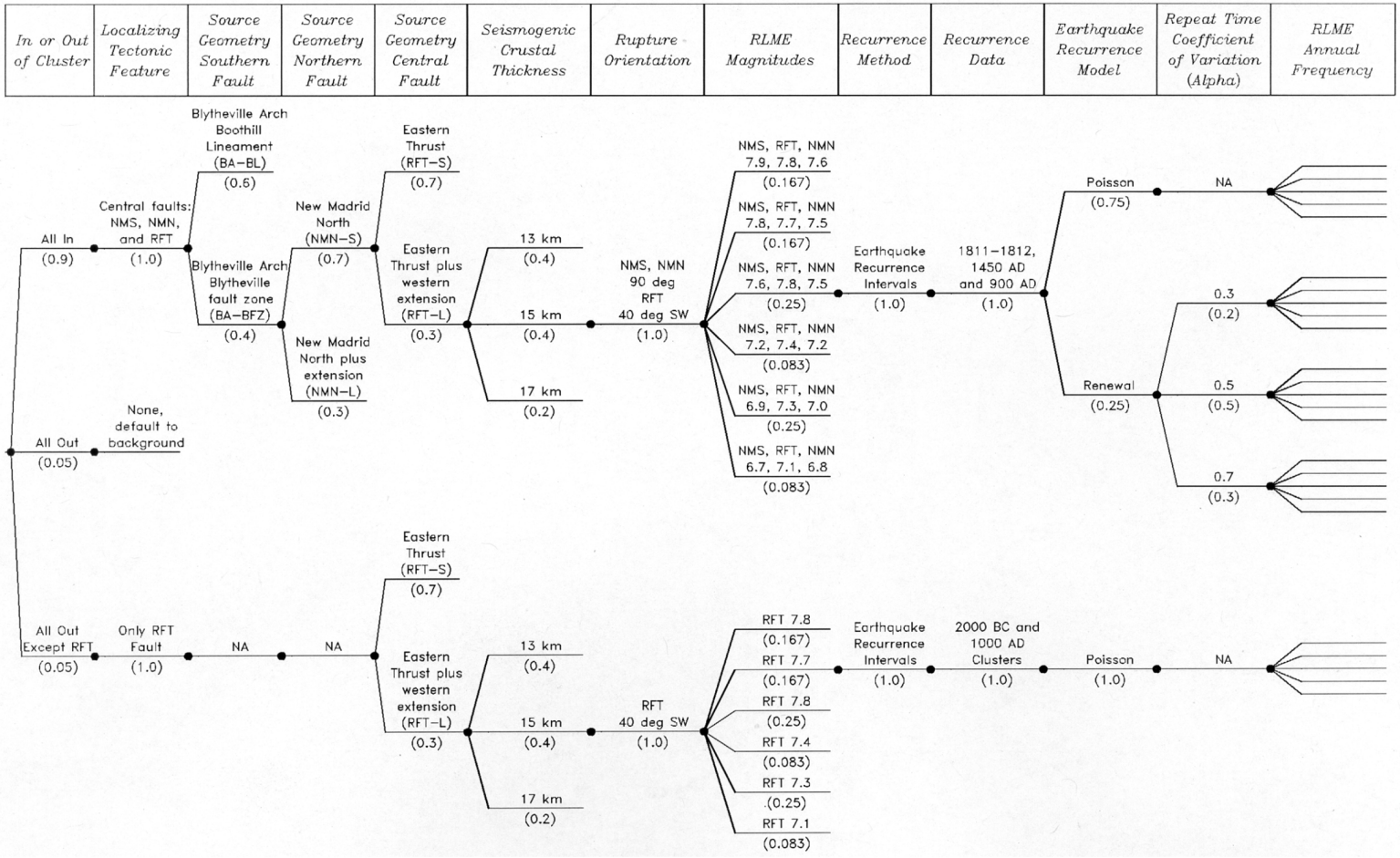

Source: Reference 2.5.2-202, Fig. 6.1.5-1

Figure 2.5.2-216 Simplified Tectonic Map Showing the Distribution of Principal Basement Faults, Rifts, and Sutures in the Midcontinent [EF3 COL 2.0-27-A]

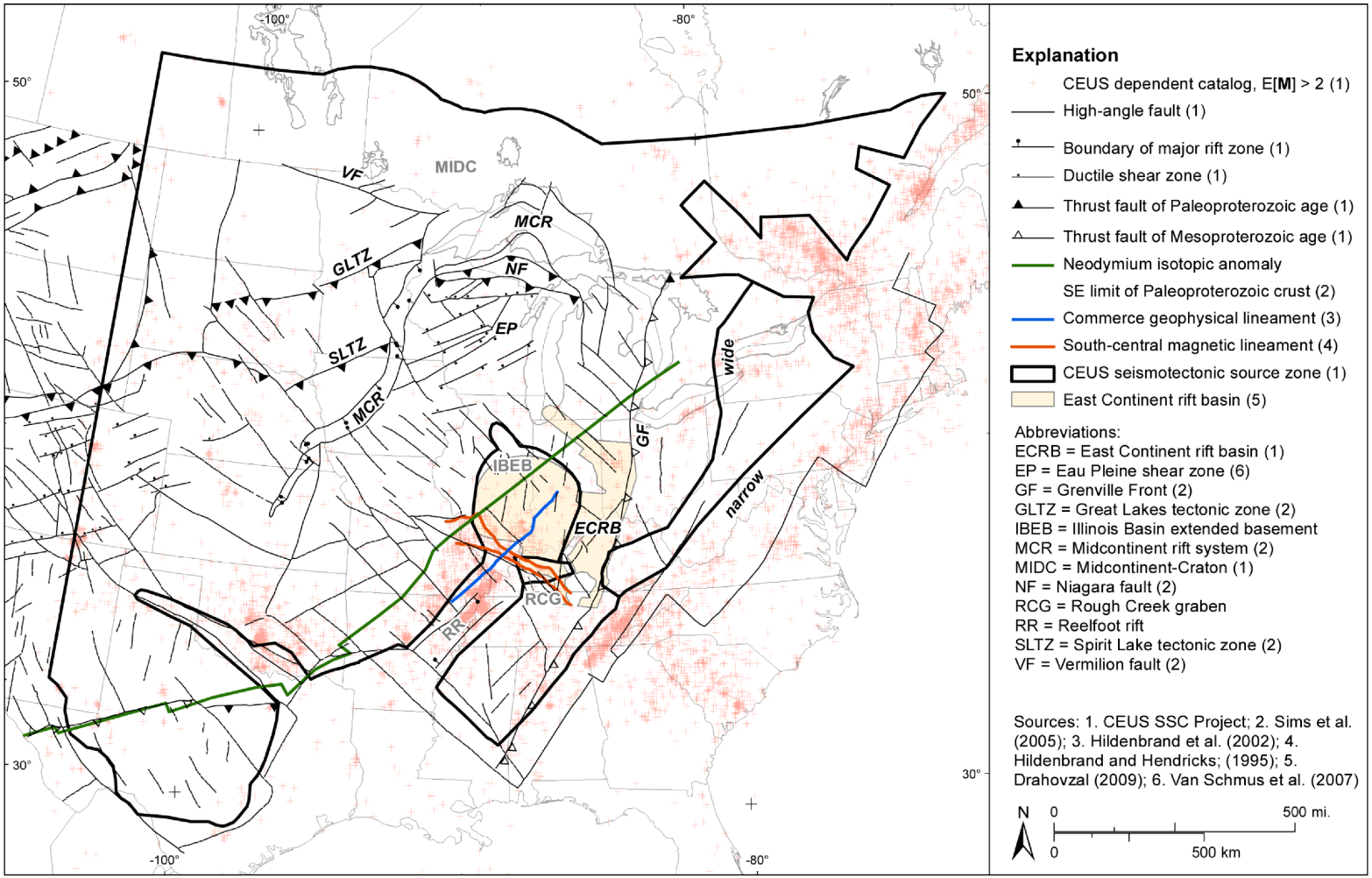

Source: Reference 2.5.2-202, Fig. 7.3.12-1

Figure 2.5.2-217 Maps Showing Major Basement Structural Features Relative to (a) Regional Magnetic Anomalies and (b) Regional Gravity Anomalies [EF3 COL 2.0-27-A]

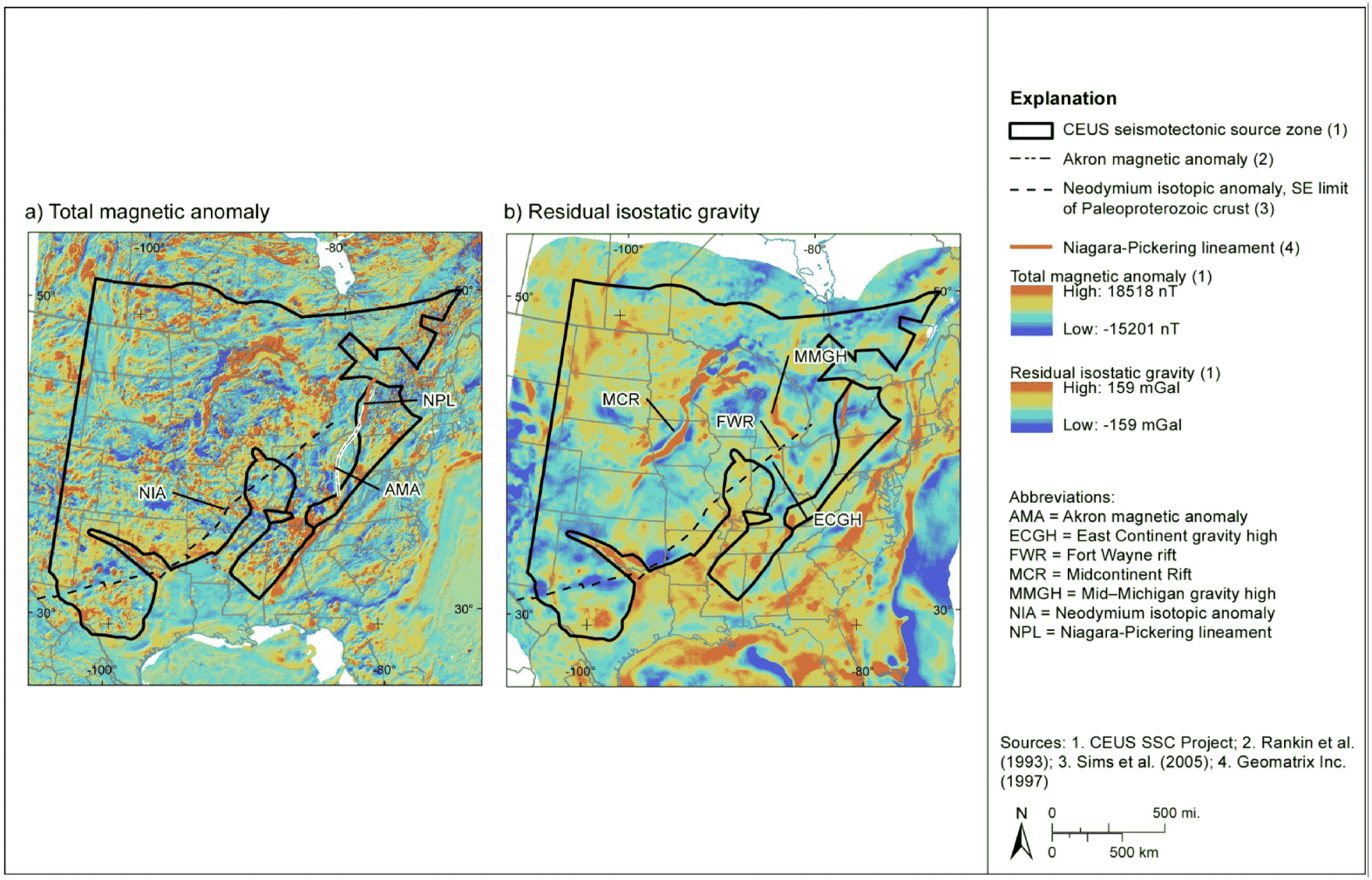

Source: Reference 2.5.2-202, Fig. 7.3.12-2

Figure 2.5.2-218 Seismicity Zones and Largest Observed Earthquakes in the MIDC Zone [EF3 COL 2.0-27-A]

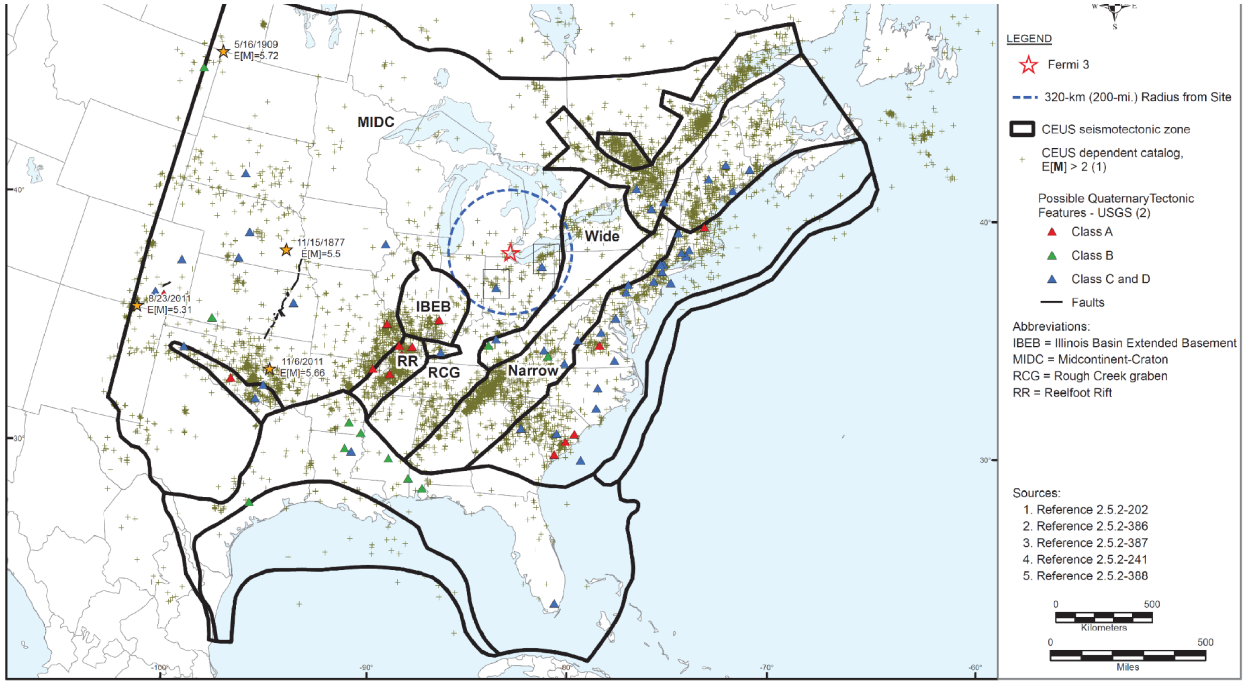

Source: Modified from Reference 2.5.2-202

Figure 2.5.2-219 Correlation of Interpreted Transitional Crust with the East Coast Magnetic Anomaly (ECMA)

[EF3 COL 2.0-27-A]

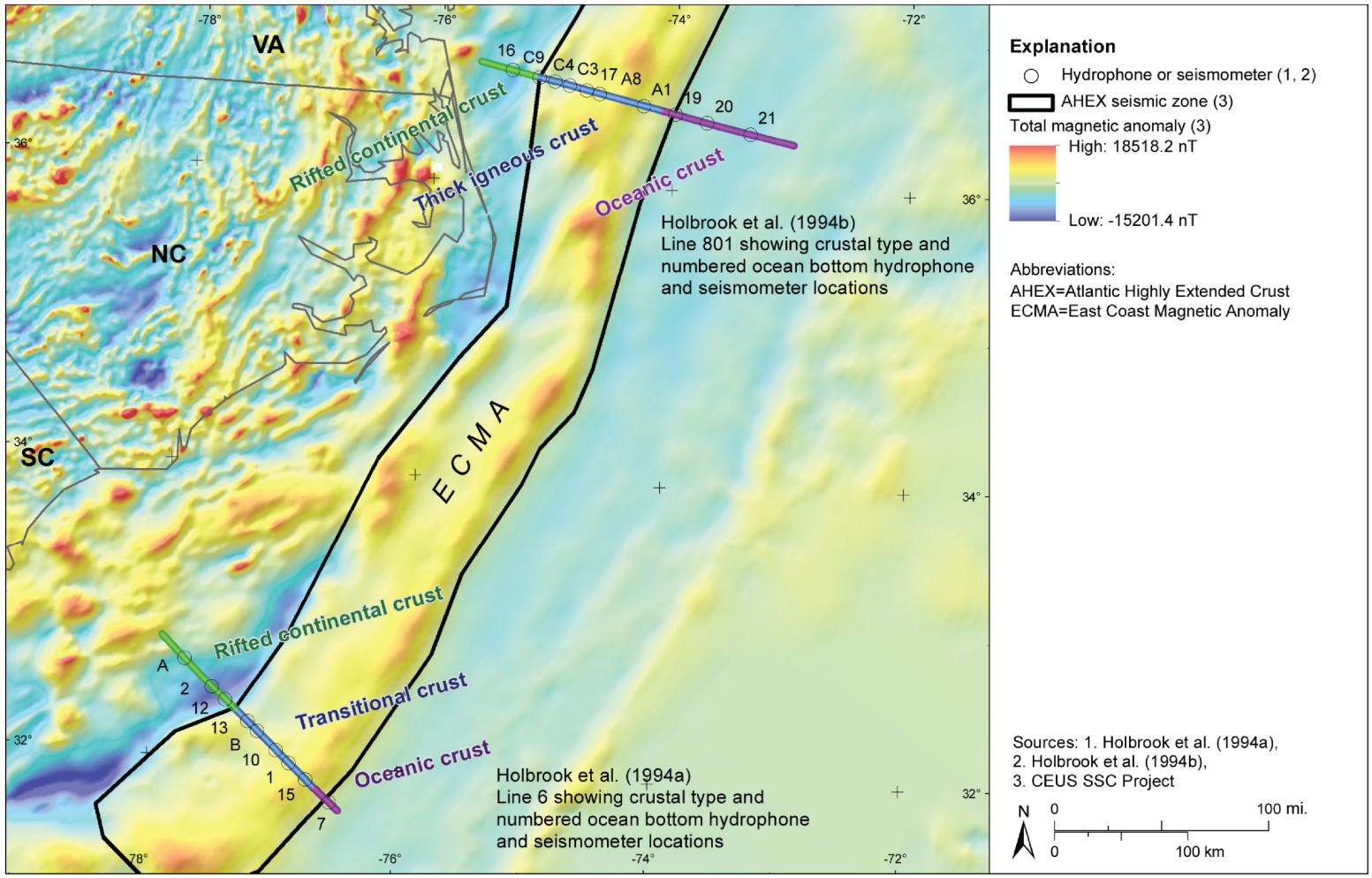

Source: Reference 2.5.2-202, Fig. 7.3.8-1

Figure 2.5.2-220 Mesozoic Basins Within the ECC-AM Seismotectonic Zone [EF3 COL 2.0-27-A]

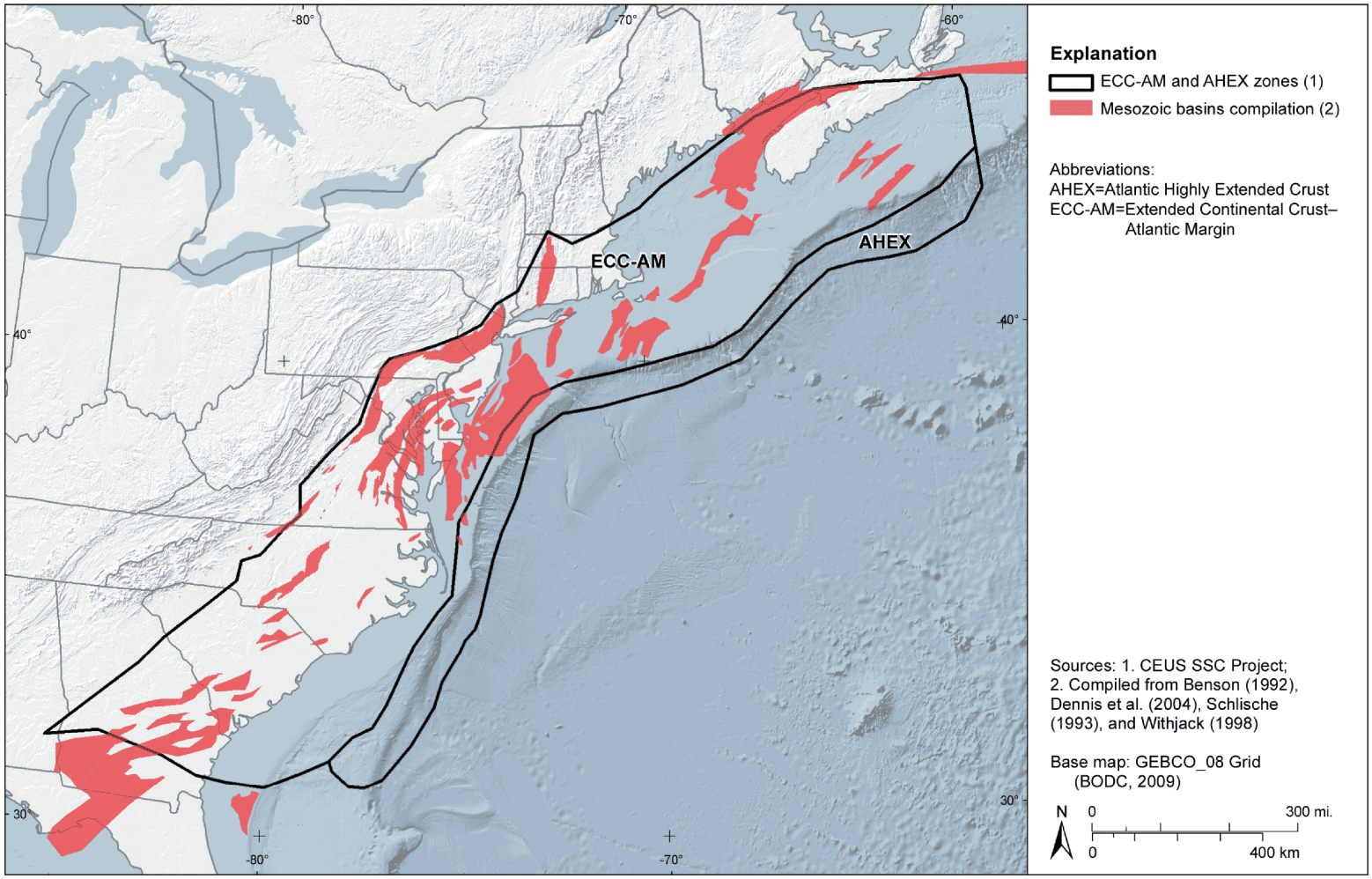

Source: Reference 2.5.2-202, Fig. 7.3.7-1

Figure 2.5.2-221 Seismicity Within the ECC-AM and AHEX Seismotectonic Zones [EF3 COL 2.0-27-A]

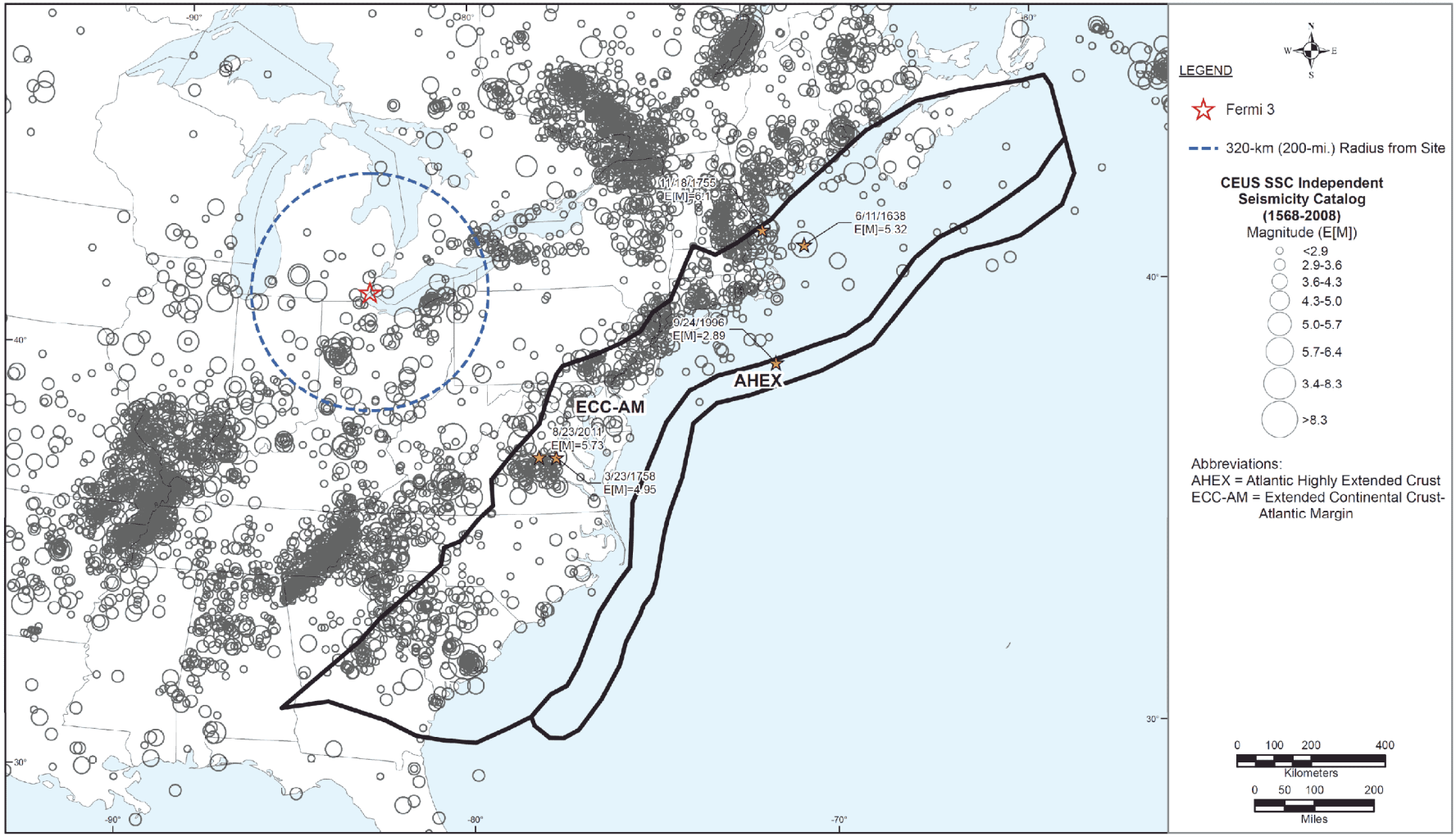

Source: Reference 2.5.2-202

Figure 2.5.2-222 Seismicity and Largest Earthquakes in the GMH Seismotectonic Zone [EF3 COL 2.0-27-A]

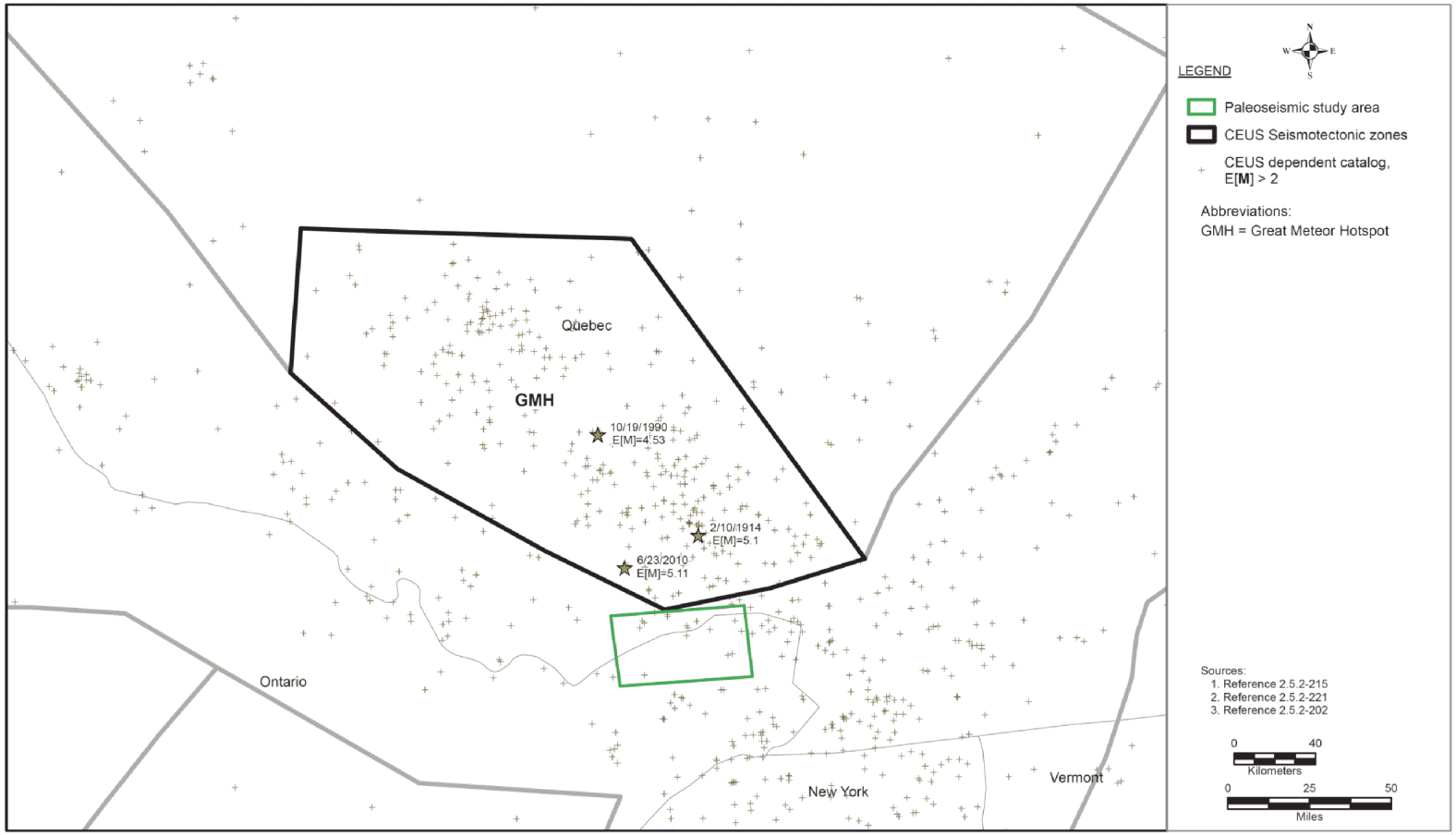

Source: Reference 2.5.2-202

Figure 2.5.2-223 Map of Paleoearthquake Energy Centers and Paleoliquefaction Features in the IBEB Seismotectonic Zone [EF3 COL 2.0-27-A]

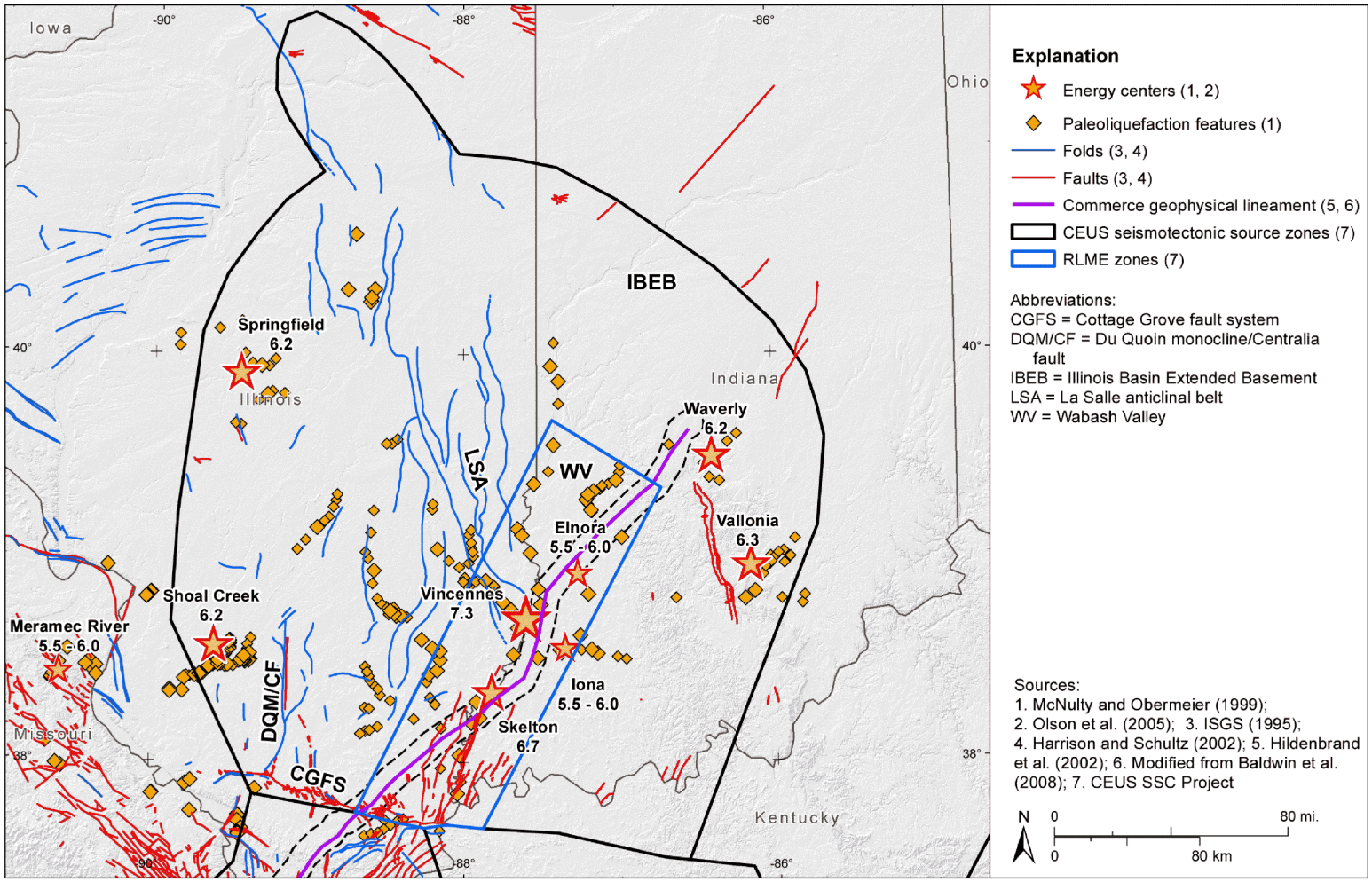

Source: Reference 2.5.2-202, Fig. 7.3.5-1

Figure 2.5.2-224 Historical Seismicity and Largest Historical Earthquakes in the IBEB Seismotectonic Zone

[EF3 COL 2.0-27-A]

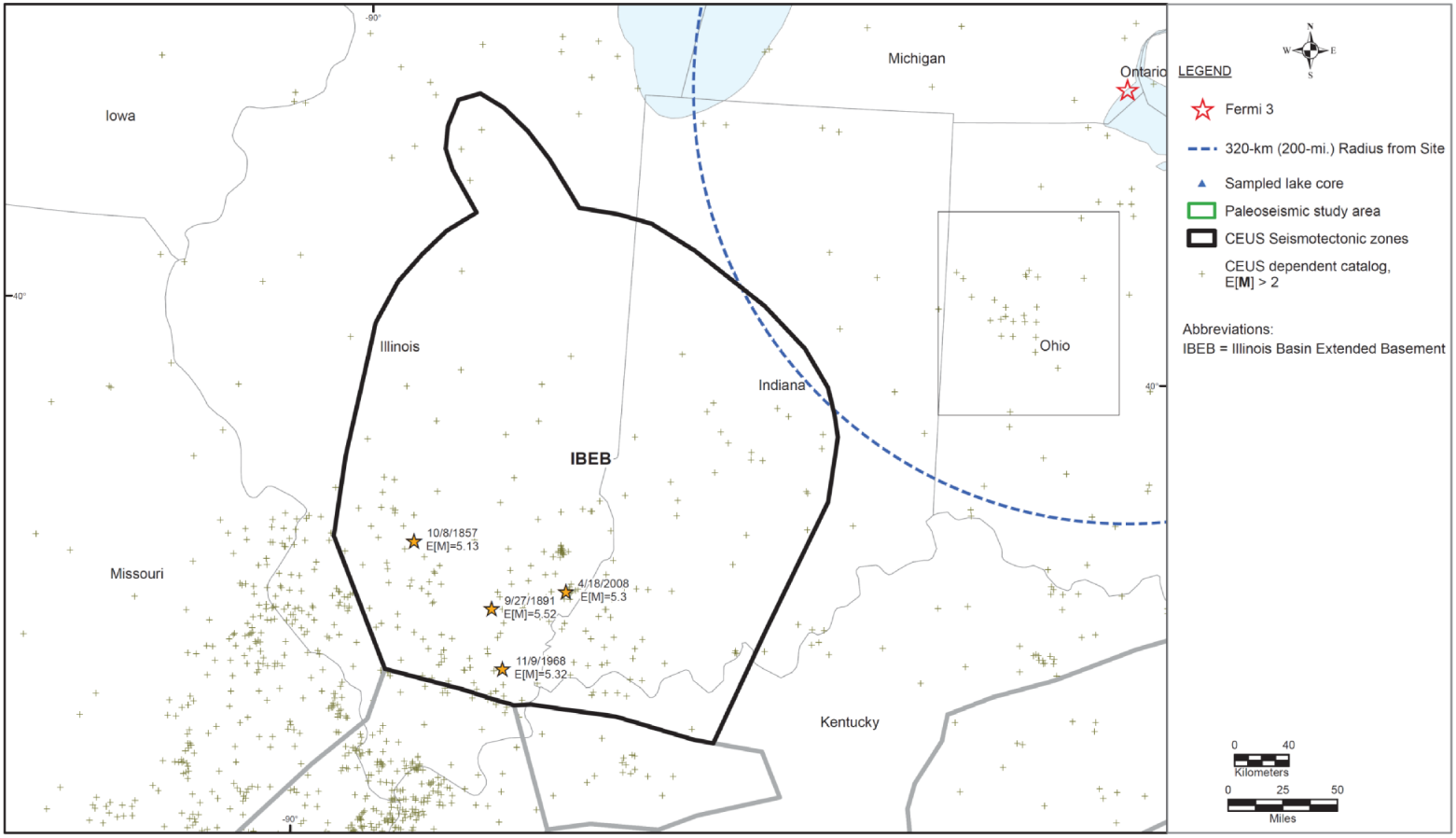

Source: Modified from Reference 2.5.2-202

Figure 2.5.2-225 Seismicity of the NAP Seismotectonic Zone [EF3 COL 2.0-27-A]

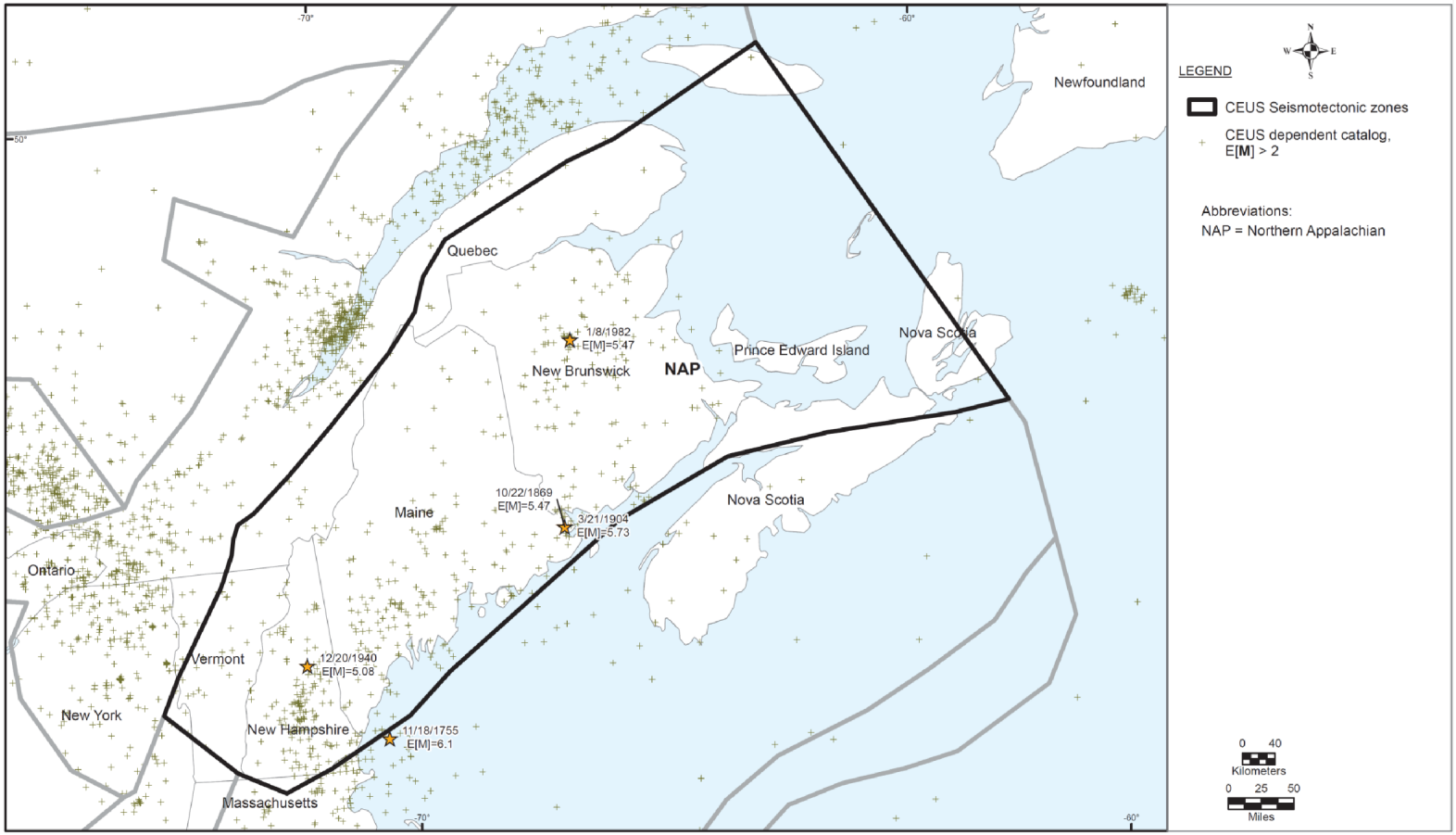

Source Reference 2.5.2-202

Figure 2.5.2-226 Seismicity and Tectonic Features of the PEZ Seismotectonic Zone [EF3 COL 2.0-27-A]

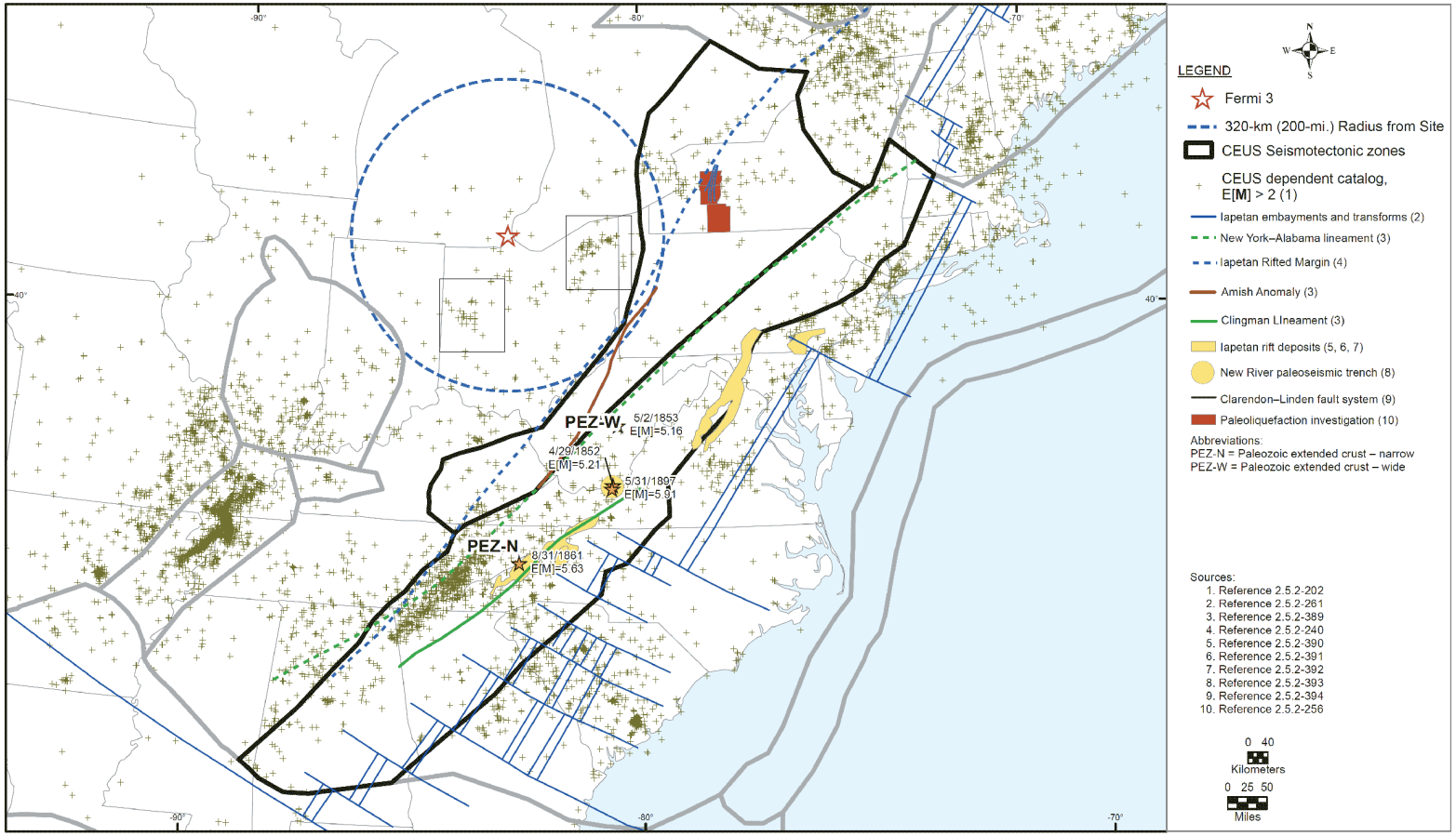

Source Reference 2.5.2-202

Figure 2.5.2-227 Map of Seismicity and Geomorphic Features and Faults in the Reelfoot Rift Seismotectonic Zone
[EF3 COL 2.0-27-A]

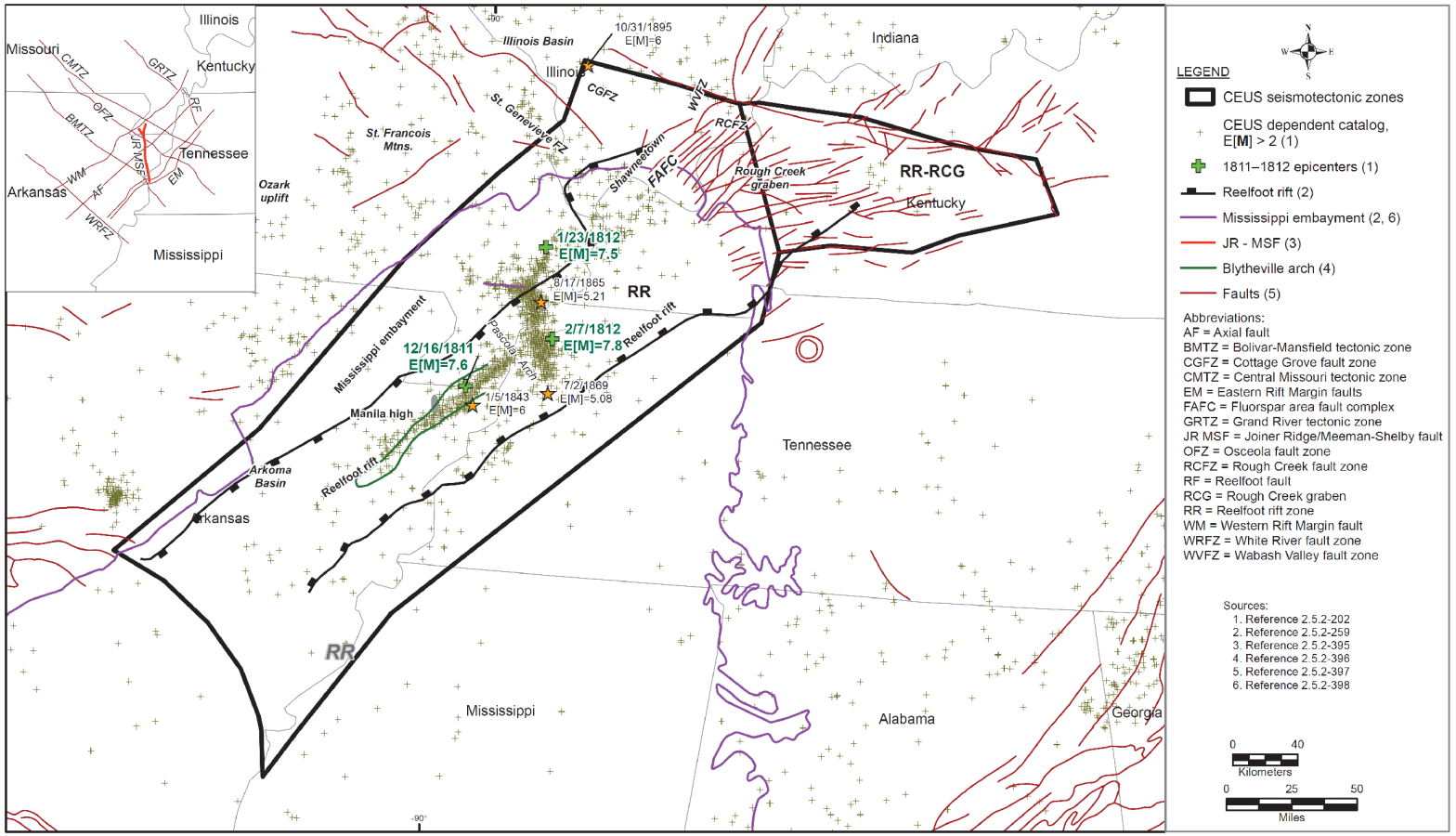

Source Reference 2.5.2-202

Figure 2.5.2-228 Significant Earthquakes and Paleoseismology of the SLR Seismotectonic Zone

[EF3 COL 2.0-27-A]

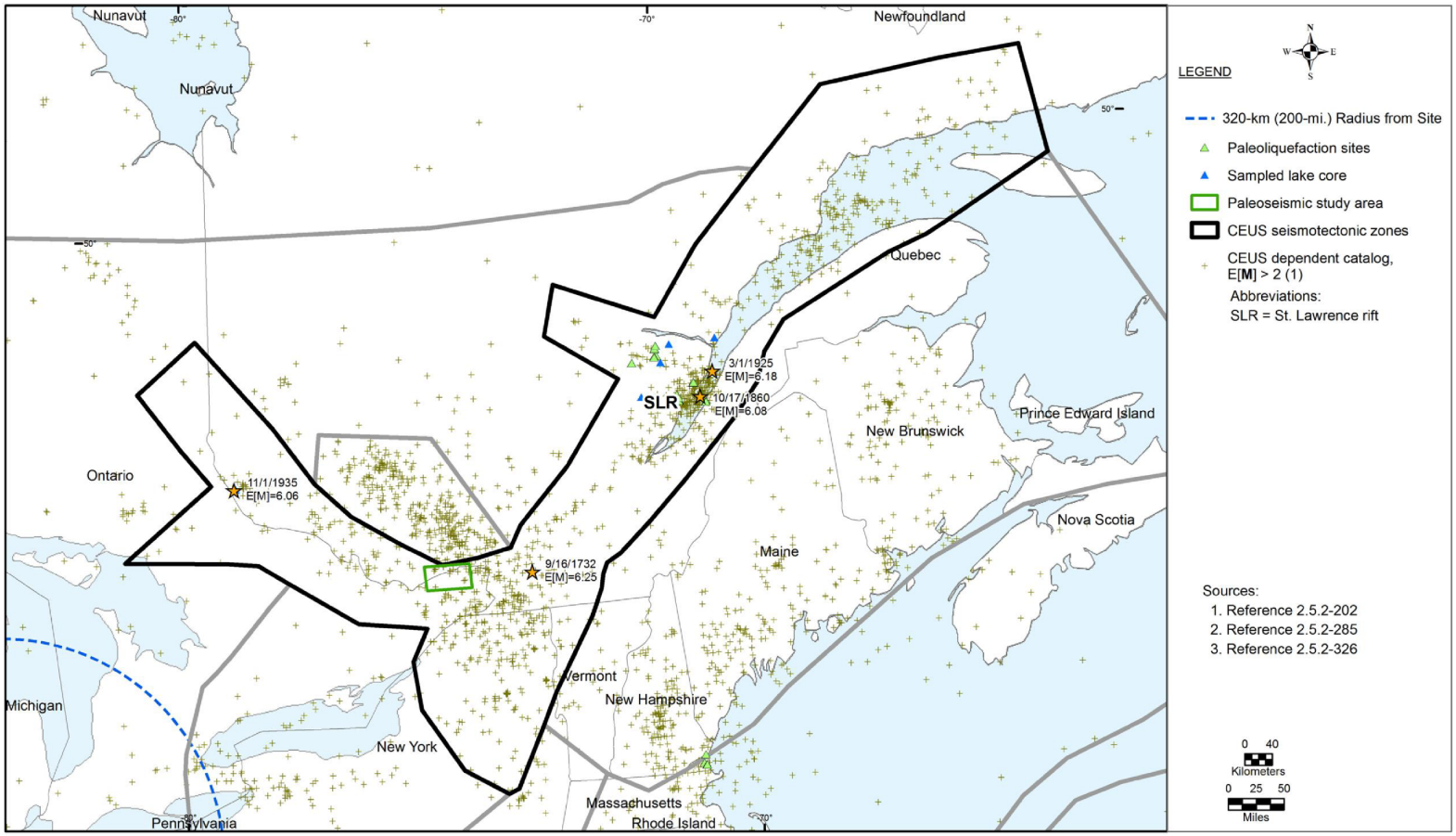

Source Reference 2.5.2-202

Figure 2.5.2-229 Geomorphic and Near-Surface Tectonic Features in the New Madrid Region and Locations of NMFS RLME Fault Sources [EF3 COL 2.0-27-A]

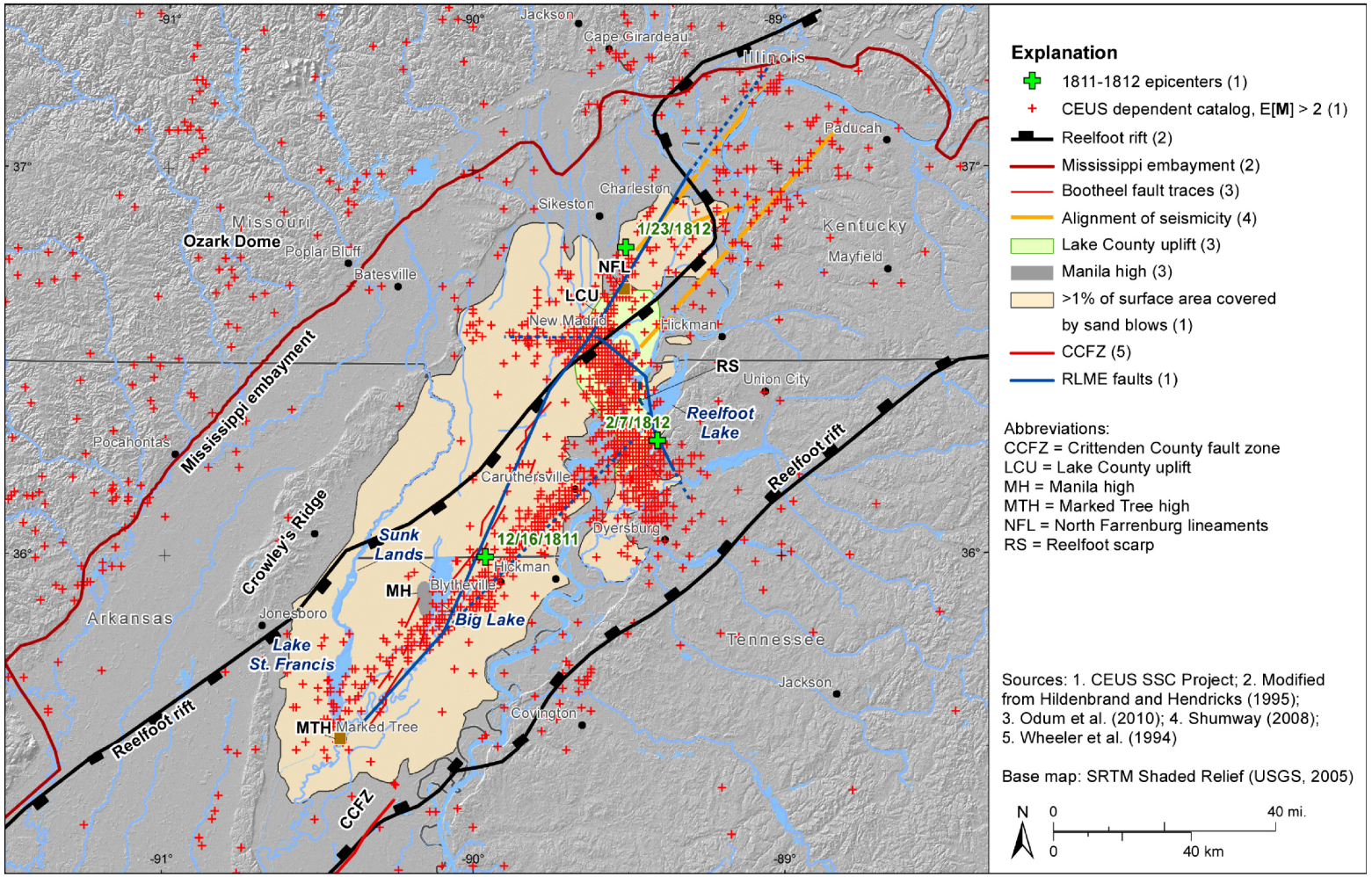

Source: Reference 2.5.2-202, Fig. 6.1.5-3

Figure 2.5.2-230 Seismicity, Subsurface Structural Features, Paleoearthquake Energy Centers, and Postulated Neotectonic Deformation in the Wabash Valley Region of Southern Illinois and Southern Indiana

[EF3 COL 2.0-27-A]

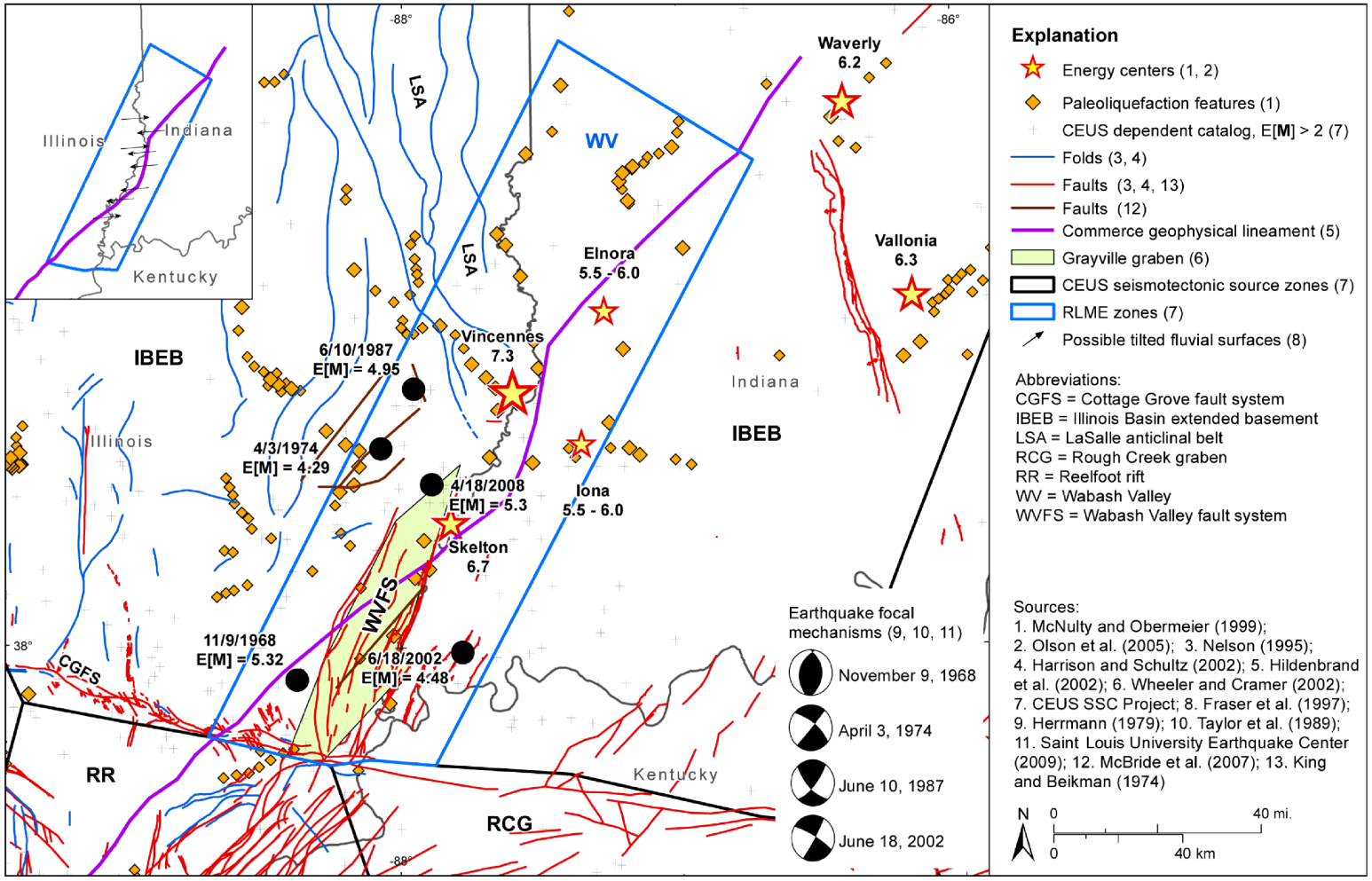

Source: Reference 2.5.2-202, Fig. 6.1.9-2

Figure 2.5.2-231 Seismicity and Tectonic Features of the Charlevoix RLME [EF3 COL 2.0-27-A]

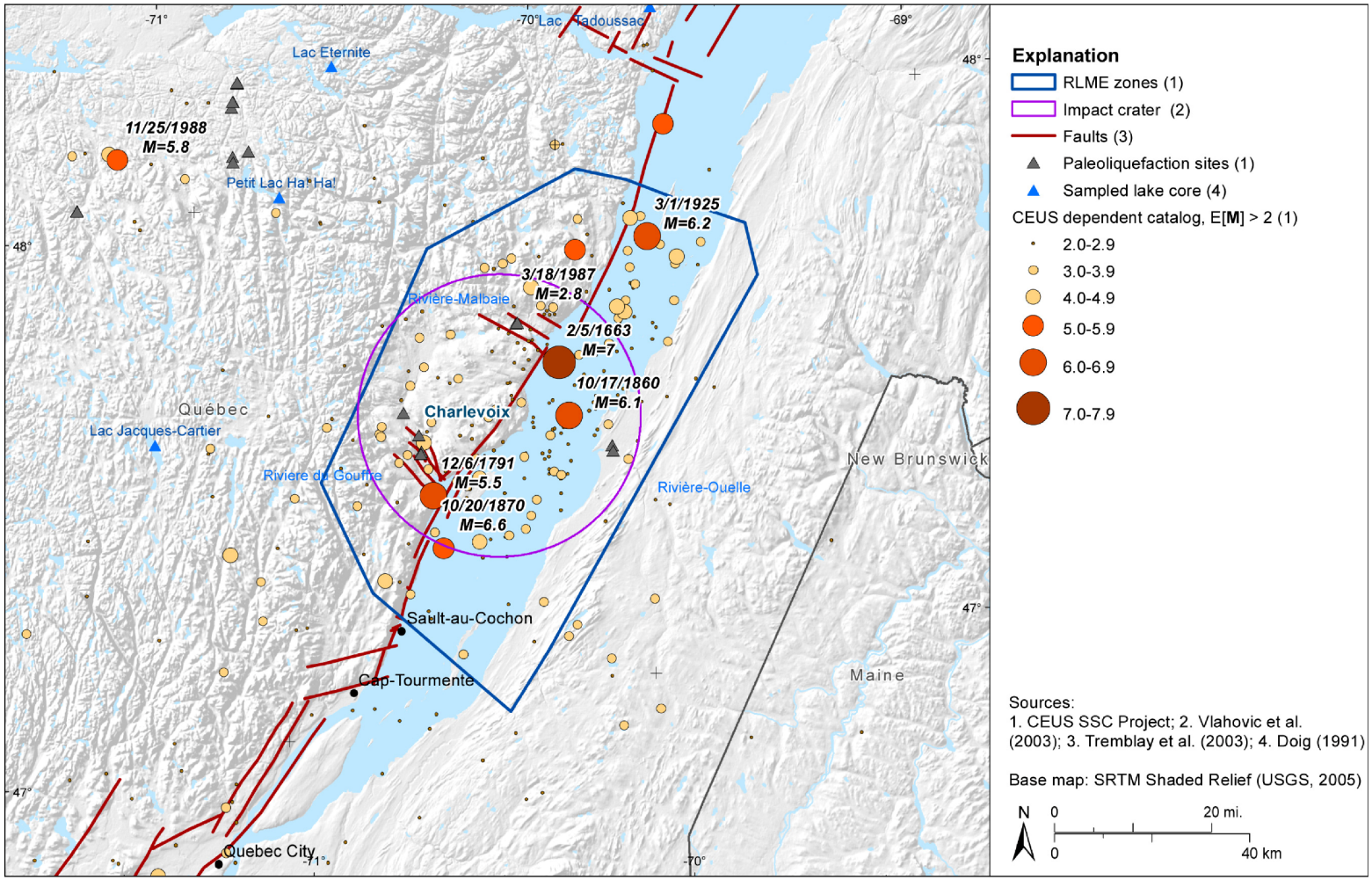

Source: Reference 2.5.2-202, Fig. 6.1.1-2

Figure 2.5.2-232 Postulated Faults and Tectonic Features in the Charleston Region with Charleston RLME Source Zones [EF3 COL 2.0-27-A]

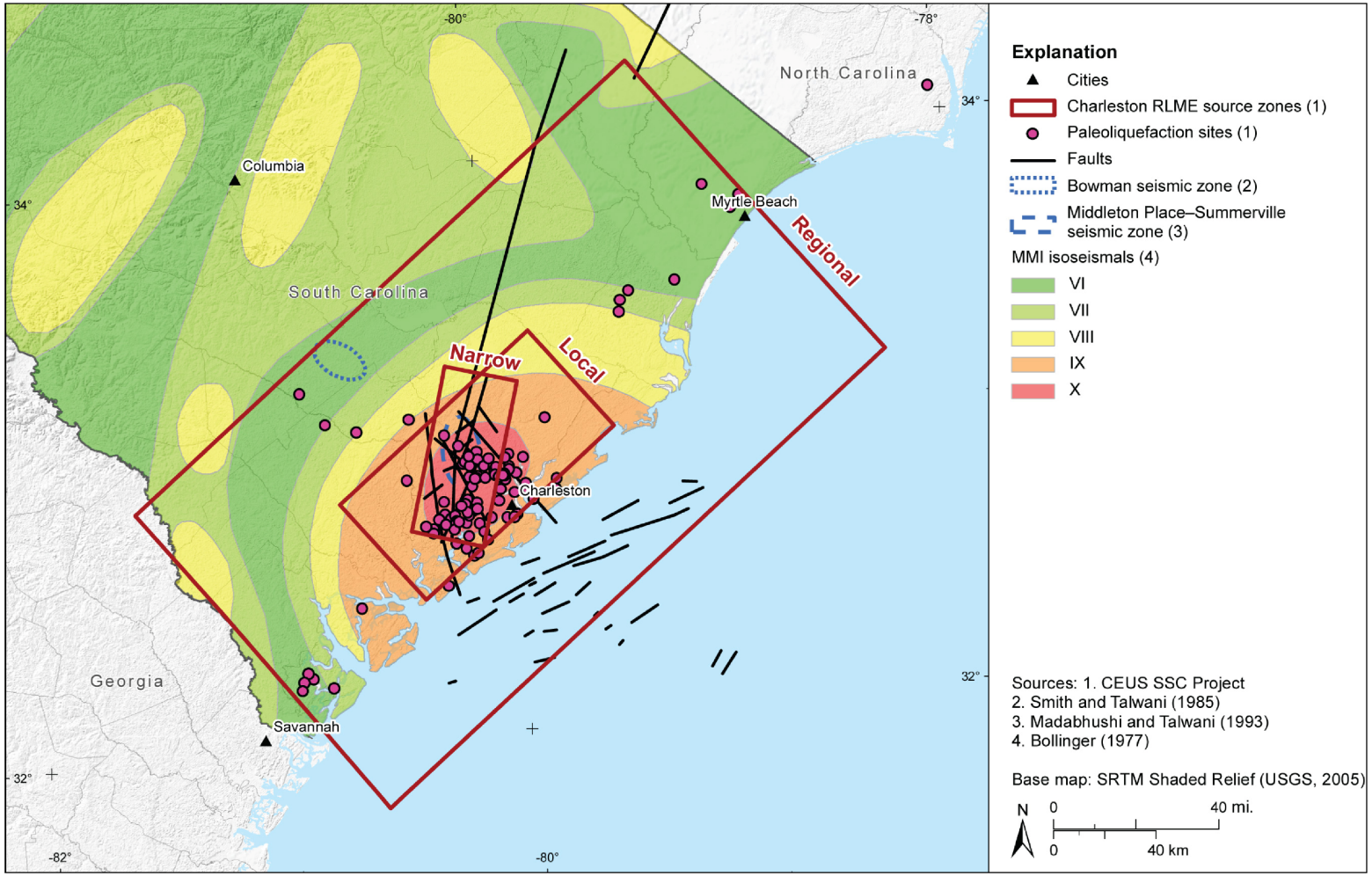

Source: Reference 2.5.2-202, Fig. 6.1.2-5a

Figure 2.5.2-233 Earthquake Catalog for CEUS SSC Model with Location of Earthquakes with E[M] Greater than 4.3 from 2009 to 2012 [EF3 COL 2.0-27-A]

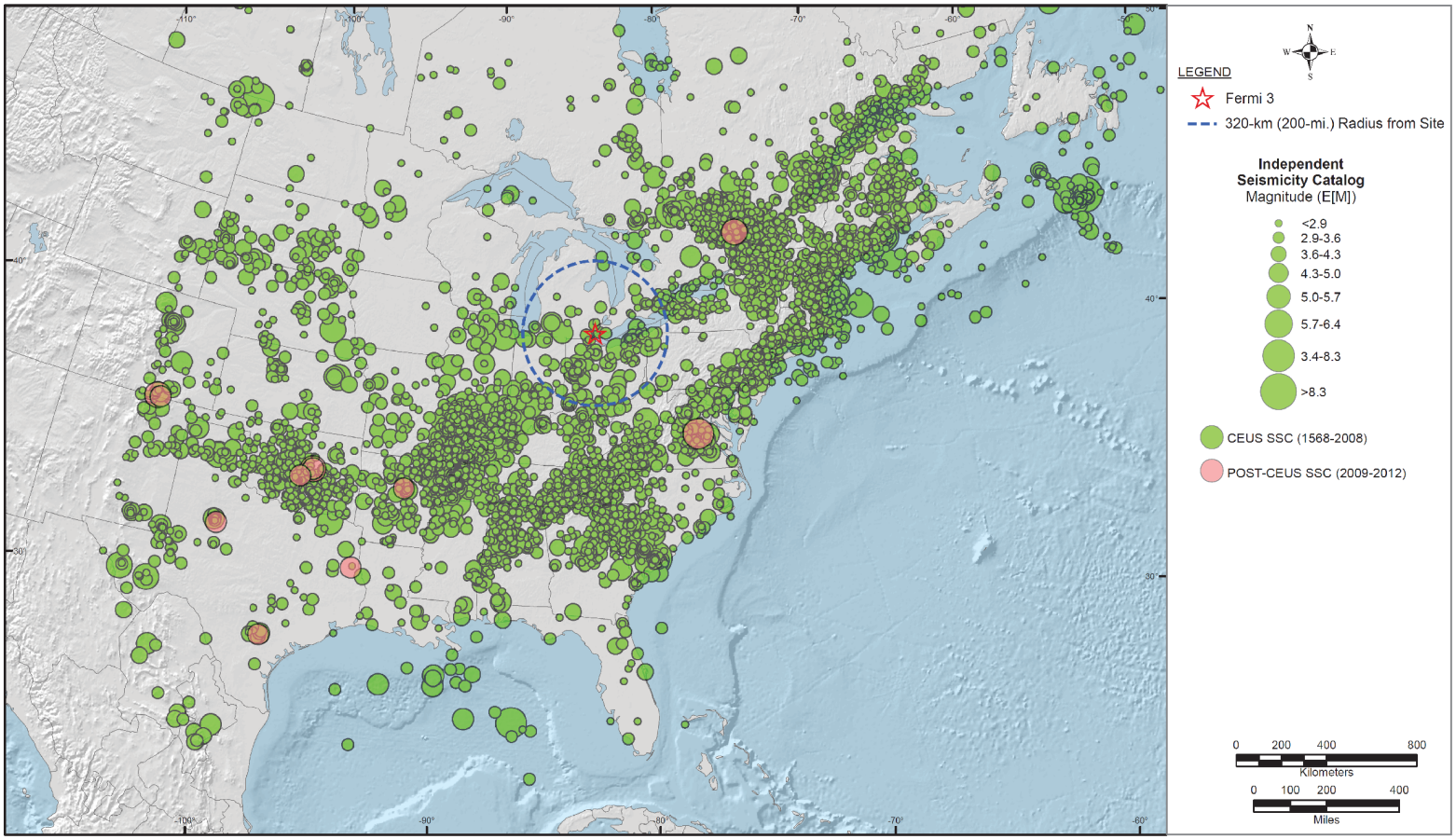

Figure 2.5.2-234 Mmax Distributions for Source Zone NMESE-W Based on NUREG-2115 Inputs and Updated Inputs
[EF3 COL 2.0-27-A]

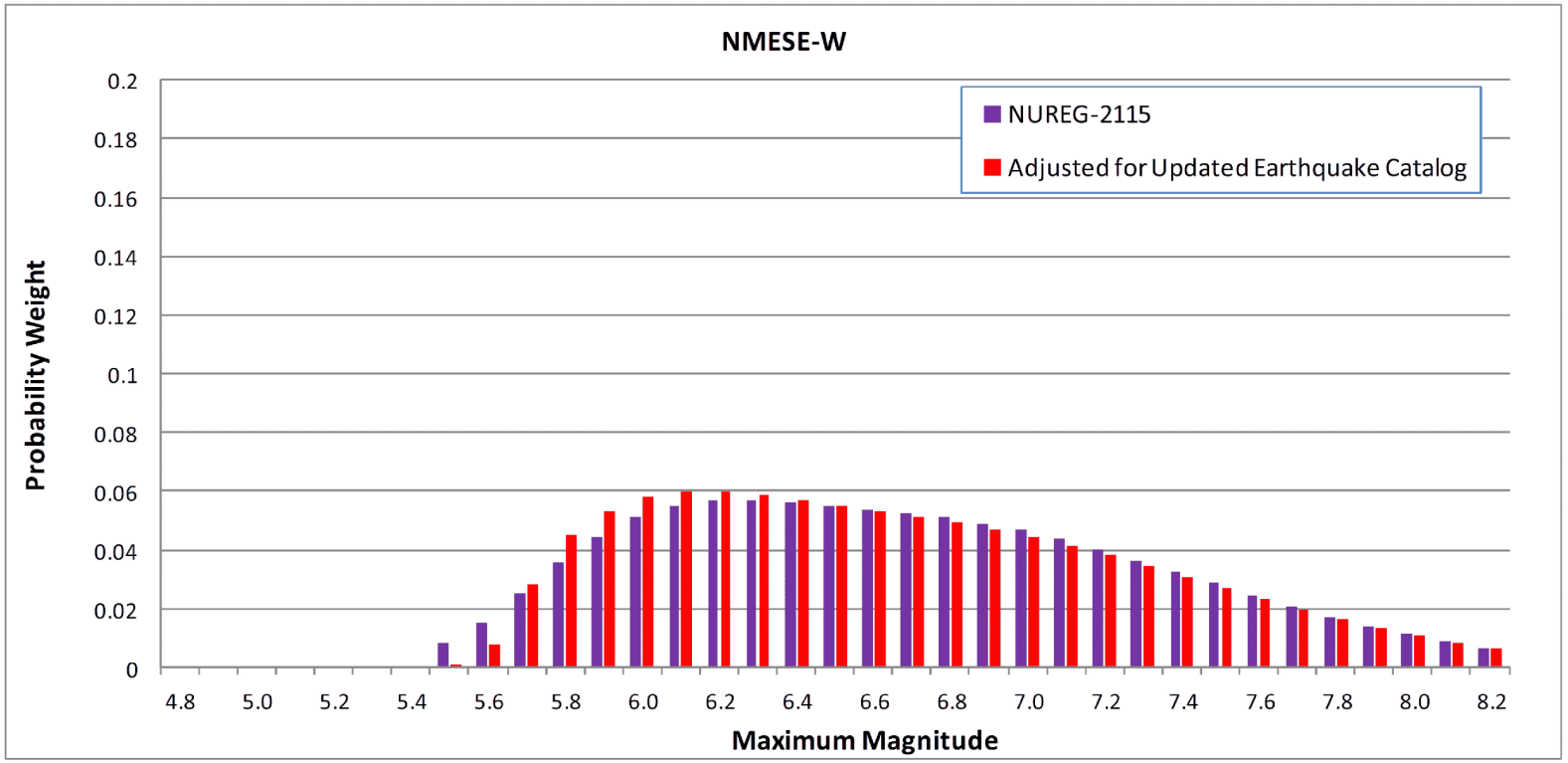

Figure 2.5.2-235 Mmax Distributions for Source Zone ECC-AM Based on NUREG-2115 Inputs and Updated Inputs

[EF3 COL 2.0-27-A]

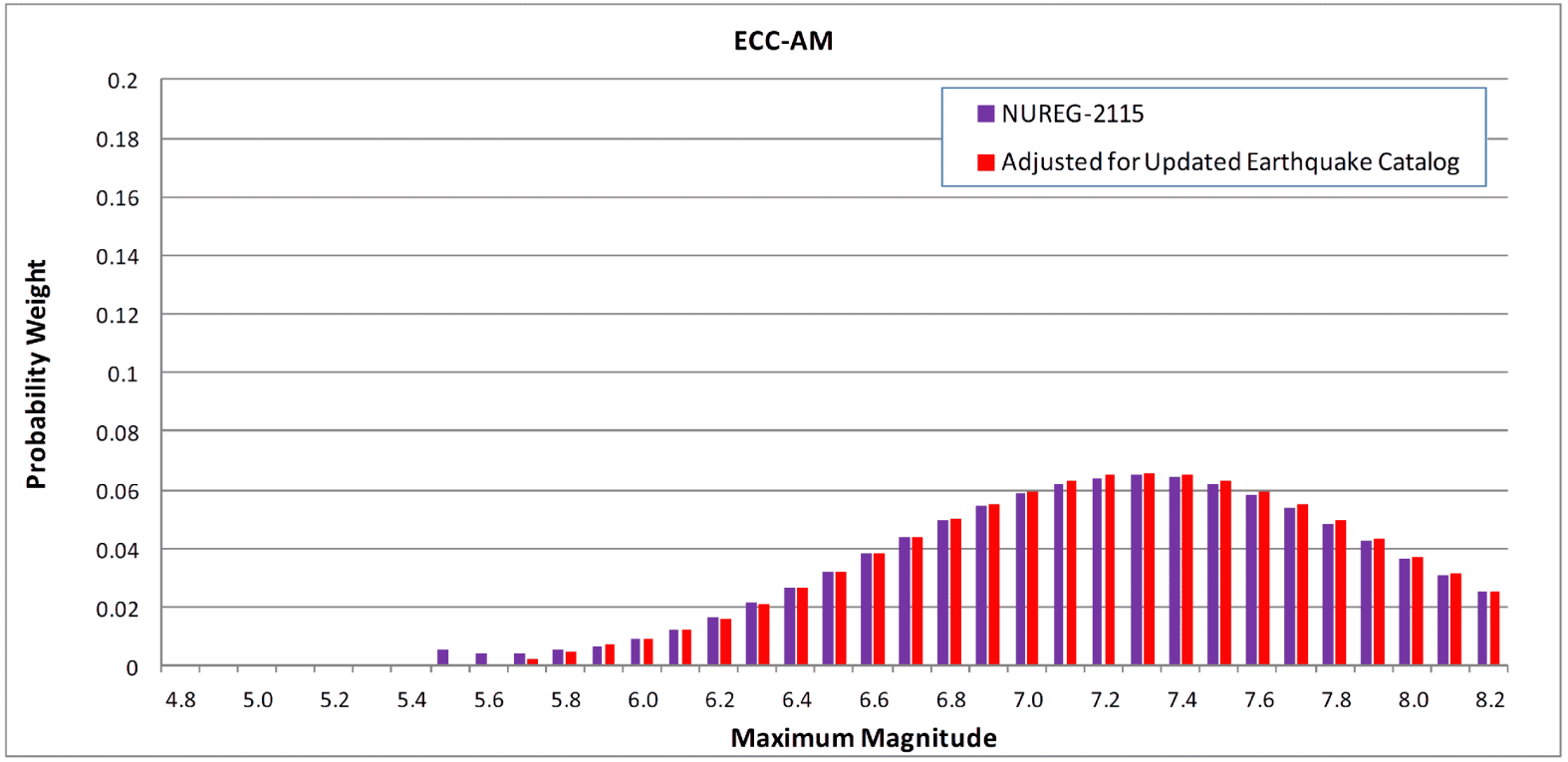

Figure 2.5.2-236 Mmax Distributions for Source Zones MIDC-A and MIDC-B Based on NUREG-2115 Inputs and Updated Inputs [EF3 COL 2.0-27-A]

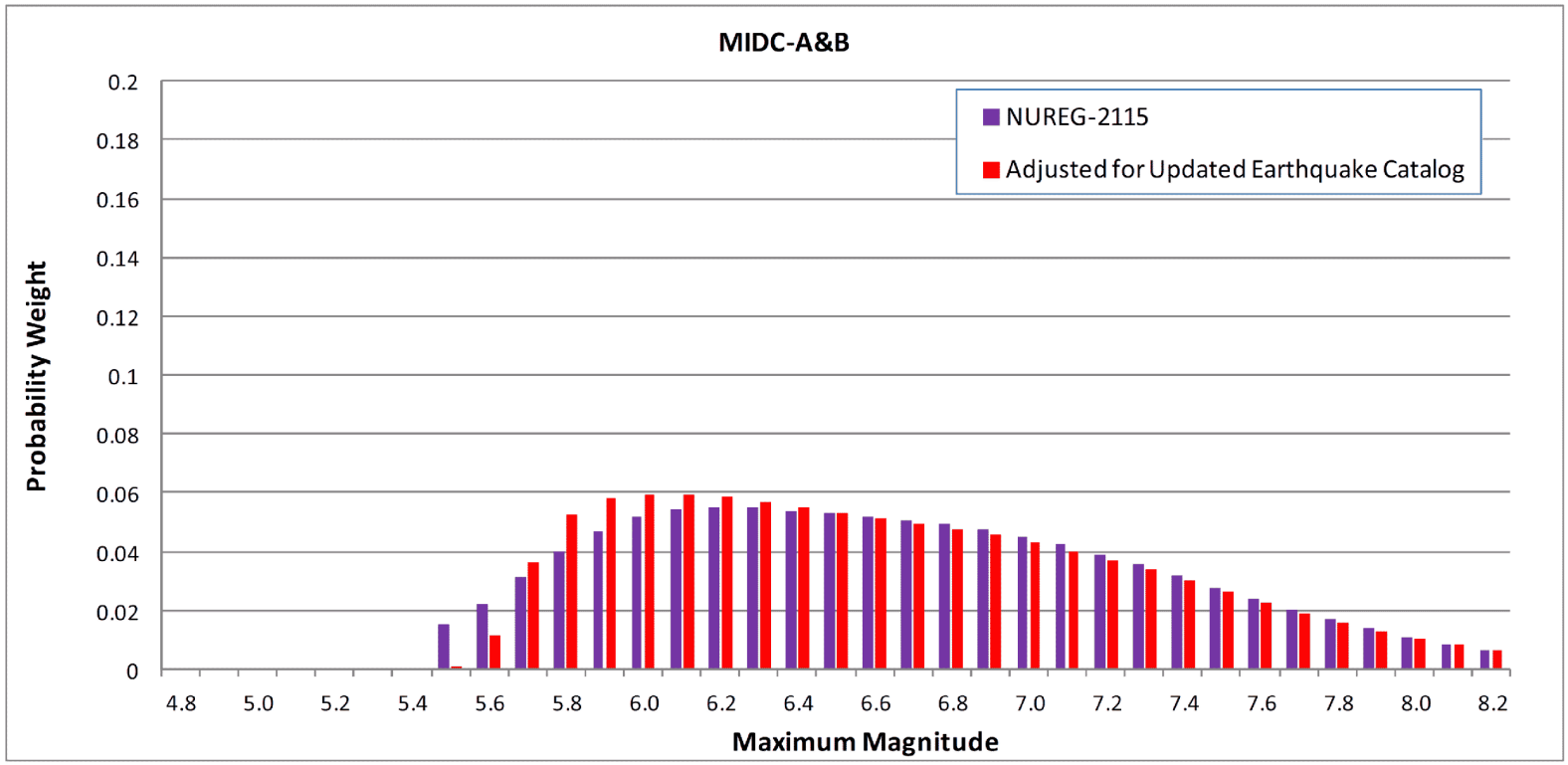

Figure 2.5.2-237 Mmax Distributions for Source Zones MIDC-C and MIDC-D Based on NUREG-2115 Inputs and Updated Inputs [EF3 COL 2.0-27-A]

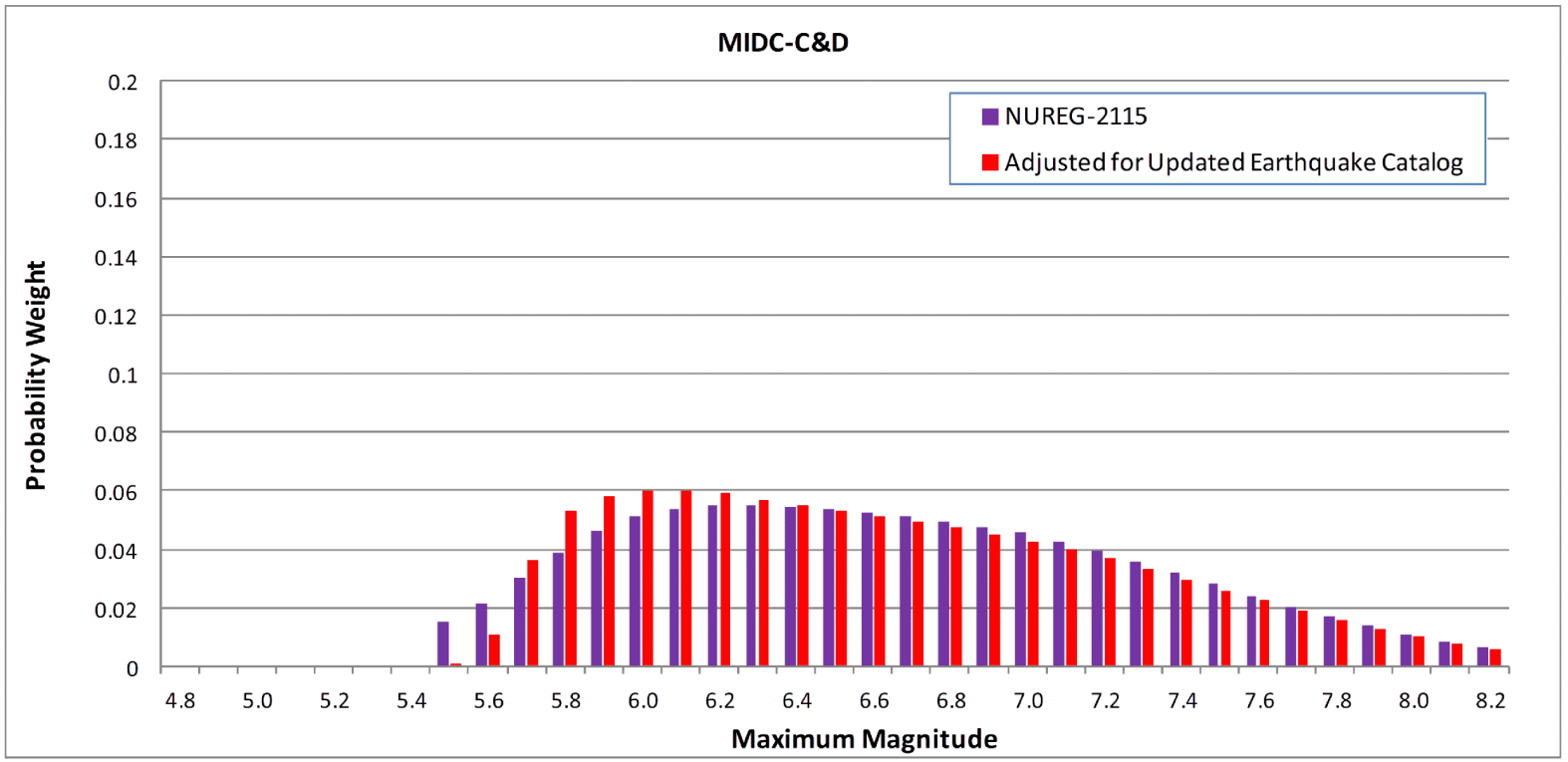

Figure 2.5.2-238 Ground Motion Characterization Logic Tree Used in the PSHA for the Fermi 3 Site [EF3 COL 2.0-27-A]

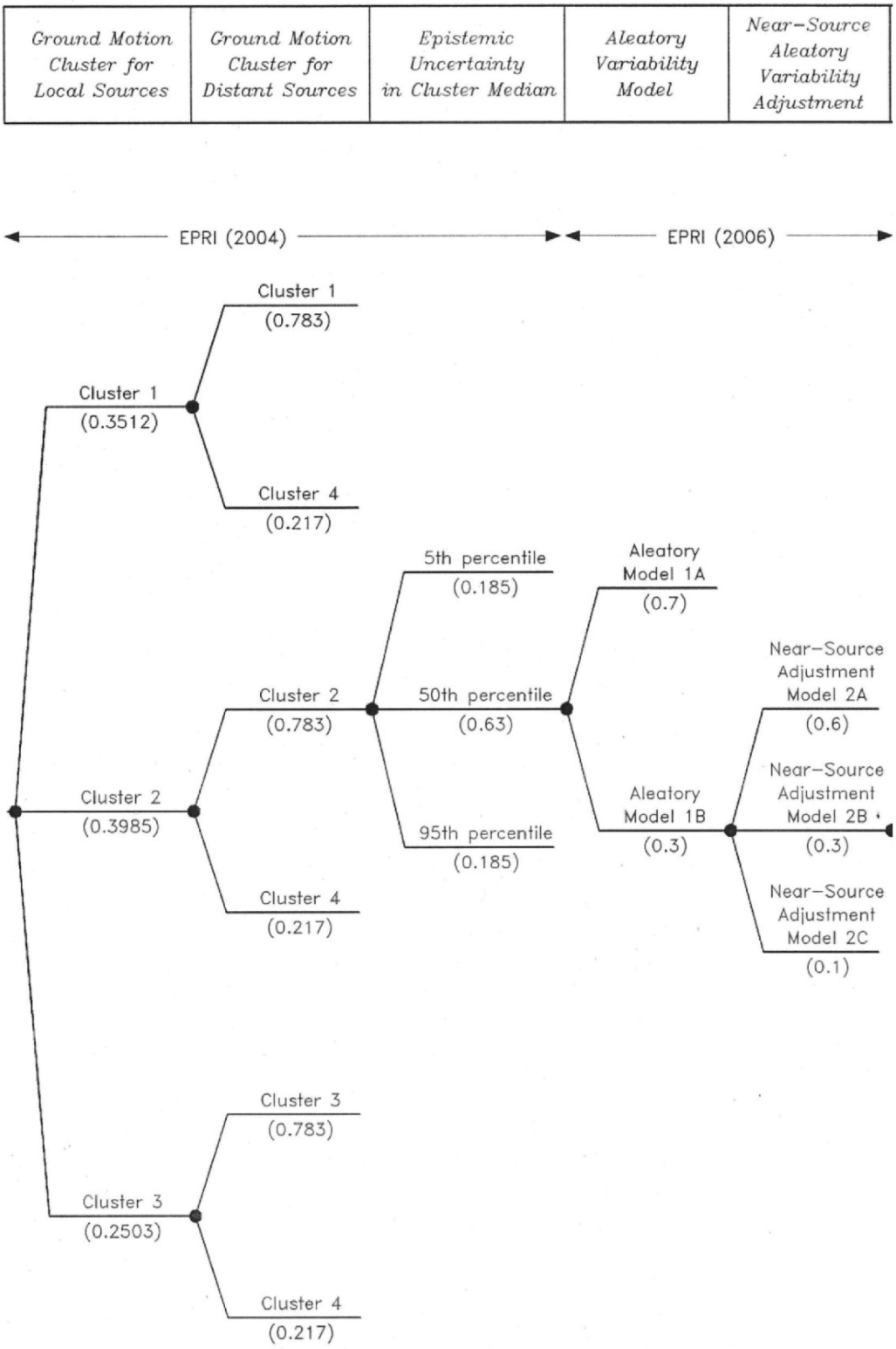

Figure 2.5.2-239a Comparison of Median Ground Motion Model Used in the PSHA with Recently Published Models - Cluster 1 [EF3 COL 2.0-27-A]

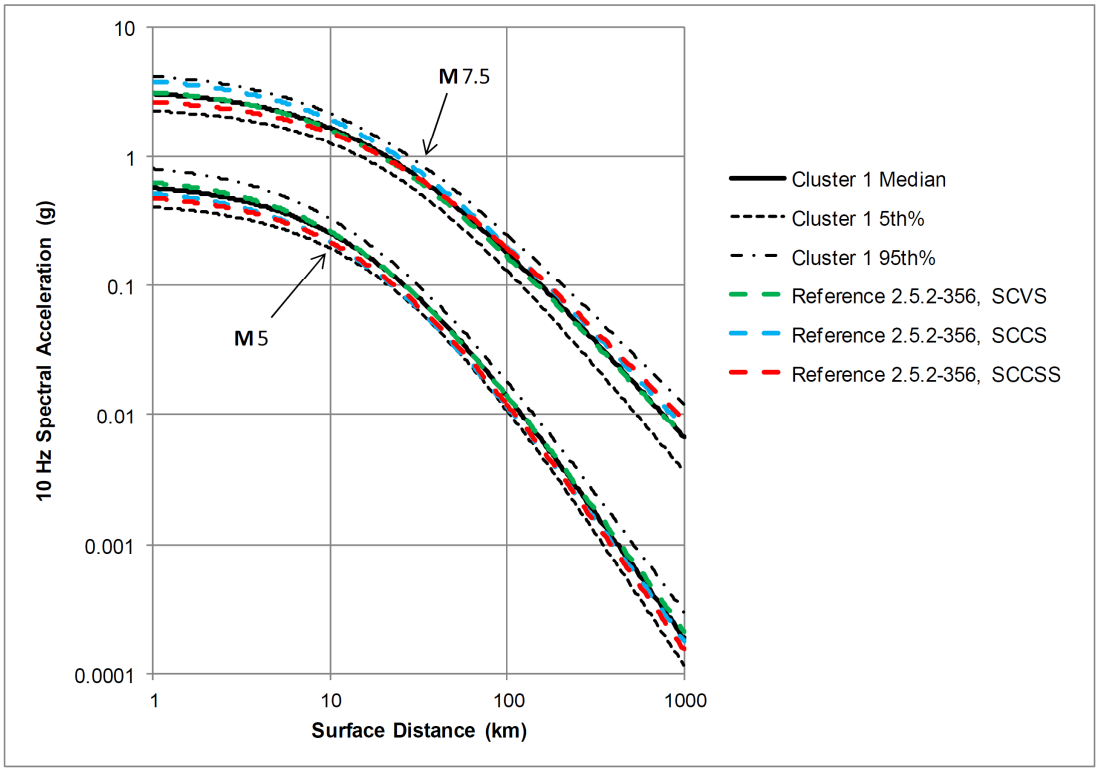

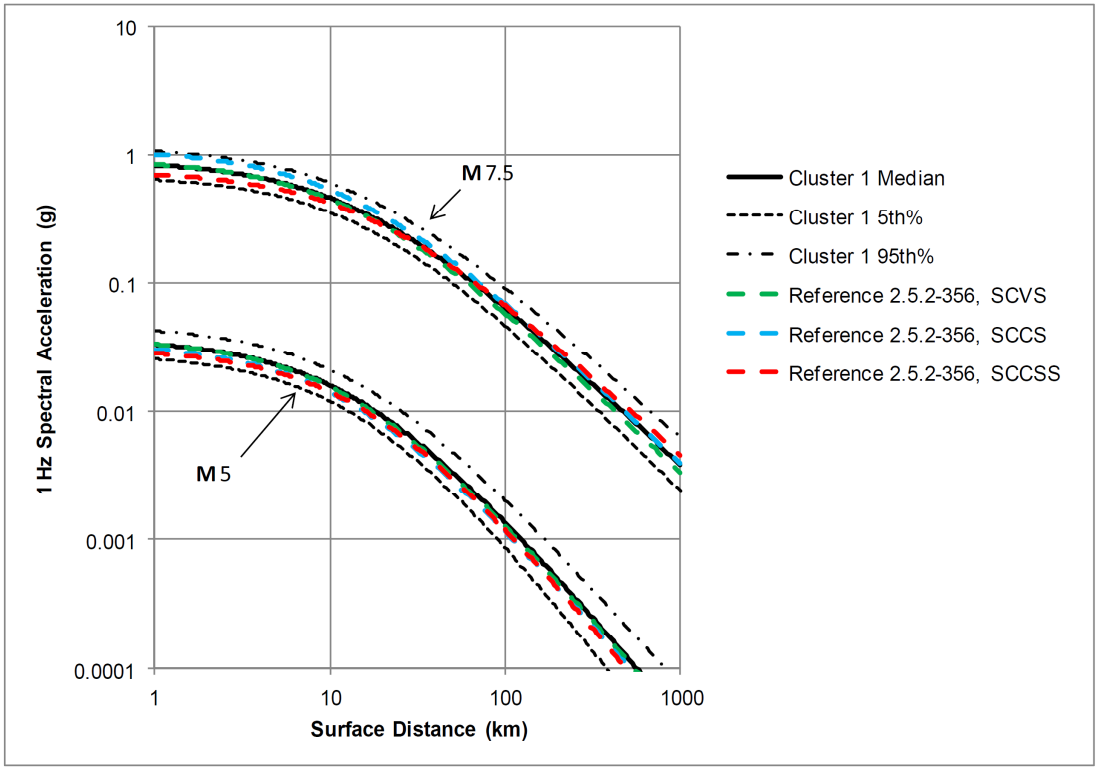

Figure 2.5.2-239b Comparison of Median Ground Motion Model Used in the PSHA with Recently Published Models - Cluster 2 [EF3 COL 2.0-27-A]

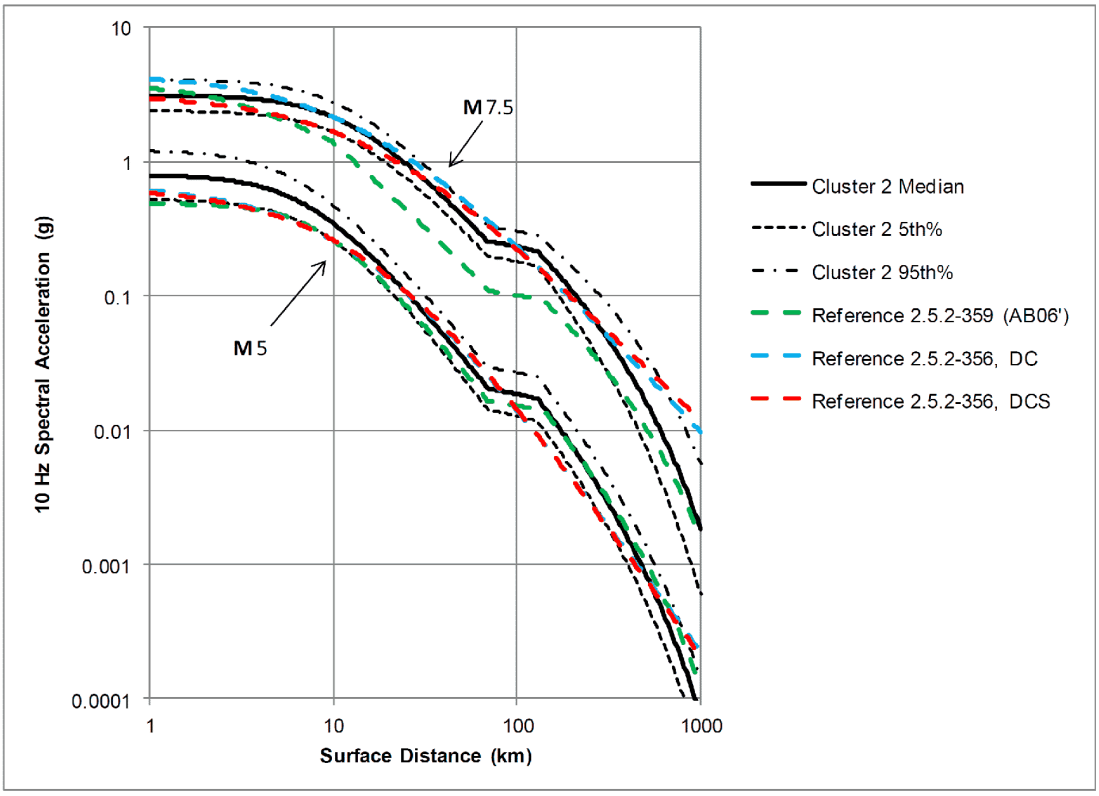

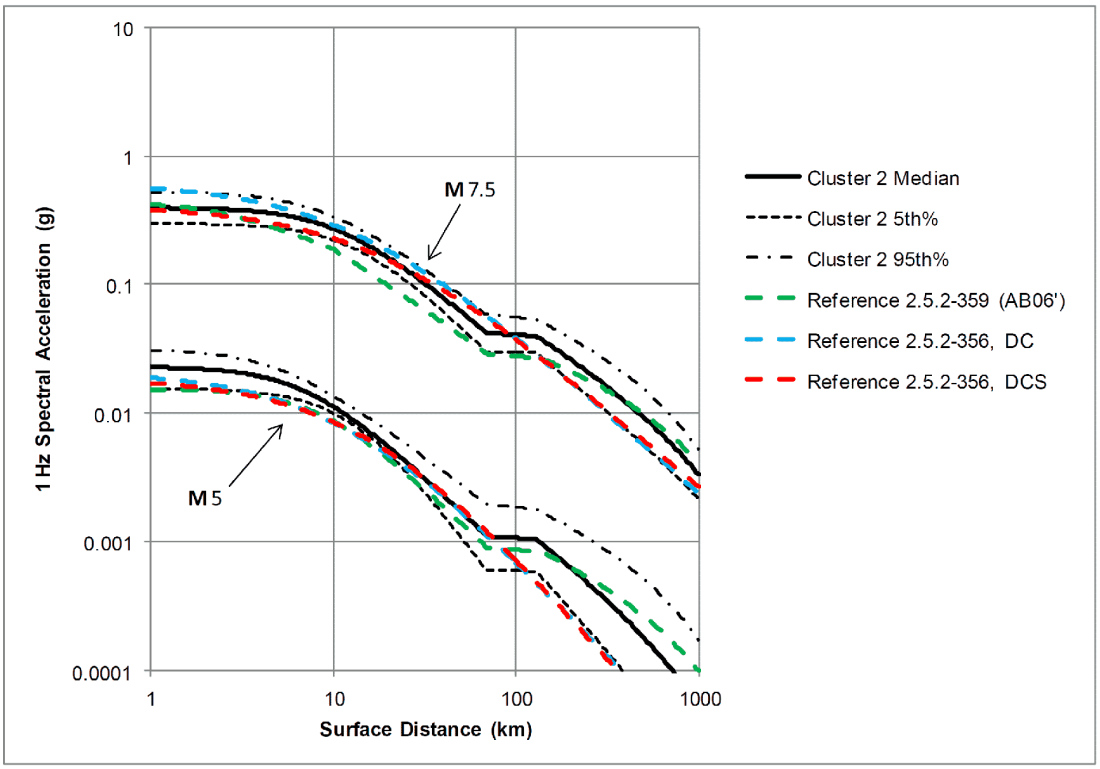

Figure 2.5.2-239c Comparison of Median Ground Motion Models Used in the PSHA with Recently Published - Cluster 3 [EF3 COL 2.0-27-A]

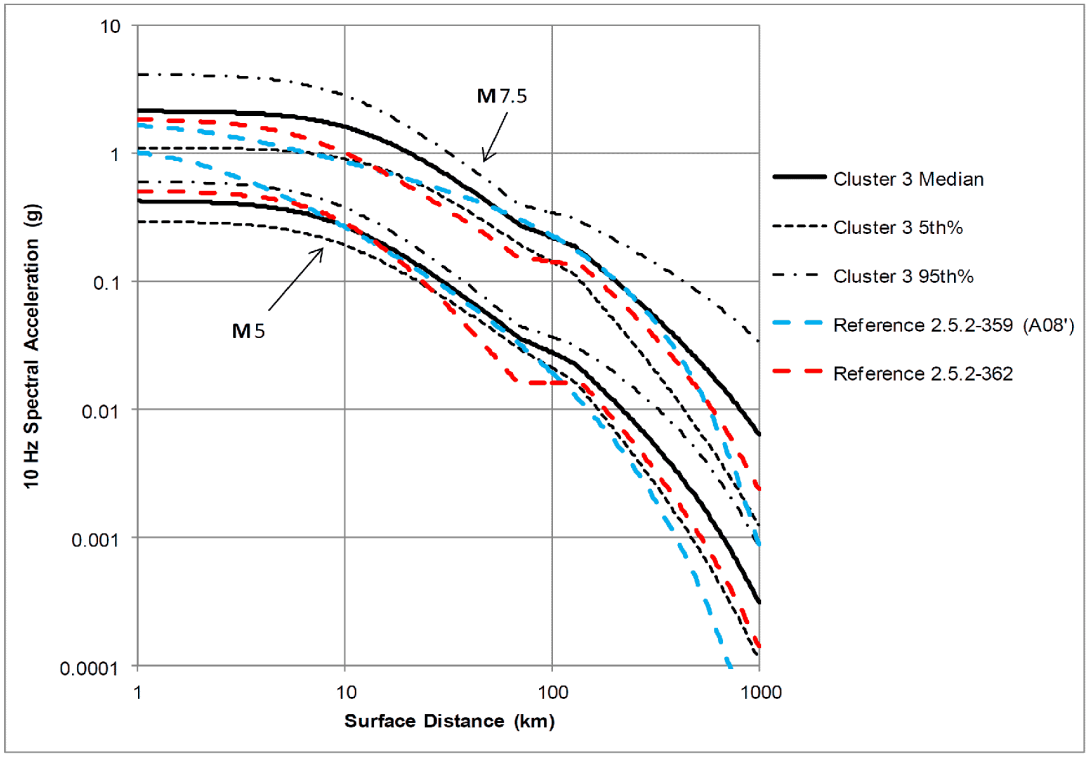

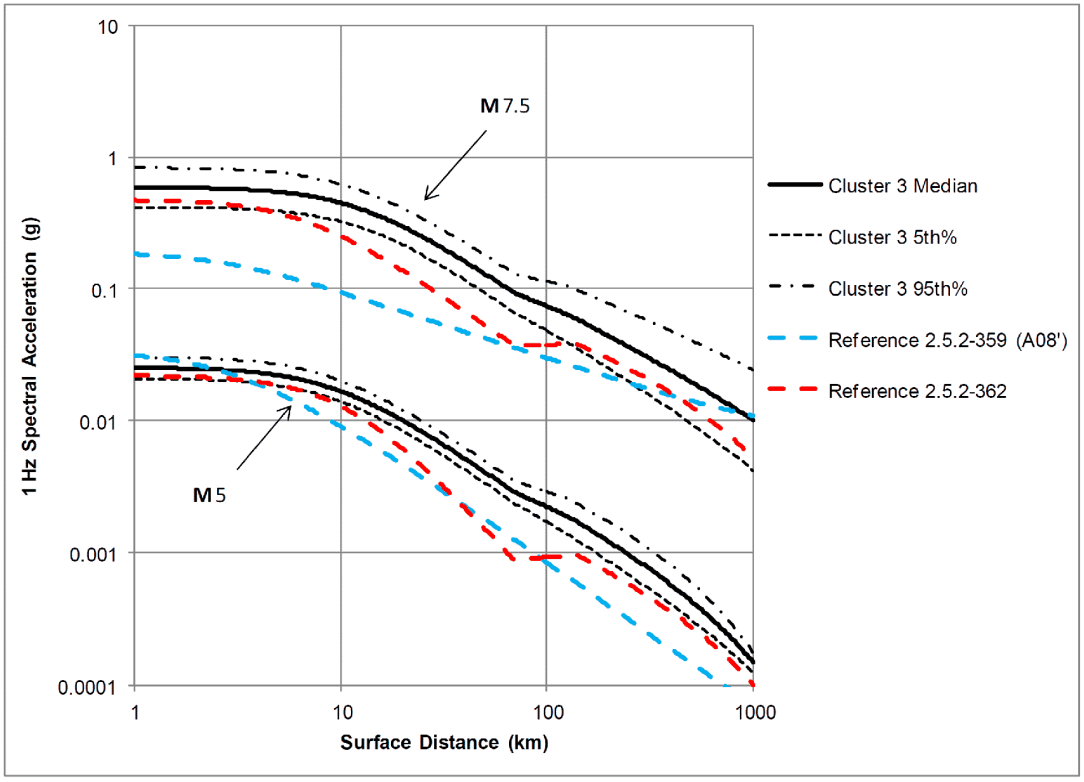

Figure 2.5.2-240 **Contribution of Individual RLME Sources to the Mean Hazard for 1 Hz Spectral Acceleration at the Fermi 3 Site** [EF3 COL 2.0-27-A]

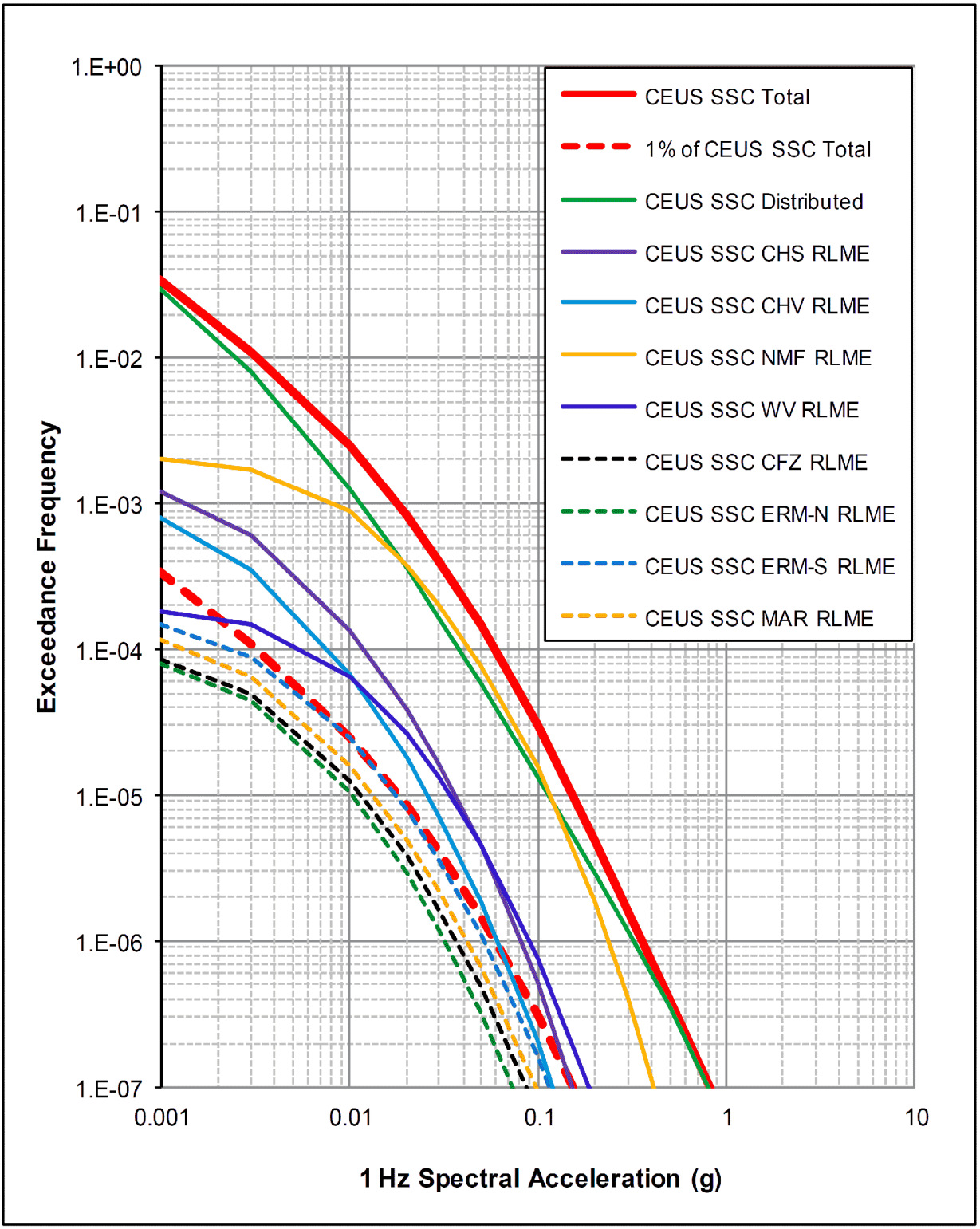

Figure 2.5.2-241 **Contribution of Individual RLME Source to the Mean Hazard for 10 Hz Spectral Acceleration at the Fermi 3 Site** [EF3 COL 2.0-27-A]

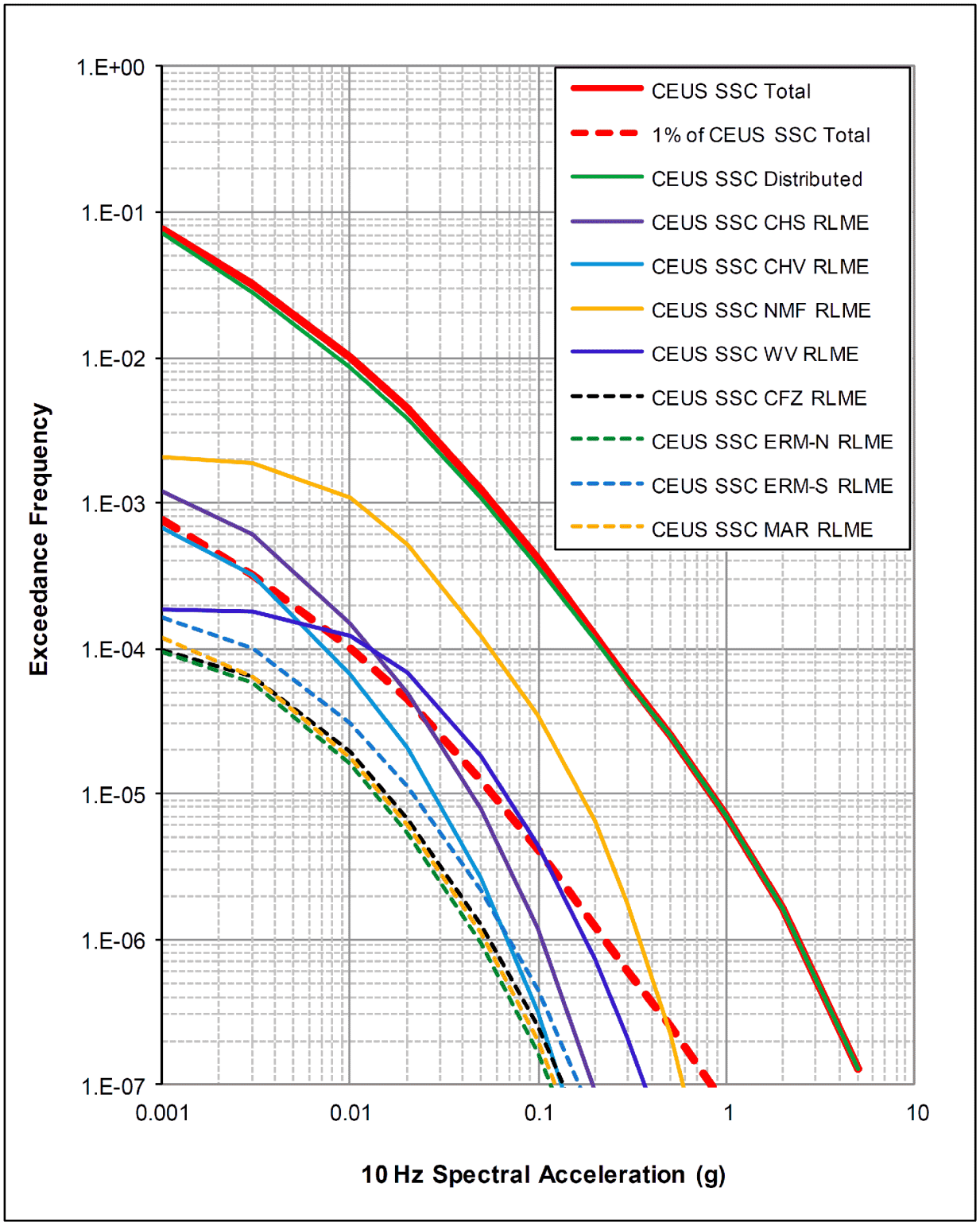

Figure 2.5.2-242 Generic CEUS Hard Rock Hazard Results for 0.5 Hz Spectral Accelerations for the Fermi 3 Site [EF3 COL 2.0-27-A]

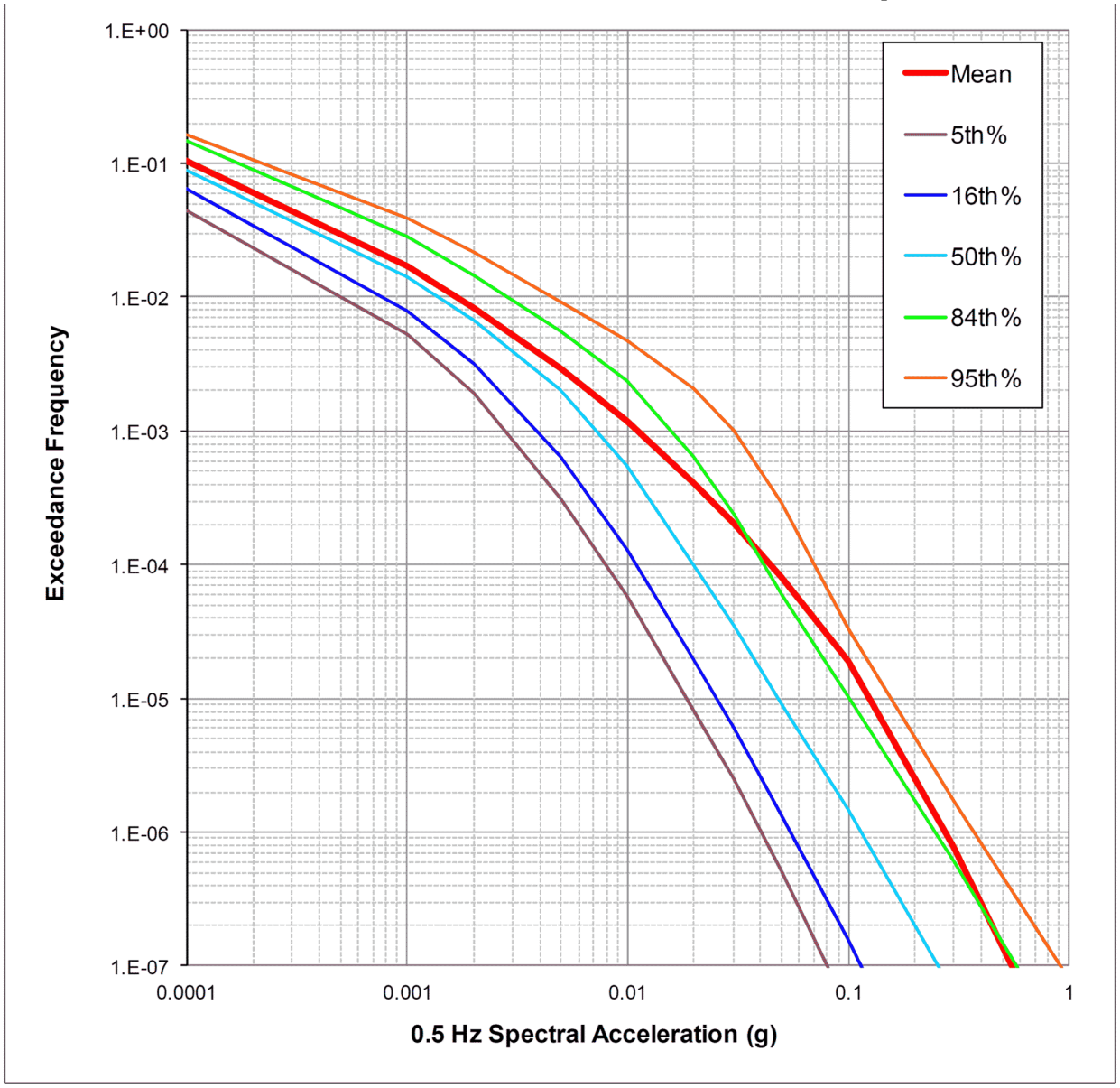

Figure 2.5.2-243 Generic CEUS Hard Rock Hazard Results for 1.0 Hz Spectral Accelerations for the Fermi 3 Site [EF3 COL 2.0-27-A]

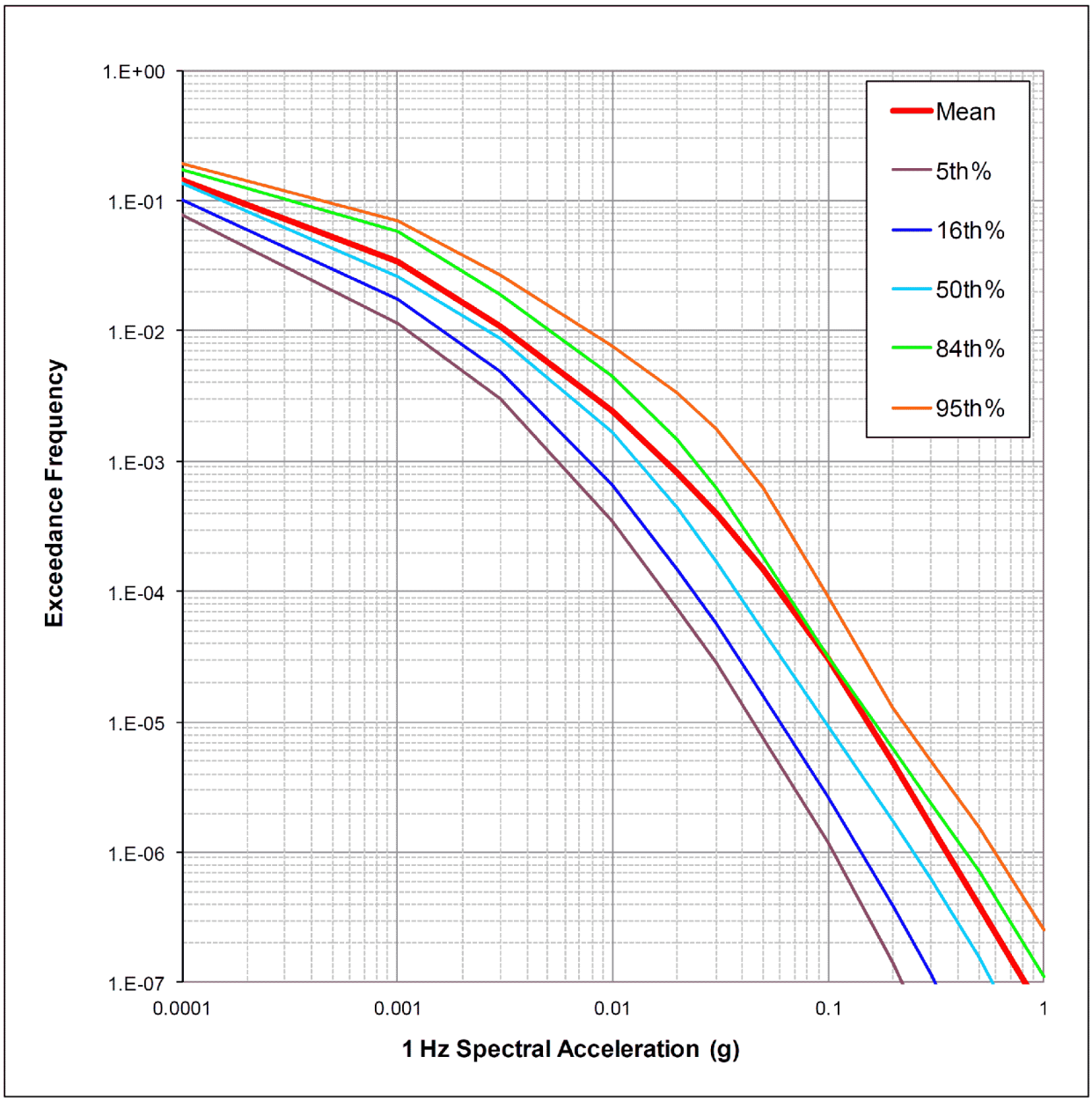

Figure 2.5.2-244 **Generic CEUS Hard Rock Hazard Results for 2.5 Hz Spectral Accelerations for the Fermi 3 Site** [EF3 COL 2.0-27-A]

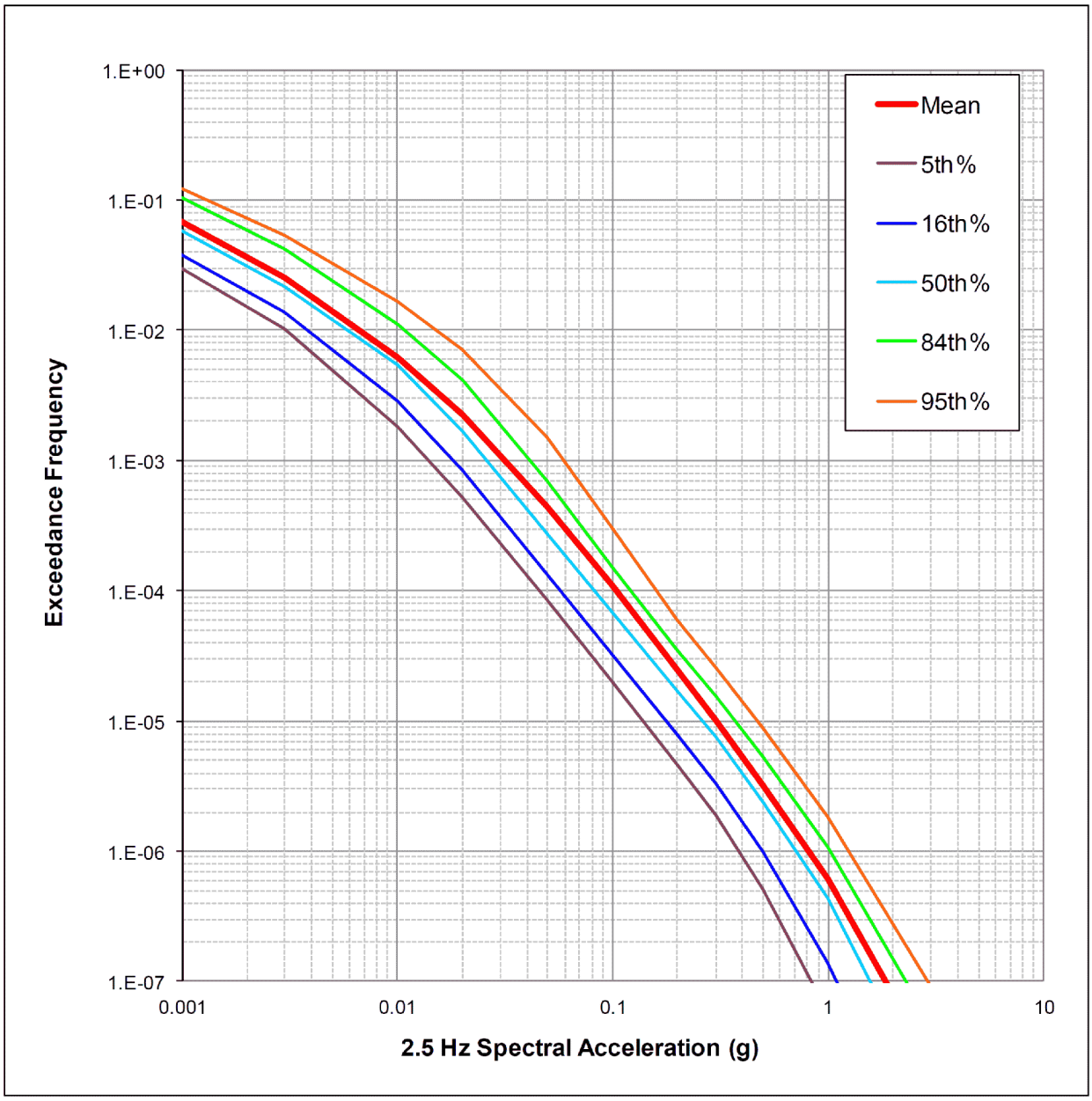

Figure 2.5.2-245 Generic CEUS Hard Rock Hazard Results for 5 Hz Spectral Accelerations for the Fermi 3 Site [EF3 COL 2.0-27-A]

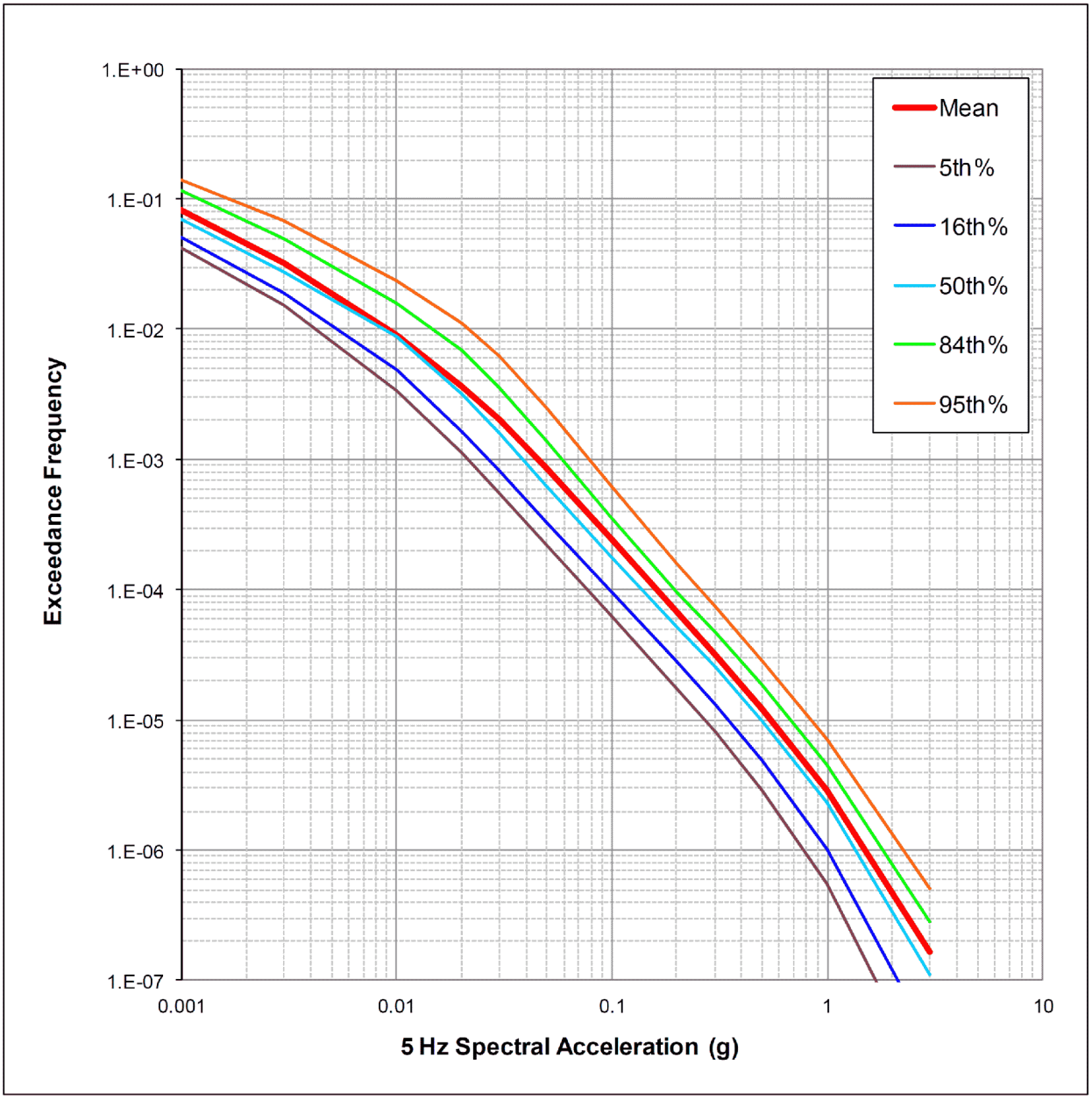

Figure 2.5.2-246 **Generic CEUS Hard Rock Hazard Results for 10 Hz Spectral Accelerations for the Fermi 3 Site** [EF3 COL 2.0-27-A]

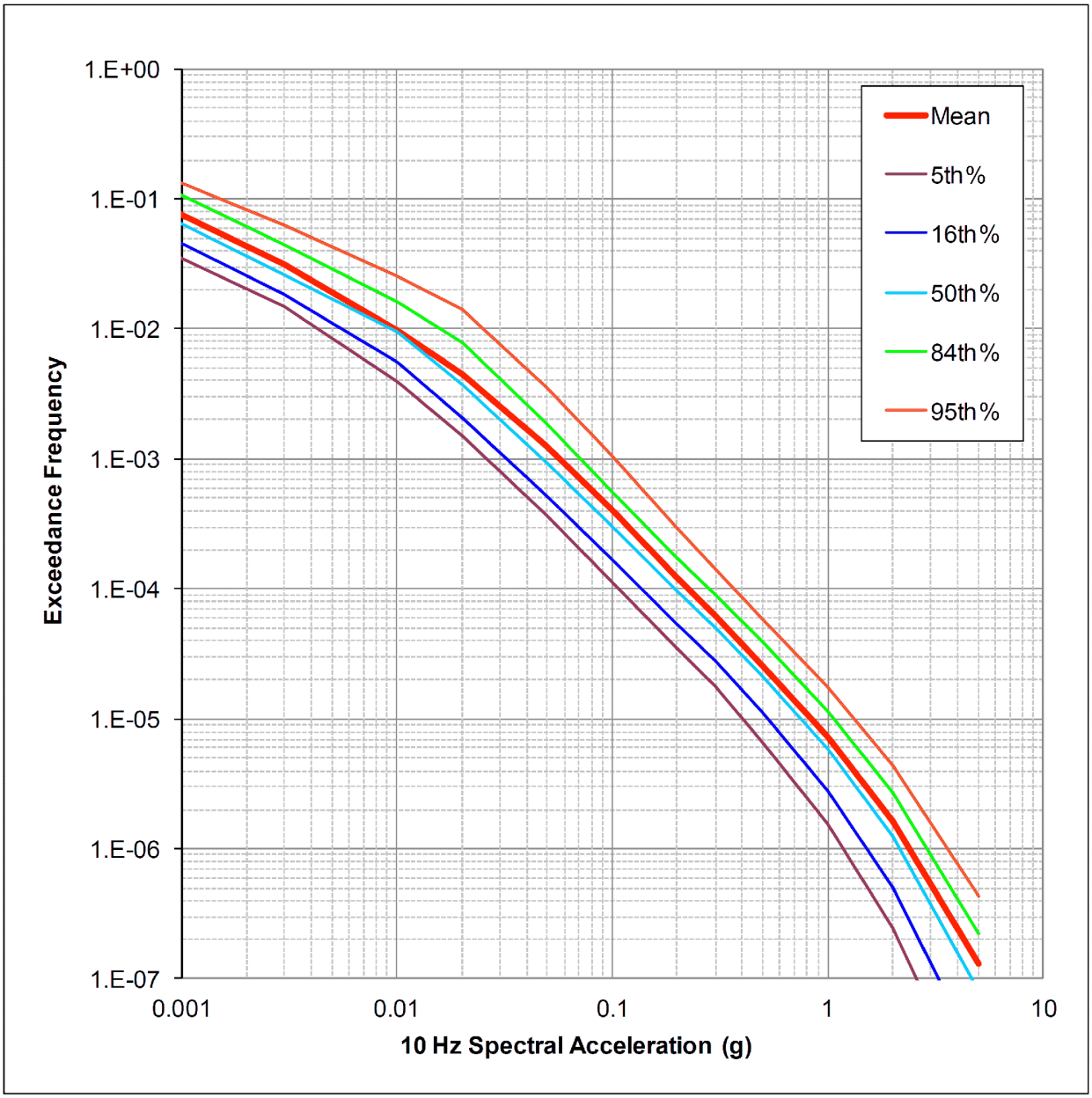

Figure 2.5.2-247 Generic CEUS Hard Rock Hazard Results for 25 Hz Spectral Accelerations for the Fermi 3 Site [EF3 COL 2.0-27-A]

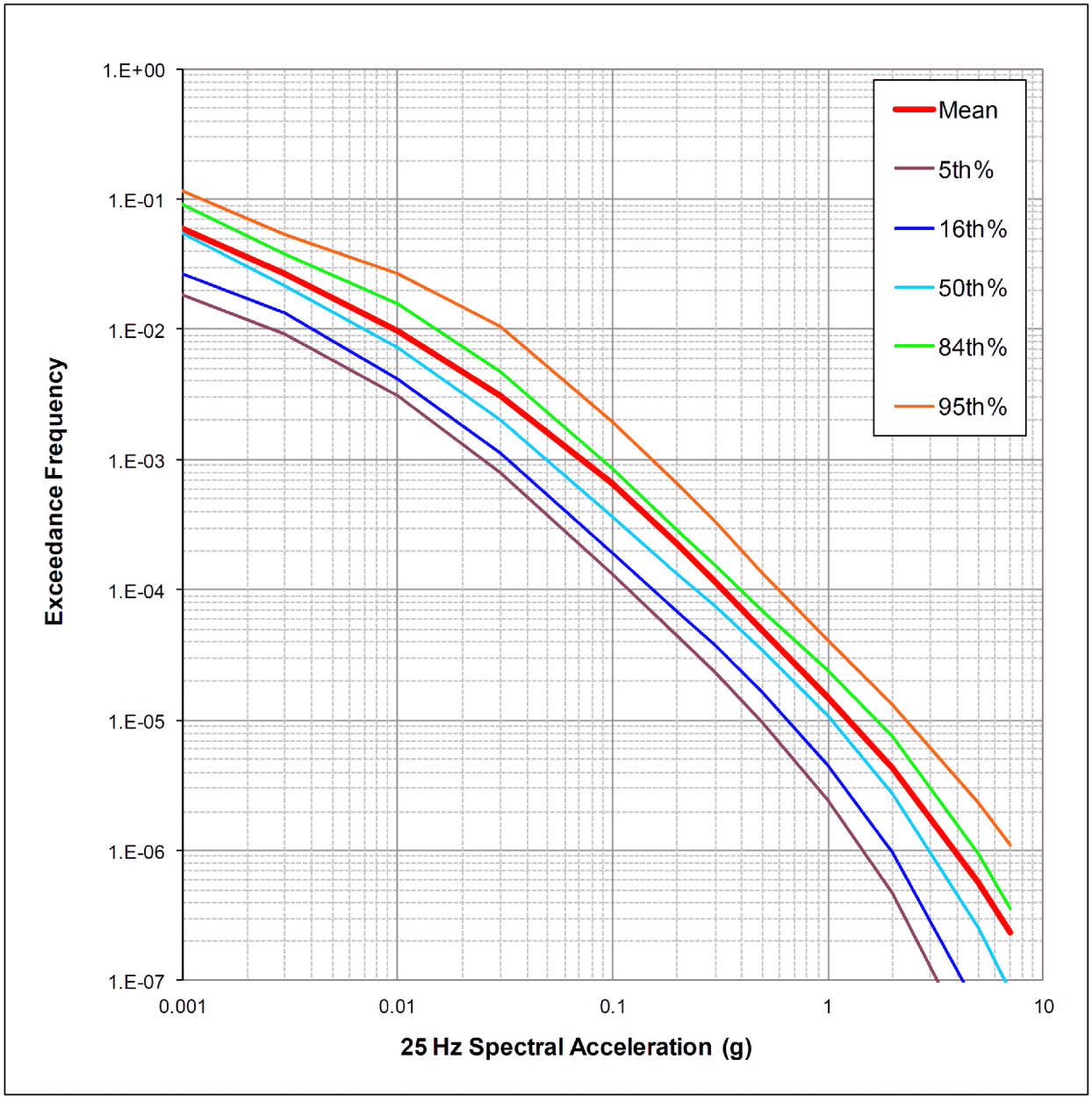

Figure 2.5.2-248 **Generic CEUS Hard Rock Hazard Results for Peak Ground Acceleration (100 Hz Spectral Accelerations) for the Fermi 3 Site**
[EF3 COL 2.0-27-A]

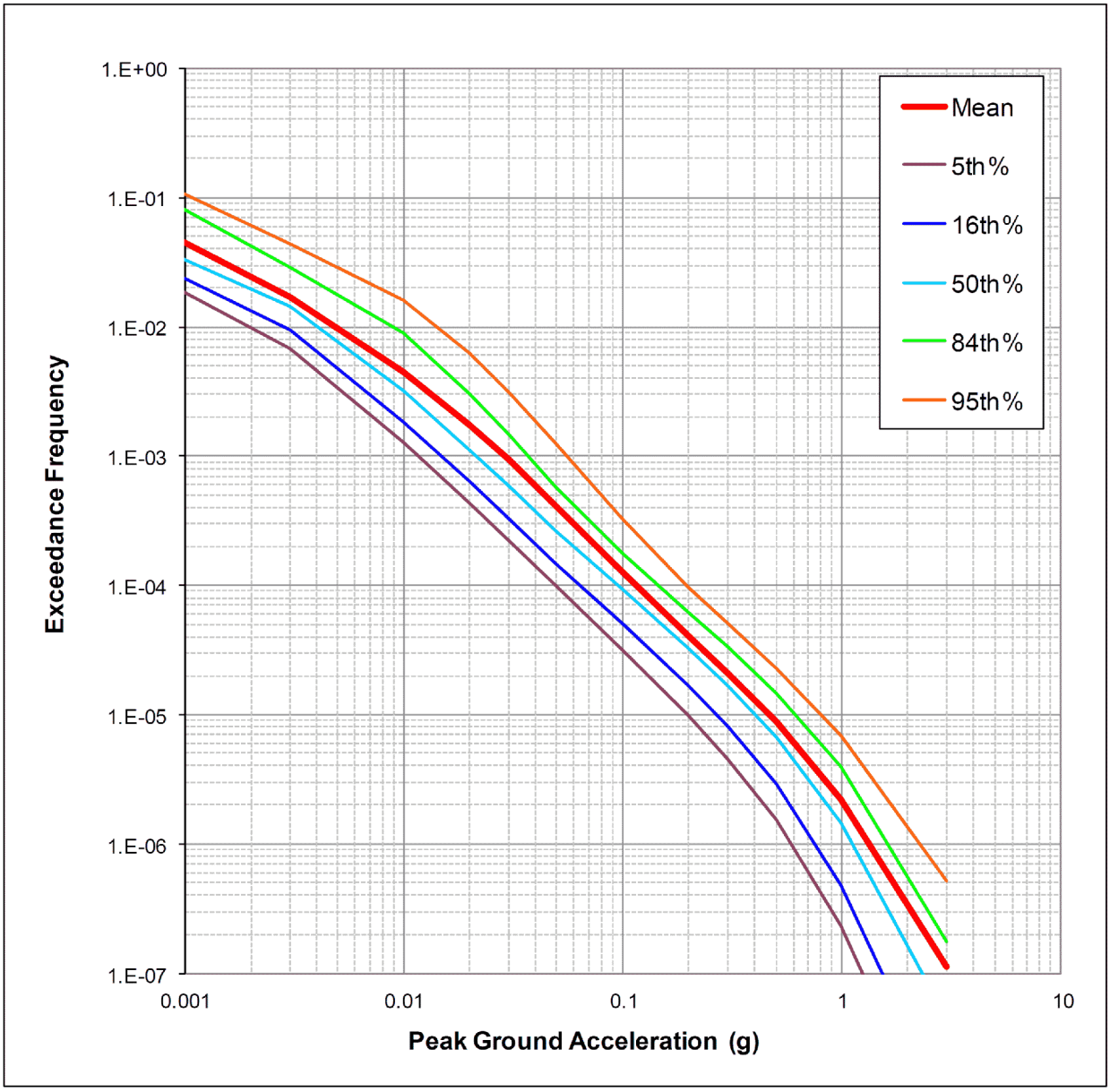

Figure 2.5.2-249 **Contribution of CEUS SSC Model Sources to the Total Mean Hazard for 0.5 Hz Spectral Acceleration** [EF3 COL 2.0-27-A]

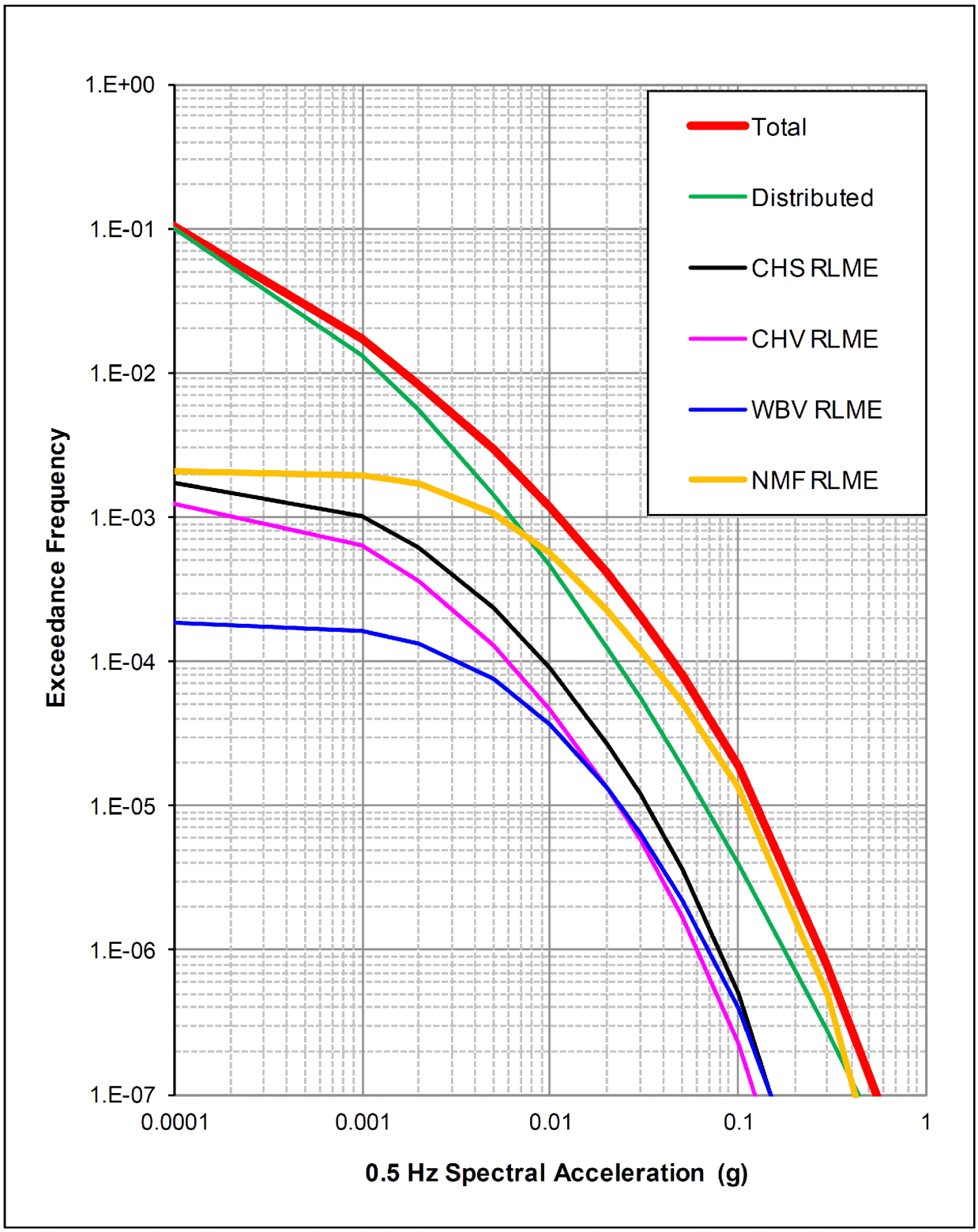

Figure 2.5.2-250 **Contribution of CEUS SSC Model Sources to the Total Mean Hazard for 1 Hz Spectral Acceleration** [EF3 COL 2.0-27-A]

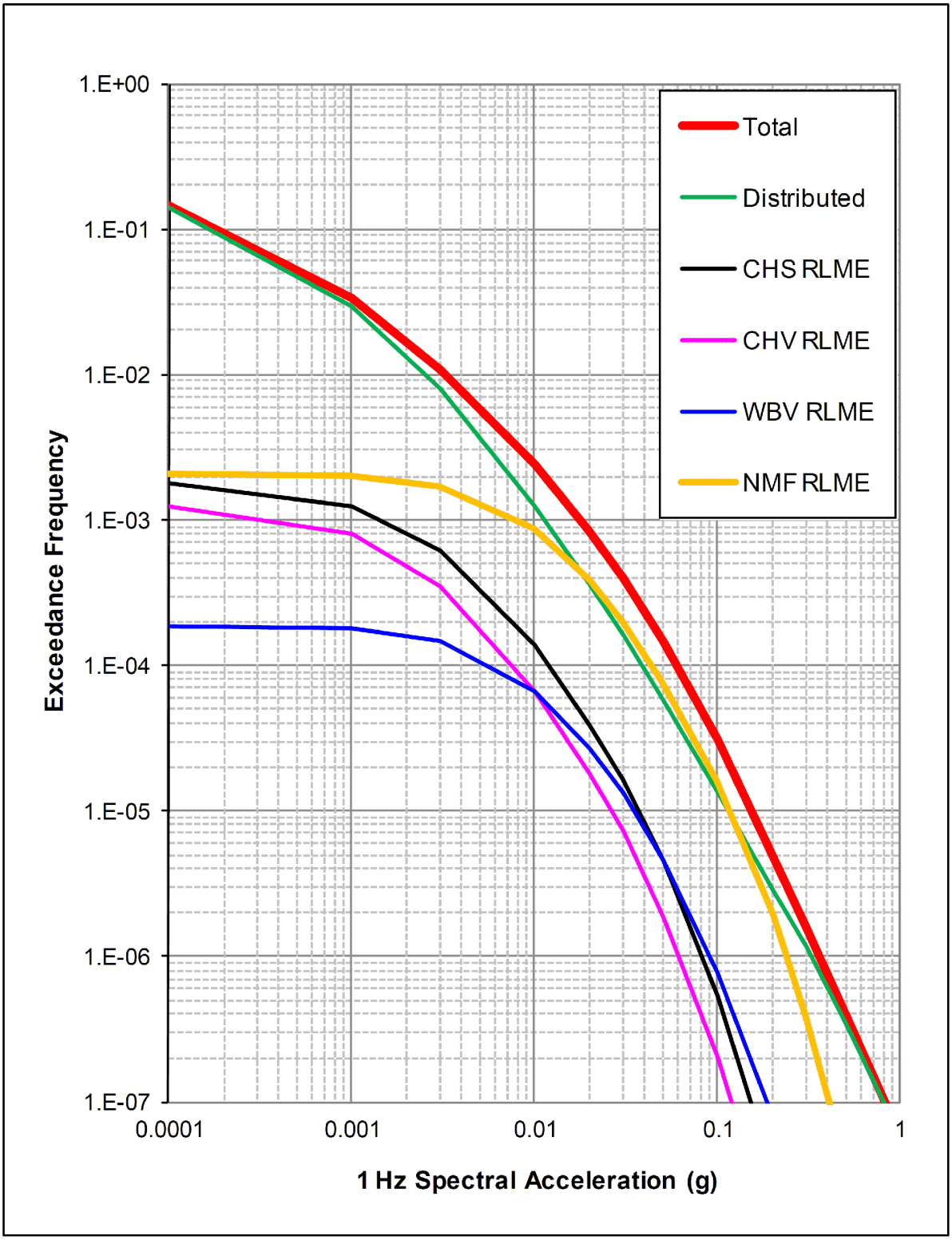

Figure 2.5.2-251 **Contribution of CEUS SSC Model Sources to the Total Mean Hazard for 2.5 Hz Spectral Acceleration** [EF3 COL 2.0-27-A]

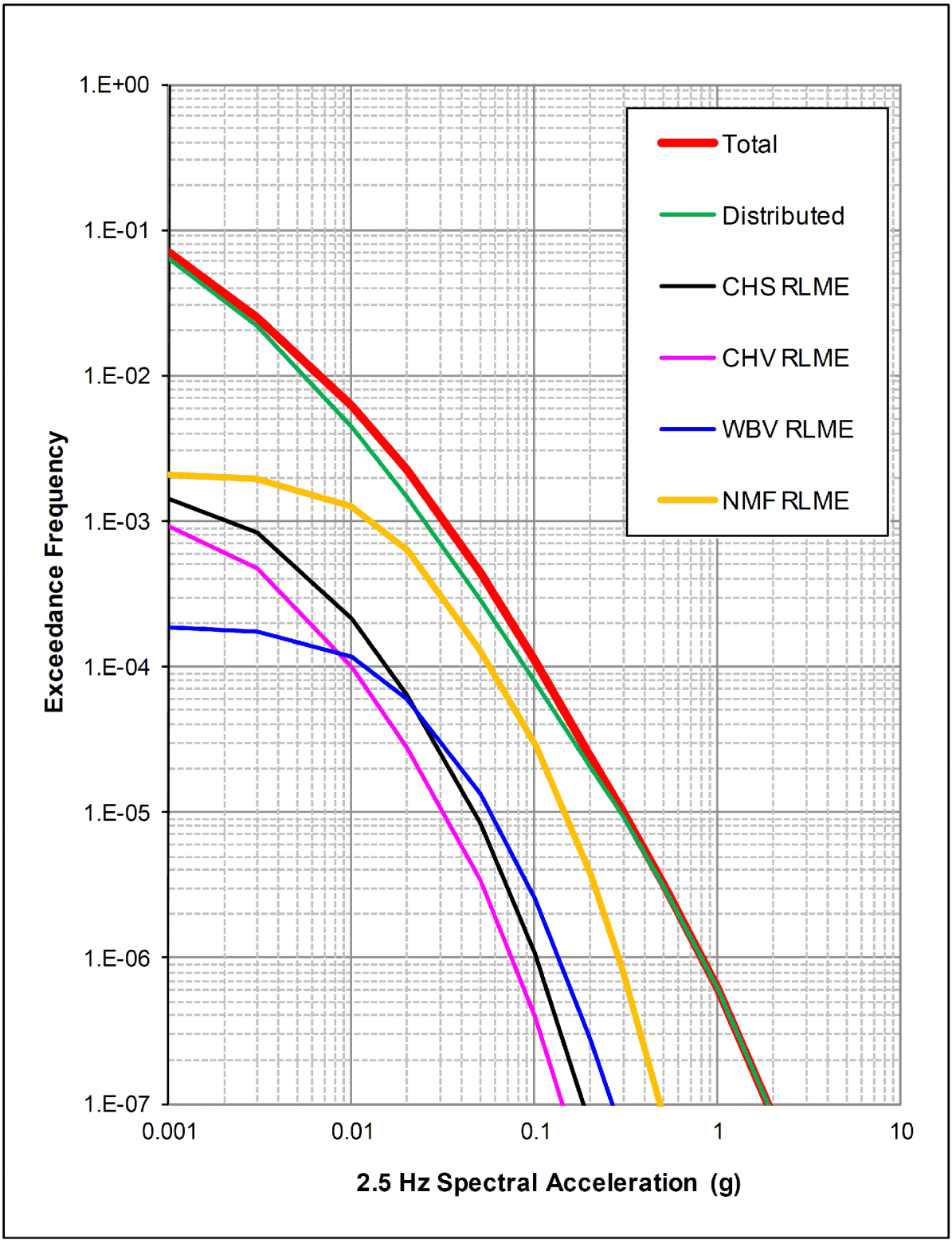

Figure 2.5.2-252 Contribution of CEUS SSC Model Sources to the Total Mean Hazard for 5 Hz Spectral Acceleration [EF3 COL 2.0-27-A]

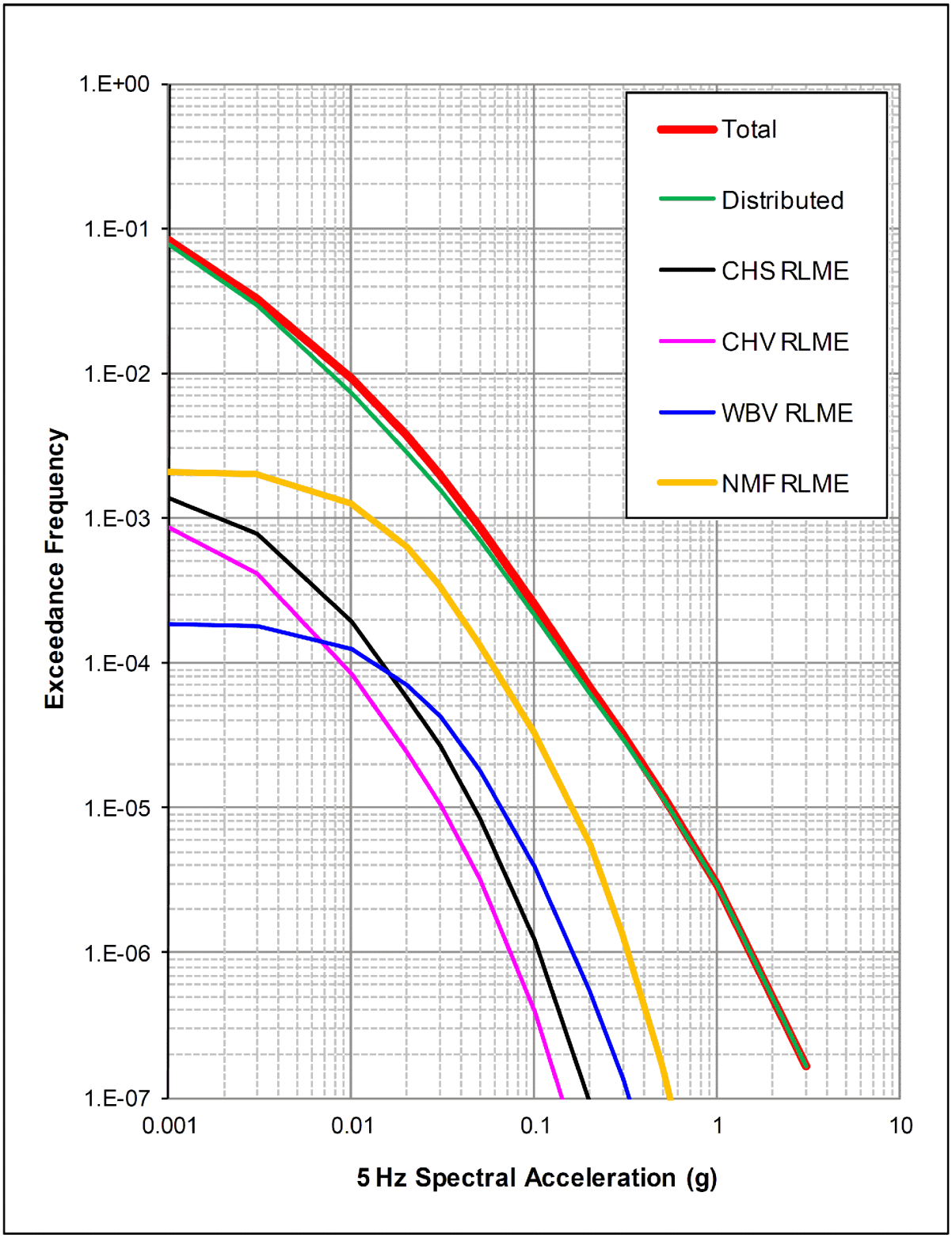

Figure 2.5.2-253 **Contribution of CEUS SSC Model Sources to the Total Mean Hazard for 10 Hz Spectral Acceleration** [EF3 COL 2.0-27-A]

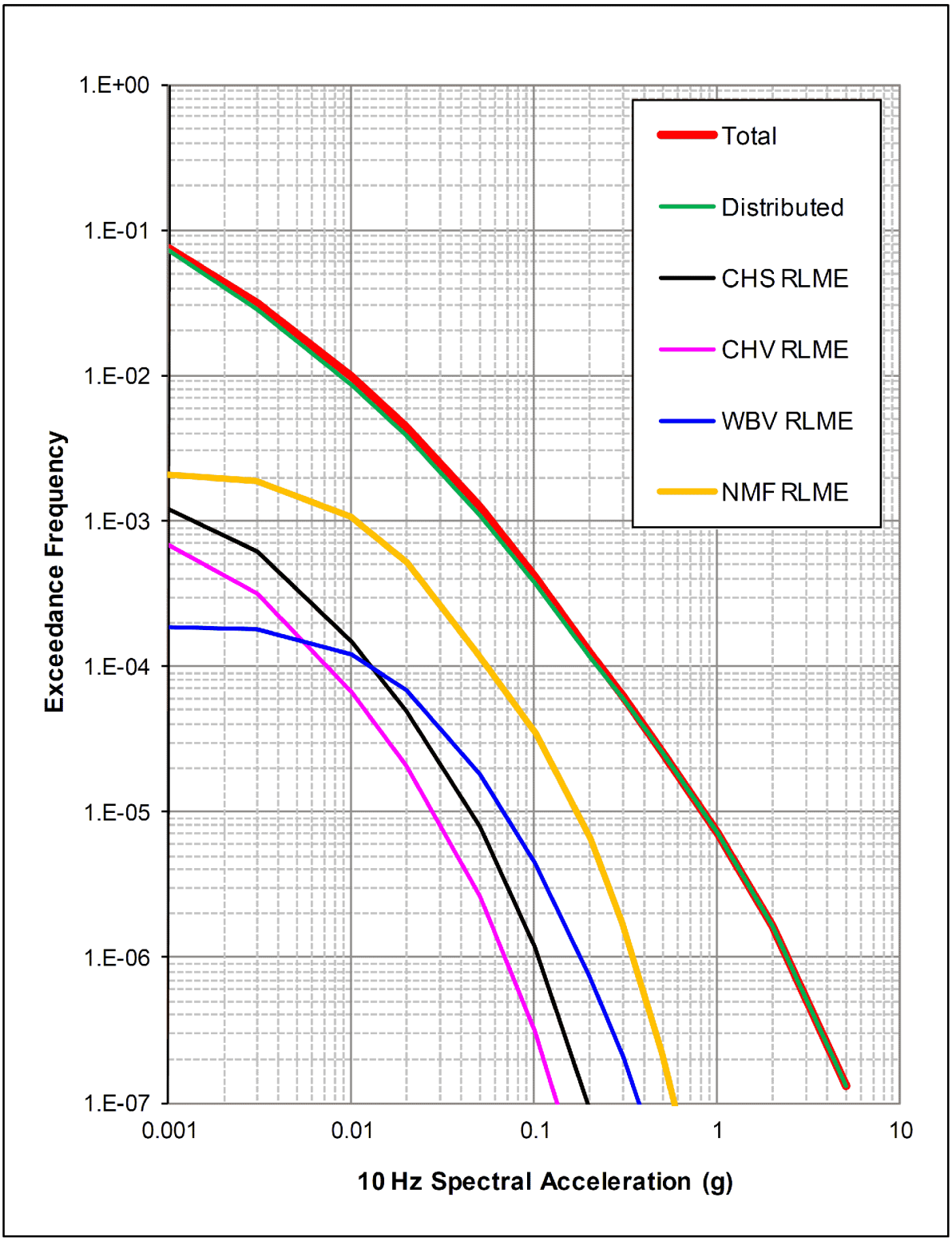

Figure 2.5.2-254 **Contribution of CEUS SSC Model Sources to the Total Mean Hazard for 25 Hz Spectral Acceleration** [EF3 COL 2.0-27-A]

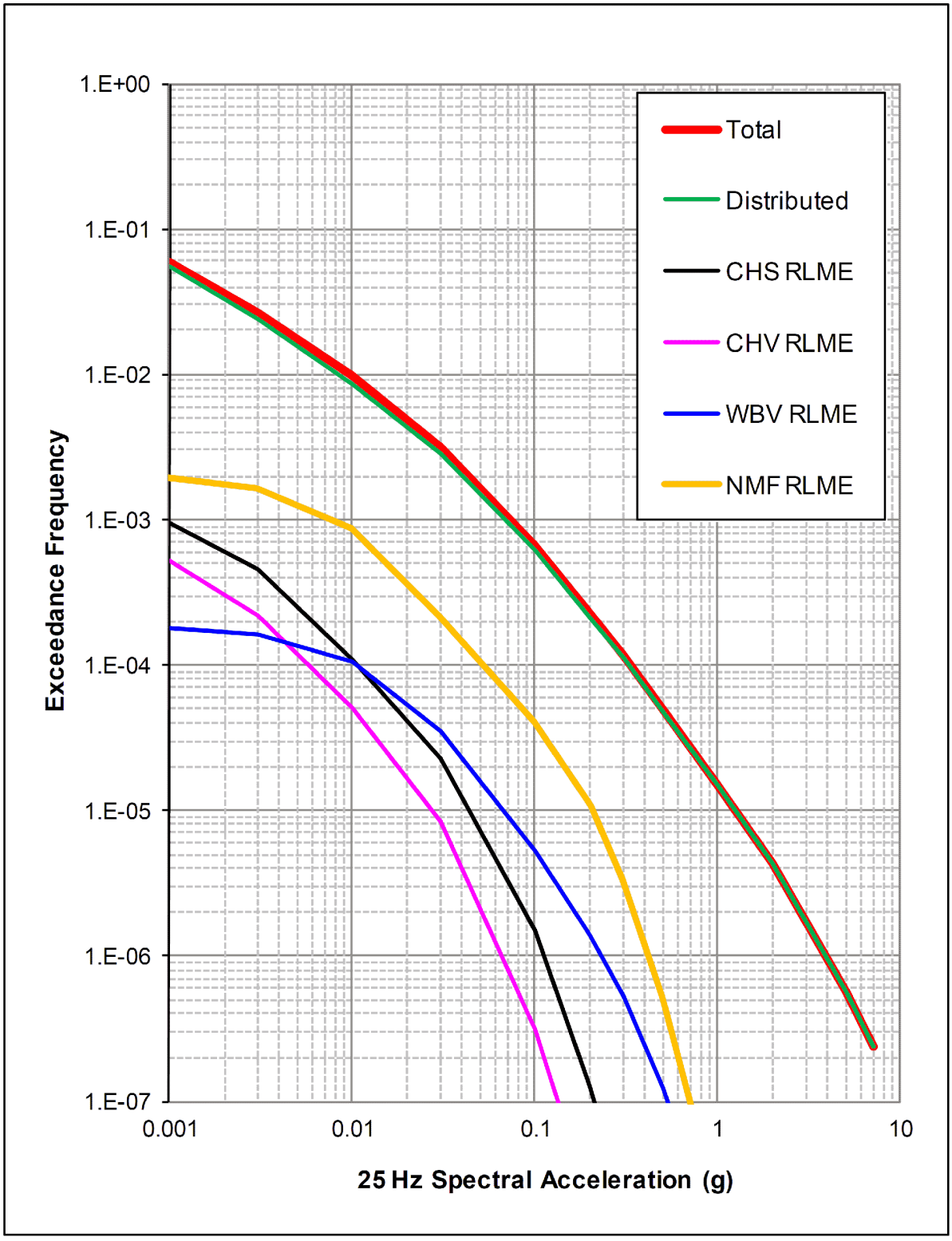

Figure 2.5.2-255 **Contribution of CEUS SSC Model Sources to the Total Mean Hazard for Peak Ground Acceleration (100 Hz Spectral Acceleration)** [EF3 COL 2.0-27-A]

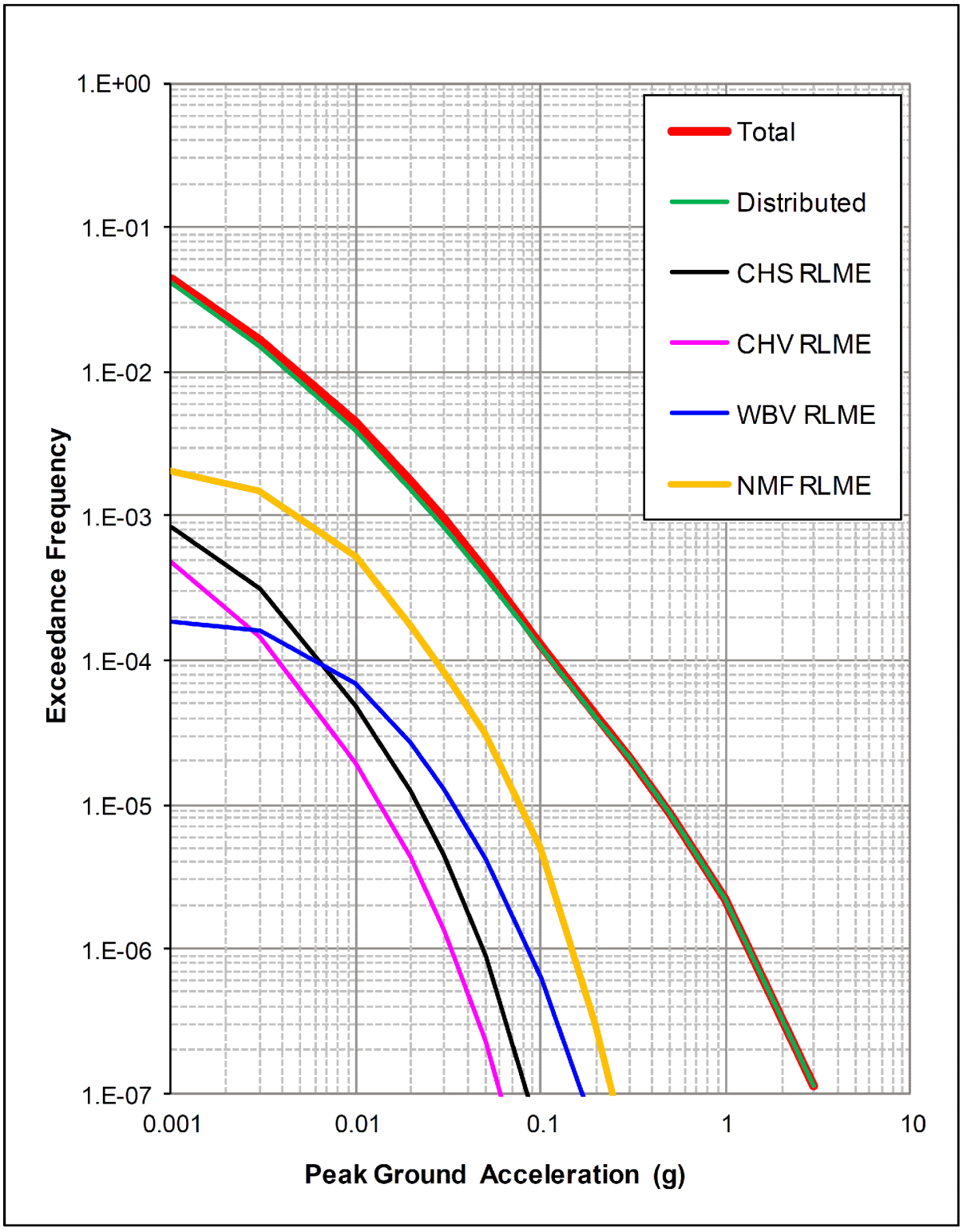

Figure 2.5.2-256 **Uniform Hazard Response Spectra for the Fermi 3 Site and Generic Hard Rock Conditions Based on the CEUS SSC Model**
[EF3 COL 2.0-27-A]

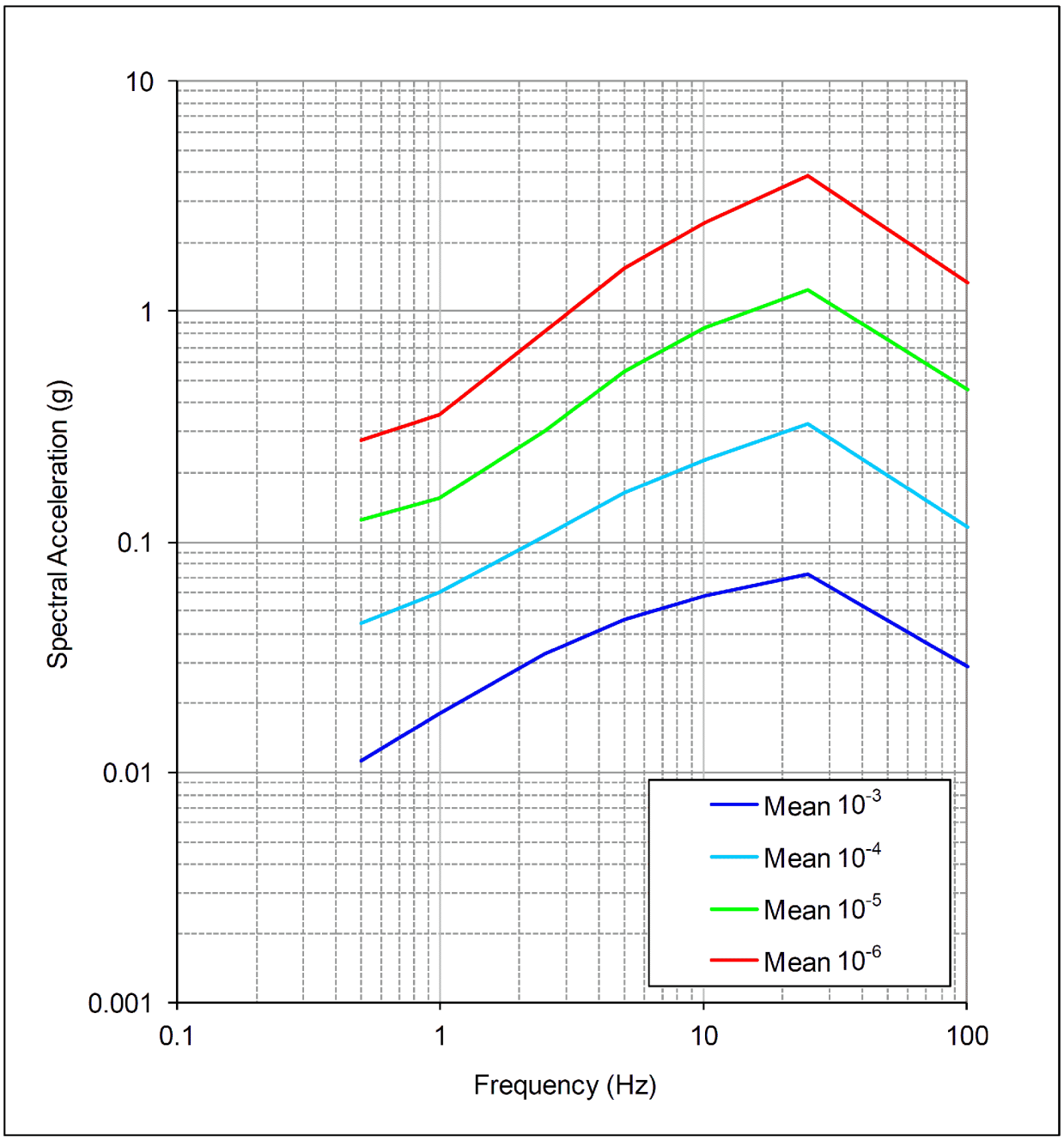

Figure 2.5.2-257 Deaggregation of Mean 10^{-3} Hazard [EF3 COL 2.0-27-A]

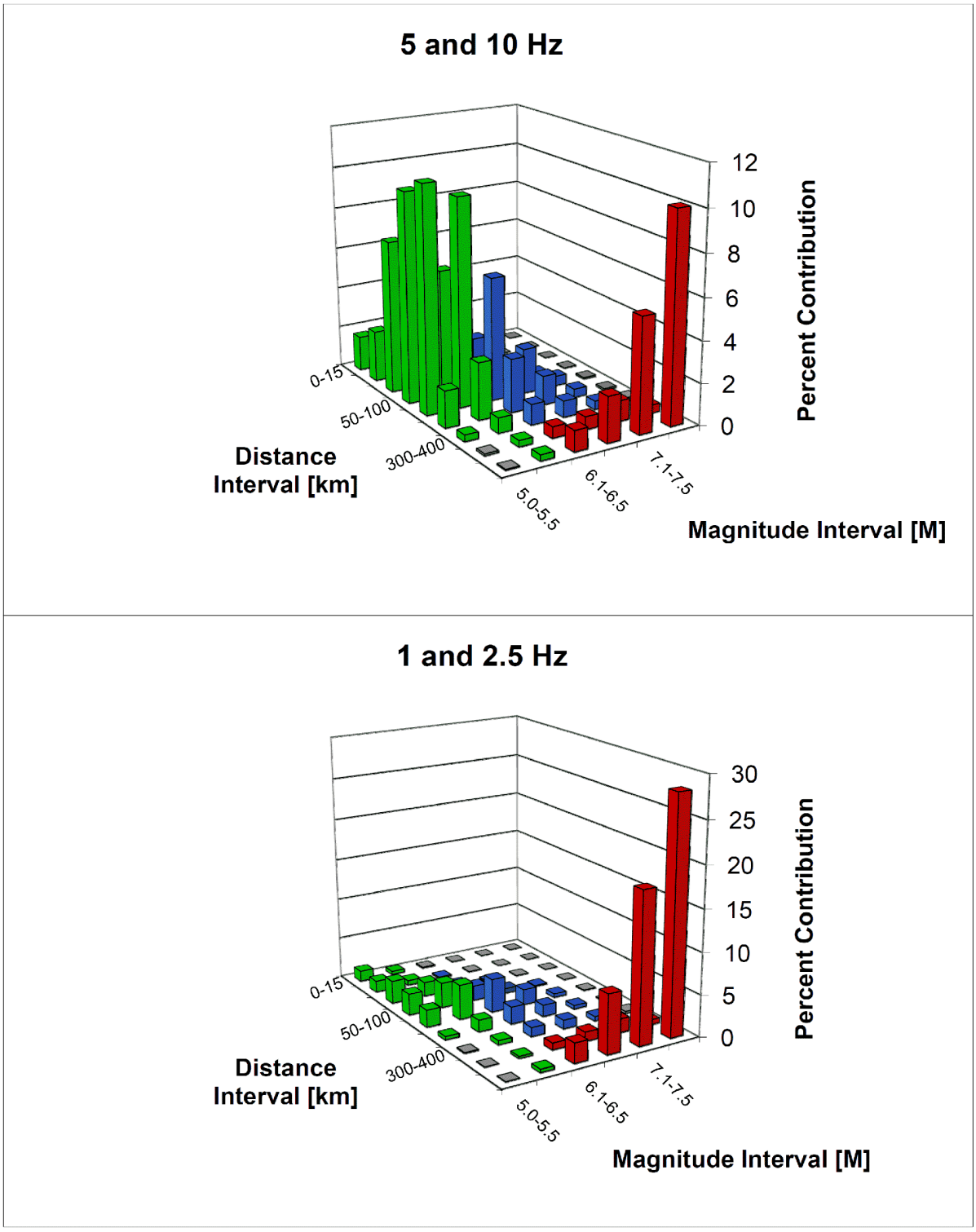

Figure 2.5.2-258 Deaggregation of Mean 10^{-4} Hazard [EF3 COL 2.0-27-A]

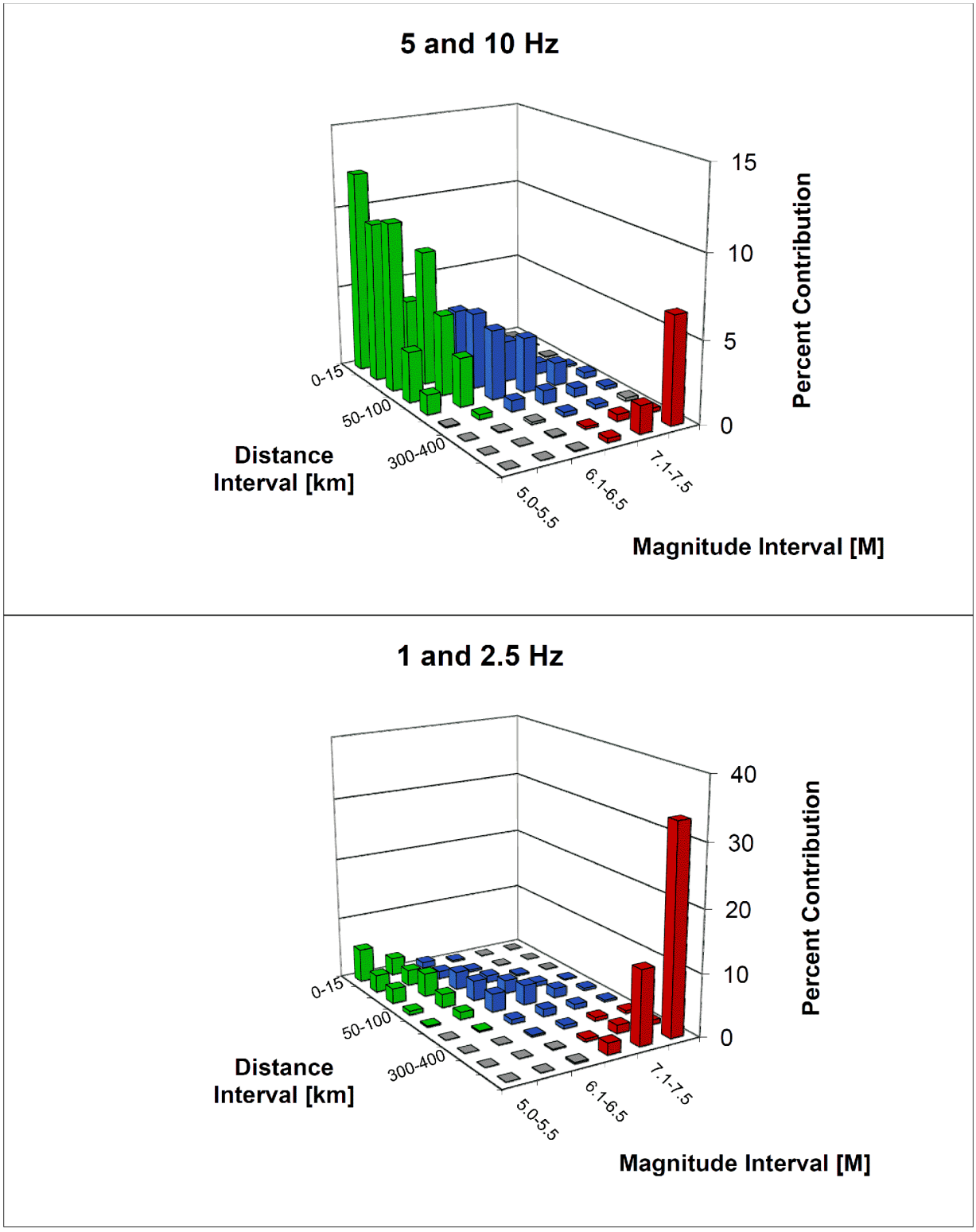

Figure 2.5.2-259 Deaggregation of Mean 10^{-5} Hazard [EF3 COL 2.0-27-A]

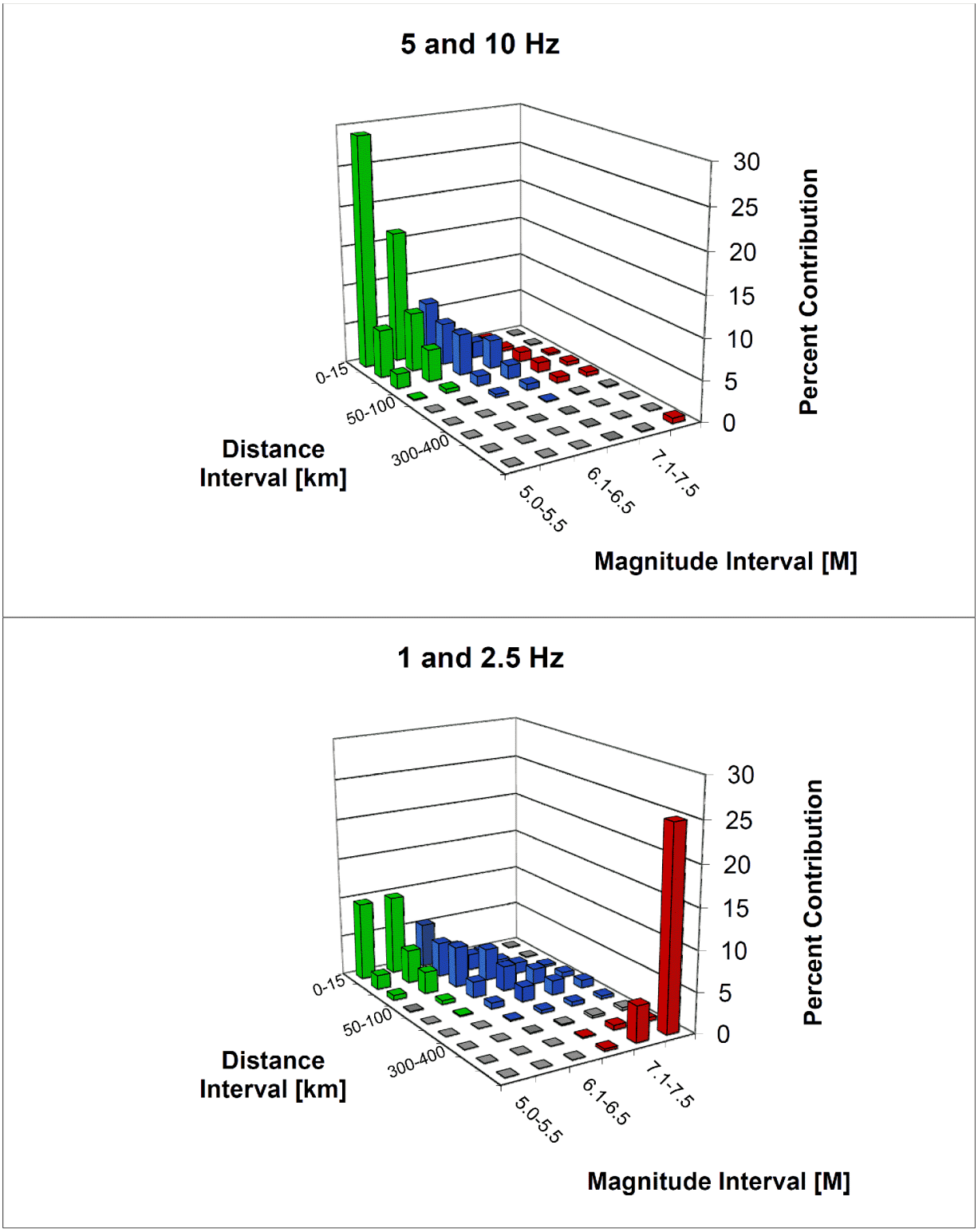

Figure 2.5.2-260 Deaggregation of Mean 10^{-6} Hazard [EF3 COL 2.0-27-A]

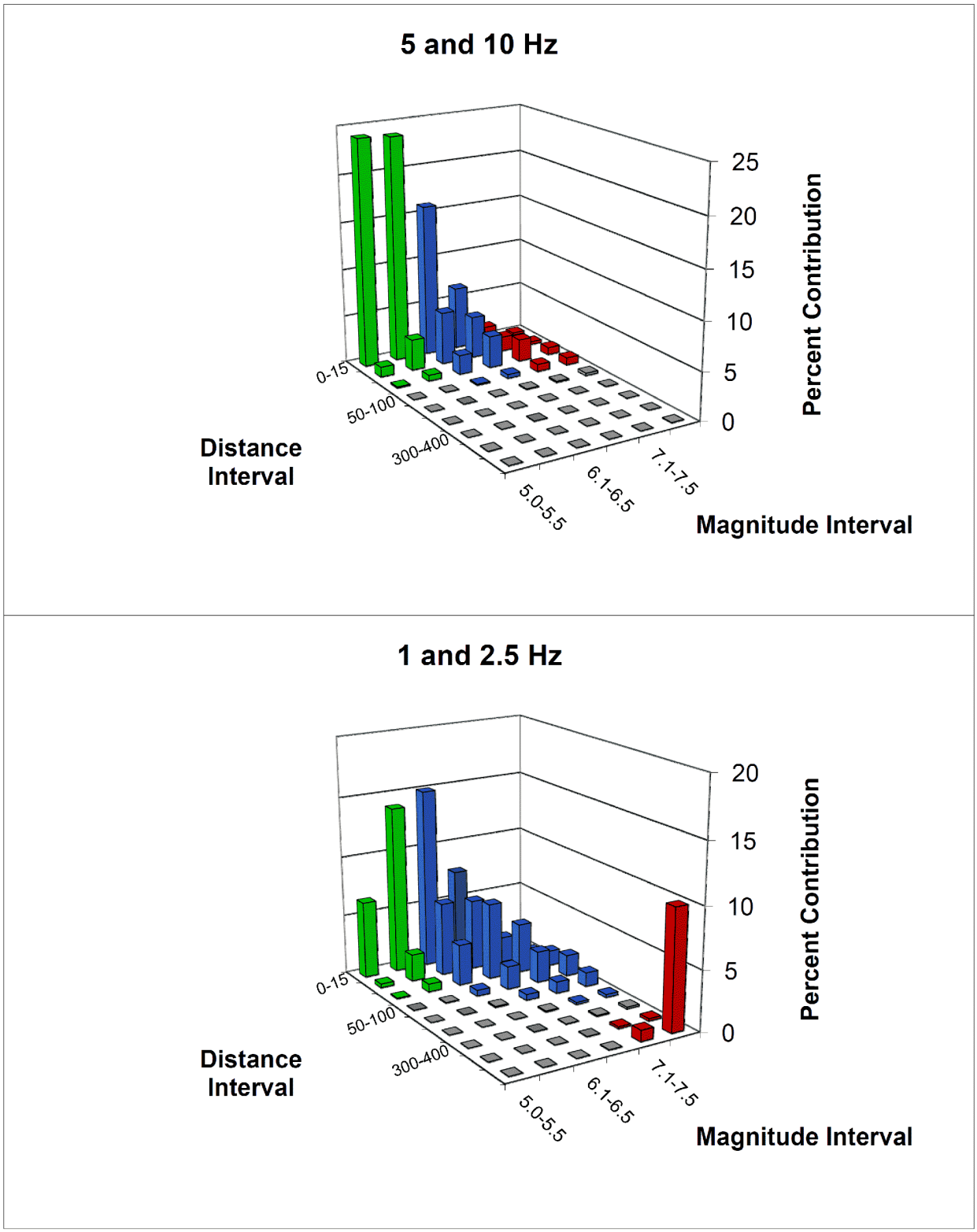

Figure 2.5.2-261 Extension of Response Spectra to 0.1 Hz [EF3 COL 2.0-27-A]

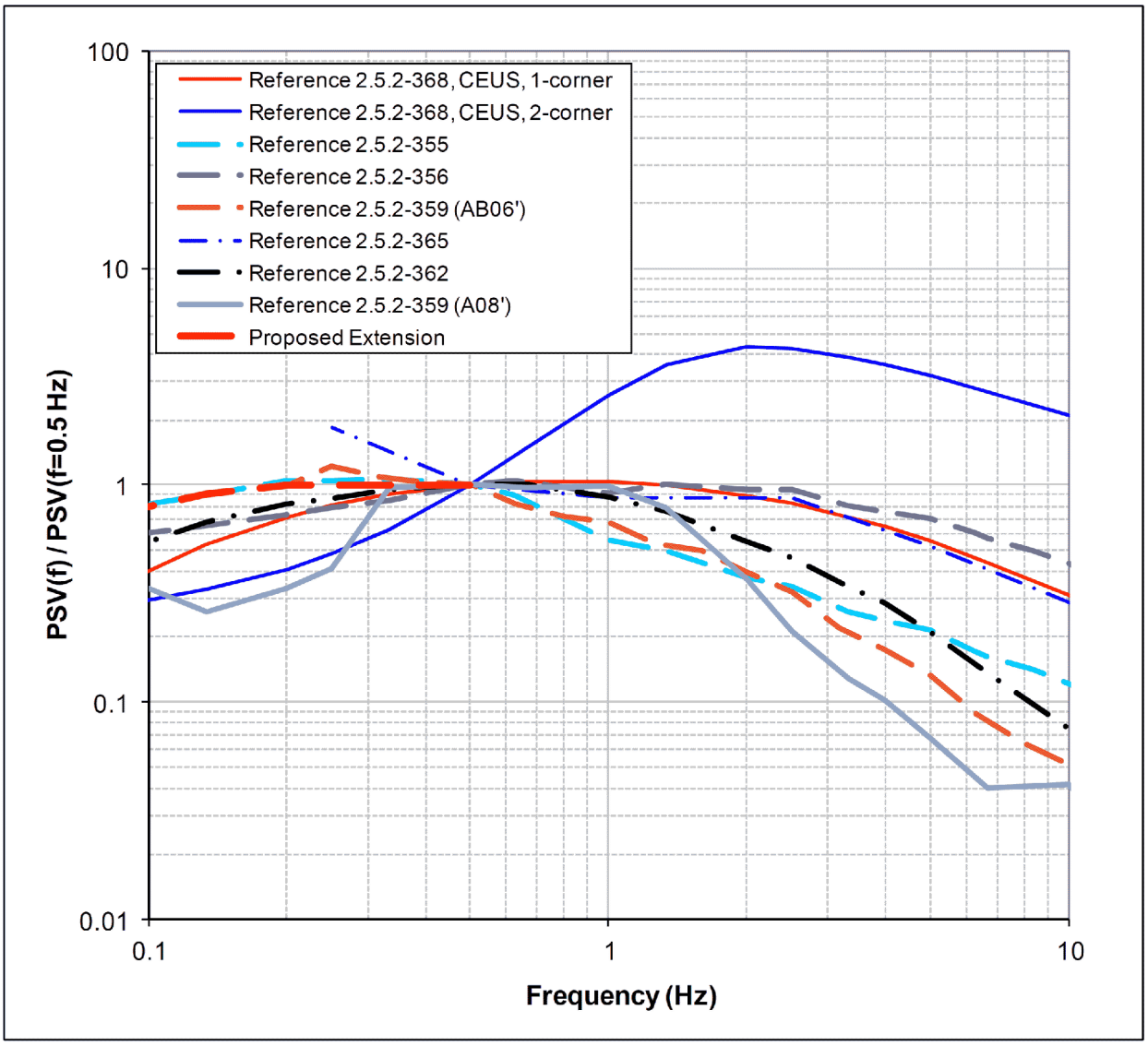

Figure 2.5.2-262 Mean 10^{-3} UHRS, RE, and DE Spectra [EF3 COL 2.0-27-A]

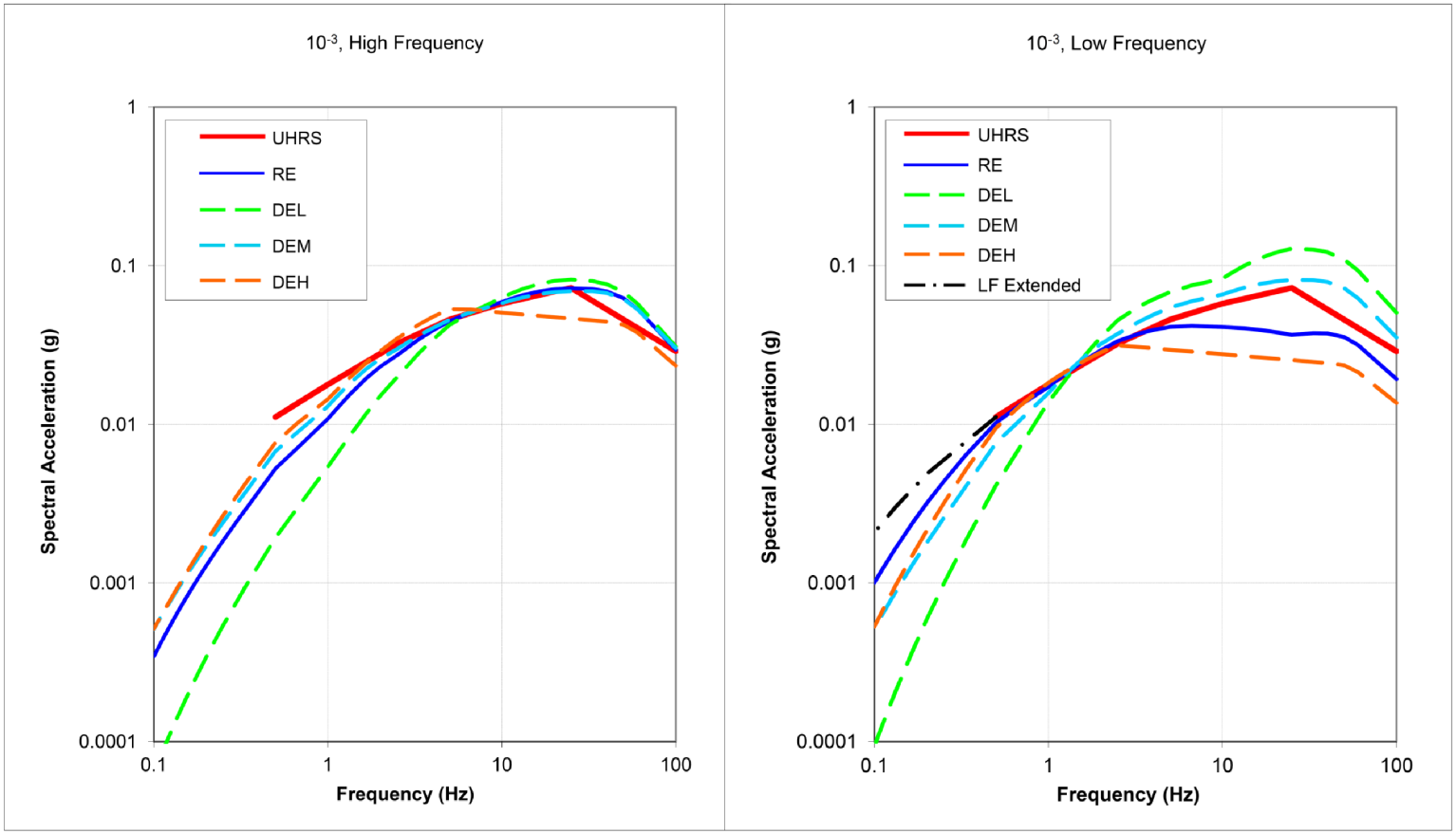

Figure 2.5.2-263 Mean 10^{-4} UHRS, RE, and DE Spectra [EF3 COL 2.0-27-A]

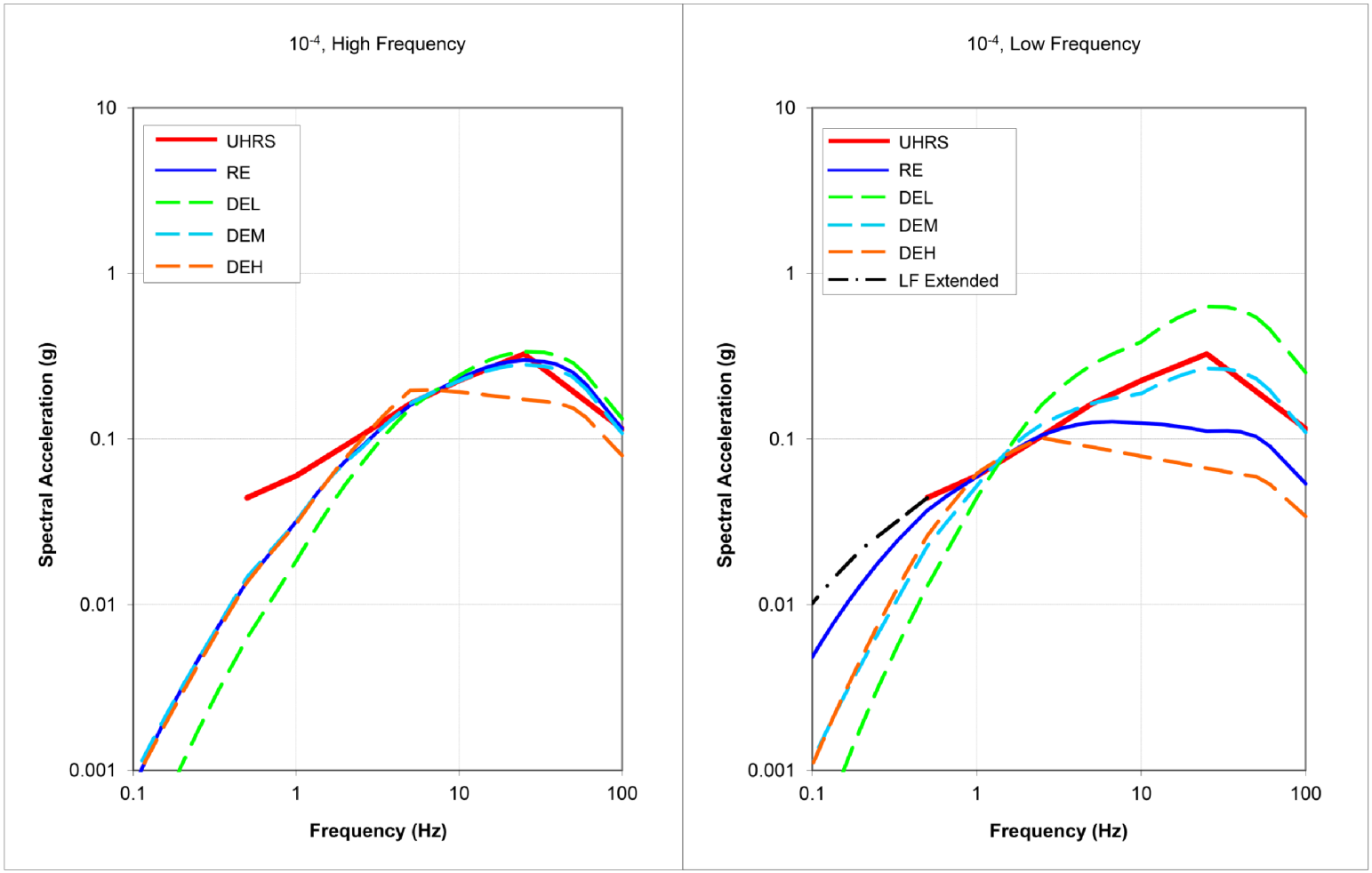

Figure 2.5.2-264 Mean 10^{-5} UHRS, RE, and DE Spectra [EF3 COL 2.0-27-A]

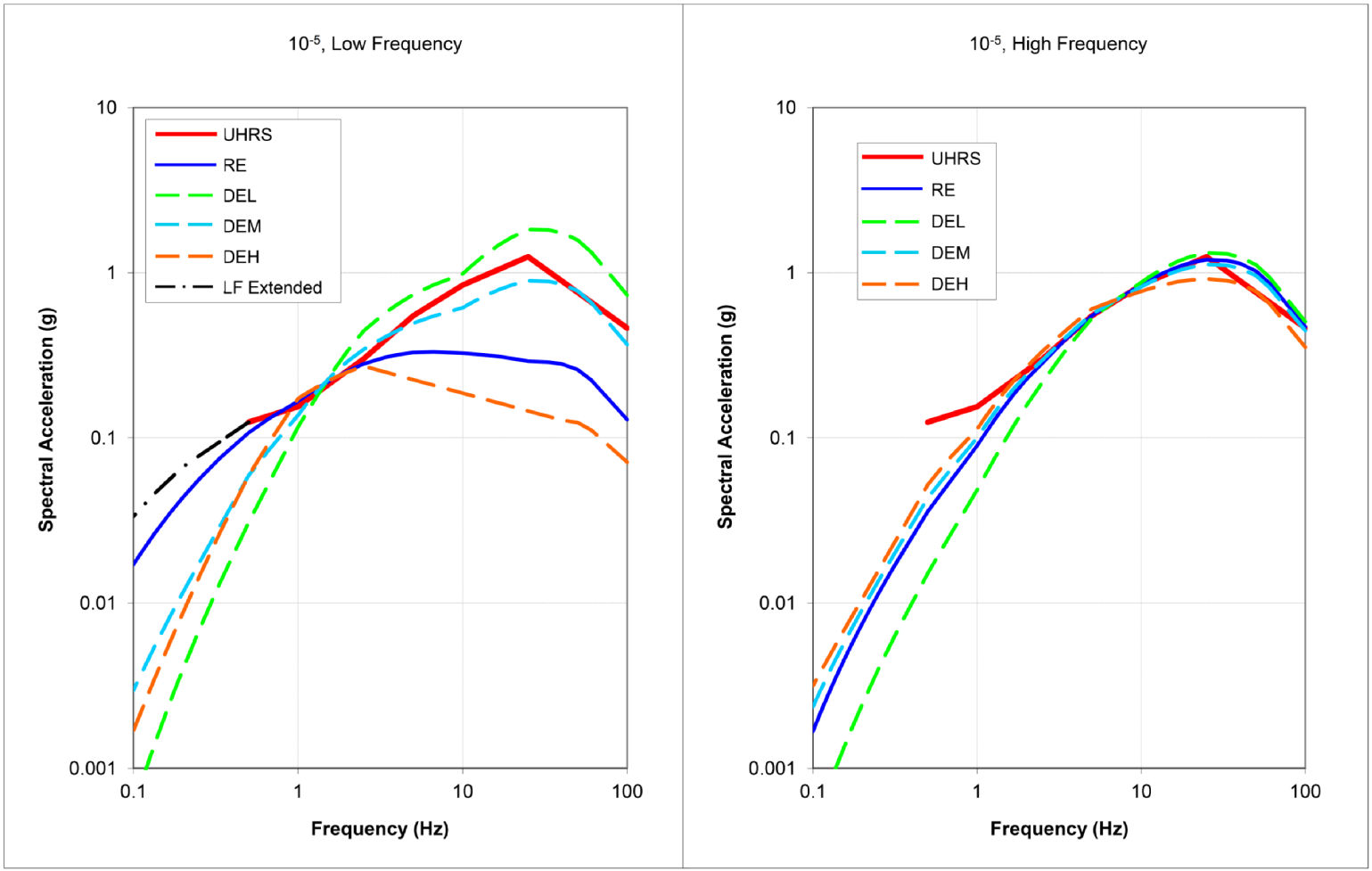

Figure 2.5.2-265 Mean 10^{-6} UHRS, RE, and DE Spectra [EF3 COL 2.0-27-A]

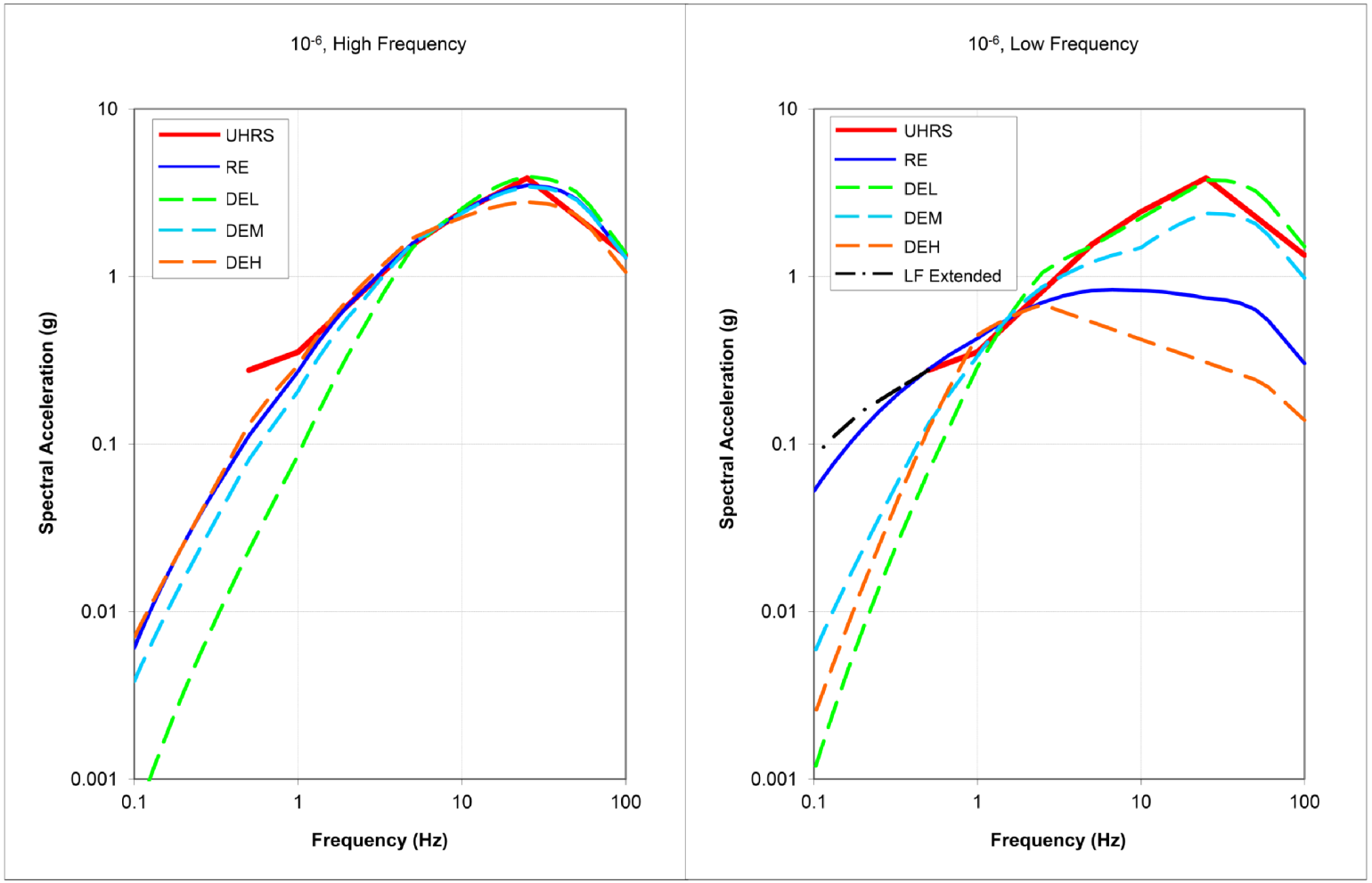

Figure 2.5.2-266 Shear Wave Velocity Data for Boring TB-C5 [EF3 COL 2.0-27-A]

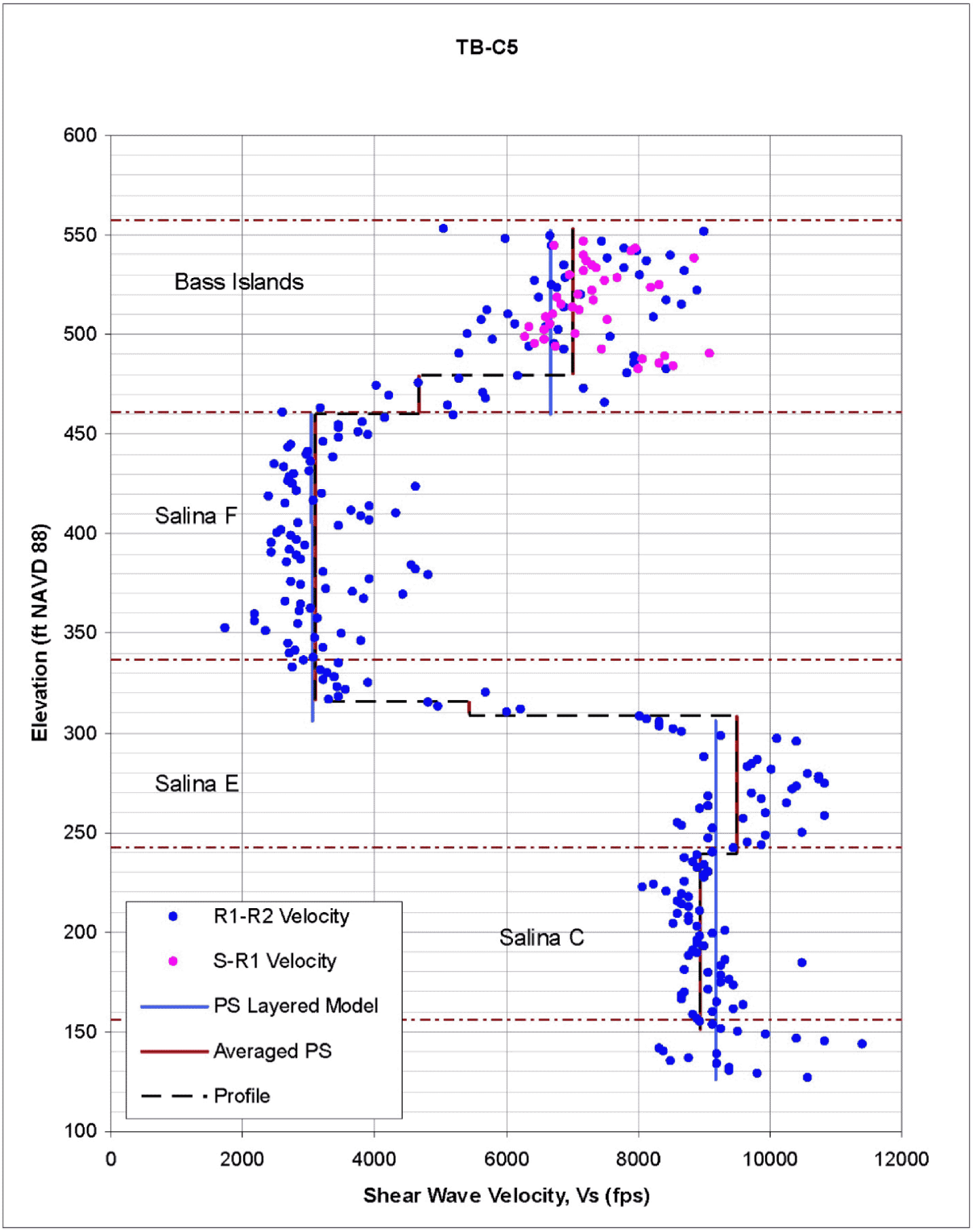

Figure 2.5.2-267 Shear Wave Velocity Data for Boring RB-C8 [EF3 COL 2.0-27-A]

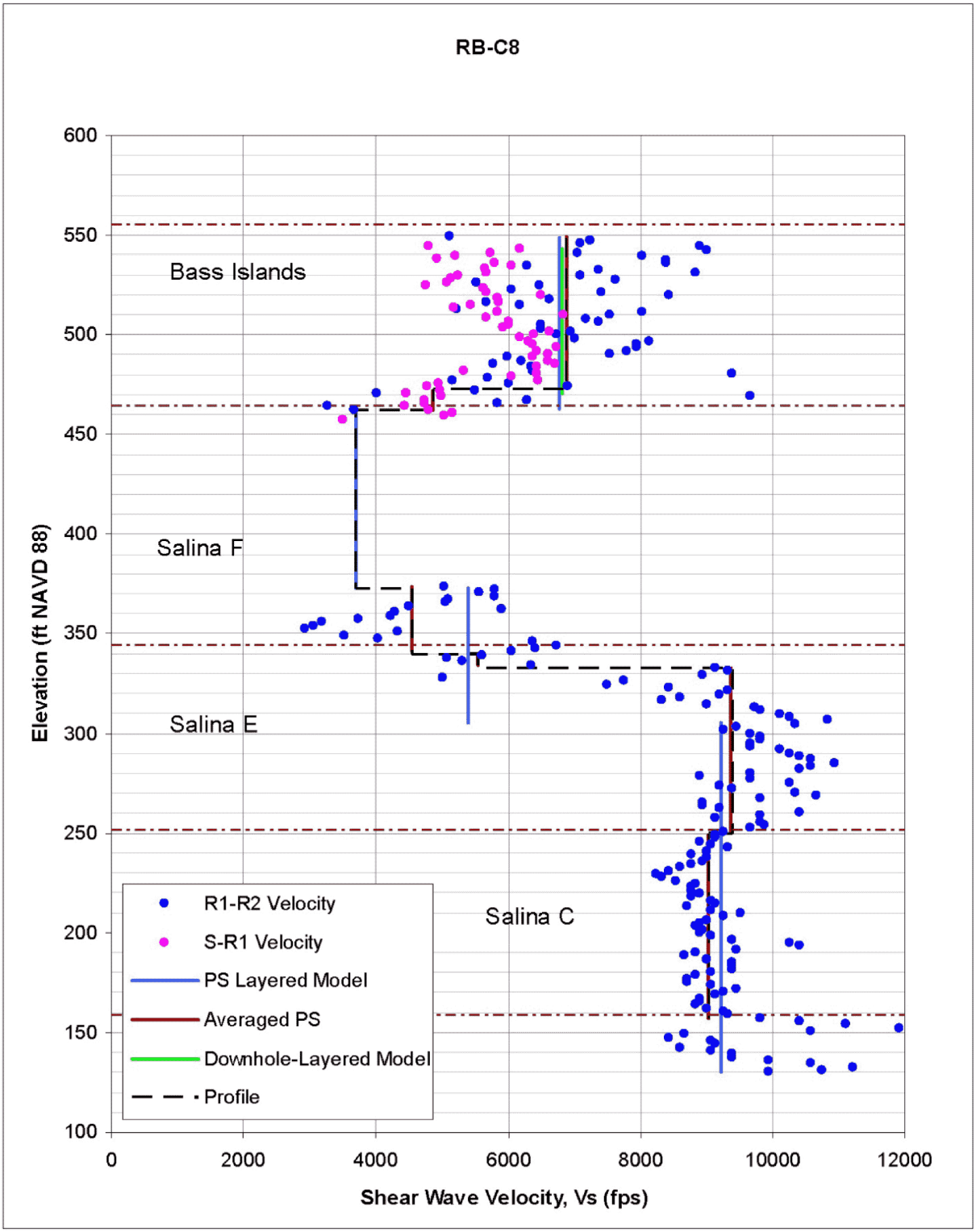

Figure 2.5.2-268 Shear Wave Velocity Data for Boring CB-C3 [EF3 COL 2.0-27-A]

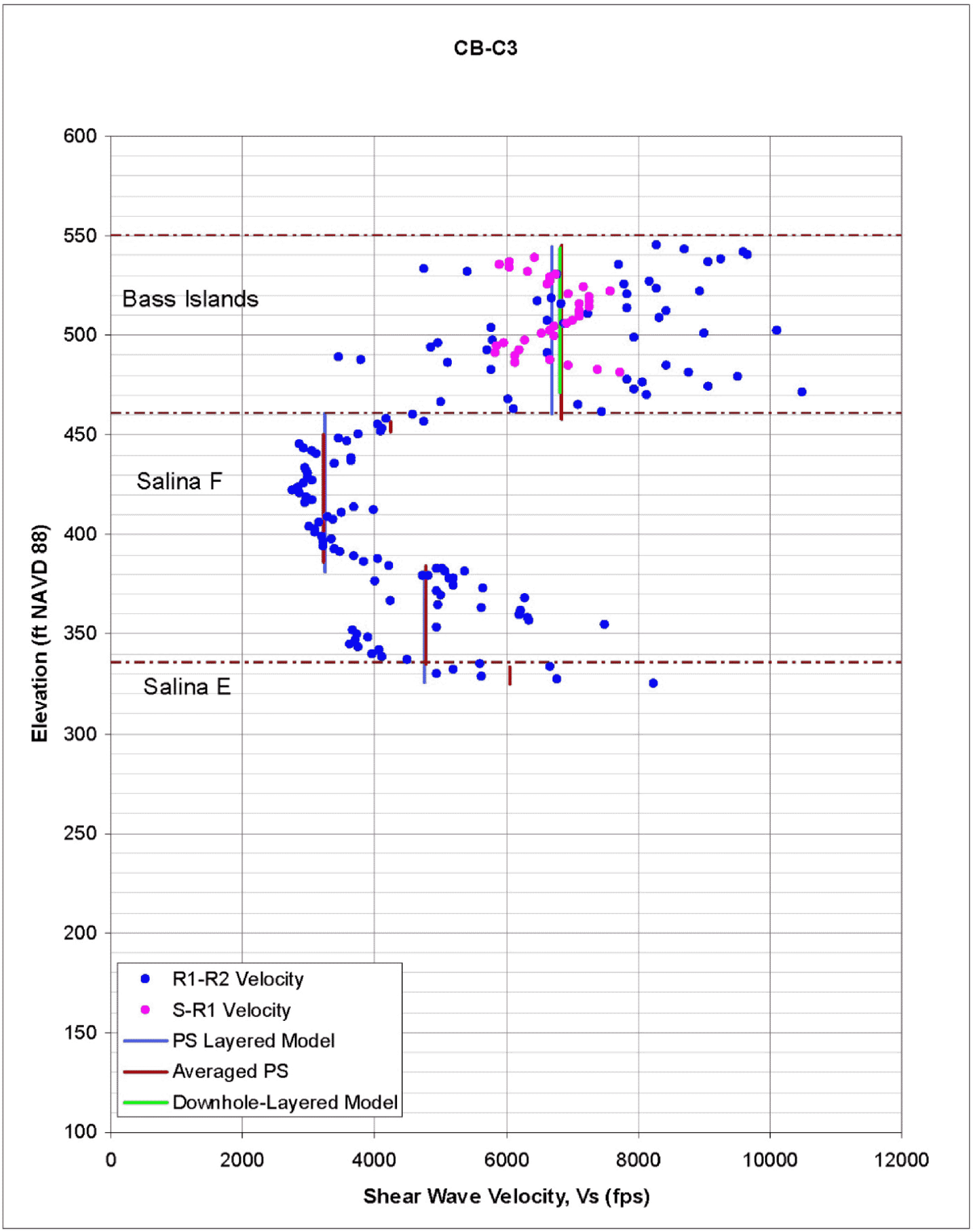

Figure 2.5.2-269 Shear Wave Velocity Data for Boring RB-C4 [EF3 COL 2.0-27-A]

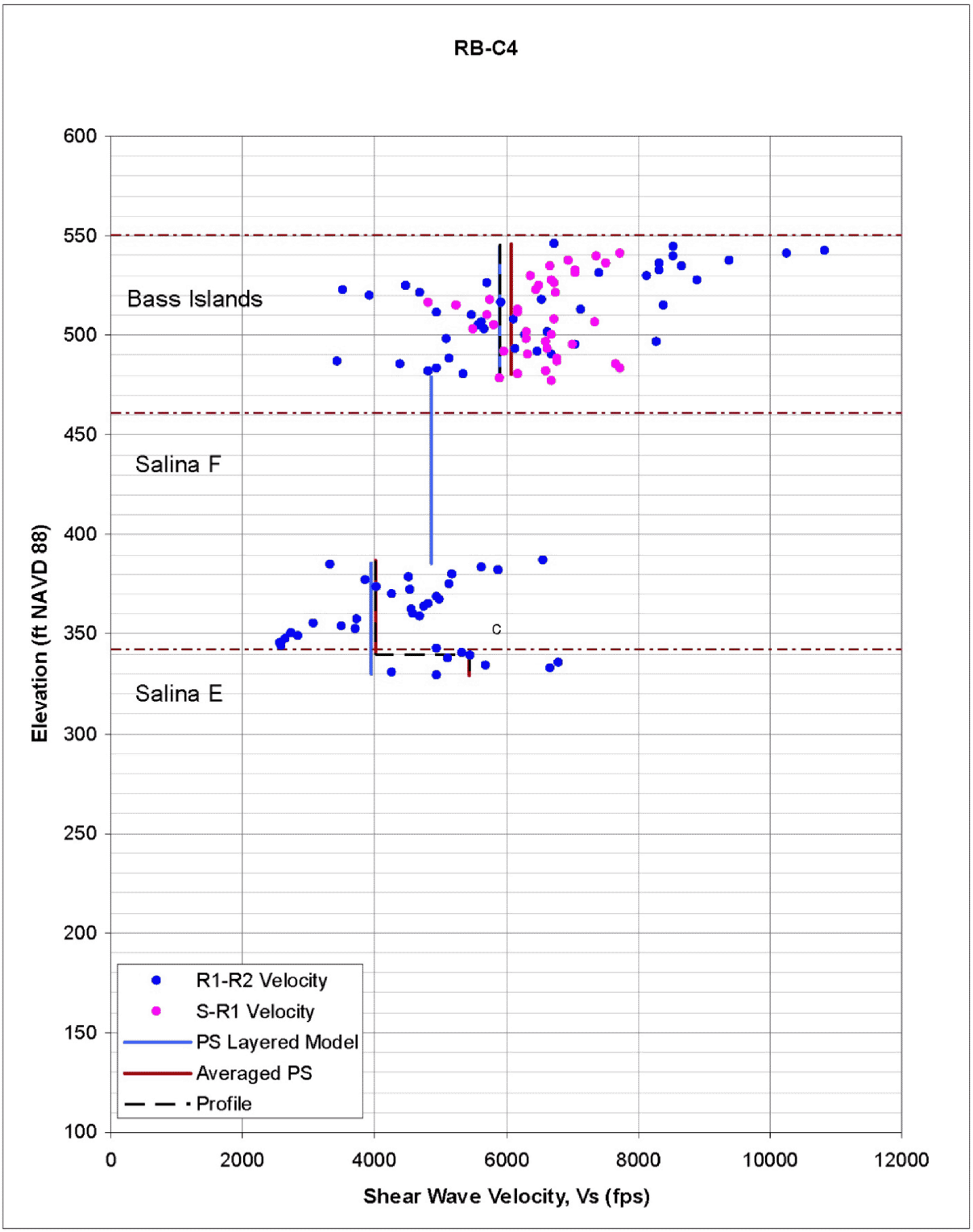

Figure 2.5.2-270 Geometric Mean Velocity Profile for Fermi 3 Site GMRS Profile
[EF3 COL 2.0-27-A]

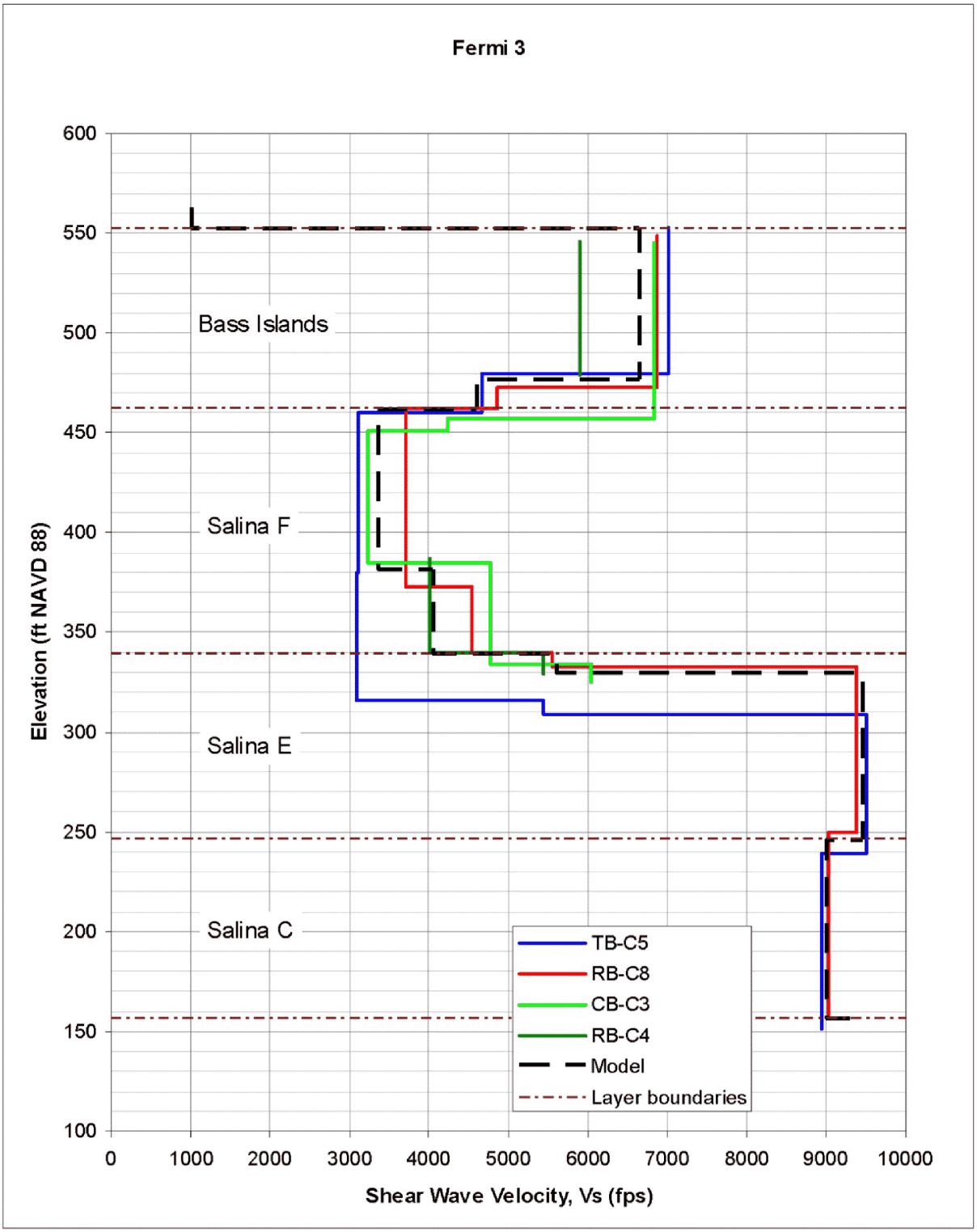

Figure 2.5.2-271 Estimation of Scattering κ [EF3 COL 2.0-27-A]

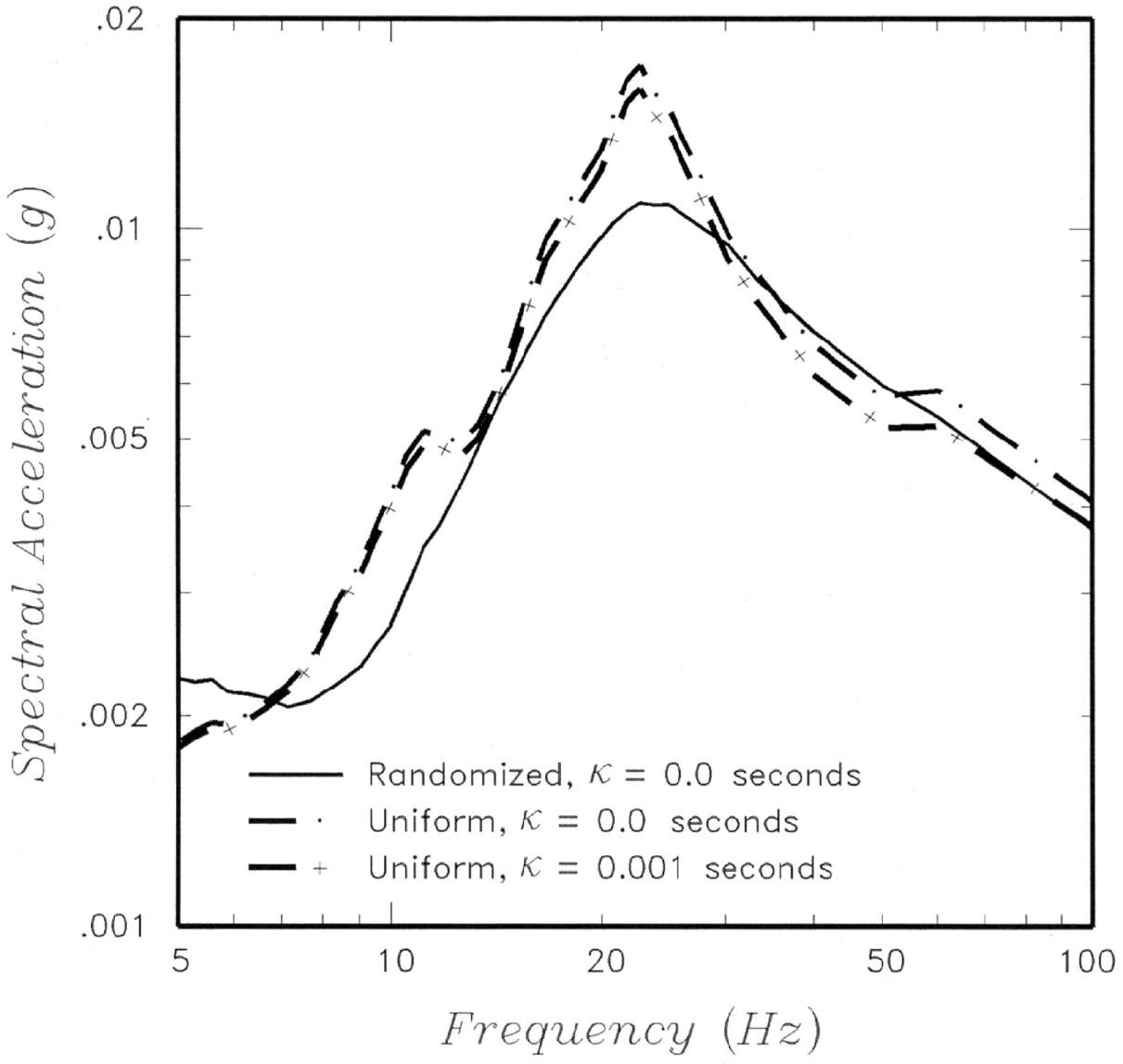

Figure 2.5.2-272 Randomized Shear-Wave-Velocity Profiles 1 to 30

[EF3 COL 2.0-27-A]

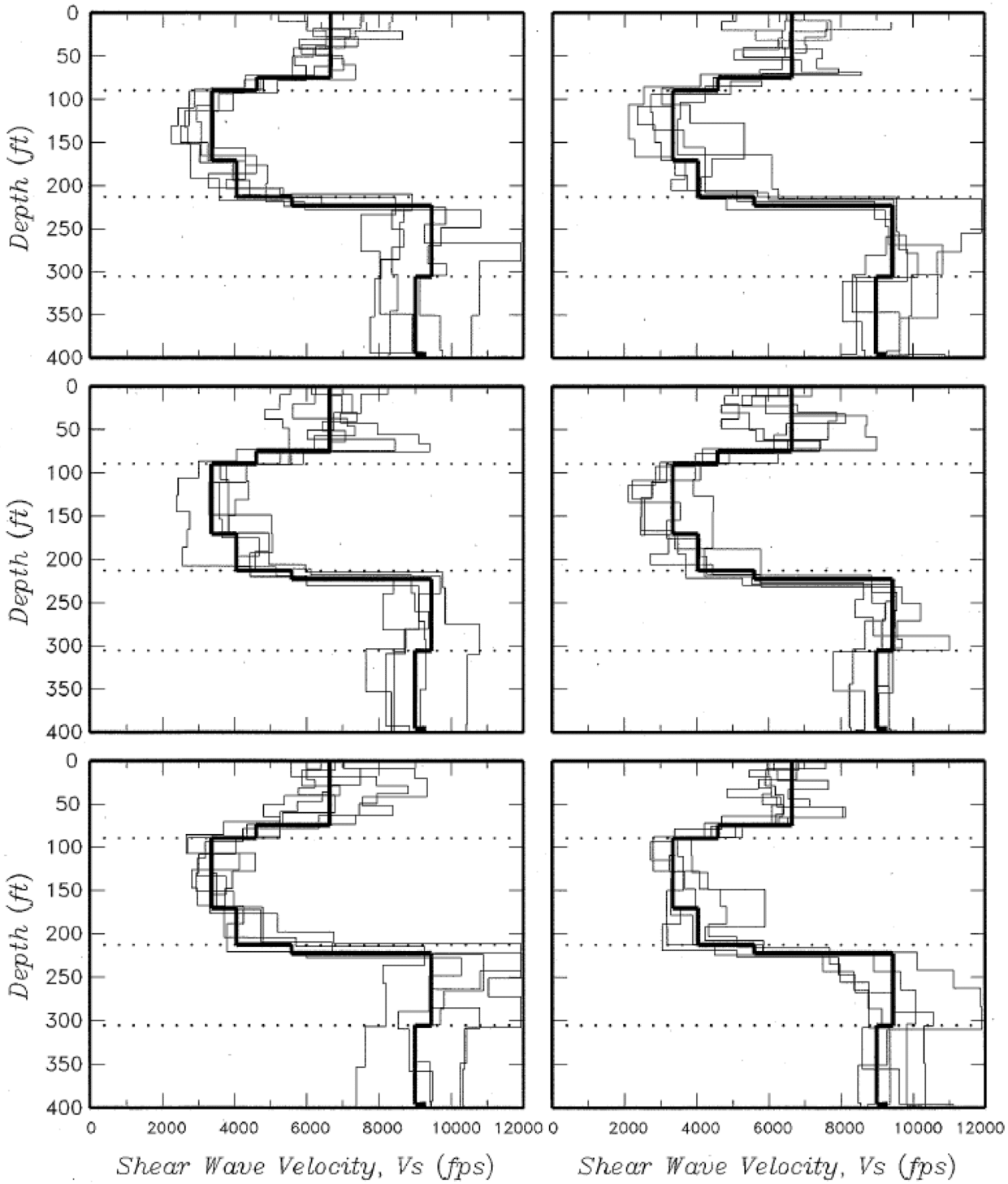

Figure 2.5.2-273 Randomized Shear-Wave-Velocity Profiles 31 to 60

[EF3 COL 2.0-27-A]

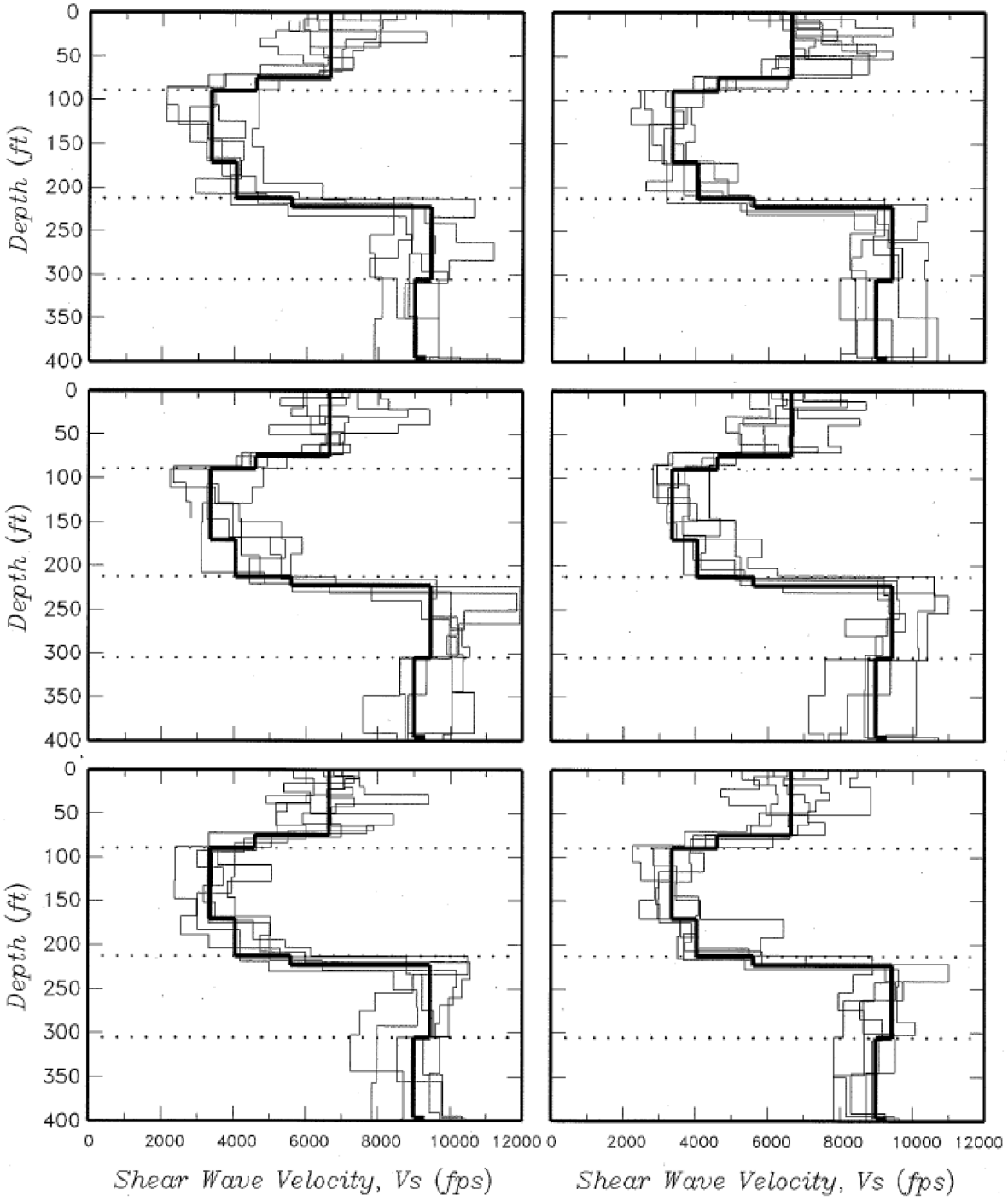

Figure 2.5.2-274 Statistics of Randomized Shear Wave Velocity Profiles
[EF3 COL 2.0-27-A]

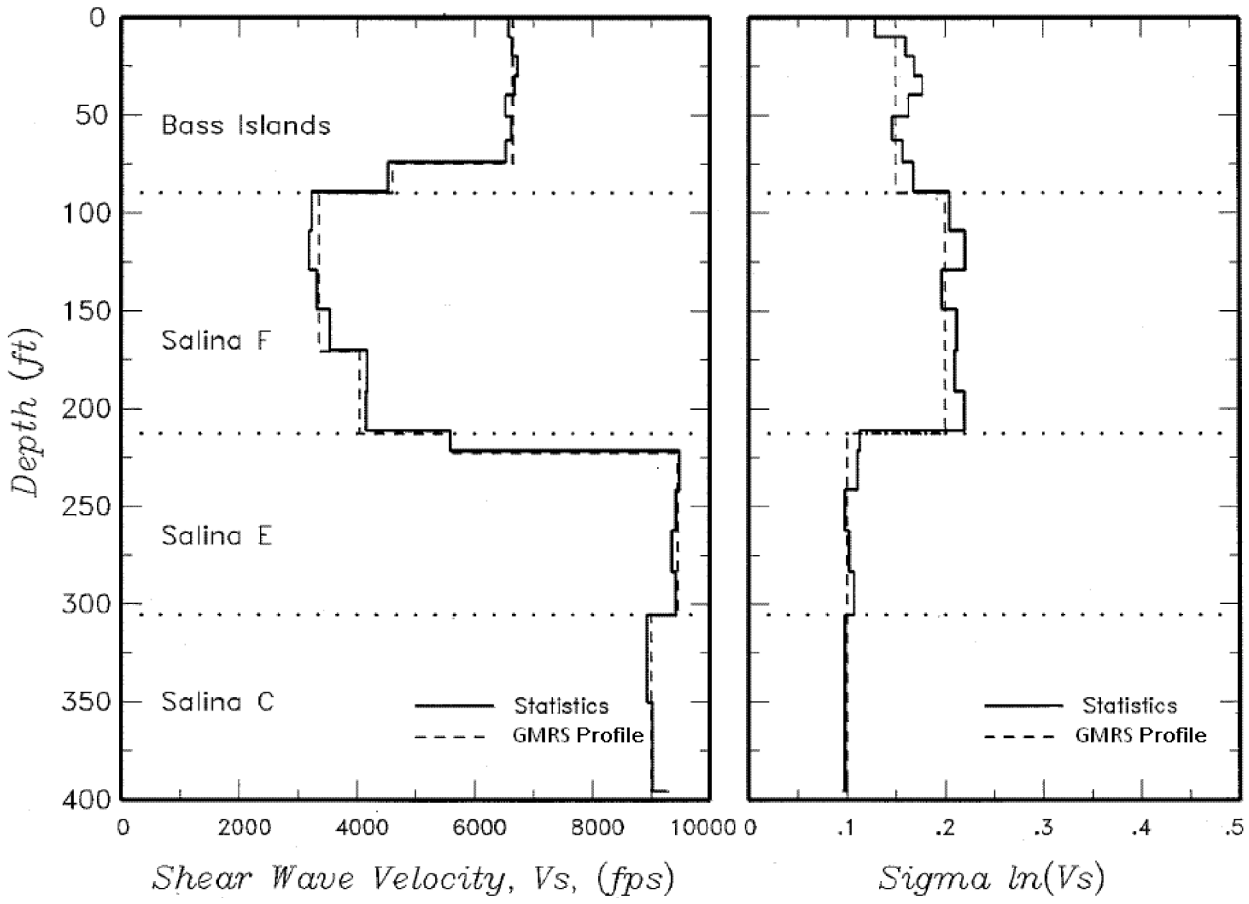

Figure 2.5.2-275 Example Response Spectra of Time Histories Used for Site Response Analyses [EF3 COL 2.0-27-A]

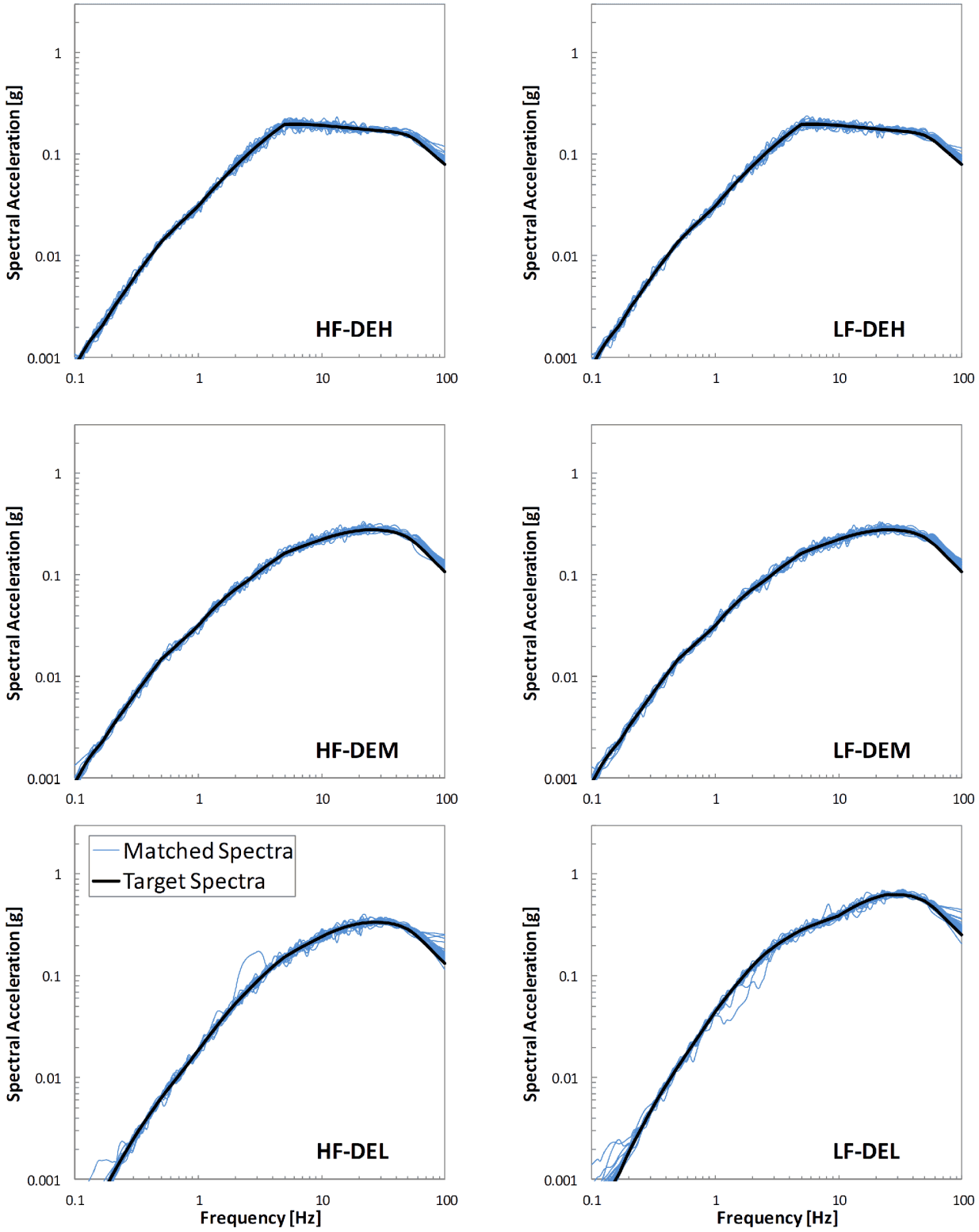

Figure 2.5.2-276 Site Response Logic Tree [EF3 COL 2.0-27-A]

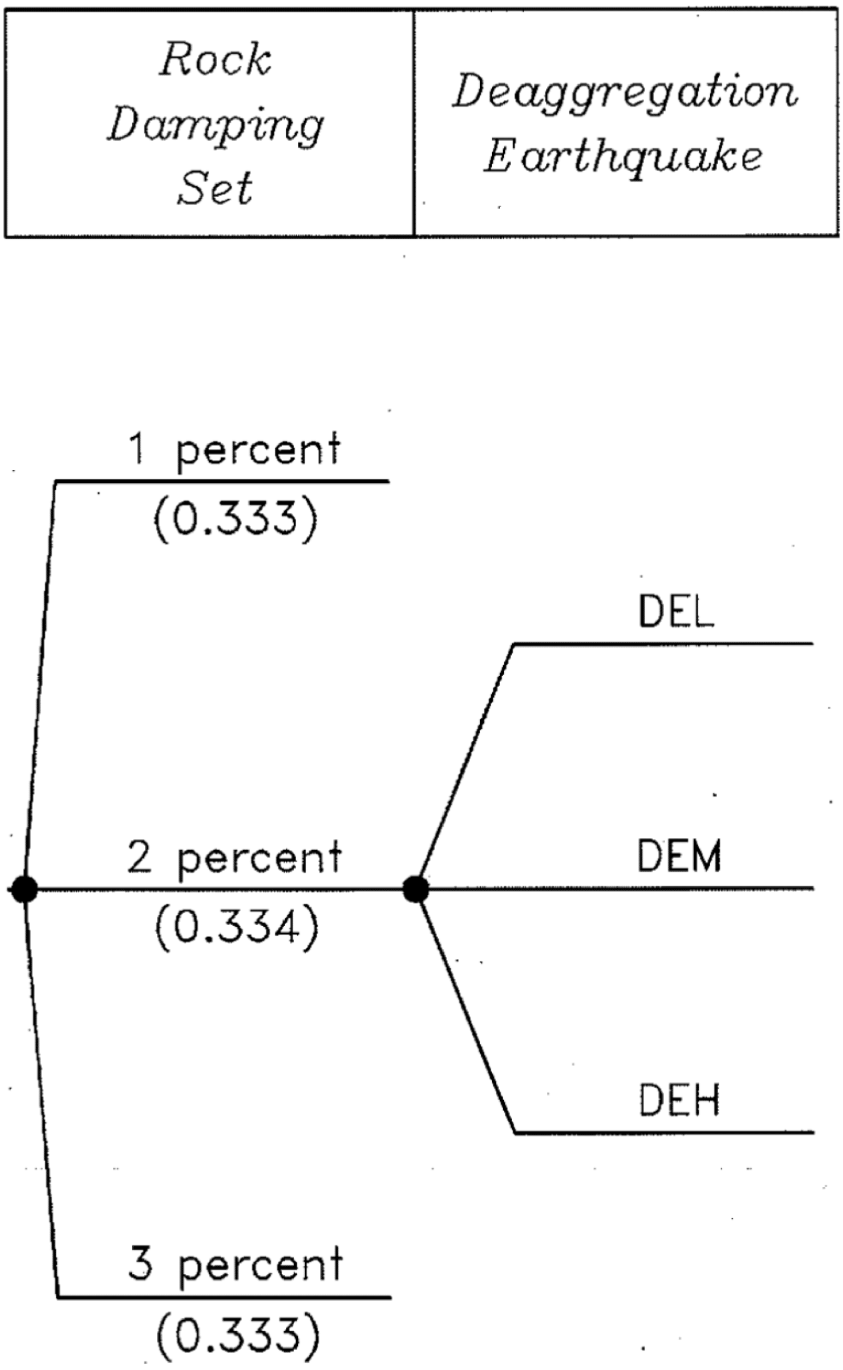

Figure 2.5.2-277 **Sensitivity of GMRS Profile Mean Site Amplification to Damping Assigned to Rock Layers at 10^{-4} Level of Exceedance**

[EF3 COL 2.0-27-A]

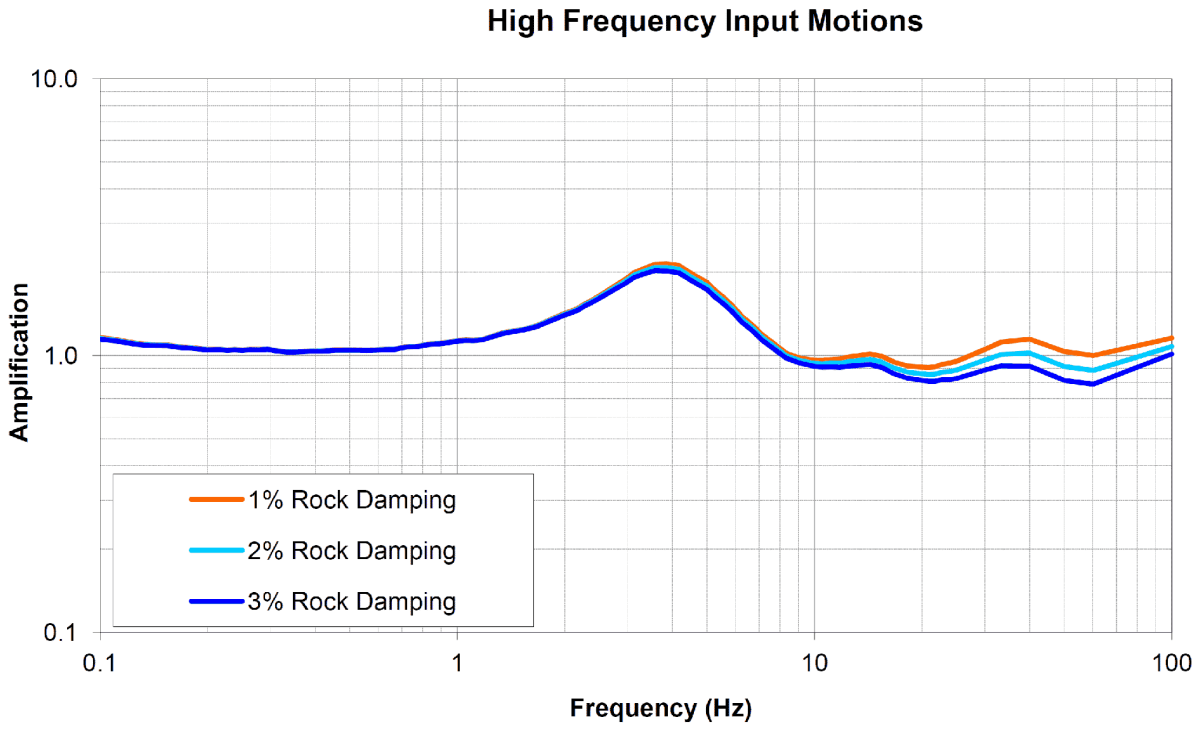

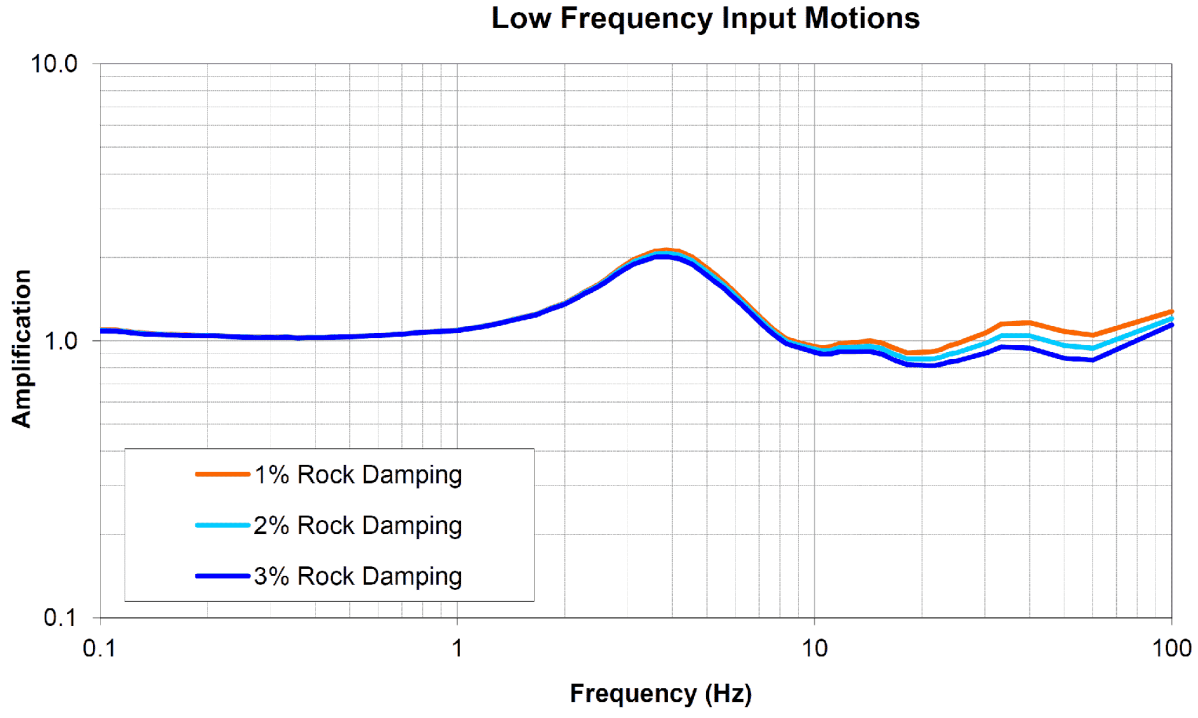

Figure 2.5.2-278 **Sensitivity of GMRS Profile Mean Site Amplification to Deaggregation Earthquake Motions at 10^{-4} Level of Exceedance**
[EF3 COL 2.0-27-A]

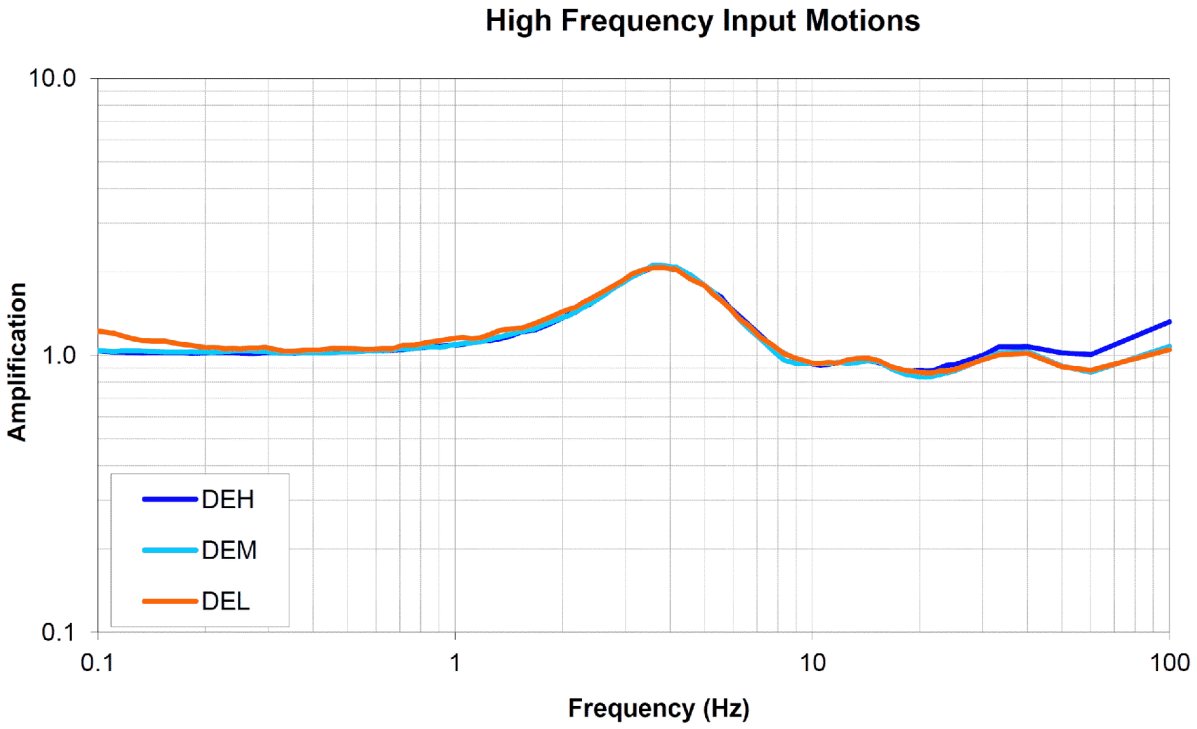

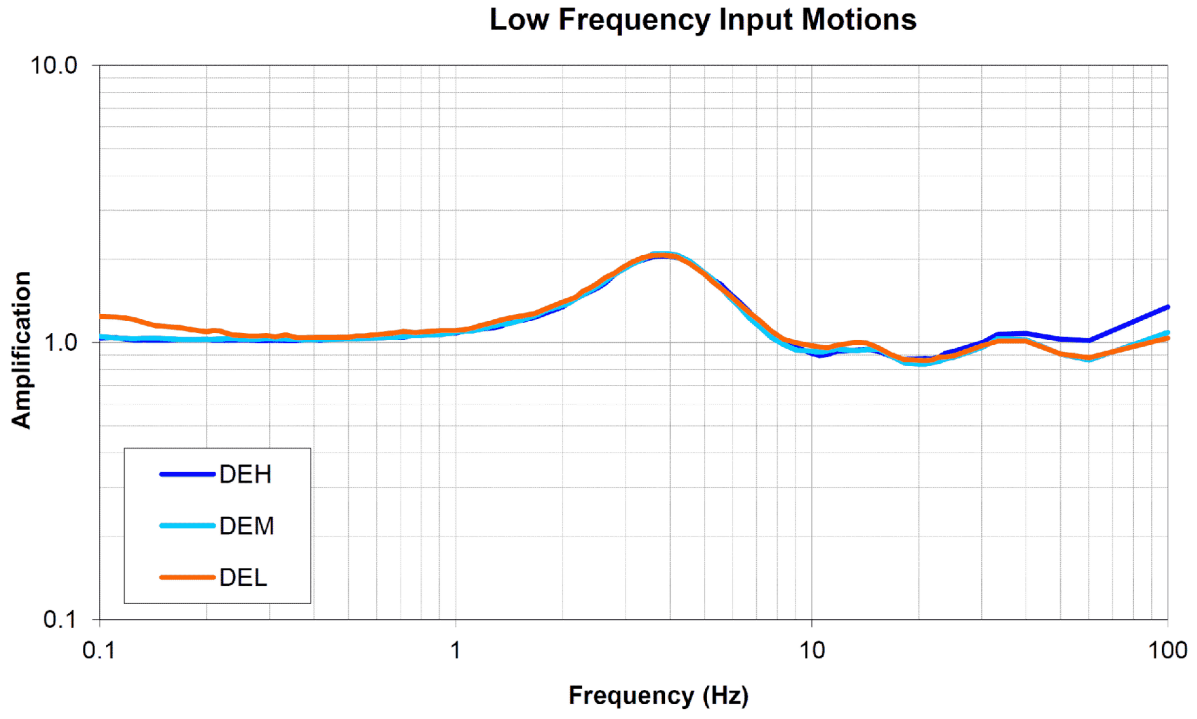

Figure 2.5.2-279 GMRS Amplification Functions for the Fermi 3 Site
[EF3 COL 2.0-27-A]

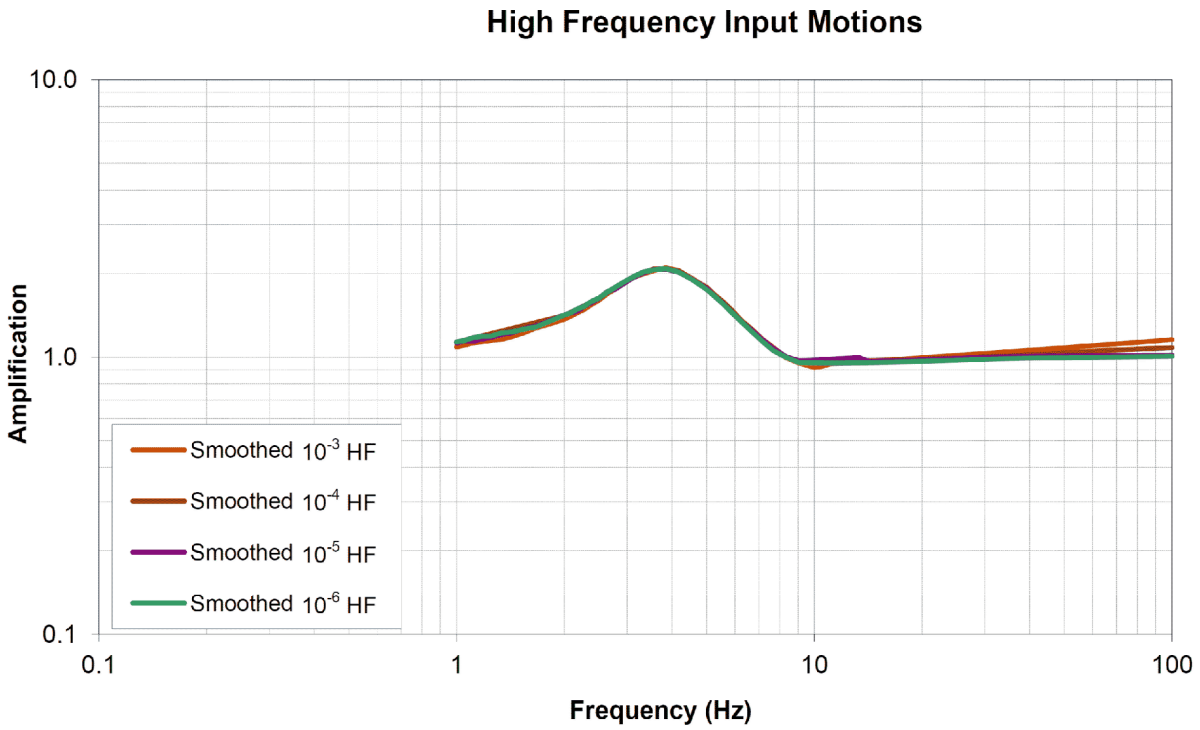

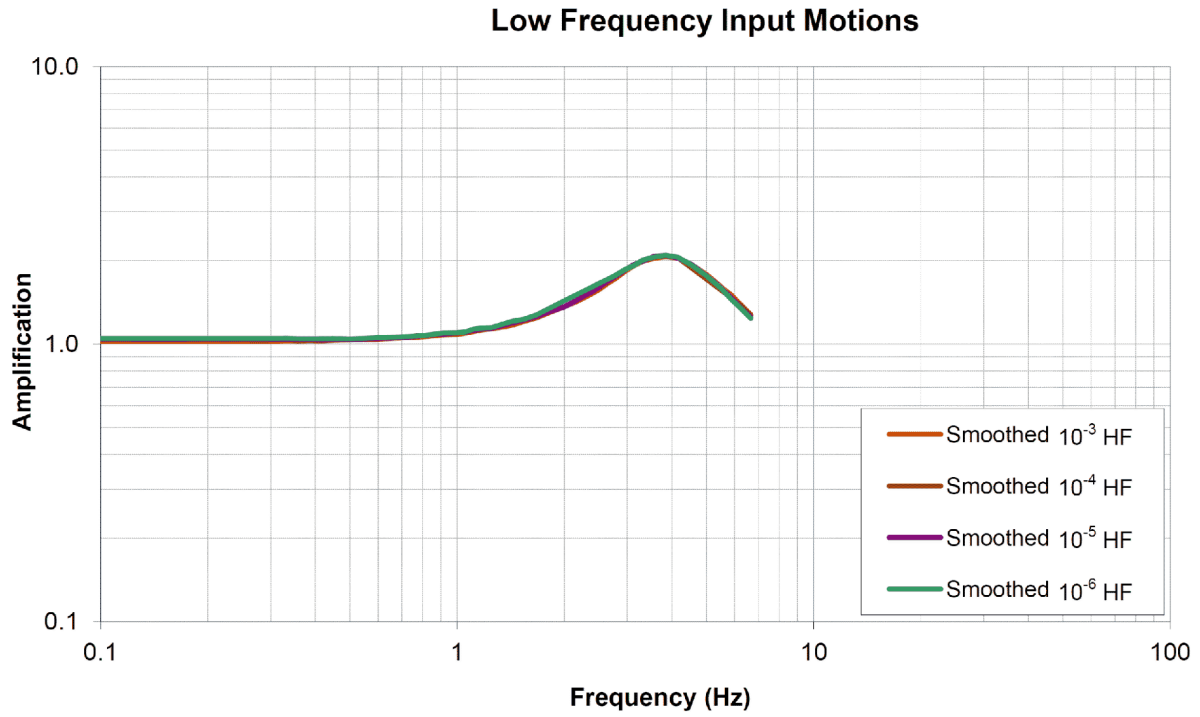

Figure 2.5.2-280 **Statistics of the Effective Strain for the GMRS Profile and 10^{-4} Motions** [EF3 COL 2.0-27-A]

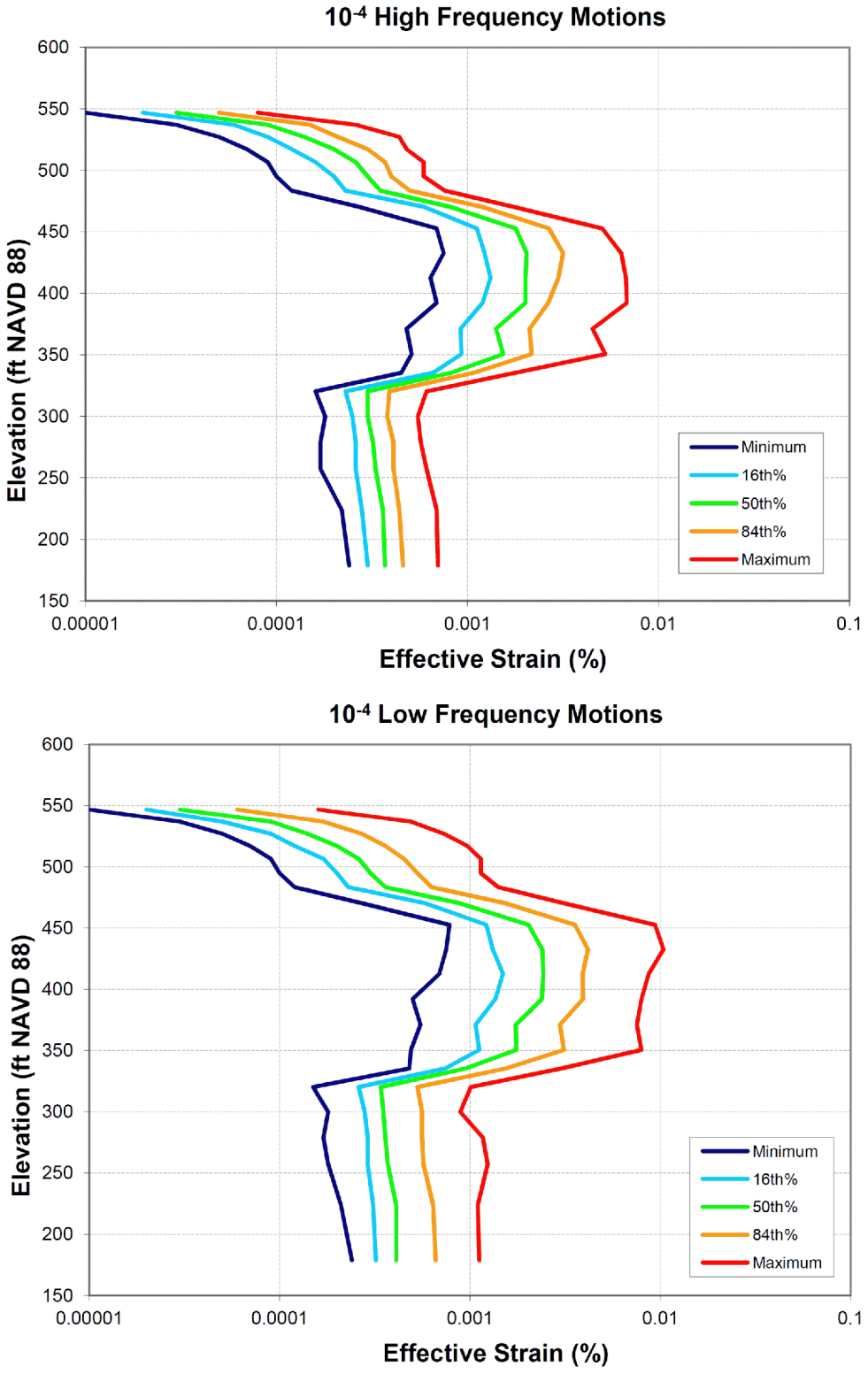

Figure 2.5.2-281 **Statistics of the Effective Strain for the GMRS Profile and 10^{-5} motions** [EF3 COL 2.0-27-A]

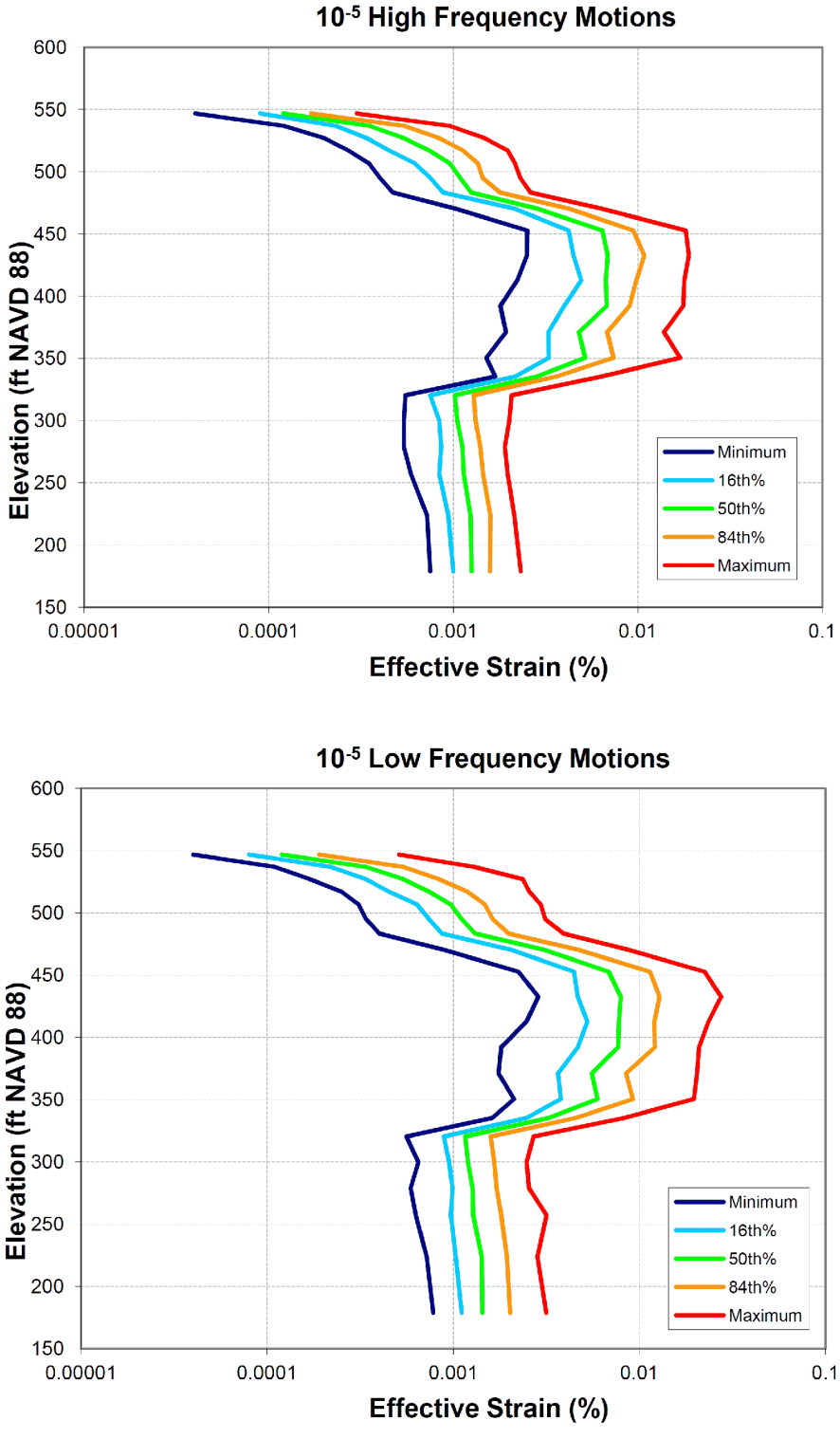

Figure 2.5.2-282 Development of the 10^{-4} Surface UHRS for the GMRS Profile
[EF3 COL 2.0-27-A]

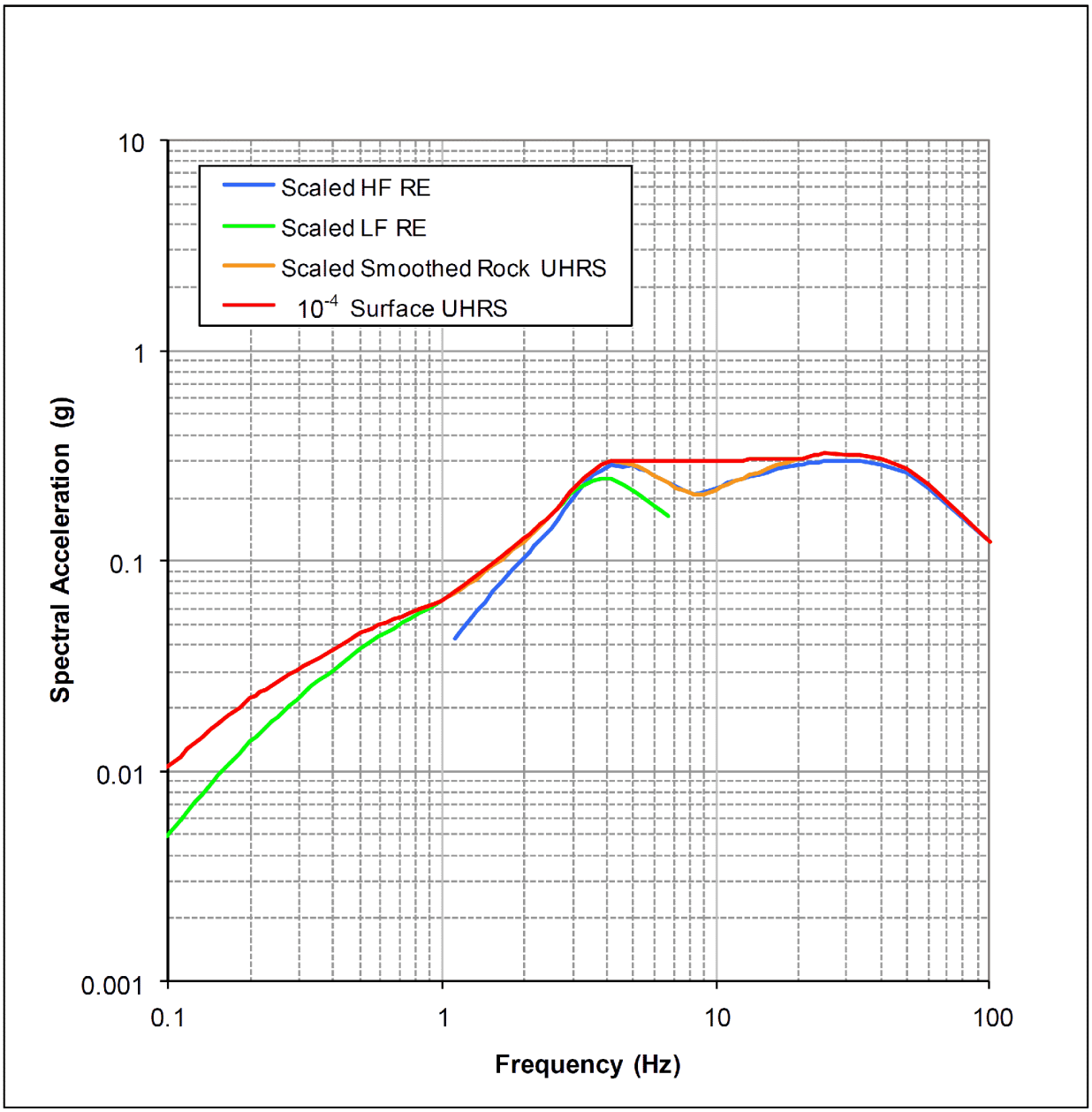

Figure 2.5.2-283 UHRS for the GMRS Elevation [EF3 COL 2.0-27-A]

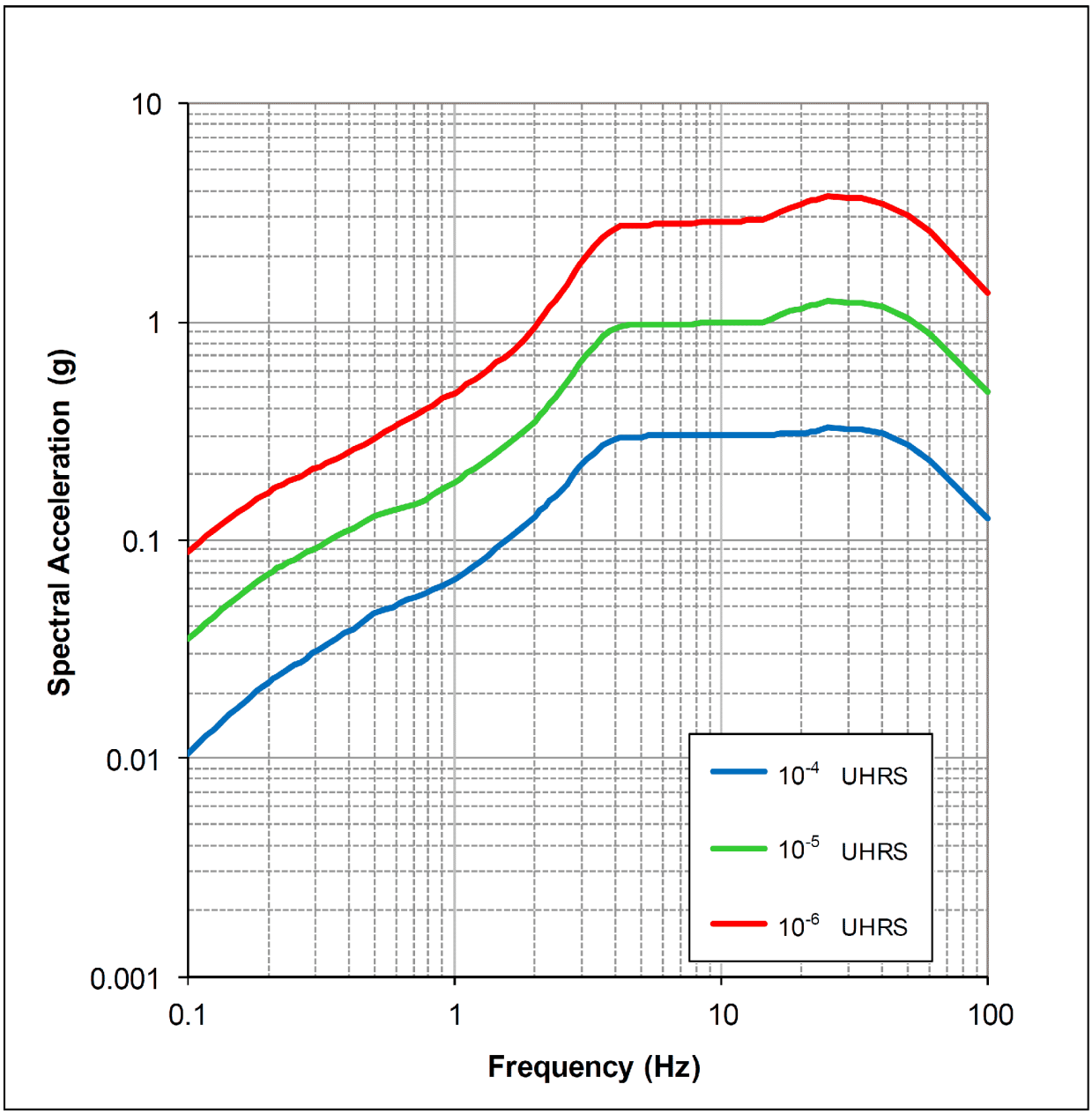

Figure 2.5.2-284 Development of Horizontal GMRS for the Fermi 3 Site
[EF3 COL 2.0-27-A]

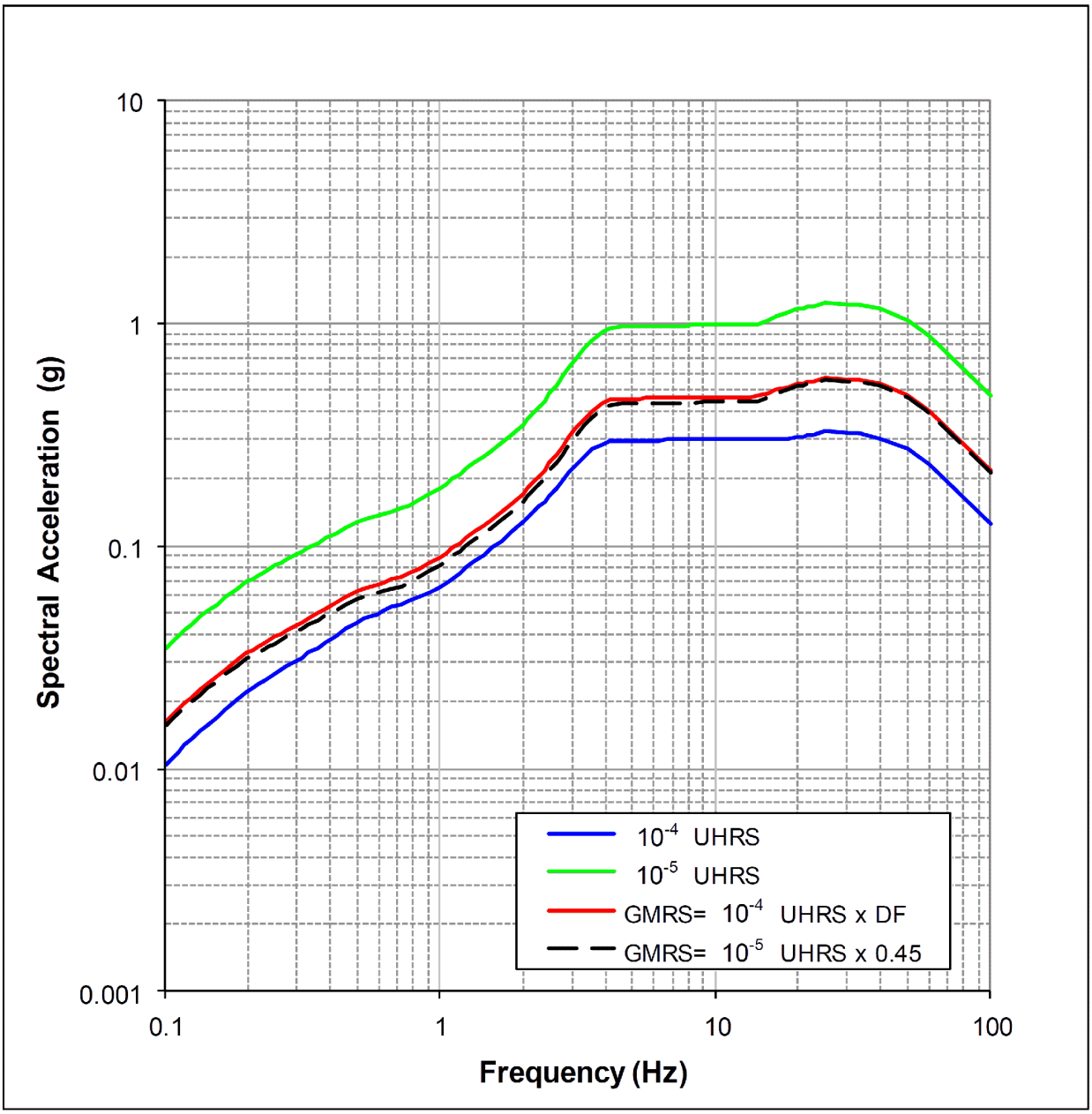

Figure 2.5.2-285 **Vertical-to-Horizontal Spectral Ratios for Generic CEUS Hard Rock** [EF3 COL 2.0-27-A]

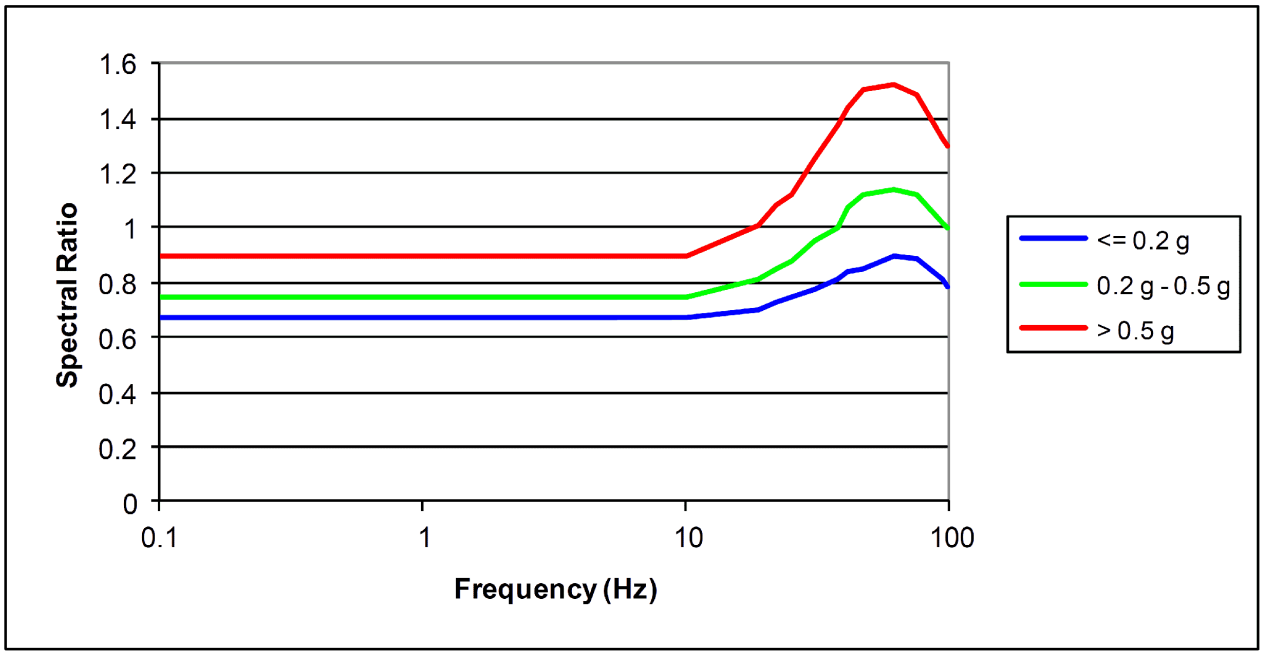

Figure 2.5.2-286 Fermi 3 GMRS (5 Percent Damping) with Comparison to CSDRS
[EF3 COL 2.0-27-A]